NONLINEAR OPTICAL GENERATION OF MULTIMODE ENTANGLED SQUEEZED THERMAL STATES

BY COLIN VENDROMIN

A thesis submitted to the

Department of Physics, Engineering Physics and Astronomy

in conformity with the requirements for

the degree of Doctorate of Philosophy

Queen's University
Kingston, Ontario, Canada
January, 2023

Abstract

Squeezed states of light exhibit a reduction of quantum noise in one of their phase-space quadratures. They can be generated via a nonlinear interaction between a laser and a nonlinear dielectric material. Multimode squeezed states of light contain entanglement in the form of correlations between the quadratures of the modes in the state. Scattering loss in the dielectric material used to generate the squeezed state reduces the amount of squeezing and the strength of the correlations between the modes in the state. In this thesis, I consider the nonlinear generation of multimode squeezed states in resonant structures. The modes of these structures are inherently lossy due to scattering and coupling loss and also form a nonorthogonal basis in general. The central result of this thesis is that I show the analytic solution of the Lindblad master equation for the density operator of the generated light in the multiple lossy nonorthogonal modes of a structure has the form of a *multimode squeezed thermal state*. I show that using the analytic solution makes it fast to calculate the amount of quadrature squeezing and the strength of the correlations between modes in the state as a function of time. I apply this theory to the nonlinear generation of a single-mode and two-mode squeezed thermal state in a microring resonator, and I optimize the coupling parameters of the ring to maximize the squeezing in the presence of loss or to obtain a two-mode squeezed thermal state in which the two modes are highly-correlated despite the loss. In addition, I derive a squeezing criterion that if the multimode squeezed thermal state obeys it can be considered as a cluster state and be used for continuous-variable quantum computing. Therefore, the multimode squeezed thermal state is the natural state to describe the nonlinearly generated light in systems of coupled-cavities and it provides a simply way to incorporate loss into a practical theory of entangled squeezed light generation, which opens a path to optimize this light for applications in quantum technologies.

Acknowledgments

I would like to first acknowledge my supervisor Marc M. Dignam for his consistent support, patience, and guidance during the four years of my PhD. I am forever grateful for the opportunity that he has given me to pursue my dream of participating in academic research. Also, I want to acknowledge my family for always believing in me and encouraging me to carry on. And I want to thank Sahar for building me up, pushing me forward, and all her emotional support.

Dedicated to the memory of my father, John Vendromin.

Statement Of Originality

I hereby certify the intellectual content of this thesis is the product of my own work. Any assistance that I received in preparing this thesis has been fully acknowledged.

Glossary of Abbreviations

CROW	Coupled-resonator optical waveguide.
CV	Continuous-variable.
LME	Gorini–Kossakowski–Sudarshan–Lindblad master equation.
MRR	Microring resonator.
MSTS	M-mode (multimode) squeezed thermal state.
MSVS	M-mode (multimode) squeezed vacuum state.
OPO	Optical parametric oscillator.
SFWM	Spontaneous four-wave mixing.
SPDC	Spontaneous parametric down-conversion.

Contents

List of Tables

List of Figures

Chapter 1

Introduction

Quantum optics is a branch of research that combines the subjects of quantum mechanics and electromagnetism. One of the first insights that these two subjects could be combined was in 1905 with Einstein's explanation of the photoelectric effect, a phenomenon whereby electrons are emitted from a material when hit with light, and the energy of the emitted electrons increases with the frequency of the incident light. At the time, the dominant theory of light was Maxwell's theory that describes light as an electromagnetic wave. However, his theory incorrectly predicted that, in the photoelectric effect experiments, the energy of the emitted electrons should increase with the intensity of the incident light. Einstein solved this problem by using Planck's postulate from quantum theory that states the energy of the electromagnetic wave is carried by quantized packets of energy proportional to frequency, called photons. Thus, he showed that the electrons were being emitted from the material because photons were colliding with the surface and imparting their energy. This gave way to the idea of the dual nature of light since it exhibits both wave and particle characteristics.

The quantization of the electromagnetic field led to quantum states of light that have no classical counterpart, such as states of light made from individual photons. One of the consequences of the quantization of the electromagnetic field is that there exists a vacuum state of the field, which has no photons but still exhibits fluctuations in the intensity of the field. Remarkably, the intensity fluctuations of the vacuum state create a measurable attractive force between parallel metal plates, placed close enough together in the vacuum, called the Casimir force [1]. Vacuum fluctuations have a negative effect on the sensitivity of measurements made with laser interferometers because the noise causes a dark count on the photon detector. However, researchers discovered a nonclassical state of light called a squeezed state that could improve the sensitivity of the interferometer [2]. Squeezed states exhibit a reduction of the vacuum fluctuations in a certain quadrature. Therefore, if a squeezed state is injected into the port of the interferometer instead of the vacuum, then the dark count of the photon detector can be reduced and the contrast between the bright and dark fringes increases.

One way to generate nonclassical states of light is with a nonlinear interaction, such as spontaneous parametric down-conversion (SPDC) [3], between a laser (called the pump) and a crystal with a second-order nonlinearity. In SPDC, pump photons from the laser are absorbed by the crystal and pairs of signal and idler photons are emitted (see Fig. 1.1). The frequency of the signal and idler photons add up to the frequency of the pump photons so that energy is conserved ($\omega_p = \omega_s + \omega_i$), and the wavevectors of the signal and idler photons add up to the wavevector of the pump photons so that momentum is conserved ($\boldsymbol{k}_p = \boldsymbol{k}_s + \boldsymbol{k}_i$). Not only is this a source of individual photons, but the emitted signal and idler photons have polarizations that are highly correlated.

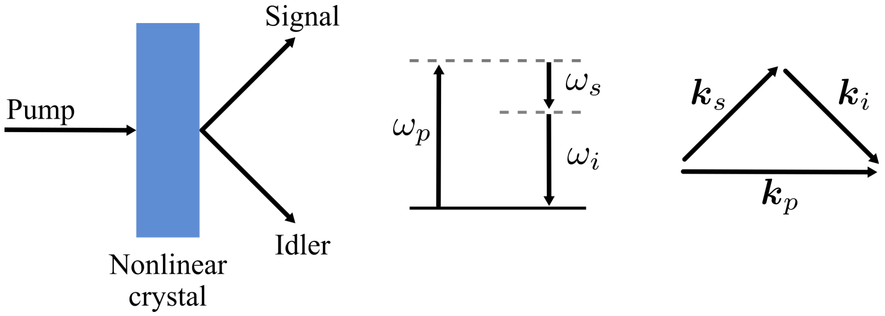

Figure 1.1: Illustration of SPDC using a nonlinear crystal (left), as well as illustrations of energy conservation (center) and momentum conservation (right).

One approach to enhance the generation of photons via SPDC is to place the nonlinear material inside an optical cavity. The wavelengths of light that are resonant with the cavity will buildup their intensity due to coherent interference. In Fig. 1.2(a) an illustration of an optical parametric oscillator (OPO) is shown. It consists of a nonlinear crystal inside of a cavity created with mirrors, that is resonant with the signal (blue) and transparent to the idler (red) and pump (purple). This OPO generates signal and idler photons via SPDC and enhances the generated signal light through coherent interference. Variations of this design include a cavity that is resonant with two of the fields (*e.g.* signal and idler) or all three fields. Another approach similar to this is to use a microring resonator (MRR), as shown in Fig. 1.2(b). It consists of a ring waveguide side-coupled to a channel, where both are made from the same nonlinear material. The pump (blue) resonantly couples from the channel into the ring, where it builds up intensity relative to the channel. This causes an enhancement in the generation rate of signal and idler photons (both shown as red) via SPDC. The signal and idler wavelengths are both resonant with the ring and they can couple out of the ring into the channel. The benefit of an MRR is that it is a compact source of nonclassical light that can be integrated into a chip.

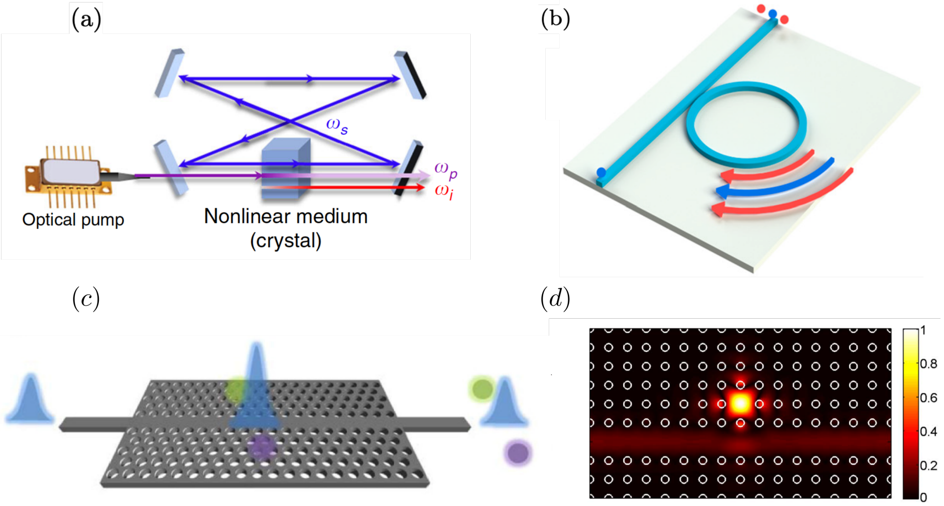

Figure 1.2: Schematics of platforms used to generate photon pairs via a nonlinear interaction with a nonlinear crystal; (a) an OPO [4], (b) a MRR [5], (c) a line-defect waveguide in a photonic crystal slab [6], and (d) a defect-cavity side-coupled to a line-defect waveguide [7].

Another platform used to generate nonclassical light is a photonic crystal slab, which can be created by drilling a lattice of airholes into a nonlinear material (see Figs. 1.2(c) and 1.2(d)). In Fig. 1.2(c) a line-defect waveguide is created in the photonic crystal by removing a row of airholes. The pump (blue) propagates in the waveguide and creates signal (green) and idler (purple) photons. For the system in Fig. 1.2(c) the group velocity for the pump pulse is small, causing its amplitude to increase and allowing for a longer interaction time for SPDC. These two factors enhance the generation rate of signal and idler photons [8]. Alternatively, a photonic crystal can be constructed where a defect-cavity is side-coupled to the waveguide. The cavity can be made to be resonant with the pump, signal, and idler light and used to enhance SPDC. In Fig. 1.2(d) the intensity of the electric field in a single mode of the structure consisting of a defect-cavity side-coupled to a waveguide is shown. The intensity of the field is larger in the cavity relative to the waveguide, similar to a MRR.

In all these structures there is photon loss due to scattering, which causes the modes of the electromagnetic field in these structures to be lossy [9, 10]. The lossy modes are eigenstates of a non-Hermitian Hamiltonian and are nonorthogonal in general. This is because the standard arguments used to prove the modes are orthogonal rely on the modes being lossless and being eigenstates of a Hermitian Hamiltonian [11]. Therefore, any realistic model of the generation of quantum states of light in these structures must take into account the effects of photon loss due to scattering and the mode nonorthogonality.

Nonclassical light also exhibits the property of entanglement, which is one of the central concepts that distinguishes quantum mechanics from classical mechanics. In 1935 Einstein, Podolsky, and Rosen (EPR) using quantum theory theoretically showed that two distant particles that share an inseparable wave function had momenta that were correlated [12]. These are known as an EPR pair. This violated the classical principle of locality, where particles can only be influenced by local interactions. For this reason, it was argued that quantum mechanics was not a complete theory and additional variables should be included to restore local reality. In 1964, Bell derived an inequality, consisting of statistical correlation measurements of the momenta of the two particles, that would be obeyed if local hidden variables were included in quantum mechanics [13]. Bell's inequality was tested experimentally in 1982, by Aspect, Grangier, and Roger [14]. In their experiment, they created EPR pairs with photons. The photon pairs were created simultaneously and sent in opposite directions where polarization measurements were done on them individually.

They found that the polarization measurements exhibited correlations that violated Bell's inequality, demonstrating experimentally that local hidden variables is not consistent with quantum theory.

Since the pioneering theory of entanglement and its experimental evidence, entangled photons have found applications in quantum teleportation [15], secure quantum key distribution [16], and quantum computing [17]. It is also possible now to create multipartite entangled photon states where the entangled state is shared between multiple parties rather than just two [18]. Examples of multipartite entangled photon states include GHZ states, W states, and cluster states [19, 20]. GHZ states are maximally entangled, meaning that each photon pair in the cluster can be projected into an EPR pair. However, the entanglement is very sensitive to photon measurement. If the polarization of a single photon in the GHZ state is measured, then all the entanglement in the state is destroyed. On the other hand, W states are resilient to photon measurement, because many photons in the W state can be measured before all the entanglement is destroyed. However, the W state is not maximally entangled. Cluster states are another multipartite entangled state that contain the best qualities from GHZ and W states. Cluster states are maximally entangled and have a high persistency of entanglement. The cluster state has gained a lot of attention from researchers because it is a resource for measurement-based quantum computing.

Fully programmable quantum computers on the order of 100 qubits are currently accessible to anyone over the cloud. In 2021, IBM announced they created a programmable quantum computer with 127 superconducting qubits, that they claim cannot be simulated by any classical computer. By the end of 2023, IBM predicts they will have a quantum processor with over 1000 qubits. Alternatively, quantum computers can be made using photons. In 2022, a company based in Toronto, Ontario called Xanadu created the first programmable photonic quantum computer, with over 216 squeezed-state qubits, that is capable of quantum computational advantage [21]. Relative to superconducting qubits, photonic qubits have the advantage that they do not require cryogenic temperatures to operate. With the progress being made by companies such as IBM and Xanadu, the future looks bright for quantum computers and their applications.

The objective of thesis is to characterize the quantum state of light that is produced via nonlinear optical processes in the multiple nonorthogonal modes of systems of coupled, lossy cavities, like the ones in Fig. 1.2. As I will show, this opens a practical path to generate optimized sources of multimode entangled light that can be used as an entanglement source for applications in quantum technologies. In the remainder of this introduction, I discuss several quantum states of light important to this thesis, quantum entanglement and some ways to characterize the entanglement in nonclassical states, and finally I introduce continuous-variable (CV) cluster states.

1.1 Quantum states of light

In quantum optics, the Heisenberg picture electric field operator for a multimode system, $\widehat{\boldsymbol{E}}(\boldsymbol{r},t)$, can be written as

$$\widehat{\boldsymbol{E}}(\boldsymbol{r},t) = i\sum_{\nu}\sqrt{\frac{\hbar\omega_\nu}{2\epsilon_0}}\left(\widehat{a}_\nu\boldsymbol{f}_\nu(\boldsymbol{r})\mathrm{e}^{-i\omega_\nu t} - \widehat{a}_\nu^\dagger\boldsymbol{f}_\nu^*(\boldsymbol{r})\mathrm{e}^{i\omega_\nu t}\right), \tag{1.1}$$

where $\widehat{a}_\nu$ and $\widehat{a}_\nu^\dagger$ are the annihilation and creation operator for a single mode of the field, ν, with the frequency ω_ν, and mode function $\boldsymbol{f}_\nu(\boldsymbol{r})$. Here the label ν serves as an index to label the mode and it may be discrete or it may be continuous, depending on the boundary conditions imposed on the mode functions. The mode functions, $\boldsymbol{f}_\nu(\boldsymbol{r})$, are a solution to the Maxwell equations with outgoing wave boundary conditions and they form a complete orthonormal basis. The annihilation and creation operators satisfy the standard bosonic commutation relation

$$\left[\widehat{a}_\nu, \widehat{a}^\dagger_{\nu'}\right] = \delta_{\nu\nu'}. \tag{1.2}$$

It is common to write the electric field operator in terms of the orthogonal quadrature operators $\widehat{X}_\nu$ and $\widehat{Y}_\nu$, since these are obervables that can be measured experimentally. They can be defined as

$$\widehat{X}_\nu \equiv \widehat{a}_\nu \mathrm{e}^{-i\theta_\nu} + \widehat{a}^\dagger_\nu \mathrm{e}^{i\theta_\nu}, \tag{1.3}$$

$$\widehat{Y}_\nu \equiv -i\widehat{a}_\nu \mathrm{e}^{-i\theta_\nu} + i\widehat{a}^\dagger_\nu \mathrm{e}^{i\theta_\nu}, \tag{1.4}$$

which have the same form as dimensionless position and momentum operators, where θ_ν is an angle in phase-space. They are orthogonal quadratures since $\widehat{Y}_\nu$ is equal to $\widehat{X}_\nu$ rotated by $\pi/2$ counter-clockwise in phase-space. Putting Eqs. (1.3) and (1.4) into Eq. (1.1), the electric field operator can be written in terms of the quadrature operators as

$$\widehat{\boldsymbol{E}}(\boldsymbol{r}, t) = -\sum_\nu \sqrt{\frac{\hbar\omega_\nu}{2\epsilon_0}} \left(\mathrm{Im}\left[\boldsymbol{f}_\nu(\boldsymbol{r})\mathrm{e}^{-i(\omega_\nu t-\theta_\nu)}\right] \widehat{X}_\nu + \mathrm{Re}\left[\boldsymbol{f}_\nu(\boldsymbol{r})\mathrm{e}^{-i(\omega_\nu t-\theta_\nu)}\right] \widehat{Y}_\nu\right). \tag{1.5}$$

This form is convenient since it can be used to relate the quantum uncertainty in the electric field operator to the variances of two orthogonal quadrature operators. Using

Eq. (1.2), the quadrature operators satisfy the commutation relation

$$\left[\widehat{X}_{\nu}, \widehat{Y}_{\nu'}\right] = 2i\delta_{\nu\nu'}. \tag{1.6}$$

The commutation relation in Eq. (1.6) implies that the orthogonal quadrature operators obey the uncertainty relation

$$\Delta X_{\nu} \Delta Y_{\nu} \geq 1, \tag{1.7}$$

where

$$\Delta X_{\nu} \equiv \sqrt{\langle \widehat{X}_{\nu}^{2} \rangle - \langle \widehat{X}_{\nu} \rangle^{2}}, \tag{1.8}$$

$$\Delta Y_{\nu} \equiv \sqrt{\langle \widehat{Y}_{\nu}^{2} \rangle - \langle \widehat{Y}_{\nu} \rangle^{2}}, \tag{1.9}$$

are the standard deviations of the quadrature operators $\widehat{X}_{\nu}$ and $\widehat{Y}_{\nu}$, respectively. The angle brackets, $\langle\rangle$, indicate that an average is to be taken with a particular state of light. I refer to $(\Delta X_{\nu})^2$ or $(\Delta Y_{\nu})^2$ as the *quadrature noise*. The quadrature noise can be measured directly with homodyne detection, where the electric field signal is mixed with a strong local oscillator at the input ports of a beamsplitter and the noise that is detected in the output port of the beamsplitter is proportional to the quadrature noise of the input signal. The quadrature of the electric field that is measured is determined by the phase of the local oscillator. For a quantum state of light, the product of its quadrature uncertainties, $\Delta X_{\nu} \Delta Y_{\nu}$, is always greater than or equal to one, as stated in Eq. (1.7). The minimum value of the uncertainty relation quantifies the vacuum fluctuations, which in terms of a photon number measurement they correspond to the dark count of the photon detector. For the quadrature operators defined in Eqs. (1.3) and (1.4), the quadrature noise for a vacuum state is equal to one.

Quantum states of light can be visualized in a phase space, that has orthogonal axes defined by X and Y (see Fig. 1.3). In classical phase space there exists a probability distribution function, $f(X,Y)$, that gives the simultaneous probability of finding the state at the point (X,Y) in phase space. In quantum optics, the uncertainty product (Eq. (1.7)) forbids this type of probability distribution in phase space that gives the simultaneous probability of finding the state at a point (X,Y). However, there exists a useful function to visualize quantum states of light called the *Wigner function*, which is generally considered a quasiprobability distribution because it can in general have negative values, unlike conventional probability distributions. The Wigner function for a quantum state of light given by the density operator $\widehat{\rho}$ is defined as

$$W(X,Y) = \frac{1}{(2\pi)^2} \iint dX'dY' \mathrm{Tr}\left(\widehat{\rho} \mathrm{e}^{-i(X'\widehat{Y}+Y'\widehat{X})}\right) \mathrm{e}^{i(X'Y+Y'X)}, \tag{1.10}$$

where Tr is the trace operation. The Wigner function is normalized according to

$$\iint dXdYW(X,Y) = 1. \tag{1.11}$$

If the Wigner function for a particular quantum state of light has a negative value anywhere in phase space, then it has no classical analogue and it is called a non-classical state of light. Examples of the Wigner function for various quantum states are shown in the subsections below.

Now the following three quantum states of light are introduced: 1) Fock states, which are eigenstates of the harmonic oscillator Hamiltonian and are the natural states used to describe light as a collection of individual photons; 2) coherent states, which are eigenstates of the annihilation operator and are the closest quantum state to a classical field; and 3) squeezed states, which exhibit a reduction of the vacuum noise in one of the quadratures of the electric field, contain the uniquely quantum property of entanglement, and are widely used in applications ranging from increased inference fringe visibility in an interferometer to quantum computing and quantum information processing.

1.1.1 Fock states

Consider a system of M modes and in each mode, labelled by ν, there are n_ν photons. The state of this system, $|\boldsymbol{n}\rangle$, is given by a tensor product of the Fock states in each mode:

$$|\boldsymbol{n}\rangle = |n_1\rangle\, |n_2\rangle \ldots |n_M\rangle\,, \tag{1.12}$$

where $|n_\nu\rangle$ (for $\nu = 1, 2, \ldots, M$) is the Fock state for the mode ν. The Fock states are orthonormal, such that

$$\langle n_\nu | n_{\nu'}\rangle = \delta_{\nu\nu'}. \tag{1.13}$$

The annihilation and creation operators $\widehat{a}_\nu$ and $\widehat{a}^\dagger_\nu$ act on the mode ν only in the full state of the system, $|\boldsymbol{n}\rangle$, and they lower or raise the photon number in that mode by one:

$$\widehat{a}_\nu \left|n_1\right\rangle \left|n_2\right\rangle \ldots \left|n_\nu\right\rangle \ldots \left|n_M\right\rangle = \sqrt{n_\nu} \left|n_1\right\rangle \left|n_2\right\rangle \ldots \left|n_\nu - 1\right\rangle \ldots \left|n_M\right\rangle , \tag{1.14}$$

$$\widehat{a}_\nu^\dagger \left|n_1\right\rangle \left|n_2\right\rangle \ldots \left|n_\nu\right\rangle \ldots \left|n_M\right\rangle = \sqrt{n_\nu + 1} \left|n_1\right\rangle \left|n_2\right\rangle \ldots \left|n_\nu + 1\right\rangle \ldots \left|n_M\right\rangle . \tag{1.15}$$

The vacuum state is defined as a Fock state with zero photons, $n_\nu = 0$. It can be written as $\left|0\right\rangle$. From Eq. (1.14) is can be seen that when the annihilation operator acts on the vacuum the result is zero, $\widehat{a}_\nu \left|0\right\rangle = 0$. A single-mode Fock state with n_ν photons can be created by repeatedly acting on the vacuum n_ν times with the creation operator,

$$\left|n_\nu\right\rangle = \frac{\left(\widehat{a}_\nu^\dagger\right)^{n_\nu}}{\sqrt{n_\nu!}} \left|0\right\rangle . \tag{1.16}$$

The number operator is defined as $\widehat{a}_\nu^\dagger \widehat{a}_\nu$, since when it acts on the system ket $\left|\boldsymbol{n}\right\rangle$ it gives the photon number for the mode ν (which follows from Eqs. (1.14) and (1.15)). Therefore, the Fock state $\left|n_\nu\right\rangle$ in Eq. (1.16) is an eigenstate of the number operator with eigenvalue n_ν,

$$\widehat{a}_\nu^\dagger \widehat{a}_\nu \left|n_\nu\right\rangle = n_\nu \left|n_\nu\right\rangle . \tag{1.17}$$

Now I will calculate the quadrature noise in a single mode ν using the Fock state in Eq. (1.16). It can be shown, using Eqs. (1.8) and (1.9), that the uncertainty in both quadratures are equal and given by

$$\Delta X_\nu = \Delta Y_\nu = \sqrt{2n_\nu + 1}. \tag{1.18}$$

The quadrature noises, $(\Delta X_\nu)^2$ and $(\Delta Y_\nu)^2$, increase linearly with the number of photons in the mode. When the photon number is zero, $n_\nu = 0$, the quadrature noise is minimized, with $(\Delta X_\nu)^2 = (\Delta Y_\nu)^2 = 1$, which is the vacuum noise. Therefore the uncertainty product for Fock states (Eq. (1.7)) is at its minimum for $n_\nu = 0$. The Wigner function of the Fock state $|1\rangle$ is shown in Fig. 1.3(a). Putting $\widehat{\rho} = |1\rangle\langle 1|$ into Eq. (1.10), we obtain

$$W(X,Y) = \frac{2}{\pi}\big(4(X^2+Y^2)-1\big)\exp\big(-2(X^2+Y^2)\big). \tag{1.19}$$

The Wigner function is centred on the point $(X,Y) = (0,0)$ since $\langle 1|\widehat{X}_\nu|1\rangle = \langle 1|\widehat{Y}_\nu|1\rangle = 0$. The spread of the Wigner function around the point $(0,0)$ is proportional to the uncertainty product in Eq. (1.18) and thus it will increase when the photon number increases. Since the Wigner function has negative values, it is a quasiprobability distribution and the Fock state has no classical analogue.

1.1.2 Coherent states

A single-mode coherent state $|\alpha_\nu\rangle$ is the eigenstate of the annihilation operator $\widehat{a}_\nu$ with eigenvalue α_ν,

$$\widehat{a}_\nu|\alpha_\nu\rangle = \alpha_\nu|\alpha_\nu\rangle\,. \tag{1.20}$$

Using Eq. (1.20), it can be shown that the expected photon number for the coherent state is given by $n_\nu = |\alpha_\nu|^2$. An M-mode coherent state, $|\boldsymbol{\alpha}\rangle$, can be defined as a

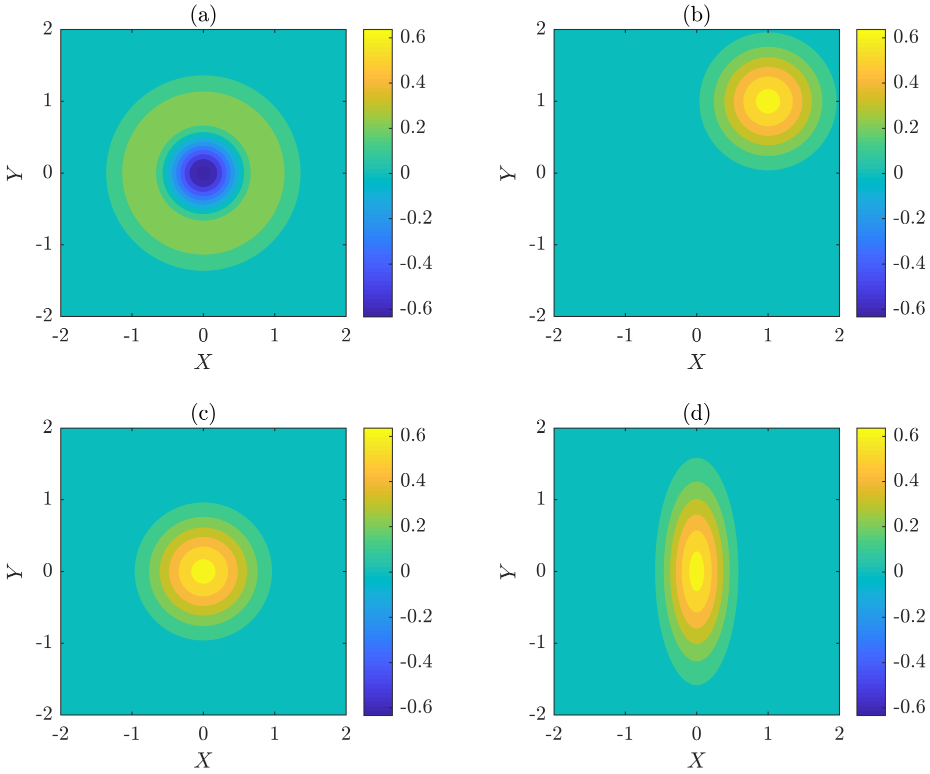

Figure 1.3: Phase-space Wigner functions for (a) the Fock state $|1\rangle$, (b) a single-mode coherent state, $|\alpha_\nu\rangle$, with complex amplitude $\alpha_\nu = \sqrt{2}\exp(i\pi/4)$, (c) the vacuum state $|0\rangle$, and (d) a single-mode squeezed vacuum state with squeezing amplitude $u_\nu = 1/2$, that is squeezed along the X-axis.

tensor product of M single-mode coherent states as

$$|\boldsymbol{\alpha}\rangle = |\alpha_1\rangle\,|\alpha_2\rangle \ldots |\alpha_M\rangle\,. \tag{1.21}$$

The eigenvalue equation for for the M-mode coherent state is

$$\widehat{a}_\nu\,|\boldsymbol{\alpha}\rangle = \alpha_\nu\,|\boldsymbol{\alpha}\rangle\,. \tag{1.22}$$

The coherent state can be constructed from the vacuum state using a unitary displacement operator $\widehat{D}(\alpha_\nu)$ as

$$|\alpha_\nu\rangle = \widehat{D}(\alpha_\nu)\,|0\rangle\,, \tag{1.23}$$

where

$$\widehat{D}(\alpha_\nu) = \exp\bigl(\alpha_\nu \widehat{a}_\nu^\dagger - \alpha_\nu^* \widehat{a}_\nu\bigr). \tag{1.24}$$

The M-mode coherent state is obtained by acting on the vacuum state with M displacement operators,

$$|\boldsymbol{\alpha}\rangle = \widehat{D}(\alpha_1)\widehat{D}(\alpha_2)\ldots\widehat{D}(\alpha_M)\,|\mathbf{0}\rangle\,. \tag{1.25}$$

The displacement operator transforms the annihilation operator $\widehat{a}_\nu$ by displacing it by the amplitude α_ν,

$$\widehat{D}^\dagger(\alpha_\nu)\widehat{a}_\nu\widehat{D}(\alpha_\nu) = \widehat{a}_\nu + \alpha_\nu. \tag{1.26}$$

The expectation value the electric field operator (Eq. (1.1)) using $|\boldsymbol{\alpha}\rangle$ is

$$\langle\boldsymbol{\alpha}|\,\widehat{\boldsymbol{E}}(\boldsymbol{r},t)\,|\boldsymbol{\alpha}\rangle = i\sum_\nu \sqrt{\frac{\hbar\omega_\nu}{2\epsilon_0}}\left(\alpha_\nu \boldsymbol{f}_\nu(\boldsymbol{r})\mathrm{e}^{-i\omega_\nu t} - \alpha_\nu^* \boldsymbol{f}_\nu^*(\boldsymbol{r})\mathrm{e}^{i\omega_\nu t}\right), \tag{1.27}$$

which looks like a classical field. Furthermore, it can be shown (using Eqs. (1.8) and

(1.9)) that the quadrature uncertainties of the electric field operator are given by

$$\Delta X_\nu = \Delta Y_\nu = 1, \tag{1.28}$$

which is the vacuum noise. The coherent state is the quantum state of light that is the closest to a classical state because it reproduces the classical field expectation value and it only contains the vacuum noise, thus minimizing the uncertainty product. The Wigner function of the single-mode coherent state $|\alpha_\nu\rangle$ is shown in Fig. 1.3(b). The Wigner function is a vacuum state ($\alpha_\nu = 0$) (see Fig. 1.3(c)) that is displaced with a displacement operator with the amplitude $\alpha_\nu = \sqrt{2}\exp(i\pi/4)$. This causes the center of the distribution to be at the point $(\langle\alpha_\nu|\,\widehat{X}_\nu\,|\alpha_\nu\rangle\,, \langle\alpha_\nu|\,\widehat{Y}_\nu\,|\alpha_\nu\rangle) = (1,1)$. The spread of the Wigner function around the point $(1,1)$ is a circle with radius ΔX_ν equal to the vacuum noise, $\Delta X_\nu = 1$. Increasing the photon number displaces the center of the Wigner function out to a larger radius, but its spread will always equal the spread of the vacuum state. Putting $\widehat{\rho} = |\alpha_\nu\rangle\langle\alpha_\nu|$ into Eq. (1.10), we obtain for the Wigner function

$$W(X,Y) = \frac{2}{\pi}\exp\bigl(-2\left((X-1)^2 + (Y-1)^2\right)\bigr), \tag{1.29}$$

where we used $\alpha_\nu = \sqrt{2}\exp(i\pi/4)$.

1.1.3 Squeezed states

In this subsection I introduce the last quantum state that will be discussed, and the most important state for this thesis. In the previous subsection, it was demonstrated that coherent states have quadrature noise equal to the noise due to vacuum fluctuations. Squeezed states of light exhibit a reduction of the noise in a particular quadrature below the vacuum noise. However, to obey the uncertainty relation, the noise in the orthogonal quadrature to the squeezed one is anti-squeezed, with a noise level above the vacuum noise. The more squeezed the noise is in a particular quadrature, the more stretched it becomes in the orthogonal quadrature, such that the product of the uncertainties is always greater than or equal to one. Squeezed states have applications in any experiments that suffer from noise due to vacuum fluctuations. Incorporating a squeezed state into the experiment, instead of vacuum, can reduce the noise in the experiment and provide more precise measurements. They have found use in a wide range of applications, such as in interferometers used for gravitational wave detection, quantum imaging systems, and quantum cryptography. Moreover, as I will show, multimode squeezed states are a source of entanglement, and they have applications in quantum computing, quantum communication, and highly entangled many-body states such as cluster states. Squeezed states can be generated experimentally by a nonlinear interaction between a coherent laser beam and a nonlinear material with a second or third order nonlinearity. The main types of nonlinear interactions to generate squeeze states that are considered in this thesis are SPDC and spontaneous four-wave mixing (SFWM).

The single-mode squeezed vacuum state, $|z_\nu\rangle$ is obtained by acting on the vacuum with the unitary squeezing operator, $\widehat{S}(z_\nu)$,

$$|z_\nu\rangle = \widehat{S}(z_\nu)\,|0\rangle\,, \tag{1.30}$$

where z_ν is the complex squeezing parameter for the mode ν, and where

$$\widehat{S}(z_\nu) = \exp\left(\frac{1}{2} z_\nu \widehat{a}_\nu^{\dagger 2} - \frac{1}{2} z_\nu^* \widehat{a}_\nu^2\right). \tag{1.31}$$

The single-mode squeezed state is formed by $\widehat{S}(z_\nu)$ creating pairs of photons out of the vacuum, where each photon pair is created in the same mode ν. The squeezing operator transformation of the annihilation operator $\widehat{a}_\nu$ is

$$\widehat{S}^\dagger(z_\nu)\widehat{a}_\nu \widehat{S}(z_\nu) = \cosh(u_\nu)\widehat{a}_\nu + \sinh(u_\nu)\mathrm{e}^{i\zeta_\nu}\widehat{a}_\nu^\dagger, \tag{1.32}$$

where u_ν is the squeezing amplitude and ζ_ν is the squeezing phase, such that the complex squeezing parameter can be written as

$$z_\nu = u_\nu \mathrm{e}^{i\zeta_\nu}. \tag{1.33}$$

The quadrature noises in the mode ν using the single-mode squeezed vacuum state $|z_\nu\rangle$ in Eq. (1.30) can be calculated using Eqs. (1.8), (1.9), and (1.32). They are

$$(\Delta X_\nu)^2 = \mathrm{e}^{2u_\nu} \sin^2\left(\frac{\zeta_\nu}{2} - \theta_\nu\right) + \mathrm{e}^{-2u_\nu} \cos^2\left(\frac{\zeta_\nu}{2} - \theta_\nu\right), \tag{1.34}$$

$$(\Delta Y_\nu)^2 = \mathrm{e}^{2u_\nu} \sin^2\left(\frac{\zeta_\nu}{2} - \theta_\nu\right) - \mathrm{e}^{-2u_\nu} \cos^2\left(\frac{\zeta_\nu}{2} - \theta_\nu\right). \tag{1.35}$$

To demonstrate quadrature squeezing below the vacuum noise, I let the phase-space angle θ_ν be $\theta_\nu = \zeta_\nu/2$. Putting this angle into Eqs. (1.34) and (1.35) results in

$$\Delta X_\nu = \mathrm{e}^{-u_\nu}, \tag{1.36}$$

$$\Delta Y_\nu = \mathrm{e}^{u_\nu}, \tag{1.37}$$

which clearly demonstrates that the noise in the $\widehat{X}_\nu$ quadrature is exponentially squeezed below the vacuum noise ($\Delta X_\nu = 1$) when the squeezing amplitude is greater than zero, $u_\nu > 0$. Consequently, the noise in the $\widehat{Y}_\nu$ quadrature is exponentially increased, so that the uncertainty relation is obeyed. The Wigner function for the single-mode squeezed vacuum state $|z_\nu\rangle$ is shown in Fig. 1.3(d). For this plot the squeezing amplitude is $u_\nu = 1/2$ and $\theta_\nu = \zeta_\nu/2$ so that the noise is squeezed along the X-axis. The Wigner function shows that there is a large uncertainty in the Y value for the squeezed state, but that the state is localized near the line $X = 0$. Putting $\widehat{\rho} = |z_\nu\rangle\langle z_\nu|$ into Eq. (1.10), we obtain for the Wigner function

$$W(X,Y) = \frac{2}{\pi}\exp\left(-\frac{1}{2}X^2\mathrm{e}^{-2u_\nu} - \frac{1}{2}Y^2\mathrm{e}^{2u_\nu}\right). \tag{1.38}$$

Other types of quadrature squeezing can be achieved by changing the phase-space angle θ_ν. For example, if $\theta_\nu = \zeta_\nu/2 + \pi/2$, then the Wigner function would be similar to the one in Fig. 1.3(d) but rotated by the angle $\pi/2$, such that the $\widehat{Y}_\nu$ quadrature would be squeezed and the $\widehat{X}_\nu$ quadrature would be anti-squeezed. As another example, squeezing in a mixture of the quadratures can be demonstrated by letting $\theta_\nu = \zeta_\nu/2 + \pi/4$. Putting this phase-angle into the Eqs. (1.8) and (1.9) results in $((\Delta X_\nu)^2 - (\Delta Y_\nu)^2)/2 = \exp(-2u_\nu)$, where now the distribution of noise is squeezed along an axis parallel to the direction in phase space defined by the angle $\pi/4$, *i.e.*, along the line $Y = X$.

1.2 Quantum entanglement

It has been shown so far that single-mode squeezed vacuum states are useful because they reduce the vacuum fluctuations in a particular quadrature. However, they do not exhibit the quantum property of entanglement. To show that squeezed states contain entanglement the concept of *multimode squeezed states* must be introduced. In these states, the photon pairs are generated into multiple modes and correlations exist between the various quadratures of the modes. Entanglement is commonly first introduced as being encoded in discrete variables such as the polarization of a photon (*e.g.*, horizontal or vertical) or the spin of an electron (*e.g.*, up or down). These are examples of two-level quantum states. However, the entanglement in multimode squeezed states is encoded in the CVs X and Y, therefore this kind of entanglement is called CV entanglement. First I discuss entangled photon pairs, then I move on to CV entanglement in two-mode squeezed states, and finally generalize these results to M-mode squeezed states.

A common way to generate entangled photon pairs is with SPDC with type-II phase matching, as illustrated in Fig. 1.4. It is a process where a nonlinear crystal is pumped with a laser and photons are emitted into two cones, one horizontally polarized and the other vertically polarized. The cones intersect along two paths labelled “1” and “2”, where it is uncertain if the light is horizontally or vertically polarized. The light along these paths can be described by the entangled state

$$|\psi\rangle = \frac{1}{\sqrt{2}} \left(|H\rangle_1 |V\rangle_2 + |V\rangle_1 |H\rangle_2 \right), \tag{1.39}$$

where H and V indicate horizontal and vertical polarization, respectively. The state in Eq. (1.39) is one of the maximally entangled Bell states. If one measures path 1 with $\langle H|_1$ ($\langle V|_1$), then path 2 is guaranteed to be in the state $|V\rangle_2$ ($\langle H|_2$). This is an example of entanglement between the discrete polarization degrees of freedom of the photon pairs. The notion of entanglement can be extended to CVs using a two-mode squeezed state.

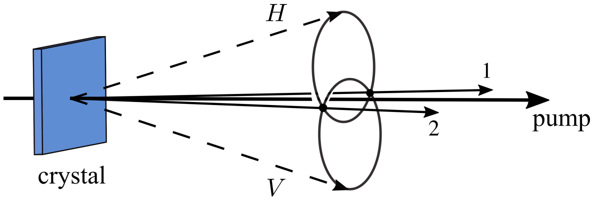

Figure 1.4: Creation of polarization-entangled photon pairs via SPDC with a nonlinear crystal.

A two-mode squeezed state can be obtained by acting on the vacuum state with a two-mode squeezing operator, defined by

$$\widehat{S}(z) \equiv \exp\left(\frac{1}{2} z \widehat{a}_1^\dagger \widehat{a}_2^\dagger - \frac{1}{2} z^* \widehat{a}_1 \widehat{a}_2\right), \tag{1.40}$$

where I have defined it such that the photon pairs are created only in the two distinct modes and I have neglected the creation of photon pairs in the same mode, *i.e.*, terms in $\widehat{S}(z)$ such as $\widehat{a}_1^{\dagger 2}$ and $\widehat{a}_2^{\dagger 2}$ are excluded, since for these processes it is assumed that the squeezing parameter is negligible. Since the squeezing operator is symmetric with respect to the interchange of the two indices, $1 \leftrightarrow 2$, there is only a single squeezing parameter, $z = u \exp(i\zeta)$, for both modes, with squeezing amplitude u and squeezing phase ζ. The two-mode squeezing transformations of the annihilation operators $\widehat{a}_1$

and $\widehat{a}_2$ are

$$\widehat{S}^\dagger(z)\widehat{a}_1\widehat{S}(z) = \cosh(u)\widehat{a}_1 + \mathrm{e}^{i\zeta}\sinh(u)\widehat{a}_2^\dagger, \tag{1.41}$$

$$\widehat{S}^\dagger(z)\widehat{a}_2\widehat{S}(z) = \cosh(u)\widehat{a}_2 + \mathrm{e}^{i\zeta}\sinh(u)\widehat{a}_1^\dagger. \tag{1.42}$$

The two-mode squeezing operator couples the two modes.

The quadrature uncertainties in both modes can be calculated using Eqs. (1.8) using the two-mode squeezed vacuum state $\widehat{S}(z)\left|0\right\rangle$, (1.9), (1.41), and (1.42). Doing this, the uncertainty is equal in both quadratures and both modes and given by

$$\Delta X_1 = \Delta Y_1 = \Delta X_2 = \Delta Y_2 = \sqrt{\cosh(2u)}. \tag{1.43}$$

The result in Eq. (1.43) shows that for either mode individually the quadrature noise is never squeezed, and furthermore since the expression does not depend on the phase-angle, the quadrature noise forms a circle in phase space. It turns out that the noise is squeezed in linear combinations of the quadratures from each mode. Consider the following operators that are formed from linear combinations of the quadrature operators:

$$\widehat{X}_{12} \equiv \frac{1}{\sqrt{2}}\left(\widehat{X}_1 - \widehat{X}_2\right), \tag{1.44}$$

$$\widehat{Y}_{12} \equiv \frac{1}{\sqrt{2}}\left(\widehat{Y}_1 + \widehat{Y}_2\right). \tag{1.45}$$

Using the two-mode squeezed vacuum state, the noise in $\widehat{X}_{12}$ is equal to the noise in

$\widehat{Y}_{12}$ and is given by

$$(\Delta X_{12})^2 = (\Delta Y_{12})^2 = \mathrm{e}^{2u} \sin^2\left(\frac{\zeta - (\theta_1 + \theta_2)}{2}\right) + \mathrm{e}^{-2u} \cos^2\left(\frac{\zeta - (\theta_1 + \theta_2)}{2}\right), \quad (1.46)$$

where θ_1 is the phase-space angle for the first mode and θ_2 is the phase-space angle for the second mode. To show that the noise in these operators is squeezed below the vacuum noise, let $\theta_1 + \theta_2 = \zeta$ in Eq. (1.46) to obtain

$$\Delta X_{12} = \Delta Y_{12} = \mathrm{e}^{-u}, \quad (1.47)$$

which clearly shows the noise is squeezed below the vacuum noise for $u > 0$. Also, the phase-space uncertainty in $\widehat{X}_1 - \widehat{X}_2$ and $\widehat{Y}_1 + \widehat{Y}_2$ is reduced, meaning that there are correlations between the quadratures $\widehat{X}_1$ and $\widehat{X}_2$ and the quadratures $\widehat{Y}_1$ and $\widehat{Y}_2$, such that a homodyne measurement of $\widehat{X}_1$ ($\widehat{Y}_1$) will reduce the set of possible results from a homodyne measurement of $\widehat{X}_2$ ($\widehat{Y}_2$). As a result, the two-mode squeezed state cannot be written as a separable tensor product of single-mode squeezed states in each mode and thus it is an entangled state. L. Duan *et. al.* [22] and R. Simon [23] derived a necessary and sufficient condition for the separability of a two-mode Gaussian state (*e.g.*, a state that has a Gaussian Wigner function). For the operators in Eqs. (1.44) and (1.45) the criterion for the two-mode squeezed state can be written as

$$(\Delta X_{12})^2 + (\Delta Y_{12})^2 \geq 2. \quad (1.48)$$

As long as this inequality is obeyed, then the two-mode squeezed state is separable. Putting the noises in Eq. (1.47) into the left-hand side of the inequality (Eq. (1.48)) results in

$$\left(\Delta X_{12}\right)^2 + \left(\Delta Y_{12}\right)^2 = 2\mathrm{e}^{-2u}. \tag{1.49}$$

Therefore the inequality is violated ($\left(\left(\Delta X_{12}\right)^2 + \left(\Delta Y_{12}\right)^2 < 2\right)$ when the noise is squeezed below the vacuum noise, that is $\exp(-u) < 1$. As an example, in Sec. 3 a two-mode squeezed state is generated in the ring modes of a MRR and it is shown that it violates the Duan-Simon inequality, demonstrating the presence of CV entanglement in the two ring modes.

Now I introduce the M-mode squeezed vacuum state (MSVS). It can be obtained by acting on the vacuum state with an M-mode squeezing operator defined by

$$\widehat{S}(\boldsymbol{z}) \equiv \exp\left(\frac{1}{2}\sum_{\nu=1}^{M}\sum_{\nu'=1}^{M} z_{\nu\nu'}\widehat{a}_{\nu}^{\dagger}\widehat{a}_{\nu'}^{\dagger} - \mathrm{H.c.}\right), \tag{1.50}$$

where $\boldsymbol{z}$ is the complex symmetric squeezing matrix, where the matrix element $z_{\nu\nu'}$ gives the squeezing parameter that couples the modes ν and ν'. The two-mode squeezing operator (Eq. (1.40)) is recovered by letting $M = 2$ and $z_{11} = z_{22} = 0$ in Eq. (1.50), and defining $z \equiv z_{12} + z_{21}$. The M-mode squeezing transformation of the annihilation operator $\widehat{a}_{\nu}$ can be written in a similar form to the single-mode case (Eq. (1.32)). It is given by [24]

$$\widehat{S}^{\dagger}(\boldsymbol{z})\widehat{a}_{\nu}\widehat{S}(\boldsymbol{z}) = \sum_{\nu'=1}^{M}\left(\left[\cosh(|\boldsymbol{z}|)\right]_{\nu\nu'}\widehat{a}_{\nu'} + \left[\sinh(|\boldsymbol{z}|)|\boldsymbol{z}|^{-1}\boldsymbol{z}\right]_{\nu\nu'}\widehat{a}_{\nu'}^{\dagger}\right), \tag{1.51}$$

where $|\boldsymbol{z}|^{-1}$ is the inverse of the matrix $|\boldsymbol{z}| = \sqrt{\boldsymbol{z}^{*}\boldsymbol{z}}$, such that $|\boldsymbol{z}|^{-1}|\boldsymbol{z}| = \mathbf{1}$, where $\mathbf{1}$ is the $M \times M$ identity matrix. The M-mode squeezing operator causes every pair of modes to couple, as long as the squeezing parameter that connects them is non-zero. I have assumed that the matrix $\boldsymbol{z}$ has an inverse and therefore is non-singular (*i.e.*, $\det(\boldsymbol{z}) \neq 0$). If $\boldsymbol{z}$ does not have an inverse, then the second sum in Eq. (1.51) is infinite. In this case, one can perform a polar decomposition on the matrix, $\boldsymbol{z} = \boldsymbol{u}\mathrm{e}^{i\boldsymbol{\zeta}}$, where $\boldsymbol{u}$ and $\boldsymbol{\zeta}$ are Hermitian. Now the squeezing transformation can be written as [25]

$$\widehat{S}^{\dagger}(\boldsymbol{z})\widehat{a}_{\nu}\widehat{S}(\boldsymbol{z}) = \sum_{\nu'=1}^{M}\left([\cosh(\boldsymbol{u})]_{\nu\nu'}\,\widehat{a}_{\nu'} + \left[\sinh(\boldsymbol{u})\mathrm{e}^{i\boldsymbol{\zeta}}\right]_{\nu\nu'}\widehat{a}^{\dagger}_{\nu'}\right). \tag{1.52}$$

The Duan-Simon inequality in Eq. (1.48) can be extended to M-mode Gaussian states to determine if a particular pair of modes, (ν, ν'), in the M-mode squeezed state are entangled. The pair of modes are separable if the following inequality is satisfied [26]:

$$(\Delta X_{\nu\nu'})^2 + (\Delta Y_{\nu\nu'})^2 \geq 2, \tag{1.53}$$

where $\widehat{X}_{\nu\nu'}$ and $\widehat{Y}_{\nu\nu'}$ are defined similar to Eqs. (1.44) and (1.45), but here the indices can take on any value from 1 to M, that is $\nu = 1, 2, \ldots, M$ and $\nu' = 1, 2, \ldots, M$. The noises in Eq. (1.53) can be calculated with Eqs. (1.8) and (1.9), using the MSVS given by $\widehat{S}(\boldsymbol{z})\,|0\rangle$. In Sec. 4 it is shown how to calculate the noise using a multimode squeezed state. The pair of modes (ν, ν') are entangled if the inequality in Eq. (1.53) is violated. This means that the pair of modes (ν, ν') cannot be separated. However, this does not exclude other modes from being separable modes. Thus, violating a single inequality such as in Eq. (1.53) does not show that the MSVS is fully inseparable, it only shows that the pair $(\nu,\ \nu')$ are inseparable.

One way to determine if the MSVS is fully inseparable is to check if it can be separated into a single-mode state in mode 1 and an $(M-1)$-mode state including the modes $2, 3, \ldots, M$. A graphical representation of a fully inseparable 4-mode state is shown in Fig. 1.5(a) and a representation of a 4-mode state where mode 1 is separate from the other modes is shown in Fig. 1.5(b). To test if the state is separable in this way the following operators are defined:

$$\widehat{X} \equiv \frac{1}{\sqrt{2}}\left(\widehat{X}_1 - \left(\frac{\widehat{X}_2 + \widehat{X}_3 + \ldots + \widehat{X}_M}{\sqrt{M-1}}\right)\right), \tag{1.54}$$

$$\widehat{Y} \equiv \frac{1}{\sqrt{2}}\left(\widehat{Y}_1 + \left(\frac{\widehat{Y}_2 + \widehat{Y}_3 + \ldots + \widehat{Y}_M}{\sqrt{M-1}}\right)\right), \tag{1.55}$$

where the noise in $\widehat{X}$ measures the correlation between $\widehat{X}_1$ and $\widehat{X}_2 + \widehat{X}_3 + \ldots + \widehat{X}_M$, and the noise in $\widehat{Y}$ measures the correlation between $\widehat{Y}_1$ and $\widehat{Y}_2 + \widehat{Y}_3 + \ldots + \widehat{Y}_M$, respectively. Clearly, if the noise in $\widehat{X}$ and $\widehat{Y}$ approaches zero, then the quadratures of mode 1 are correlated with the sum of the quadratures of modes $2, 3, \ldots, M$. Thus, the MSVS is not separable into these two groups of modes. It was shown by P. van Loock and A. Furusawa [26] that the violation of a single condition,

$$(\Delta X)^2 + (\Delta Y)^2 \geq \frac{2}{M-1}, \tag{1.56}$$

is sufficient to demonstrate M-partite entanglement. Therefore, if the sum of the noises in $\widehat{X}$ and $\widehat{Y}$ are less than $2/(M-1)$, then the MSVS is fully inseparable. When $M = 2$, the bipartite inequality in Eq. (1.53) is recovered.

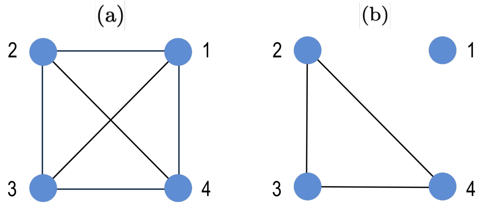

Figure 1.5: Graphical representations of two different 4-mode states. The state in (a) is fully inseparable since each mode is maximally connected, as indicated by the black lines. However, the state in (b) is partially separable since mode 1 can be separated from the other modes $(2, 3, 4)$.

1.3 Continuous-variable cluster states

Cluster states are a specific type of entangled state consisting of a large number of qubits [20]. Quantum logic gates such as the controlled-not gate, the Pauli gates, and the Hadamard gate can be encoded in the cluster and an arbitray computation using any combination of these can be executed by performing single qubit measurements in a particular basis and in a particular order [19, 27]. Thus, the cluster serves as a universal source for any quantum computation. Cluster states can be extended to CVs [28–32]. The CV cluster state can be made from a large number of entangled single-mode squeezed states. Thus, it is an application of a multimode entangled squeezed state.

Cluster states were originally introduced as a class of M-qubit quantum states that are generated in arrays of qubits (two-level quantum states) with an Ising-type interaction [20]. The procedure for creating an M qubit cluster state starts by placing each qubit at a unique lattice site on a d-dimensional lattice $(d = 1, 2, 3)$. This defines the initial state of the qubits to be a separable tensor product state. The cluster state is created by entangling nearest-neighbours on the lattice with an interaction Hamiltonian equivalent to the quantum Ising model, or alternatively with controlled phase gates. The cluster state is maximally entangled, meaning that any pair of qubits in the cluster can be projected into a pure Bell state by doing local measurements on the other qubits. This property allows quantum information to propagate through the cluster since it means that a qubit can be teleported from one site of the cluster to any other site. Also, the cluster has a high persistency of entanglement, meaning that the entanglement persists even after many local measurements. For an M qubit cluster state it takes $M/2$ measurements to completely destroy all the entanglement. Since each measurement performed in a quantum computation reduces the entanglement in the cluster, having a high persistency of entanglement means that the cluster contains all the entanglement required for any quantum computation, provided that the cluster is large enough [19].

CV cluster states can be prepared in a similar way to qubit cluster states. To start, a collection of M eigenstates of the $\widehat{Y}$ quadrature, $|Y\rangle$, are prepared in a separable product state, where the states $|Y\rangle$ satisfy $\hat{Y}\,|Y\rangle = Y\,|Y\rangle$. The states can be organized on a graph, where each state is assigned to a node of the graph and a real symmetric adjacency matrix $\boldsymbol{A}$ is defined for the graph [33, 34]. The initial separable state is defined as $|0\rangle_1\,|0\rangle_2 \ldots |0\rangle_M$. To generate the cluster state, the initial state is acted upon with collection of CV controlled-phase operators, $\widehat{C}_z(\boldsymbol{A})$, given by

$$\widehat{C}_z(\boldsymbol{A}) = \prod_{j,j'=1}^{M} \exp\left(\frac{i}{4} A_{jj'} \widehat{X}_j \widehat{X}_{j'}\right), \tag{1.57}$$

where $A_{jj'}$ is equal to the weight of the edge connecting node j to node j' and the factor of $1/4$ in the argument of the exponential is included for convenience. The elements of the adjacency matrix $\boldsymbol{A}$ determine which two nodes the operators $\widehat{C}_z(\boldsymbol{A})$

are applied to and the strength of the interaction. In Fig. 1.6(a) an example of a quantum circuit for preparing a 4-mode CV cluster state is shown that uses the controlled-phase operation to entangle the states. The CV cluster state for the graph defined by $\boldsymbol{A}$ is then

$$|\phi\rangle = \widehat{C}_z(\boldsymbol{A})\, |0\rangle_1 \, |0\rangle_2 \ldots |0\rangle_M \,. \tag{1.58}$$

In Fig. 1.6(b) an example graph for a 4-mode CV cluster state, with a weighted adjacency matrix, is shown.

I now derive an eigenvalue equation that the state must satisfy in order for it to be a cluster state [31]. The initial state is a stabilizer state of the eigenvalue equation

$$\prod_{j=1}^{M} \exp\Big(-i\widehat{Y}_j\Big)\, |0\rangle_1 \, |0\rangle_2 \ldots |0\rangle_M = |0\rangle_1 \, |0\rangle_2 \ldots |0\rangle_M \,. \tag{1.59}$$

Putting Eq. (1.59) into Eq. (1.58) and using the fact that $\widehat{C}_z^{\dagger}(\boldsymbol{A})\widehat{C}_z(\boldsymbol{A}) = \mathbf{1}$, results in

$$|\phi\rangle = \widehat{K}\, |\phi\rangle \,, \tag{1.60}$$

where it can be shown (using the well known Baker-Campbell-Hausdorff formula and the commutator in Eq. (1.6)) that [32]

$$\widehat{K} \equiv \exp\left(-i \sum_{j=1}^{M} \widehat{Y}_j + i \sum_{j,j'=1}^{M} A_{jj'} \widehat{X}_{j'} \right). \tag{1.61}$$

Therefore $\widehat{K}$ stabilizes the cluster state $|\phi\rangle$ (via Eq. (1.60)). This means that the argument of the exponential in $\widehat{K}$ satisfies the nullifier equation for each node j

$$\left(\widehat{Y}_j - \sum_{j'=1}^{M} A_{jj'}\widehat{X}_{j'}\right)|\phi\rangle = 0. \tag{1.62}$$

The nullifier equation (Eq. (1.62)) is the defining equation for the cluster state. It uniquely determines $|\phi\rangle$ up to a phase factor. Each node j of the cluster must satisfy Eq. (1.62), where the sum over j' includes all the nodes connected to node j, by an edge with weight equal to $A_{jj'}$.

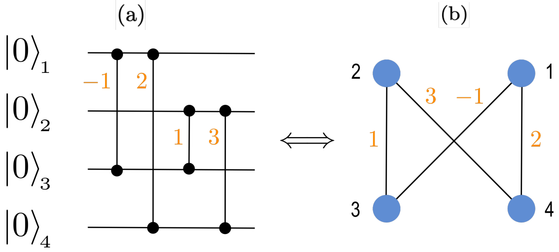

Figure 1.6: (a) Quantum circuit to generate a 4-mode cluster state, where controlled-phase $\widehat{C}_z(\boldsymbol{A})$ operations (represented with vertical black lines) are applied between the states, and (b) the equivalent representation using the graph defined by the adjacency matrix $\boldsymbol{A}$, that determines the weight (orange numbers) of every edge connecting a pair nodes in the cluster.

The eigenstates $|Y\rangle$ are unphysical because they represent a state that has a definite eigenvalue Y in the $\widehat{Y}$ quadrature. Thus requires infinite squeezing in the $\widehat{Y}$ quadrature (see the uncertainty relation in Eq. (1.7)). For this reason, the cluster state made from them represents an ideal CV cluster state. In practice, the initial state of the graph is taken to be a collection of finite-squeezed states instead, which are entangled using the controlled-phase gates according to $\boldsymbol{A}$. The resulting cluster state does not satisfy the nullifier equation (Eq. (1.62)) due to the presence of finite squeezing. However, P. van Loock *et. al.* [31] and N. C. Meniccuci *et. al.* [34] define an approximate CV cluster state as one that is made from entangled finite-squeezed states and exhibits correlations in combinations of the quadratures of the modes. The multimode squeezed state $|\phi\rangle$ is an approximate CV cluster state if the covariance of the nullifier operator in Eq. (1.62) is sufficiently close to zero,

$$\mathrm{cov}\left(\widehat{Y}_j - \sum_{j'=1}^{M} A_{jj'}\widehat{X}_{j'}\right) \to 0, \tag{1.63}$$

where the arrow → indicates that the noise in the nullifier operator goes to zero as the squeezing amplitude increases. Thus for an infinitely squeezed state the noise is exactly equal to zero. In Sec. 6 the covariance in Eq. (1.63) using a multimode squeezed state is evaluated, and a condition for the squeezing parameters is derived such that the covariance will go to zero in the limit of infinite squeezing. Therefore under the right conditions the multimode squeezed state is an approximate CV cluster state, meaning it can be used a source of entanglement for CV quantum computing.

1.4 Thesis overview

The overview of this thesis is as follows. Chapters 2, 3, and 4 constitute the three published manuscripts that I co-wrote with my supervisor Marc M. Dignam and Chapter 5 consists of an unpublished manuscript, that we submitted and is currently being reviewed. The outline for Chapters 2 - 5 is as follows. In Chapter 2, an MRR is optimized to generate a maximally-squeezed single-mode squeezed thermal state in the ring. In Chapter 3, the theory of the nonlinear generation of an entangled two-mode squeezed thermal state is developed, and it is applied to an MRR to generate CV entanglement between the quadratures of two ring-modes. In

Chapter 4, the two-mode theory of Chapter 3 is generalized to the nonlinear generation of an M-mode squeezed thermal state (MSTS) in M orthogonal quasimodes of a coupled-cavity structure. In Chapter 5, the MSTS solution is extended to incorporate the nonorthogonal quasimodes of a coupled-cavity structure. Chapter 6 is a regular chapter, in which I derive a condition on the squeezing parameters of the MSTS in order for it to be classified as an approximate CV cluster state. Finally, in Chapter 7 I conclude and discuss future directions for the work presented in this thesis.

Chapter 2

Optimization of a Lossy Microring Resonator System for the Generation of Quadrature-Squeezed States

In this work, we model and optimize the generation of a squeezed thermal state via SPDC in a single ring-mode of an MRR. The theory for generating the squeezed thermal state was originally derived by John Sipe [35]. We applied his theory to the generation of the state in the MRR, optimized the parameters of the ring to maximize the squeezing, and derived an analytic expression for the pump pulse inside the ring. This work is published as a regular article in Physical Review A [36].

Abstract – The intensity buildup of light inside a lossy microring resonator can be used to enhance the generation of squeezed states via SPDC. In this work, we model the generation of squeezed light in a microring resonator that is pumped with a Gaussian pulse via a side-coupled channel waveguide. We theoretically determine the optimum pump pulse duration and ring-to-channel coupling constant to minimize the quadrature noise (maximize the squeezing) in the ring for a fixed input pump energy. We derive approximate analytic expressions for the optimal coupling and pump

pulse duration as a function of scattering loss in the ring. These results will enable researchers to easily determine the optimal design of microring resonator systems for the generation of quadrature-squeezed states.

2.1 Introduction

Squeezed states are a type of nonclassical light that are characterized by squeezing of the quantum uncertainty in a given quadrature below the level of vacuum noise. They can be used in a variety of contexts, including in applications where quadrature noise is a major concern, such as optical communications [37] and interferometers [2, 38, 39]. Squeezed states can also be used as the starting point to create entangled states of light. Weakly-squeezed states can be used as a source of entangled photons, which can be used for quantum teleportation [40] and quantum cryptography [16]. Single-mode squeezed states can be combined using waveguide couplers to create quadrature-entangled states [41]. In addition, two-mode quadrature-squeezed states are a source of CV entanglement, which can also be used for quantum computation [42] and quantum information [43]; such states are important as they are generally more robust to loss than two-photon entangled states [44].

One way to generate squeezed states of light is via SPDC, where a strong coherent pump field interacts with a material that has a $\chi^{(2)}$ nonlinearity [45]. The conversion efficiency of pump photons into signal and idler pairs can be enhanced by enclosing the nonlinear interaction within a cavity that is resonant with the pump. In this case, if it is a multimode cavity, where a second mode is resonant at the signal and idler frequencies, then it can play a dual role, by ensuring that essentially all generated pairs end up in a single cavity mode.

MRRs have been shown to enhance SPDC efficiency [46]. Thus, they are promising structures for on-chip applications such as entangled photon pair generation for quantum communication [47] and generating squeezed light for discrete and CV entanglement [48–51]. The schematic diagram of an MRR is shown in Fig. 2.1. The ring waveguide has a radius chosen such that it has resonant modes at the frequencies of the pump and the squeezed light. The straight waveguide (channel) and ring are in proximity to each other, such that pump and squeezed light can be evanescently coupled in and out of the resonator.

Considerable theoretical work has been done on a Hamiltonian treatment of SPDC and SFWM in lossy MRRs [52–55]. The general approach is to solve the Heisenberg equations of motion for the mode operators in the ring and channel. This procedure is applicable to both the weak pumping limit for generating entangled photon pairs and the strong pumping limit for generating quadrature squeezing. For example single-mode quadrature squeezing of -10dB in the channel of a lossy SiN MRR was recently shown to be theoretically achievable [48], using a 100pJ Gaussian input pulse of duration 30ps. Experimentally, about 4dB [49] to 5dB [56] of squeezing has been inferred on-chip with SiN MRR s. Both the theory and experimental demonstration of quadrature squeezing in lossy MRR s provides a promising path forward for creating a practical CV entangled states for quantum computing applications.

Recent experimental work has demonstrated that one can tune the squeezing level generated in coupled MRRs; by increasing the coupling efficiency, Dutt *et al.* [57] demonstrated experimentally an increase of the on-chip squeezing level in a SiN resonator from -0.9dB to -3.9dB. Although this and other work demonstrate the promise of MRRs for generating squeezed light, it appears that very little has been done on the *optimization* of the MRR to obtain maximum squeezing.

In this paper, we theoretically study the quadrature squeezing inside a lossy MRR pumped by a Gaussian input pulse. We focus on the optimization of the pump pulse duration and ring-channel coupling, in order to achieve the conditions that maximize the squeezing in the presence of scattering loss.

We consider the case of squeezed-state generation via SPDC in a single mode of the ring. To allow us to compare the squeezing achieved for different pump durations, in all that follows, the energy of the input pulse is held constant when the pulse duration is changed. We model the dynamics of the density operator for the state in the ring in the presence of loss using the Lindblad master equation (LME) for a cavity with a single lossy mode. It has recently been shown that the general solution to this LME is a single-mode squeezed thermal state [35] characterized by a time-dependent squeezing amplitude, squeezing phase, and a thermal photon number. Using this solution, we model the squeezed thermal state in the MRR as a function of time, and derive an approximate analytic expression for the maximum squeezing in the presence of loss.

Our theoretical approach is somewhat different from what is commonly done in the literature. The strength of our method is that, because we know that the density operator inside the ring is always a squeezed thermal state, the time-dependent properties of the state in the ring, such as the variance of the quadrature operator and expectation value of the number operator, can be easily determined by simply solving for the time dependence of the thermal photon number and squeezing parameter of the state. Of course, our study is restricted to a single-mode squeezed state in the ring, but this condition is easily satisfied by limiting the bandwidth of the input pulse, and carefully phase-matching the desired pump mode and squeezed light mode in the ring.

Using our exact solution for the time evolution of the state, we derive approximate but accurate analytic expressions for the optimum coupling value and optimum pump pulse duration for a fixed pump energy. We show that they are in excellent agreement with full numerical simulations when the pump and ring configuration is relatively close to the optimal. We find that the optimum pulse duration depends on the loss in the ring and is in the range of of 10 to 60 times the ring round-trip time. We also show that the optimum coupling is slightly below critical coupling (undercoupling).

The paper is organized as follows. In section 2.2.1 we review the theory of the coupling of a pulsed classical pump field from a channel waveguide into the ring, discuss practical limitations on the pump pulse duration for generation in a single-mode, and determine the exact and approximate expressions for the time-dependent pump field inside the lossy ring. In section 2.2.2 we present the theory behind the generation of a squeezed thermal state in a single leaky mode for a pulsed pump. In section 2.3 we model the system and develop approximate analytic expressions for the optimal pulse duration, coupling constant and quadrature noise for a given ring loss. Finally, in section 2.4 we present our conclusions.

2.2 Theory

In this section we present the theory behind the generation of squeezed light inside an MRR. The system consists of a ring resonator waveguide of radius R side-coupled to a straight waveguide (the channel) (see Fig. 2.1). Both waveguides are made from a material with a nonlinear $\chi^{(2)}$ response. We treat the ring resonator as an optical cavity that generates squeezed light in a single leaky mode. The mode is leaky due both to scattering loss and coupling to the channel. The input field to the system is a classical pump pulse ($E_1(t)$) propagating in the channel. The bandwidth of the input pulse is limited such that it only couples appreciably into a single mode inside the ring, with frequency, ω_P. Once inside the ring, the pump will produce squeezed light in a separate mode with frequency, ω_S, that is half the frequency of the pump, *i.e.* $\omega_S = \omega_P/2$. In section 2.2.1 we study the frequency response of the ring using a transfer matrix approach in the presence of loss, and derive exact and approximate expressions for the time-dependent pump field inside the ring. In section 2.2.2 we give the solution to the LME for the quantum state of light generated inside the ring.

2.2.1 Time-Dependent Pump Field Inside the Ring Resonator

In this section we present the theory to obtain the time dependence of the pump field inside the ring resonator and examine the dependence of the field build-up in the ring on the pump pulse duration, the scattering loss in the ring, and the coupling between the channel and ring waveguides.

The classical pump pulse field, $E_1(t)$, incident on the ring resonator is taken to be a classical Gaussian pulse of the form

$$E_1(t) = E_1^{(+)}(t) + E_1^{(-)}(t),$$

where

$$E_1^{(+)}(t) = E_0\sqrt{\frac{T_R}{\tau}}\exp\left(-2\ln(2)\frac{t^2}{\tau^2}\right)\exp(-i\omega_P t), \tag{2.1}$$

and $E^{(-)}(t) = \left[E^{(+)}(t)\right]^*$. Here τ is the duration of the pulse (FWHM of the intensity), ω_P is the pulse carrier frequency, T_R is the ring round-trip time (discussed in more detail below), and E_0 is the amplitude of the pulse. The factor of $1/\sqrt{\tau}$ is included so that the energy of the pulse is independent of the pulse duration. We do this so that we can study the squeezing level in the ring for many different pumping durations, with a constant amount of energy going into the system. In the following, only the positive frequency part of the input field is needed, because we are using the rotating wave approximation.

In calculating the coupling of the field in and out of the ring, it is easier to work in the frequency domain. We define the Fourier transform of the time-dependent field as

$$\tilde{E}(\omega) = \int_{-\infty}^{\infty} E^{(+)}(t) \exp(i\omega t) dt, \tag{2.2}$$

and the inverse Fourier transform as

$$E^{(+)}(t) = \frac{1}{2\pi} \int_{-\infty}^{\infty} \tilde{E}(\omega) \exp(-i\omega t) d\omega. \tag{2.3}$$

The Fourier transform of the input pulse of Eq. (2.1) is

$$\tilde{E}_1(\omega) = \tilde{E}_0 \sqrt{\frac{\tau}{T_R}} \exp\left(-\frac{(\omega - \omega_P)^2 \tau^2}{8 \ln 2}\right), \tag{2.4}$$

where $\tilde{E}_0 \equiv E_0 T_R \sqrt{\pi/(2\ln(2))}$. The bandwidth $\Delta\omega$ (FWHM in frequency) of the input pulse is related to the pulse duration τ by $\Delta\omega = 4\ln(2)/\tau$.

The fields in the ring and channel are assumed to couple at a point, as indicated

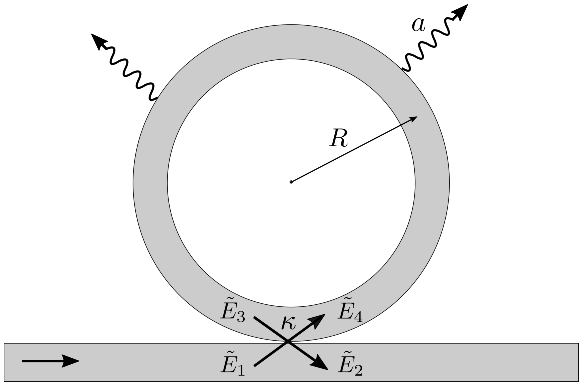

Figure 2.1: Schematic of the ring resonator coupled to a channel waveguide. The field components incident to the coupling point are $\tilde{E}_1$ in the channel and $\tilde{E}_3$ in the ring. The field components leaving the coupling point are $\tilde{E}_2$ in the channel and $\tilde{E}_4$ in the ring. The cross-coupling coefficient is κ, and the attenuation in the ring is a.

in Fig. 2.1. The fields incident on the coupling point are $\tilde{E}_1(\omega)$ in the channel and $\tilde{E}_3(\omega)$ in the ring. The fields leaving the coupling point are $\tilde{E}_2(\omega)$ in the channel and $\tilde{E}_4(\omega)$ in the ring. The input and output field components are defined at locations just to the left and right of the coupling point, respectively. The input and output fields are related by a transfer matrix as

$$\begin{pmatrix} \tilde{E}_4(\omega) \\ \tilde{E}_2(\omega) \end{pmatrix} = \begin{pmatrix} \sigma & i\kappa \\ i\kappa & \sigma \end{pmatrix} \begin{pmatrix} \tilde{E}_3(\omega) \\ \tilde{E}_1(\omega) \end{pmatrix}, \tag{2.5}$$

where σ and κ are real numbers called the self- and cross- coupling coefficients, respectively. This is the form of the transfer matrix that is commonly used [58]. The coupling is assumed to occur at a single point, so the field components that pass through the coupling point and stay in the same waveguide do not acquire a phase. However, the field components that cross-over into the other waveguide at the coupling point do acquire the phase i. This phase is needed in order to conserve power across the coupling point (*i.e.*, the transfer matrix must be unitary). Additionally, the coupling is assumed to be lossless, so we obtain the relation $|\sigma|^2 + |\kappa|^2 = 1$. The fields $\tilde{E}_4(\omega)$ and $\tilde{E}_3(\omega)$ are related by,

$$\tilde{E}_3(\omega) = a \exp(i\Theta)\tilde{E}_4(\omega). \tag{2.6}$$

Here, a, is the field attenuation after one circuit of the ring (excluding any coupling to the straight waveguide); this is related to the scattering power-loss coefficient, α_{sc}, in the ring by $a = \exp(-\alpha_{\text{sc}} 2\pi R/2)$. In what follows, we assume that a is frequency independent, and also that a and κ are independent of each other. The single-circuit phase shift Θ in the ring is given by $\Theta = 2\pi R k$, where $k = 2\pi n_{\text{eff}}/\lambda$, where n_{eff} is the effective index of refraction for the pump mode in the ring and λ is the free space wavelength. The phase shift can also be expressed as,

$$\Theta = \omega T_R, \tag{2.7}$$

where $T_R = n_{\text{eff}} 2\pi R/c$ is the ring round-trip time. For light that is on resonance with a mode in the ring, the phase shift is $\Theta = 2\pi m$, where m is a positive integer (the mode number). Thus, in order to ensure that the pump frequency is on resonance with the ring, it is chosen to be $\omega_P = 2\pi m_P/T_R$, where m_P is the pump mode number. In all that follows, we will scale the time, the pump duration, and the pump pulse amplitude by the round-trip time T_R; consequently, all of the results that follow are independent of the ring radius and mode number.

We choose the frequency of the generated photons to be $\omega_S = \omega_P/2$ (where S stands for "squeezed light"), such that the mode number for the squeezed light is $m_S = m_P/2$. The coupling coefficients are assumed to be frequency independent.

This is a good approximation as long as the pump pulse is in a single mode. We assume that the ring waveguide dimensions have been chosen such that the squeezed light mode has the same n_{eff} as the pump mode (*i.e.*, they are phase matched). This has been demonstrated in an AlN ring resonator [51] for a waveguide with a height of 1μm and a width of 1.10μm, and in AlGaAs nanowaveguides [59].

Using Eqs. (2.5) and (2.6), we find that the field inside the ring is given by

$$\tilde{E}_3(\omega) = \frac{i\sqrt{1-\sigma^2}\, a \exp(i\omega T_R)}{1 - \sigma a \exp(i\omega T_R)} \tilde{E}_1(\omega). \tag{2.8}$$

The ratio of intensity inside the ring to the incident intensity in the channel is defined as the buildup factor,

$$\mathcal{B}(\omega) \equiv \left| \frac{\tilde{E}_3(\omega)}{\tilde{E}_1(\omega)} \right|^2 = \frac{(1-\sigma^2)a^2}{1 - 2\sigma a \cos(\omega T_R) + \sigma^2 a^2}. \tag{2.9}$$

It is maximized for light that is on resonance with the ring, *i.e.* $\cos(\omega T_R) = 1$. Using $\omega = \omega_P$ in Eq. (2.9) gives the maximum value of the buildup factor,

$$\mathcal{B}(\omega_P) = \frac{\left(1-\sigma^2\right) a^2}{\left(1-\sigma a\right)^2}. \tag{2.10}$$

The value of a that maximizes Eq. (2.10) is $a = \sigma$. This is known as *critical coupling*.

To ensure that the squeezed light will be generated mostly in a single mode with frequency ω_S we require that the pump pulse almost exclusively couples into a single mode in the ring with frequency ω_P. In Fig. 2.2(a) we demonstrate that with an incident pulse with duration $\tau = 2T_R$ (thick line), virtually all of the pulse intensity couples into a single ring resonance (thin red line). In contrast, in Fig. 2.2(b) we show that by reducing the pulse duration to $\tau = T_R/4$, the broadening of the pulse in frequency causes some of its intensity to couple into adjacent modes. Thus, in all that follows, we restrict ourselves to pulses with duration $\tau \geq T_R$ to ensure the squeezed light is generated almost entirely in a single mode. Although two-mode squeezed light could also be generated in a number of different mode pairs that satisfy energy conservation, we assume that generation in those other modes is suppressed because they are not well phase matched.

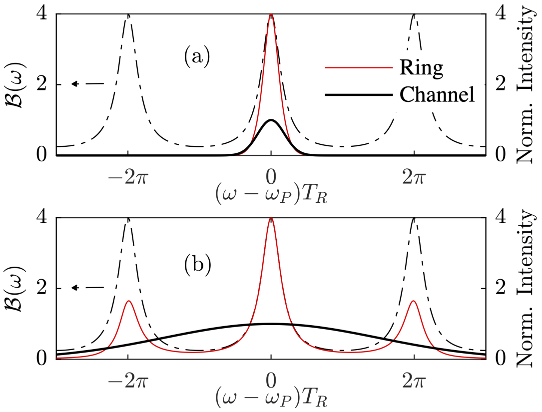

Figure 2.2: The intensity buildup (in three ring modes) of the pump pulse with a duration of (a) $\tau = 2T_R$ and (b) $\tau = T_R/4$. The normalized intensity of the input pulse in the channel is $|\tilde{E}_1|^2/\tilde{E}_0^2$ (thick curve), and the normalized intensity of the pulse in the ring, after its intensity has built up, is $|\tilde{E}_3|^2/\tilde{E}_0^2$ (thin red curve). The buildup factor (dashed line) and intensity are calculated with $\sigma = 0.6$ and $a = 1$.

The intensity decay rate Γ of light in the ring cavity is given by,

$$\Gamma \equiv \frac{\alpha_{\text{tot}} 2\pi R}{T_R} = \frac{1}{T_R}\left[\ln\left(\frac{1}{\sigma^2}\right) + \ln\left(\frac{1}{a^2}\right)\right], \tag{2.11}$$

where α_{tot} is the total loss coefficient for the ring. It is given by $\alpha_{\text{tot}} = \alpha_{\text{sc}} + \alpha_{\text{cpl}}$, where α_{sc} is given above, and α_{cpl} is defined by the equation $\sigma = \exp\left(-\alpha_{\text{cpl}} 2\pi R/2\right)$ [60] and is the power-loss coefficient due to light coupling out of the ring into the channel.

To obtain strong squeezing in the ring, the intensity decay rate multiplied by the round-trip time must be small, *i.e.*, $\Gamma T_R \ll 1$. If the loss is small enough such that $(1-\sigma a) \ll 1$ then from Eq. (2.11), we obtain,

$$\Gamma \approx \frac{2(1-\sigma a)}{T_R}. \tag{2.12}$$

The decay rate Γ gives an estimate of the width of the peaks in the the buildup factor.

The time-dependent pump field, $E_3(t)$, inside the ring just to the left of the coupling point (see Fig. 2.1) is calculated by taking the inverse Fourier transform of Eq. (2.8), giving:

$$E_3\left(\tilde{t}\right) = \frac{i\kappa a E_0}{\sqrt{\pi}} \exp\left(-i2\pi m_P \tilde{t}\right) \sqrt{\frac{\tilde{\tau}}{8\ln 2}} \int_{-\infty}^{\infty} d\Omega \frac{\exp\left(-\Omega^2\tilde{\tau}^2/(8\ln 2) - i\Omega\tilde{t}\right)}{\exp(-i\Omega) - \sigma a}, \tag{2.13}$$

where $\Omega \equiv (\omega - \omega_P)T_R$, $\tilde{t} \equiv t/T_R$, and $\tilde{\tau} \equiv \tau/T_R$. The integral is real because we integrate Ω from $-\infty$ to ∞. This is the general expression that we use in our simulations. In the low-loss limit, where $(1-\sigma a) \ll 1$, the integral in Eq. (2.13) can be evaluated using Voigt functions [61] (see Appendix A.1), and we obtain the approximate expression

$$|E_3\left(\tilde{t}\right)| = \frac{\sqrt{\pi}\kappa a \tilde{\tau}\, e^{y\left(\tilde{t}\right)^2} \operatorname{erfc}\left[y\left(\tilde{t}\right)\right]}{\sqrt{8\ln 2}} \left|E_1^{(+)}\left(\tilde{t}\right)\right|, \tag{2.14}$$

where

$$y\left(\tilde{t}\right) \equiv \frac{(1-\sigma a)\tilde{\tau}}{\sqrt{8\ln(2)}} - \frac{\sqrt{8\ln(2)}\tilde{t}}{2\tilde{\tau}}, \tag{2.15}$$

and $\operatorname{erfc}(y) = 1 - \operatorname{erf}(y)$, where $\operatorname{erf}(y)$ is the error function. In the following sections, we shall use this expression to optimize the incident pump pulse duration to achieve the greatest nonlinear response in the ring. We note parenthetically that Eq. (2.14) would also be useful for calculating classical nonlinear processes such as second harmonic generation or SPDC in a ring resonator, using the undepleted pump approximation.

In this section, we have derived an expression for the time-dependent pump field inside the ring, which we shall use in the following section to calculate the generation of the squeezed state.

2.2.2 Quadrature Squeezing Inside a Lossy Ring Cavity

In this section we present the main theory behind quadrature squeezing inside the ring.

The Hamiltonian for light inside the ring, using the undepleted pump approximation, is given by [62]

$$\widehat{H} = \widehat{H}_0 + \gamma E_3(t)\widehat{b}^{\dagger 2} + \gamma^* E_3^*(t)\widehat{b}^2, \tag{2.16}$$

where the interaction-free part of the Hamiltonian is $\widehat{H}_0 = \hbar\omega_S \widehat{b}^\dagger \widehat{b}$, and the last two terms account for the SPDC process. The operator $\widehat{b}$ is the annihilation operator for the squeezed light photons in the ring. The nonlinear coupling coefficient between the pump, $E_3(t)$, and squeezed light is $\gamma = \hbar\omega_P \chi^{(2)}_{\text{eff}}/n^2_{\text{eff}}$, where $\chi^{(2)}_{\text{eff}}$ is an effective nonlinear susceptibility that depends on the intrinsic nonlinear susceptibility of the ring material and spatial mode profiles in the ring [63]. Note that we neglect any nonlinear interactions in the channel waveguide, because the pump intensity is much smaller there. The pump field is given in Eq. (2.13), where only the positive frequency part is used, as we are using the rotating wave approximation.

The effects of scattering and coupling losses on the dynamics of the generated light in the ring can be modelled using the LME for the density operator $\widehat{\rho}$ [64]:

$$\frac{d\widehat{\rho}}{dt} = -\frac{i}{\hbar}\left[\widehat{H}, \widehat{\rho}\right] + \Gamma\left(\widehat{b}\widehat{\rho}\widehat{b}^{\dagger} - \frac{1}{2}\widehat{b}^{\dagger}\widehat{b}\widehat{\rho} - \frac{1}{2}\widehat{\rho}\widehat{b}^{\dagger}\widehat{b}\right), \tag{2.17}$$

where Γ is the decay rate for the squeezed light generated in the cavity. It is given in Eq. (2.11), where now σ and a correspond to the coupling and loss parameter for the squeezed light. For simplicity, we have assumed that the squeezed light and the pump have the same coupling and loss parameters, but it is straightforward to generalize this within our theory. The effects of thermal photon populations are negligible at room temperature for the optical frequencies of interest, and so they are not included.

It was recently shown [35] that the exact solution to Eq. (2.17) for the Hamiltonian given in Eq. (2.16) is a *squeezed thermal state*, which can be written as,

$$\widehat{\rho}(t) = \widehat{S}(z(t))\widehat{\rho}_{\text{th}}(\beta(t))\widehat{S}^{\dagger}(z(t)), \tag{2.18}$$

where

$$\widehat{\rho}_{\text{th}}(\beta(t)) = \left(1 - \mathrm{e}^{-\beta(t)\hbar\omega_P/2}\right)^{-1} \mathrm{e}^{-\beta(t)\widehat{H}_0} \tag{2.19}$$

is the density operator for a thermal state at an effective time-dependent temperature $T(t) = (k_{\text{B}}\beta(t))^{-1}$, where k_{B} is the Boltzmann constant. In what follows, rather than use the effective temperature, we characterize this thermal state by the average thermal photon number, which is given by

$$n_{\text{th}}(t) = \left(\mathrm{e}^{\beta(t)\hbar\omega_P/2} - 1\right)^{-1}. \tag{2.20}$$

The operator $\widehat{S}$ is a unitary squeezing operator, given by

$$\widehat{S}(z(t)) = \exp\frac{1}{2}\left(z^*(t)\widehat{b}^2 - z(t)\widehat{b}^{\dagger 2}\right), \tag{2.21}$$

with a complex squeezing parameter $z(t) = r(t)\exp(i\phi(t))$. The form of the state given in Eq. (2.18) is only a solution to the LME if the squeezing amplitude u, squeezing phase ϕ, and average thermal photon number n_{th} obey the following three nonlinear coupled first order differential equations:

$$\frac{1}{\Gamma}\frac{dr(t)}{dt} = \frac{g(t)}{2} - \frac{\cosh r(t)\sinh r(t)}{2n_{\mathrm{th}}(t)+1}, \tag{2.22}$$

$$\frac{d\phi(t)}{dt} = -\omega_P, \tag{2.23}$$

$$\frac{1}{\Gamma}\frac{dn_{\mathrm{th}}(t)}{dt} = \sinh^2 r(t) - n_{\mathrm{th}}(t). \tag{2.24}$$

Here,

$$g(t) \equiv \frac{4|\gamma||E_3(t)|}{\hbar\Gamma} \tag{2.25}$$

is a dimensionless function of time that we will refer to as the pumping strength [35]; it is the ratio of the pumping rate to the total decay rate of the squeezed light in the cavity. It is constructed such that when $g(t) = 1$, the rate of signal generation in the ring equals the signal loss out of the ring. Using the approximate expression for the field in Eq. (2.14), we can write the pumping strength as,

$$g\left(\tilde{t}\right) = g_0\frac{\kappa a}{\tilde{\Gamma}}\sqrt{\frac{\tilde{\tau}}{8\ln 2}}\exp\left(\frac{-2\ln(2)\tilde{t}^2}{\tilde{\tau}^2}\right)\sqrt{\pi}\mathrm{e}^{y(\tilde{t})^2}\mathrm{erfc}\left[y\left(\tilde{t}\right)\right], \tag{2.26}$$

where $\tilde{\Gamma} \equiv \Gamma T_R$ and $g_0 \equiv 4|\gamma|E_0 T_R/\hbar$ is a dimensionless parameter. The pumping strength is the function that drives the squeezing processes, and directly affects the amount of squeezing in the ring. A large peak value in the pumping strength will generate substantial quadrature squeezing. In Fig. 2.3, the pumping strength in the ring is plotted as a function of time for $a = \sigma = 0.99$ (critical coupling) and $g_0 = .413$. Initially ($t = -\infty$), the pumping strength in the ring is zero. As the input pulse starts coupling into the ring the pumping strength begins to build up. At $t = 0$, the input pulse takes on its peak value at the coupling point in the channel. Some time later the pumping strength reaches its peak value. As can be seen, this time and the maximum value that the pumping strength reaches depend on the duration of the input pulse τ in the channel. For a short input pulse duration of $\tilde{\tau} = 1$, the pumping strength very quickly builds up to its peak value. The longer the input pulse becomes, the more time it takes for this to occur. For very long input pulses, the peak pumping strength will scale as $1/\sqrt{\tau}$, but the dependence on the pump duration is more complicated for shorter pulses and as can be seen, the maximum pumping strength is in fact achieved for intermediate pulse durations. We denote the input pulse duration that maximizes the peak pumping strength by τ_g. In Appendix A.2, we derive the following approximate but accurate expression for τ_g in the low-loss limit $(1 - \sigma a) \ll 1$:

$$\tilde{\tau}_g \approx 0.342 \frac{\sqrt{8 \ln 2}}{1 - \sigma a}. \tag{2.27}$$

Also in Appendix A.2, we show that a pulse duration of τ_g given in Eq. (2.27) causes the pumping strength to peak at the time

$$\tilde{t}_{peak} = \frac{1}{2(1 - \sigma a)}, \tag{2.28}$$

which is $1/\tilde{\Gamma}$, assuming that $(1-\sigma a) \ll 1$.

Before proceeding, we note that we could have used the field $E_4(t)$ rather than $E_3(t)$ and produced similar results. They are related by $E_3(t) = aE_4(t-T_R)$. However, the field $E_3(t)$ is a more conservative representation of the field inside the ring, because it has been reduced by the attenuation loss of one additional round trip relative to $E_4(t)$.

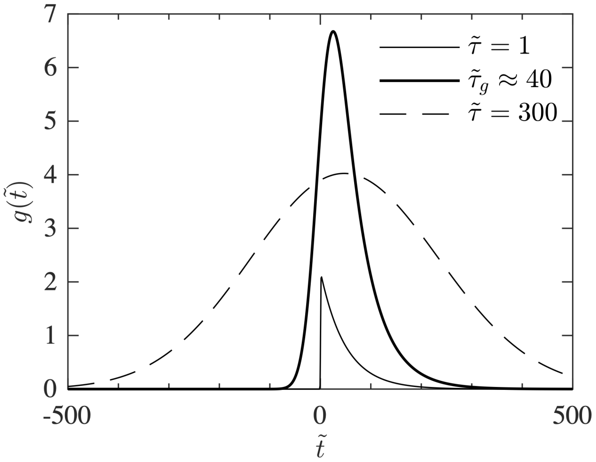

Figure 2.3: The pumping strength $g\left(\tilde{t}\right)$ in the ring for $\sigma = a = 0.99$ (critical coupling) generated with a short input pulse ($\tilde{\tau} = 1$) (solid thin line), a pulse $\tau = \tau_g$ that gives the highest peak in g (solid bold line), and a long pulse ($\tilde{\tau} = 300$) (dashed line).

The initial conditions for equations (2.22) to (2.24) are evaluated at an early time, t_i (< 0), when the incident pump pulse amplitude is negligible. The initial state of the system is the vacuum state, which means that $r(t_i) = 0$ and $n_{\text{th}}(t_i) = 0$. We set the initial squeezing phase, $\phi(t_i)$, to be $\phi(t_i) = 0$, so that the time-dependent phase is given by $\phi(t) = -\omega_P(t-t_i)$. In numerical calculations, the absolute value of the initial time must be chosen such that $|t_i| \gg \tau$.

The numerical solution of the coupled equations (2.22) to (2.24) enable us to determine the time-dependent level of quadrature squeezing in the ring. To this end, quadrature operators $\widehat{X}$ and $\widehat{Y}$ are defined as,

$$\widehat{X} = \widehat{b}^{\dagger}\mathrm{e}^{-i\theta(t)} + \widehat{b}\mathrm{e}^{i\theta(t)}, \tag{2.29}$$

$$\widehat{Y} = -i\left(\widehat{b}^{\dagger}\mathrm{e}^{-i\theta(t)} - \widehat{b}\mathrm{e}^{i\theta(t)}\right). \tag{2.30}$$

Here the quadrature phase $\theta(t)$ is defined as $\theta(t) \equiv \omega_S(t - t_i)$. We include this phase so that the expectation value of the quadrature does not contain fast oscillations in time, because this choice cancels with the phase $\phi(t)$ of the squeezed state. The noise in the $\widehat{X}$ and $\widehat{Y}$ quadratures is defined as the square root of the variance, and written as ΔX and ΔY. Using Eq. (2.18) they can be shown to be given by, [65]

$$\Delta X(t) = \sqrt{2n_{\mathrm{th}}(t) + 1}\,\mathrm{e}^{-r(t)}, \tag{2.31}$$

$$\Delta Y(t) = \sqrt{2n_{\mathrm{th}}(t) + 1}\,\mathrm{e}^{r(t)}. \tag{2.32}$$

Multiplying Eqs. (2.31) and (2.32) together gives,

$$\Delta X(t)\Delta Y(t) = 2n_{\mathrm{th}}(t) + 1. \tag{2.33}$$

If $n_{\mathrm{th}} = 0$, then $\Delta X \Delta Y = 1$ and a squeezed vacuum state is recovered, with $\Delta X = \exp(-r)$ and $\Delta Y = \exp(r)$. With our choice of quadrature operators, the noise in either quadrature for a vacuum state ($r = 0$) is simply $\Delta X = 1$ and $\Delta Y = 1$. Therefore, squeezing below the vacuum noise in the $\widehat{X}$ quadrature occurs when $\Delta X < 1$ in Eq. (2.31). The expectation value of the photon number for the squeezed thermal state can be shown to be given by [65]

$$\langle \widehat{n} \rangle \equiv \left\langle \widehat{b}^{\dagger}\widehat{b} \right\rangle = n_{\mathrm{th}}(t) \cosh\left(2r(t)\right) + \sinh^2\left(r(t)\right). \tag{2.34}$$

When $n_{\mathrm{th}} = 0$, the expectation value of the photon number is $\sinh^2(r)$, which is the result obtained for a squeezed vacuum state.

2.3 Results and Discussion

In this section, we present our numerical solutions to the set of equations (2.22) to (2.24). We solve them using a fourth-order Runge-Kutta method; the total run time for a given configuration is on the order of a few seconds on a standard PC. We also derive an approximate analytic expression for the minimum quadrature noise in terms of the peak pumping strength, and an expression for the optimum choice of σ (or alternatively, κ) that produces the global minimum in the quadrature noise. In addition, we numerically determine the pulse duration that produces the minimum quadrature noise for a given κ and show that it is close to τ_g, as given in Eq. (2.27). We discuss the effects of scattering loss a on the quadrature noise, and the optimum coupling coefficient and pulse duration. Finally, we study the sensitivity of the minimum quadrature noise to a phase offset due to imperfect homodyne detection.

In the remainder of this paper, we use the following values for our pump and ring parameters. We take the ring material to be AlGaAs with $\chi^{(2)}_{\mathrm{eff}} = 100\,\mathrm{pm/V}$ [52], $n_{\mathrm{eff}} = 2.85$, and $\omega_P = 2\pi \times 135.73\,\mathrm{THz}$ ($\lambda_P = 775\,\mathrm{nm}$). The amplitude of the input pulse E_0 can be written in terms of the total pump pulse energy U as,

$$E_0 = \left(\frac{4\ln 2}{\pi}\right)^{1/4} \sqrt{\frac{2U}{\mathcal{A} c\, n_{\mathrm{eff}} \epsilon_0 T_R}}, \tag{2.35}$$

where $\mathcal{A} = 0.71\,\mu\mathrm{m}^2$ is the cross-sectional area of the ring waveguide, ϵ_0 is the permittivity of free space, and c is the speed of light. The energy of the incident pulse is chosen to be $U = 0.188\,\mathrm{pJ}$ (independent of the pulse duration). This value of U produces a substantial amount of squeezing, but generally does not lead to significant pump depletion, even for low-loss cavities.

The radius of the ring required to give a resonance at the pump frequency is $R = m_P c/(\omega_P n_{\mathrm{eff}})$, where we have used Eq. (2.7) with $\omega = \omega_P$ and $\Theta = 2\pi m_P$. We choose the pump mode number to be $m_P = 200$, which makes the ring radius approximately equal to $R \approx 25\,\mu\mathrm{m}$. The ring round trip time is given by $T_R = 2\pi R n_{\mathrm{eff}}/c$, and in this case is $T_R \approx 1.47\,\mathrm{ps}$. We present our results in terms of the dimensionless parameters; $\tilde{t} \equiv t/T_R$ and $\tilde{\tau} \equiv \tau/T_R$. Once this is done, the only place where R enters our model is in the amplitude of the pumping strength in Eq. (2.26). Thus in order to make our results independent of R we require $E_0 T_R$ be constant. We collect all the dimensional parameters above into the single dimensionless constant, g_0, which was introduced in Eq. (2.26). For the above choice of parameters, $g_0 = 0.413$.

2.3.1 Dynamics of the squeezing process

We begin by examining the time-dependent quadrature noise ΔX in the ring in Fig. 2.4a for $\sigma = a = 0.99$ (critical coupling), for an input pulse duration of $\tilde{\tau} = 300$. Initially the pumping strength is zero and the quadrature noise is equal to the vacuum noise $\Delta X = 1$. As the pumping strength builds up, the quadrature noise gets squeezed below the vacuum noise $\Delta X < 1$. We find that the quadrature noise is a minimum at approximately (but not exactly) the time at which the pumping strength is at its peak, that is, at $\tilde{t}_{\text{min}} \approx 40$ (indicated by the vertical line). Finally, when the pump pulse couples out of the ring, the quadrature noise returns to the vacuum noise. The time-dependent squeezing amplitude r and thermal photon number n_{th} are shown in Fig. 2.4b for the same parameters. As the squeezing amplitude increases, the quadrature noise is squeezed by the factor $\exp(-r)$. However, the trade off is that the thermal photon number also increases, which results in an increase in the quadrature noise by the factor $\sqrt{2n_{\text{th}} + 1}$. Thus the minimum quadrature noise does not happen when the squeezing amplitude is maximum, but instead at an earlier time closer to when the pumping strength is maximum and the thermal photon number is much less than its peak value.

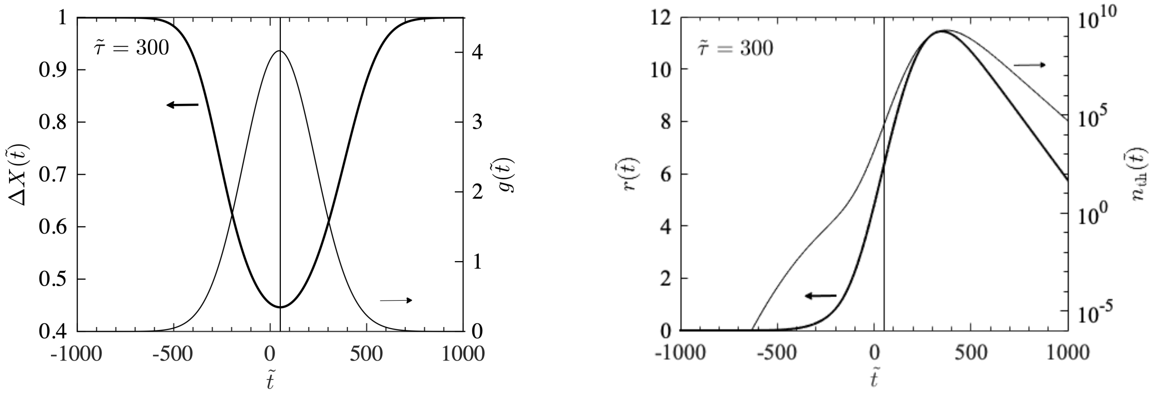

(a) (b)

Figure 2.4: (a) The quadrature squeezing ΔX (thick line) and pumping strength g (thin line) as a function of time, and (b) the squeezing amplitude r (thick line) and thermal photon number n_{th} (thin line) as a function of time for an input pulse duration of $\tilde{\tau} = 300$ and coupling constant $\sigma = a = 0.99$. The time at which ΔX is minimum is $\tilde{t}_{\text{min}} \approx 40$ is indicated by the vertical line.

In Fig. 2.5a, we examine a similar setup as above, except our input pump pulse has a much shorter duration of $\tilde{\tau} = 1$. Here, the pumping strength quickly reaches its peak value and does not spend much time building up in the ring. The quadrature noise is not as squeezed as it was with the long pulse. Additionally, with the short pulse, the minimum quadrature noise does not occur at the same time as when the pumping strength is at its peak. In this case the peak pumping strength occurs at approximately $\tilde{t} \approx 2$ and the minimum quadrature noise occurs at approximately $\tilde{t}_{\text{min}} \approx 26$. The time-dependent squeezing amplitude and thermal photon number are shown in Fig. 2.5b for the same short pulse. The thermal photon number is significantly smaller now, so the factor $\sqrt{2n_{\text{th}} + 1}$ is less detrimental to the squeezing. As a result we find that the minimum quadrature noise now occurs closer to the time when the squeezing amplitude is at its peak value.

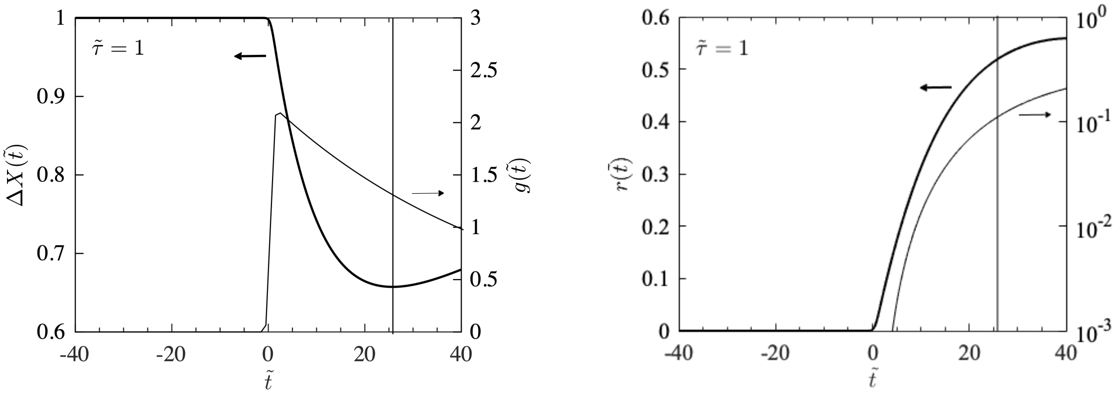

(a) (b)

Figure 2.5: The same plots as in Fig. 2.4 but for an input pulse duration of $\tilde{\tau} = 1$. Note that now the time at which ΔX is minimum is $\tilde{t}_{\text{min}} \approx 26$.

Having examined the two extreme cases of a long pulse and short pulse, we now consider the most interesting case for quadrature squeezing. We pump the ring with an input pulse duration τ_g (given by Eq. (2.27)) that gives the greatest peak value of the pumping strength. For $\sigma = a = 0.99$, $\tilde{\tau}_g \approx 40$. In Fig. 2.6a the time-dependent quadrature noise is shown for this pulse. When compared to the short and long pulse, we find that this duration produces the greatest quadrature squeezing. The minimum quadrature noise occurs at roughly the same time as the peak value of the pumping strength; using Eq. (2.28) the peak pumping strength occurs at $\tilde{t}_{peak} \approx 25$, while the quadrature noise is a minimum, at $\tilde{t}_{\min} \approx 29$. The time-dependent squeezing amplitude and thermal photon number for this pulse duration are shown in Fig. 2.6b. The peak squeezing amplitude is reduced by a factor of approximately 2 compared to the long pulse. However, the depletion of the squeezing amplitude is counteracted by the thermal photon number being reduced by a factor of roughly 10^5. This shows that the thermal noise is much more sensitive to the duration of the input pulse than the squeezing amplitude is, and therefore it is better to err on the side of using a relatively shorter pulse in a lossy MRR .

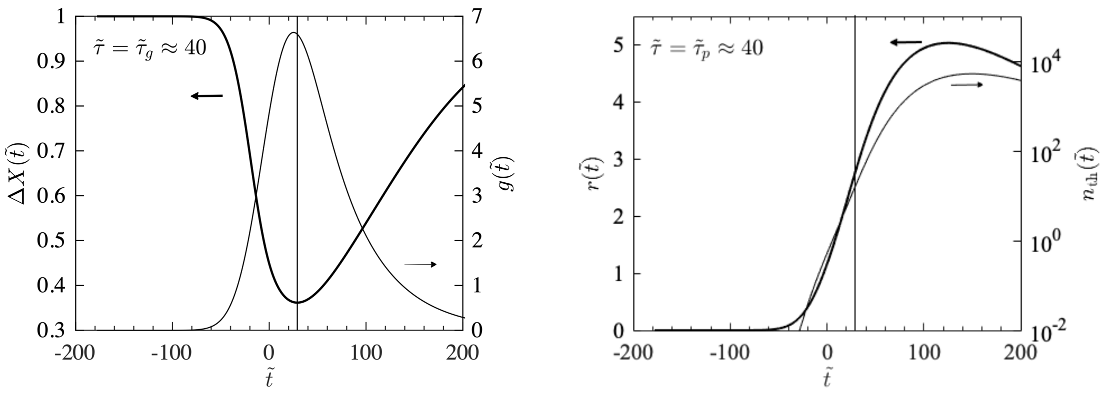

(a) (b)

Figure 2.6: The same plots as in Fig. 2.4 but for an input pulse duration of $\tilde{\tau} = \tilde{\tau}_g \approx 40$. Note that now the time at which ΔX is minimum is $\tilde{t}_{\min} \approx 29$.

Minimum in the quadrature noise

We have demonstrated how the minimum in ΔX depends on the pulse duration τ. Here we derive an analytic expression for the minimum quadrature noise ΔX_{min}. Setting the derivative of $\Delta X(t)$ in Eq. (2.31) equal to zero at the time t_{min} and simplifying gives,

$$\left.\frac{dn_{\text{th}}(t)}{dt}\right|_{t=t_{\text{min}}} - \left(2n_{\text{th}}(t_{\text{min}})+1\right)\left.\frac{dr(t)}{dt}\right|_{t=t_{\text{min}}} = 0. \tag{2.36}$$

Replacing the derivatives in Eq. (2.36) with Eq. (2.22) and Eq. (2.24) and using Eq. (2.31) to simplify gives,

$$\Delta X_{\text{min}}(\tau) = \frac{1}{\sqrt{1+g(t_{\text{min}},\tau)}}, \tag{2.37}$$

where $g(t_{\text{min}},\tau)$ is the pumping strength evaluated at the time when the quadrature noise is at its minimum. In general, we evaluate $g(t_{\text{min}},\tau)$ numerically in order to calculate the minimum quadrature noise for a given σ, a, and τ. If the input pulse duration is close to or larger than τ_g, then the value of the pumping strength at the time when the quadrature noise is minimum is roughly the same as the peak value of the pumping strength (see Figs. 2.4a and 2.6a). Thus, we can neglect the difference between $g(t_{\text{min}})$ and the peak value of the pumping strength. That is, if the pulse duration is considerably longer than T_R, then the pumping strength does not vary appreciably over a time scale of a few round-trips of the ring. This approximation improves the longer the pulse. Conversely, this approximation is not valid for the setup in Fig. 2.5a for the short pulse, as we discussed earlier. Let $g_{\text{max}}(\tau)$ denote the peak pumping strength as a function of τ. Then, since for pulses durations $\tau \gg T_R$

$g_{\max}(\tau) \approx g(t_{\min}, \tau)$, we obtain the following approximate expression for the minimum quadrature noise:

$$\Delta X_{\min}(\tau) \approx \frac{1}{\sqrt{1 + g_{\max}(\tau)}}, \quad (\tau \gtrsim \tau_g). \tag{2.38}$$

Therefore the minimum quadrature noise is expressed in terms of the peak pumping strength, for which we have an expression in Eq. (2.26). The advantage of Eq. (2.38) is that it gives the minimum quadrature noise as a function of τ and σ; without having to solve the coupled differential equations numerically. Additionally, letting $\tau = \tau_g$ in Eq. (2.38), and using Eq. (2.27) and Eq. (2.28), gives the following result,

$$\Delta X_{\min}(\tau_g) \approx \left[1 + 0.653\, \frac{g_0 a}{\tilde{\Gamma}} \sqrt{\frac{1-\sigma^2}{1-\sigma a}}\right]^{-\frac{1}{2}}. \tag{2.39}$$

This is the minimum quadrature noise in the ring for the pulse duration of τ_g, as a function of σ and a. For a given σ and a, we will show in the next section that this expression approximately gives the best quadrature squeezing. We will assess the accuracy of the expression given in Eqs. (2.38) and (2.39) below.

2.3.2 Dependence of the minimum quadrature noise on pulse duration and coupling

The minimum quadrature noise depends on the pulse duration τ, coupling σ, and scattering loss a. Thus far, the numerical results that we have presented have been only for the case of very low scattering loss at critical coupling ($\sigma = a = 0.99$), and for only three pulses. We have shown that, compared to a short and long pulse, τ_g generates the best quadrature squeezing for a given σ and a. In this section, we present numerical results for the maximum quadrature squeezing as a function of the coupling constant and pump duration for different scattering loss in the ring. We will show that the choice of critical coupling, although an obvious starting point, is not the optimal choice in order to achieve the global minimum in the quadrature noise for a given a. In fact, we find the global minimum in the quadrature noise is in the undercoupled ($\sigma > a$) regime and derive an approximation analytic expression for the optimal coupling.

Our analysis is done by computing the minimum quadrature noise $\Delta X_{\text{min}}(\tau, \kappa)$ as a function of pulse duration and coupling for different attenuation constants a. Then we numerically determine the optimal choices for the pulse duration and coupling, and finally compare them to approximate analytic expressions that we derive.

In Fig. 2.7 we plot the minimum quadrature as a function of the coupling coefficient and pulse duration for four different loss parameters a. First, in Fig. 2.7a, we consider the case where there is no scattering loss ($a = 1$). In this case, the minimum quadrature noise decreases as the cross-coupling constant κ goes to zero (or σ goes to one). Consequently, we find no optimum value of κ that gives a global minimum in the quadrature noise. This is expected, because as κ goes to zero, the buildup factor continues to increase without bound. In the figure, there are two hatched areas. The darker hatching (around $\kappa = 0.1$) is where the expectation value of the number of generated photons is at least 1% of the average number of pump photons ($\langle n_{\text{pump}} \rangle \sim 2 \times 10^6$); thus, our undepleted pump approximation is becoming less accurate. The second, lighter hatching (where $\kappa < 0.1$) indicates when our simulations break down, because the decay rate $\tilde{\Gamma}$ goes to zero as κ goes to zero. The blue dotted line in the figure indicates the computed pulse duration that gives the best quadrature squeezing for a given κ. The red curve is the input pulse duration $\tau_g(\kappa)$ given by Eq.

(2.27). The fact that τ_g fits agrees well with the computed optimal pulse duration means that the minimum in the quadrature noise is approximately where the peak pumping strength is the greatest. For short pulses, or pulses larger than τ_g, the peak pumping strength is too small in the ring and we see that the squeezing gets worse.

We now consider how introducing scattering loss into the ring affects the squeezing. When there is loss, the buildup factor has a peak value at critical coupling $\kappa = \sqrt{1-a^2}$ (or $\sigma = a$). In Fig. 2.7b the scattering loss is $a = 0.99$. Consequently, there is substantial squeezing at the peak in the buildup factor at critical coupling (indicated by the vertical line), and the squeezing gets worse away from the peak, as κ goes to zero (undercoupling) or one (overcoupling). We observe excessive photon generation, at least as much as 1% of the average number of photons in the pump pulse (hatched area), for pulses longer than τ_g near critical coupling. The optimum squeezing point (indicated by the red circle) is at a κ that is lower than critical coupling in the undercoupled regime, where the buildup of pump intensity is less, but the cavity decay rate is smaller. This shows that in order to achieve the largest squeezing it is preferable to have a lower cavity decay rate than that obtained at critical coupling.

In Figs. 2.7c and 2.7d we increase the attenuation loss in the ring to $a = 0.98$ and $a = 0.95$, respectively. As the scattering loss in the ring is increased, critical coupling shifts to higher κ and so does the optimum point (indicated by a red circle); however, it still remains in the undercoupled regime. In addition, the optimum point shifts to shorter pulses, which is expected, because the longer the pulse is, the more thermal photons are generated. Our approximate expression $\tau_g(\kappa)$ is still in quite good agreement with the numerical results, but is not as accurate as when the loss was very low ($a = 0.99$). This is because it is an approximate expression that is valid only when $(1 - \sigma a) \ll 1$ (see Appendix A.1). Interestingly, it still fits quite well at the optimum coupling point, with a difference of less than $2.3T_R$ or a relative error of 18% when $a = 0.95$. Using the approximate value for the pulse duration in this case only leads to a 1% increase in the quadrature noise relative to the optimal value.

An approximate expression for the optimum coupling value σ_{opt} (or κ_{opt}) is given by minimizing $\Delta X_{\min}(\tau_g)$ in Eq. (2.39) with respect to σ for a fixed a. Doing this we obtain,

$$\sigma_{\text{opt}}(a) \approx \frac{-1 + \sqrt{3a^2 + 1}}{a}. \tag{2.40}$$

This is a good approximation as long as $(1 - \sigma a) \ll 1$ and $\tau \gtrsim \tau_g$. In Fig. 2.8 we compare the σ_{opt} given by Eq. (2.40) (curve) to the numerically-computed value (circles). We find the analytic result fits well for $a \geq 0.9$. Note that as the scattering loss increases, the difference between critical coupling (dashed line) and σ_{opt} increases. Thus, for lossy systems the optimum coupling value σ_{opt} shifts closer to one (undercoupling) as compared to critical coupling. This compensates for the decrease in a and makes the decay rate smaller. We note that the difference between the quadrature noise at critical coupling and optimum coupling is generally small; for $a = 0.95$, the quadrature noise is reduced by only ~ 0.3 dB, and for $a = 0.99$ by only ~ 0.2 dB (see Figs. 2.7d and 2.7b). However, it is useful to know that one should err on the side of undercoupling if possible.

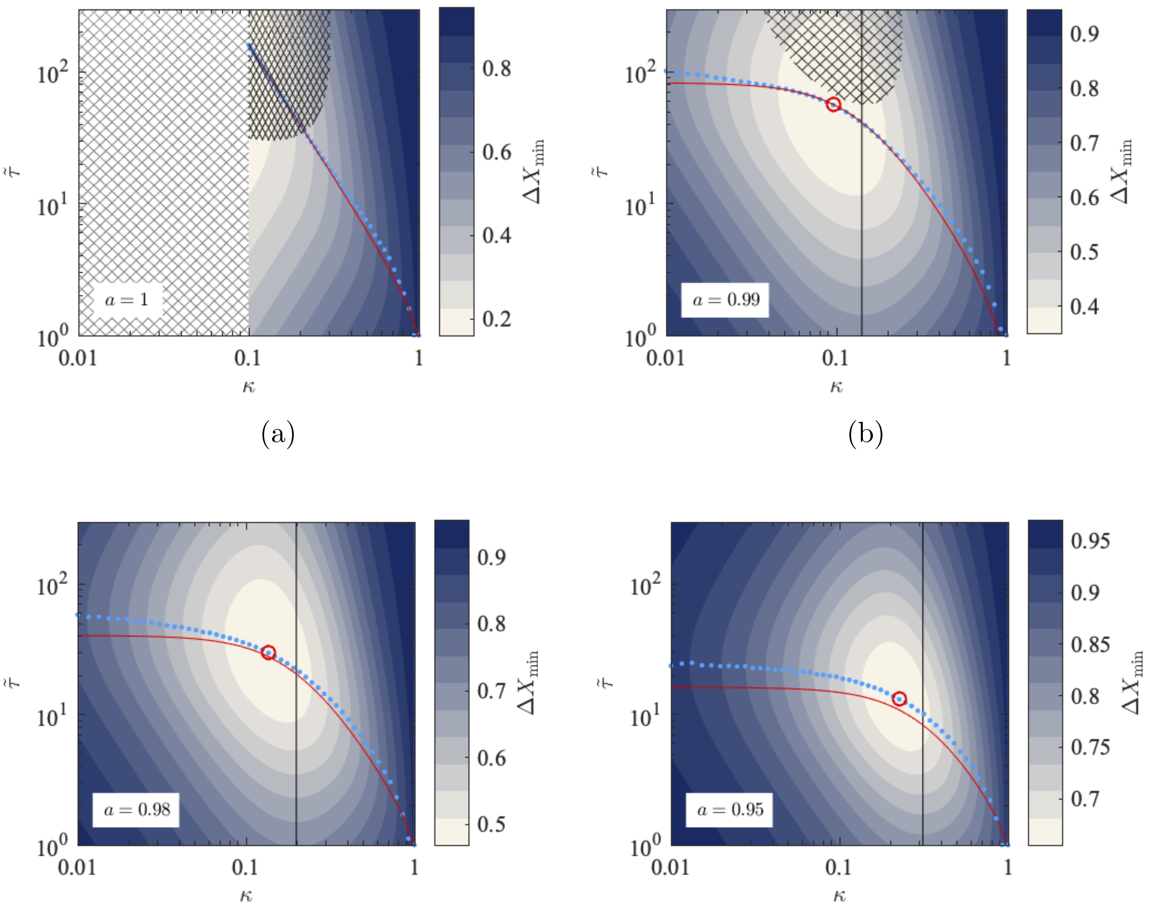

(a) (b)

(c) (d)

Figure 2.7: The minimum quadrature noise $\Delta X_{\min}$ as a function of the input pulse duration $\tilde{\tau}$ and cross-coupling constant κ for an attenuation constant of (a) $a = 1$, (b) $a = 0.99$, (c) $a = 0.98$, and (d) $a = 0.95$. The blue dots indicate the computed pulse duration needed to minimize $\Delta X_{\min}$ for a given κ. The solid red line is the pulse duration $\tilde{\tau}_g(\kappa)$ as a function of κ given by Eq. (2.27). The red circles in (b)-(d) mark the point at which the quadrature noise is at a global minimum for the given value of a. The vertical black line in (b)-(d) indicates critical coupling ($\sigma = a$, *i.e.*, $\kappa = \sqrt{1 - a^2}$). The light hatched area in (a) marks the parameter space where our simulation does not converge. The dark hatched areas in (a) and (b) indicate regions where the number of generated photons is in excess of 1% of the of photons in the incident pump.

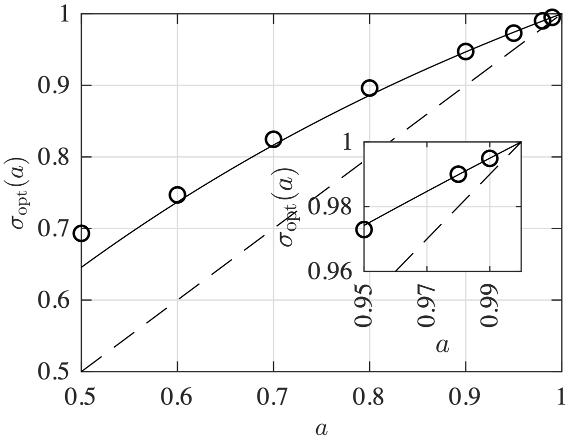

Figure 2.8: The computed optimum self-coupling constant (circles) and the approximate optimum coupling constant given by Eq. (2.40) (solid line), as a function of attenuation loss a. The dashed line indicates critical coupling.

2.3.3 Comparing the analytic expression for the minimum quadrature noise to the numerical results

Generating the 3D plots in Fig. 2.7 is a relatively time-consuming process. To solve Eqs. (2.22) - (2.24) for each τ and κ, and at each time-step, we have do the integral in Eq. (2.13) to obtain the pumping strength. To greatly speed-up this process we can instead use the approximate expression for $\Delta X_{\min}(\tau)$ given by Eq. (2.38), which gives the minimum quadrature noise as a function of the peak pumping strength, $g_{\max}(\tau)$. The maximum value of $g_{\max}(\tau)$ can then be determined using the analytic expression for $g(\tau)$ given in Eq. (2.26). The relative error between the approximate expression for the minimum quadrature noise in Eq. (2.38) and the numerical result is defined as,

$$\text{Error} \equiv \left| 1 - \sqrt{\frac{1+g(t_{\min})}{1+g_{\max}}} \right|, \tag{2.41}$$

so that when $g_{\max} = g(t_{\min})$ the error is zero. In Figs. 2.9a and 2.9b we plot the relative error as a function of τ and κ for (a) $a = 0.99$ and (b) $a = 0.95$, respectively. As expected, the relative error approaches zero for long pulses. For $a = 0.99$, at the optimum point (indicated by a red circle in Fig. 2.9a), the relative error is approximately 0.02%. This reinforces our assumption that $g_{\max} \approx g(t_{\min})$ when $\tau \gtrsim \tau_g$ and $a \approx 1$. The relative error increases when the scattering loss increases. However, for $a = 0.95$, the relative error is still only $\approx 1\%$, indicating that the approximation can still be used confidently when $a \geq 0.95$.

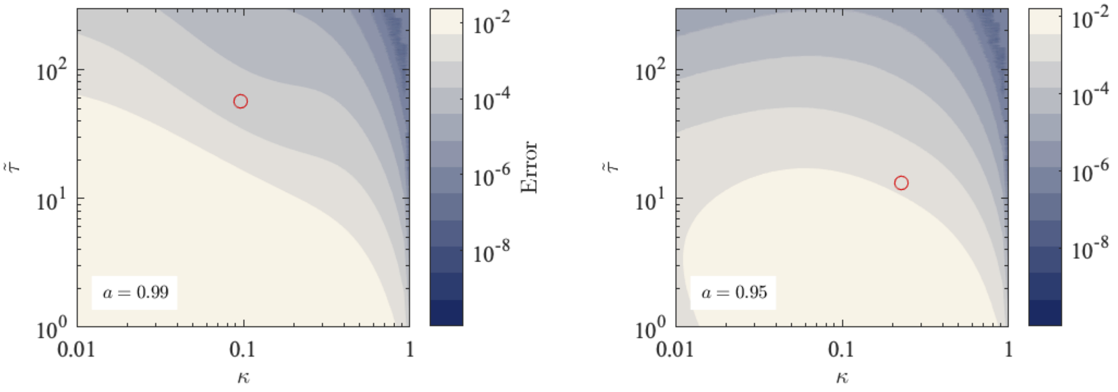

(a) (b)

Figure 2.9: The absolute value of the relative error (see Eq. (2.41)) between the approximate expression for the minimum quadrature noise and the numerically computed result, as a function of the coupling coefficient and pulse duration for (a) $a = 0.99$ and (b) $a = 0.95$. The red circles in (a) and (b) mark the point at which the quadrature noise is at a global minimum for the given value of a.

Letting $\sigma = \sigma_{\text{opt}}$ in Eq. (2.39), we obtain the following approximate expression for the global minimum in the quadrature noise $\Delta X_{\text{opt}} \equiv \Delta X_{\min}(\tau_{\text{opt}}, \sigma_{\text{opt}})$ as a function of the loss parameter a:

$$\Delta X_{\text{opt}} \approx \left[1 + \frac{0.653 g_0}{\tilde{\Gamma}(\sigma_{\text{opt}})} \sqrt{\frac{a^2 - \left(1 - \sqrt{3a^2+1}\right)^2}{2 - \sqrt{3a^2+1}}}\right]^{-\frac{1}{2}}, \tag{2.42}$$

where the cavity decay rate at the optimum coupling is given by,

$$\tilde{\Gamma}(\sigma_{\text{opt}}) = -2\ln\left(-1 + \sqrt{3a^2+1}\right). \tag{2.43}$$

The optimum pulse duration τ_{opt} is approximately given by $\tau_g(\sigma_{\text{opt}}) \equiv \tau_{\text{opt}}$,

$$\tilde{\tau}_{\text{opt}}(a) \approx 0.342 \frac{\sqrt{8\ln 2}}{2 - \sqrt{3a^2+1}}. \tag{2.44}$$

The expression in Eq. (2.42) can be used to determine the approximate optimum squeezing level in the ring as a function of a. In Fig. 2.10 (a) we compare the computed optimum squeezing level (in dB) (circle) to the value obtained with the expression in Eq. (2.42) (curve). As can be seen, the agreement is excellent, with a maximum relative error of 3% (that is an absolute difference of 0.06dB) when $a = 0.9$. The globally-optimal squeezing level (for the range of a considered) is approximately -9.15dB for $a = 0.99$ and $\sigma = 0.995$. In Fig. 2.10 (b), we also show the computed anti-squeezing level (*i.e.*, ΔY) (circles), when the squeezing is optimal. We see that for the global optimum in the squeezing, the anti-squeezing level is approximately 44dB. Such a high level of anti-squeezing might be of concern if there is some jitter in the homodyne detection, such that one is not measuring the light at the time when it is maximally-squeezed. In the same figure, we show that by cutting the pulse duration in half (*i.e.* $\tau_{\text{opt}}/2$ (stars)), the anti-squeezing level reduces to approximately 26dB, while the squeezing level is only modestly affected (see the stars in Fig. 2.10 (a)) (a change of less than 3%, or ~ 0.3 dB for $a = 0.99$). This result is useful for applications trying to achieve fault-tolerant quantum computing in noisy environments [42,66,67].

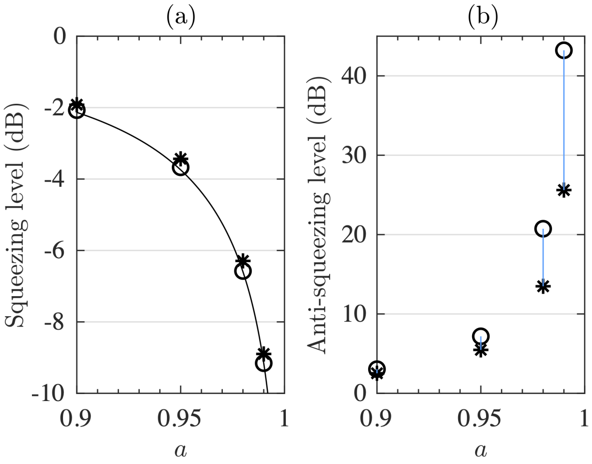

Figure 2.10: (a) The computed squeezing and (b) anti-squeezing level versus scattering loss a, for the optimum coupling constant κ_{opt} when $\tau = \tau_{\text{opt}}$ (circles) and when $\tau = \tau_{\text{opt}}/2$ (stars). The curve in (a) is our analytic expression for the squeezing, given by Eq. (2.42).

2.3.4 Sensitivity of the minimum quadrature noise to a phase offset

Thus far we have assumed that the measurement of ΔX is perfect; that is, the phase of the local oscillator in a homodyne measurement is exactly matched to the phase of the squeezed light signal. We now allow for a small phase offset, $\delta\theta$, between the phase of the signal and local oscillator, and study the effect it has on the measured quadrature noise. Letting $\theta(t) = -\phi(t)/2 + \delta\theta$ in the original definition for the quadrature operator in Eq. (2.29), the quadrature variance now is,

$$\left(\Delta X_{\delta\theta}\right)^2 = \left(2n_{\text{th}}(t) + 1\right)\left(\cosh 2r(t) - \cos\left(2\delta\theta\right)\sinh 2r(t)\right). \tag{2.45}$$

We interpret $\delta\theta$ as the angular deviation from the $\widehat{X}$ quadrature in phase-space. If $\delta\theta = 0$ then the squeezing ΔX is measured; and if $\delta\theta = \pi/2$, then the anti-squeezing ΔY is measured. In Fig. 2.11, we plot the minimum quadrature noise that is measured if the phase offset is $\delta\theta = 5\,\text{mrad}$ and the attenuation loss in the ring is $a = 0.99$. We chose this value of phase offset, because it is close to what was found in a recent experiment [68]. The hatched region shows where the measured quadrature noise is greater than the vacuum noise ($\Delta X > 1$). We find that the quadrature noise has increased at the previous optimum point that we found for an offset of zero (indicated by the red circle) to $\Delta X \approx 0.8$. One can correct for the increase in noise caused by the phase offset by reducing the pulse duration to approximately $\tilde{\tau}_{\text{opt}}/2 \approx 26$. Doing so reduces the squeezing level to approximately $\Delta X \approx 0.37$, which is close to the optimum level for an offset of zero ($\Delta X \approx 0.35$). Note that the new optimal point (when there is phase offset) occurs for essentially the same coupling constant and only the pulse duration needs to be adjusted. Note also that there are a number of combinations of τ and κ that achieve a squeezing level of $\Delta X < 0.4$ where one could work. The results are most sensitive to a phase offset when the scattering loss is small (a close to 1). For $a \leq 0.98$, a phase offset of $5\,\text{mrad}$ did not significantly perturb the minimum squeezing level at τ_{opt} and κ_{opt}.

2.4 Conclusion

In this work we have studied the time-dependent squeezing process in a lossy MRR pumped by a Gaussian pulse. We derived approximate analytic expressions for the optimum pulse duration (Eq. (2.27)) and optimum ring-channel coupling constant (Eq. (2.40)) for a fixed pump energy. Using these optimal parameters, we derived

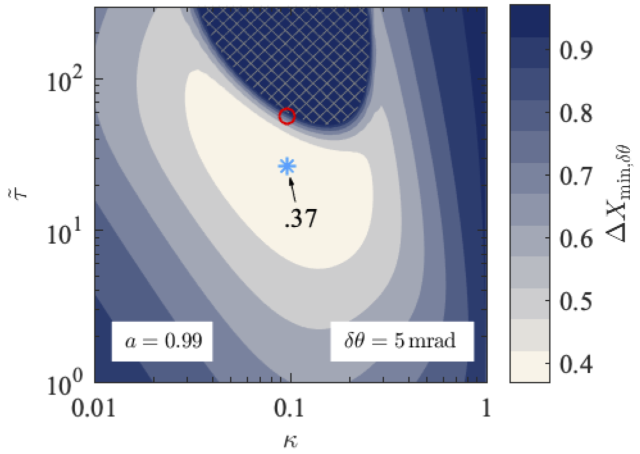

Figure 2.11: The minimum quadrature noise $\Delta X_{\delta\theta}(t_{\min}, \tau, \kappa)$ for a phase deviation of $\delta\theta = 5\,\mathrm{mrad}$ as a function of the coupling constant and the pulse duration. The blue star indicates the optimal operating point, while the red circle gives the optimum point found when $\delta\theta = 0$. The hatched area indicates where the noise is greater than the vacuum noise ($\Delta X_{\delta\theta} > 1$).

an analytic expression for the maximum squeezing level achievable for a ring with a given loss a (Eq. (2.42)). We found that for the chosen pump energy of 0.188 pJ and a scattering loss of $a = 0.99$, the optimal coupling constant and pulse duration are $\sigma_{\text{opt}} = 0.995$ and $\tau_{\text{opt}} = 56T_R$, while for a scattering loss of $a = 0.95$ we find optimal values of $\sigma_{\text{opt}} = 0.974$ and $\tau_{\text{opt}} = 13T_R$. Under these optimal conditions, we demonstrated a maximum squeezing level of -9.15dB and -3.67dB for $a = 0.99$ and $a = 0.95$, respectively. Furthermore, we demonstrated that by reducing the pulse duration at optimal coupling, the anti-squeezing level can be drastically reduced, while the squeezing level is only modestly affected. Moreover, we showed that our model shows how one can reduce the impact of homodyning phase noise on the squeezing simply by reducing the pump pulse duration from the nominally optimal value. We believe that the analytic expressions that we have developed for this system will help researchers looking to optimize the design of ring resonator systems for the generation of squeezed light.

Chapter 3

Continuous-variable entanglement in a two-mode lossy cavity: An analytic solution

In the previous chapter, a numerical method was developed to model the nonlinear generation of a squeezed thermal state in an MRR. However, the theory is only capable of modelling a degenerate squeezing process, where the photons are generated at a single frequency, and this means that it cannot be used to study the important case where the quadratures of the signal and idler fields are correlated. In this work, we derive a numerical method to model a non-degenerate squeezing process and study the CV entanglement between the quadratures of two ring-modes in an MRR. This work is published as a regular article in Physical Review A [69].

Abstract – Continuous-variable (CV) entanglement is a valuable resource in the field of quantum information. One source of CV entanglement is the correlations between the $\widehat{X}$ and $\widehat{Y}$ quadratures of photons in a two-mode squeezed state of light. In this paper, we theoretically study the generation of squeezed states, via spontaneous parametric downconversion (SPDC), inside a two-mode lossy cavity that is pumped with a classical optical pulse. The dynamics of the density operator in the cavity is

modelled using the Lindblad master equation, and we show that the solution to this model is the density operator for a two-mode squeezed thermal state, with a time-dependent squeezing amplitude and average thermal photon number for each mode. We derive an expression for the minimum correlation variance inside the cavity that depends crucially on the difference in the losses between the two modes. We apply our analytic solution to the important example of an MRR that is pumped with a Gaussian pulse. The expressions that we derive will help researchers optimize CV entanglement in lossy cavities.

3.1 Introduction

Entanglement serves as a basis for many applications in the field of quantum information [43], such as quantum teleportation [40, 70] and quantum key distribution [16, 71]. Entanglement can occur as correlations between discrete variables of two particles, such as the polarization of two photons, or as the correlations between CVs, such as the quadratures of photons. In quantum-optical approaches to quantum computing, those that use discrete-variable entanglement can achieve high-fidelity operations, but are currently limited by imperfect generation and detection of single photons [41]. The use of CV entanglement has the advantage that the entanglement is shared between many photons, but it is not able to achieve as high fidelity operations [41]. To remedy this trade-off and attempt to achieve large-scale quantum computing, hybrid approaches that utilize both CV and discrete-variable have been demonstrated [72].

In the context of quantum optics, two-mode squeezed states are routinely used as a source of CV entanglement. They can be generated by mixing two single-mode squeezed states on a beam-splitter [41], or via a nonlinear interaction [73] such as SPDC (SPDC), where a strong coherent pump field interacts with a material that has a $\chi^{(2)}$ nonlinearity. The resulting two beams of squeezed light are entangled by the correlations between the quadratures of the photons in each beam.

The amount of CV entanglement in the squeezed state increases with the amount of squeezing, so in the limit of infinite squeezing the two-mode squeezed state resembles a maximally-entangled EPR state [74]. To enhance the amount of squeezing, and thus entanglement, it is beneficial for the SPDC interaction to occur in a cavity that is resonant with the pump field, as well as the generated signal and idler fields.

In this work, we model the evolution of a squeezed state inside a lossy multimode cavity. We model the evolution with the LME. We show that the solution to this model is a two-mode squeezed thermal state for all time, with time-dependent squeezing amplitude, and thermal photon number for each mode.

In previous work [35] we studied single-mode squeezed states in a lossy cavity. We modelled the dynamics of the generated squeezed light using the LME for a single-mode lossy cavity and derived the solution for the state in the cavity to be a squeezed thermal state. This present work builds on our previous work by including two modes that have different frequencies and loss rates. As one of the main results in this paper, we derive an analytic expression for the minimum correlation variance in the cavity as a function of the time-dependent squeezing and mode thermal photon numbers. This expression includes an explicit dependence on the mode losses and shows that the correlation variance is minimized when the losses of the two modes are equal.

An important structure for generating CV entanglement is an MRR side-coupled to a waveguide. It enhances the nonlinear interaction that produces squeezed light and can be integrated on a chip [46, 51, 75, 76]. In the second part of the paper, we apply our model to a side-coupled ring resonator that is pumped with a Gaussian pulse that is coupled in from the linear waveguide. We derive an analytic expression for the minimum correlation variance in the ring that depends on the pump duration, coupling and scattering loss in the ring.

The paper is organized as follows. In Sec. 3.2 we derive the two-mode squeezed thermal state solution, and give a set of coupled first-order differential equations for the squeezing amplitude and thermal photon numbers of each mode. Using our solution for the state in the cavity, in Sec. 3.3 we derive an expression for the inseparability of the state, the minimum correlation variance in the cavity, that depends on the pump pulse, and we derive analytic results for the steady-state solution for a continuous pump. In Sec. 3.4 we apply our theory to the example of generating CV entanglement in a side-coupled MRR pumped with a Gaussian input pulse. Finally in Sec. 3.5 we present our conclusions.

3.2 The Lindblad master equation for a two-mode lossy cavity

In this section we derive the solution to the LME for the generation of a two-mode squeezed state in a lossy cavity. The cavity is pumped with a strong pump field, and signal and idler photon pairs are generated via SPDC (SPDC) with frequencies ω_1 and ω_2, respectively. We assume that the cavity is resonant at the frequencies of the signal and idler. Treating the pump as a strong classical field and neglecting depletion of the pump due to the nonlinear interaction, the Hamiltonian for the signal and idler photons in the cavity is given by [62]

$$\widehat{H} = \hbar\omega_1 \widehat{b}_1^\dagger \widehat{b}_1 + \hbar\omega_2 \widehat{b}_2^\dagger \widehat{b}_2 + \gamma^* \mathcal{E}_P^*(t) \widehat{b}_1 \widehat{b}_2 + \gamma \mathcal{E}_P(t) \widehat{b}_1^\dagger \widehat{b}_2^\dagger, \tag{3.1}$$

where, $\widehat{b}_1$ ($\widehat{b}_1^\dagger$) and $\widehat{b}_2$ ($\widehat{b}_2^\dagger$) destroy (create) photons in the cavity in the mode 1 and 2 with frequency ω_1 and ω_2, respectively. The last two terms in Eq. (3.1) account for the nonlinear SPDC interaction that generates the two-mode squeezed light, where the second-order nonlinear coefficient is $\gamma = -i\hbar\chi^{(2)}\sqrt{\omega_1\omega_2}$, where $\chi^{(2)}$ is an effective second-order nonlinear susceptibility. Here $\mathcal{E}_P(t)$ is the positive frequency part of the time-dependent classical electric field, $E_P(t)$, where $E_P(t) = \mathcal{E}_P(t) + \mathcal{E}_P^*(t)$. In all that follows, only the positive frequency part of the electric field is used, because counter-rotating terms can be neglected.

To gain some insight into the state of the light inside the cavity, first consider the case that the cavity is lossless and the pump is a continuous wave with $\mathcal{E}_P(t) = \mathcal{E}_0 \exp(-i(\omega_1 + \omega_2)t)$. Then the state evolves in time with a unitary two-mode squeezing operator [62] given by

$$\widehat{S}(z) = \mathrm{e}^{z^* \widehat{b}_1 \widehat{b}_2 - z \widehat{b}_1^\dagger \widehat{b}_2^\dagger}, \tag{3.2}$$

with a time-dependent complex squeezing parameter $z = r\exp(i\phi)$, related to the pump amplitude by $z = it\gamma\mathcal{E}_0/\hbar$.

Now we consider the general case where the cavity has loss and there is a pulsed pump. In this case, the dynamics of the density operator $\widehat{\rho}$ in the cavity are modelled using the LME [64]:

$$\frac{d\widehat{\rho}}{dt} = -\frac{i}{\hbar}\left[\widehat{H}, \widehat{\rho}\right] + \frac{1}{2}\sum_{j=1}^{2} \Gamma_j \left(2\widehat{b}_j \widehat{\rho} \widehat{b}_j^\dagger - \widehat{b}_j^\dagger \widehat{b}_j \widehat{\rho} - \widehat{\rho} \widehat{b}_j^\dagger \widehat{b}_j\right), \tag{3.3}$$

where the loss of the cavity is captured by intensity decay rates Γ_1 and Γ_2 for modes 1 and 2, respectively. With the inclusion of loss, the state does not simply evolve in time by operating with a squeezing operator.

The main result of this paper is the derivation of the solution to the system of Eqs. (3.1) and (3.3). First, however, we consider a simpler situation where there is no pump in the cavity ($\mathcal{E}_P(t) = 0$), so that the last two terms in the Hamiltonian in Eq. (3.1) are zero. In this case, we assume that the initial state is a two-mode thermal state, which is formed by the product of single-mode thermal states:

$$\widehat{\rho}_{\text{th}} = \prod_{j=1}^{2} (1 - x_j) (x_j)^{\widehat{n}_j} , \tag{3.4}$$

where

$$x_j = \exp\left(-\frac{\hbar\omega_j}{k_B T_j}\right) \tag{3.5}$$

and $\widehat{n}_j$ is the photon number operator for the mode j. Here, k_B is the Boltzmann constant and T_j is the effective temperature of mode j. The average number of photons in the thermal state in each mode n_j is given by

$$n_j = \frac{x_j}{1 - x_j}. \tag{3.6}$$

We now prove that the state in the cavity remains a two-mode thermal state for all time, with an average thermal photon number that decays exponentially over time. This means that the solution to Eq. (3.3) when there is no interaction term in the Hamiltonian in Eq. (3.1) can be written as

$$\widehat{\rho}(t) = \widehat{\rho}_{\text{th}}(t), \tag{3.7}$$

where $\widehat{\rho}_{\text{th}}(t)$ is given in Eq. (3.4), except now the variable x_j is time-dependent due to the dynamical thermal photon number. Rearranging Eq. (3.7) we obtain

$$1 = [\widehat{\rho}_{\text{th}}(t)]^{-1/2}\,\widehat{\rho}(t)\,[\widehat{\rho}_{\text{th}}(t)]^{-1/2}\,, \tag{3.8}$$

where we have used the fact that the thermal state operator is Hermitian. Taking the time derivative of both sides of Eq. (3.8) yields

$$0 = \frac{d}{dt}\left(\widehat{\rho}_{\text{th}}^{-1/2}\widehat{\rho}\widehat{\rho}_{\text{th}}^{-1/2}\right). \tag{3.9}$$

Applying the chain rule, we obtain

$$0 \;=\; \frac{d\widehat{\rho}_{\text{th}}^{-1/2}}{dt}\widehat{\rho}\widehat{\rho}_{\text{th}}^{-1/2} + \widehat{\rho}_{\text{th}}^{-1/2}\frac{d\widehat{\rho}}{dt}\widehat{\rho}_{\text{th}}^{-1/2} + \widehat{\rho}_{\text{th}}^{-1/2}\widehat{\rho}\frac{d\widehat{\rho}_{\text{th}}^{-1/2}}{dt}. \tag{3.10}$$

Simplifying Eq. (3.10) using the derivative of $\widehat{\rho}$ in Eq. (3.3) and the identity in Eq. (3.8), we eliminate $\widehat{\rho}$ from all the terms in Eq. (3.10), and are left with terms that only contain $\widehat{\rho}_{\text{th}}$ and its derivative. Then, using the thermal state in Eq. (3.4), we obtain

$$0 \;=\; \sum_{j=1}^{2}\left(\widehat{n}_j + \frac{x_j}{x_j - 1}\right) D_j, \tag{3.11}$$

where

$$D_j = -\frac{1}{x_j}\frac{dx_j}{dt} + \Gamma_j\left(x_j - 1\right). \tag{3.12}$$

In order for Eq. (3.11) to be true for all times we must have that $D_j = 0$, which has the solution

$$x_j(t) = \frac{1}{1 + \mathcal{C}\mathrm{e}^{\Gamma_j t}}, \tag{3.13}$$

where $\mathcal{C}$ is a constant determined by the initial conditions. Using Eqs. (3.5) and (3.6), we can rewrite Eq. (3.13) as

$$n_j(t) = n_j(0)\mathrm{e}^{-\Gamma_j t}, \tag{3.14}$$

which says that the average photon number in each mode decays from an initial value $n_j(0)$ at the rate Γ_j. Thus, if we start with a thermal state, it will remain a thermal state for all times, but with different time-dependent temperatures for the two modes.

Our focus now is to include the pump, so that the last two terms in the Hamiltonian in Eq. (3.1) are not zero. In this case, as we shall see, the two-mode thermal state will be squeezed with the two-mode squeezing operator $\widehat{S}$ in Eq. (3.2). Therefore, we propose that the solution to Eq. (3.3) is the squeezed two-mode thermal state

$$\widehat{\rho}(t) = \widehat{S}(z(t))\widehat{\rho}_{\mathrm{th}}(t)\widehat{S}^{\dagger}(z(t)), \tag{3.15}$$

where now the thermal photon number and squeezing parameter are time-dependent. Rearranging Eq. (3.15) we obtain

$$1 = \left[\widehat{\rho}_{\mathrm{th}}(t)\right]^{-1/2} \widehat{S}^{\dagger}(z(t))\widehat{\rho}\widehat{S}(z(t)) \left[\widehat{\rho}_{\mathrm{th}}(t)\right]^{-1/2}. \tag{3.16}$$

Taking the time derivative of both sides, we obtain

$$0 = \frac{d}{dt}\left(\widehat{\rho}_{\mathrm{th}}^{-1/2}\widehat{S}^{\dagger}\widehat{\rho}\widehat{S}\widehat{\rho}_{\mathrm{th}}^{-1/2}\right). \tag{3.17}$$

Applying the chain rule gives

$$\begin{aligned} 0 = {} & \frac{d\widehat{\rho}_{\mathrm{th}}^{-1/2}}{dt}\widehat{S}^{\dagger}\widehat{\rho}\widehat{S}\widehat{\rho}_{\mathrm{th}}^{-1/2} + \widehat{\rho}_{\mathrm{th}}^{-1/2}\widehat{S}^{\dagger}\widehat{\rho}\widehat{S}\frac{d\widehat{\rho}_{\mathrm{th}}^{-1/2}}{dt} + \widehat{\rho}_{\mathrm{th}}^{-1/2}\frac{d\widehat{S}^{\dagger}}{dt}\widehat{\rho}\widehat{S}\widehat{\rho}_{\mathrm{th}}^{-1/2} + \widehat{\rho}_{\mathrm{th}}^{-1/2}\widehat{S}^{\dagger}\widehat{\rho}\frac{d\widehat{S}}{dt}\widehat{\rho}_{\mathrm{th}}^{-1/2} \\ & + \widehat{\rho}_{\mathrm{th}}^{-1/2}\widehat{S}^{\dagger}\frac{d\widehat{\rho}}{dt}\widehat{S}\widehat{\rho}_{\mathrm{th}}^{-1/2}. \end{aligned} \tag{3.18}$$

Following a process similar to the one above in the case of no pump, we simplify the terms in Eq. (3.18) and show (see Appendix B.1) that for the equality to be satisfied for all times, the thermal photon numbers ($n_1(t)$ and $n_2(t)$), squeezing amplitude ($r(t)$), and squeezing phase ($\phi(t)$) must be solutions of the following first-order coupled differential equations:

$$\frac{dn_1}{dt} = n_1\left(\Gamma_2\sinh^2 r - \Gamma_1\cosh^2 r\right) + \Gamma_2\sinh^2 r, \tag{3.19}$$

$$\frac{dn_2}{dt} = n_2\left(\Gamma_1\sinh^2 r - \Gamma_2\cosh^2 r\right) + \Gamma_1\sinh^2 r, \tag{3.20}$$

$$\frac{dr}{dt} = \frac{i}{2\hbar}\left(\mathcal{E}_P\gamma \mathrm{e}^{-i\phi} - \mathcal{E}_P^*\gamma^*\mathrm{e}^{i\phi}\right) - \frac{\cosh(r)\sinh(r)}{n_1+n_2+1}\left(\frac{\Gamma_1+\Gamma_2}{2} + \frac{\Gamma_1-\Gamma_2}{2}\left(n_2-n_1\right)\right), \tag{3.21}$$

$$\frac{d\phi}{dt} = -\left(\omega_1+\omega_2\right) + \frac{\left(\mathcal{E}_P\gamma\mathrm{e}^{-i\phi} + \mathcal{E}_P^*\gamma^*\mathrm{e}^{i\phi}\right)}{\hbar\tanh(2r)}, \tag{3.22}$$

where we have omitted the time-dependencies in all variables and $\mathcal{E}_P(t)$ for simplicity. Eqs. (3.19) to (3.22) describe the dynamics of the squeezing of the state in the cavity. If we let the decay rates of the two modes be identical, *i.e.* $\Gamma_1 = \Gamma_2$, this set of equations reduces to the single mode squeezing equations from our previous work [36]. Note that Eq. (3.22) only depends on the sum-frequency frequency $\omega_s = \omega_1 + \omega_2$. Thus, the dynamics of the squeezed state does not depend on the individual frequencies of the signal and idler photons, except implicitly through the effective nonlinearity, γ.

In order to obtain a specific solution to this set of first-order differential equations, an initial state in the cavity must be specified. In all that follows, we take the initial state in the cavity to be the vacuum. We define an initial time t_i when the state in the cavity is vacuum, that is $r(t_i) = 0$, and $n_j(t_i) = 0$, respectively. This causes the denominator of the second term in Eq. (3.22) to be zero, because $\tanh(2r(t_i)) = 0$. In order to eliminate the singularity, we choose the initial squeezing phase such that the numerator of the second term is zero

$$\mathcal{E}_P(t_i)\gamma \mathrm{e}^{-i\phi(t_i)} + \mathcal{E}_P^*(t_i)\gamma^* \mathrm{e}^{i\phi(t_i)} = 0, \tag{3.23}$$

where the initial pump in the cavity $\mathcal{E}_P(t_i)$ is arbitrarily small but not zero. If we let the pump and nonlinear parameter be written as a general complex number as $\mathcal{E}_P(t_i)\gamma = |\mathcal{E}_P(t_i)||\gamma|\mathrm{e}^{i\theta - i\omega_s t_i}$, then the solution to Eq. (3.23) for the initial squeezing phase is $\phi(t_i) = -\pi/2 - \theta + \omega_s t_i$ [77]. Requiring that the first derivative of $\phi(t)$ at t_i and the next time-step $t_i + \Delta t$ are equal, it can be shown that the squeezing phase for all future times is given by

$$\phi(t) = -\omega_s t + \phi(t_i) \tag{3.24}$$

Therefore if the initial state is vacuum, then the squeezing phase does not depend on the thermal photon numbers or squeezing amplitude, and simply rotates around the origin of phase space with the sum-frequency ω_s.

Using the expression in Eq. (3.24) for $\phi(t)$ in Eq. (3.21), the equation for the squeezing amplitude becomes,

$$\frac{dr}{dt} = \frac{|\mathcal{E}_P(t)||\gamma|}{\hbar} - \frac{\cosh(r)\sinh(r)}{n_1+n_2+1}\left(\frac{\Gamma_1+\Gamma_2}{2} + \frac{\Gamma_1-\Gamma_2}{2}(n_2-n_1)\right). \tag{3.25}$$

It is convenient to write Eqs. (3.19), (3.20), and (3.25) in terms of the dimensionless parameter $\tilde{t} = \Gamma_+ t$, where $\Gamma_\pm = (\Gamma_1 \pm \Gamma_2)/2$. Doing this, we obtain

$$\frac{dr}{d\tilde{t}} = \frac{g(\tilde{t})}{2} - \frac{\cosh(r)\sinh(r)}{n_1+n_2+1}\left(1+\zeta\left(n_2-n_1\right)\right), \tag{3.26}$$

$$\frac{dn_1}{d\tilde{t}} = n_1\left((1-\zeta)\sinh^2 r - (1+\zeta)\cosh^2 r\right) + (1-\zeta)\sinh^2 r, \tag{3.27}$$

$$\frac{dn_2}{d\tilde{t}} = n_2\left((1+\zeta)\sinh^2 r - (1-\zeta)\cosh^2 r\right) + (1+\zeta)\sinh^2 r, \tag{3.28}$$

where ζ is defined as

$$\zeta \equiv \frac{\Gamma_-}{\Gamma_+} = \frac{\Gamma_1-\Gamma_2}{\Gamma_1+\Gamma_2}, \tag{3.29}$$

and is proportional to the difference of the two decay rates, and $g(t)$ is the pumping strength in the ring; it is defined as the rate of light generation in the cavity divided by the average decay rate of light out of the cavity

$$g(t) \equiv \frac{2|\mathcal{E}_P(t)||\gamma|}{\hbar\Gamma_+}. \tag{3.30}$$

Because the decay rates must be positive, it follows that $|\zeta| < 1$. When $\zeta = 0$, the decay rates of the modes are equal, the thermal photon numbers are the same, and consequently the coupled equations reduce to the single-mode squeezing case.

In summary, we have shown that the solution to the LME for the generation of a two-mode squeezed state in a lossy cavity is a two-mode squeezed thermal state and we have derived a set of coupled first-order differential equations that describe the dynamics of the state as a function of the pumping strength and cavity decay rates for each mode. We now use the two-mode squeezed thermal state to give a condition for the CV entanglement in the cavity, and derive an expression for the minimum correlation variance.

3.3 Continuous-variable entanglement in a two-mode squeezed thermal state

In this section we give the entanglement condition for the light in the cavity and derive a semi-analytic expression for the minimum correlation variance as a function of the pump and the thermal photon number difference between the two modes.

We define the quadrature operators $\widehat{X}_{12}$ and $\widehat{Y}_{12}$, that are linear combinations of the quadrature operators for mode 1 and 2,

$$\widehat{X}_{12} \equiv \frac{\widehat{b}_1 \mathrm{e}^{-i\theta_1} + \widehat{b}_1^\dagger \mathrm{e}^{i\theta_1}}{2} - \frac{\widehat{b}_2 \mathrm{e}^{-i\theta_2} + \widehat{b}_2^\dagger \mathrm{e}^{i\theta_2}}{2}, \tag{3.31}$$

$$\widehat{Y}_{12} \equiv \frac{\widehat{b}_1 \mathrm{e}^{-i\theta_1} - \widehat{b}_1^\dagger \mathrm{e}^{i\theta_1}}{2i} + \frac{\widehat{b}_2 \mathrm{e}^{-i\theta_2} - \widehat{b}_2^\dagger \mathrm{e}^{i\theta_2}}{2i}. \tag{3.32}$$

The quadrature noises in $\widehat{X}_{12}$ and $\widehat{Y}_{12}$ are equal and using the two-mode squeezed thermal state are given by

$$\left\langle(\Delta X_{12})^2\right\rangle = \left\langle(\Delta Y_{12})^2\right\rangle = \frac{1}{2}\left(1+n_1+n_2\right)\left(\cosh(2r) - \cos\left(\phi-\theta_1-\theta_2\right)\sinh(2r)\right), \tag{3.33}$$

where ϕ is the time-dependent squeezing phase in Eq. (3.24). For certain phase relationships between $\theta_1(t)$, $\theta_2(t)$, and $\phi(t)$, the quadrature noise is reduced below vacuum. Choosing the relationship between the quadrature phases be $\theta_1(t)+\theta_2(t) = \phi(t)$, the fast oscillations are removed and the quadrature noise is exponentially squeezed to give

$$\left\langle(\Delta X_{12})^2\right\rangle = \frac{1}{2}\left[1+n_1(t)+n_2(t)\right]\mathrm{e}^{-2r(t)}. \tag{3.34}$$

In the limit of infinite squeezing, $r \to \infty$, the uncertainty in the relative quadrature operator goes to zero, $\langle(\Delta X_{12})^2\rangle \to 0$. Thus, a measurement on $\widehat{X}_1$ would reduce the uncertainity of a measurement on $\widehat{X}_2$ to zero, such that the two modes are perfectly correlated. However, for finite squeezing the two modes will not be perfectly correlated. To determine when there is entanglement between the two modes and to obtain a measure of how robust the entanglement is, we define the correlation variance as the sum of the quadrature noises in the relative position and momentum operators

$$\Delta^2_{1,2} = \left\langle(\Delta X_{12})^2\right\rangle + \left\langle(\Delta Y_{12})^2\right\rangle, \tag{3.35}$$

and using Eq. (3.34) we obtain

$$\Delta^2_{1,2}(t) = \left[1+n_1(t)+n_2(t)\right]\mathrm{e}^{-2r(t)}. \tag{3.36}$$

It has been proved by Duan *et al.* [22] and Simon [23] that the two-mode squeezed state is inseparable when the correlation variance is less than 1,

$$\Delta^2_{1,2}(t) < 1. \tag{3.37}$$

This condition is achieved when the exponential squeezing factor ($\exp(-2r)$) overcomes the thermal noise factor in front.

The correlation variance in Eq. (3.36) is time dependent because the squeezing amplitude and thermal photon numbers are time dependent. If we assume that the pump is pulsed, then there should be a time when the correlation variance is minimized. In order to find an expression for the minimum of the correlation variance we find the extreme point of Eq. (3.36), $i.e.$ we solve the following equation:

$$\left.\frac{d\Delta^2_{1,2}}{dt}\right|_{t=t_{min}} = 0. \tag{3.38}$$

Simplifying this equation by using Eq. (3.26) to Eq. (3.28) we obtain,

$$\left(\Delta^2_{1,2}\right)_{min} = \frac{1+\zeta\left[n_2(t_{min})-n_1(t_{min})\right]}{1+g(t_{min})}. \tag{3.39}$$

Thus, even a small difference in the decay rates of the two modes can cause an increase in the minimum value of the correlation variance. In situations where we can treat $|\zeta|$ as a small perturbation, we can neglect the second term in the numerator of Eq. (3.39) and write,

$$\left(\Delta^2_{1,2}\right)_{min} \approx \frac{1}{1+g(t_{min})}. \tag{3.40}$$

This represents an ideal case, when the two decay rates for the modes are the same and we can drop the ζ dependence. In this case, the correlation variance is always decreased by increasing the pumping strength. We do not have an expression for the time when the correlation variance is minimum, t_{min}, so Eq. (3.39) and Eq. (3.40) must still be evaluated numerically. However, when the pump field is pulsed then, as we show in the example below, it is often a good approximation to replace $g(t_{min})$ with the peak value of the pump in the cavity, g_{max}.

3.3.1 Steady-state solution

Before considering the specific case of the response of a ring resonator system to a *pulsed* pump, we briefly discuss the *steady-state* solution for the correlation variance of a two-mode squeezed thermal state generated in a cavity that is pumped with a continuous-wave pump field. The squeezing amplitude and thermal photon numbers for each mode of the generated squeezed state are modelled using Eq. (3.26) to Eq. (3.28) with a constant pumping strength g. The steady-state solution is found by setting the time derivatives of the squeezing amplitude and thermal photon numbers to zero. This results in the steady-state solutions

$$r = \frac{1}{2}\tanh^{-1}(g), \tag{3.41}$$

$$1 + n_1 + n_2 = \frac{(1-\zeta^2)\sqrt{1-g^2}}{1-g^2-\zeta^2}. \tag{3.42}$$

Note that the steady-state squeezing amplitude is infinite at $g = 1$, and in Eq. (3.42) the right-hand side is infinite at $g = \sqrt{1-\zeta^2}$. In fact, steady-state solutions do not exist unless

$$g < \sqrt{1-\zeta^2}. \tag{3.43}$$

Putting Eqs. (3.41) and (3.42) into Eq. (3.36), we obtain for the steady-state correlation variance

$$\Delta^2_{1,2} = \frac{(1-\zeta^2)(1-g)}{1-g^2-\zeta^2}. \tag{3.44}$$

When $\zeta = 0$, the steady-state correlation variance is $\Delta^2_{1,2} = 1/(1+g)$, which is the same as Eq. (3.40), with t_{min} being interpreted as the time that the steady-state occurs. Furthermore, for a fixed ζ, the value of g that minimizes the correlation variance in Eq. (3.44) is $g = 1-|\zeta|$. Putting this g in Eq. (3.44), the minimum value of the correlation variance in the steady-state is simply

$$\left(\Delta^2_{1,2}\right)_{min} = \frac{1+|\zeta|}{2}. \tag{3.45}$$

This result shows that in the steady-state one can never achieve a correlation variance less than 1/2 (that is the 3dB limit). Additionally, it shows that even if the individual cavity losses are large, one can still achieve the minimum correlation variance by making the difference between the losses of the two modes the same. In the next section, we will discuss the results of the correlation variance for a two-mode squeezed thermal state generated in a side-coupled ring resonator using a pulsed pump.

3.4 Example: generating continuous-variable entanglement in a ring resonator

In this section we apply our formalism to a ring resonator, which is optimized to produce a highly entangled state, and we study the dynamics of the correlation variance. In previous work [36], we treated the same problem but for degenerate squeezing, where the signal and idler have the same frequency. In this example, we will generalize our previous results to the case where the signal and idler are distinguishable by their frequency and loss.

MRR s can be fabricated using electron-beam lithography in a variety of semiconducting materials with third order nonlinearities, such as GaAs, LN, SiN, and AlN. Because they have multiple resonances, they can result in the intense pump fields needed for nonlinear interactions, such as SPDC. Thus, they have been employed by several groups to generate squeezed light [56, 57, 78–80]. Moreover, they can be engineered such that one mode is resonant with the pump field, while other modes are resonant with the signal and idler modes that contain the generated squeezed light. Due to the micrometer scale of MRR s, they can be integrated into a chip platform that reduces the overall size of optical experiments. MRR s have been shown to be capable of generating single-mode squeezed light with squeezing levels that are large enough to meet the requirements for CV quantum computation [80]. For example, these devices are being used to generate CV-entangled light for quantum information processing on a scalable chip platform [81].

The ring resonator system we consider, shown in Fig. 3.1, consists of a straight waveguide (channel) side-coupled to a ring waveguide with radius R. Both the ring and channel are made from the same material that has a nonlinear $\chi^{(2)}$ response, but we ignore the nonlinear interaction in the channel, since the pump field is much weaker there than in the ring. The classical pump field incident on the ring is taken to be a classical Gaussian pulse. The positive frequency part of the pump field in the channel takes the form

$$\mathcal{E}_{CH}(t) = \mathcal{E}_0\sqrt{\frac{T_R}{\tau}}\exp\left(-2\ln(2)\frac{t^2}{\tau^2}\right)\exp(-i\omega_P t), \tag{3.46}$$

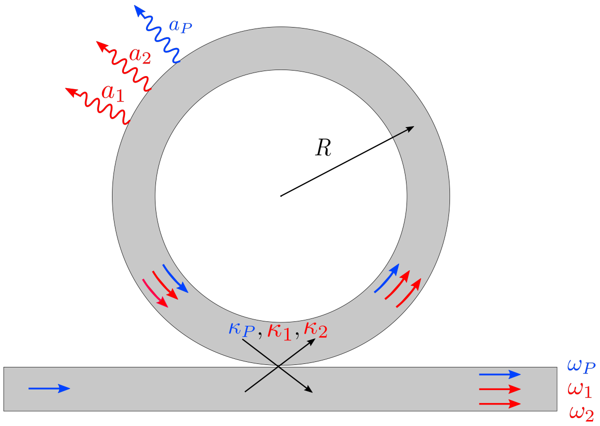

Figure 3.1: Schematic of the ring resonator side-coupled to a channel waveguide. The thick arrows represent the components of the pump field (blue) with frequency ω_P, incident from the left, and the signal and idler fields (both red) with frequencies ω_1 and ω_2, respectively. The cross-coupling coefficients and scattering loss parameters for the pump, signal, and idler fields are κ_P, κ_1, and κ_2 and a_P, a_1, and a_2, respectively.

where $\mathcal{E}_0$ is the amplitude, τ is the FWHM of the intensity of the Gaussian, ω_P is the central frequency, and $T_R = 2\pi R n_{\text{eff}}/c$ is the ring round-trip time, where n_{eff} is the effective index for the pump. We scale the amplitude by $1/\sqrt{\tau}$ so that the pulse energy is a constant that is independent of its duration. The coupling of the pulse into the ring happens at a single coupling point, as indicated in Fig. 3.1. The pump field in the ring, $\mathcal{E}_R(\omega)$, is calculated using a transfer matrix approach [36, 60], and is related to the field in the channel by

$$\mathcal{E}_R(\omega) = \frac{i\kappa_P a_P \, \mathrm{e}^{i\omega T_R}}{1 - \sigma_P a_P \, \mathrm{e}^{i\omega T_R}} \mathcal{E}_{CH}(\omega), \tag{3.47}$$

where $\mathcal{E}(\omega)$ is the Fourier transform of $\mathcal{E}(t)$ defined as

$$\mathcal{E}(\omega) = \int_{-\infty}^{\infty} \mathcal{E}(t) \, \mathrm{e}^{i\omega t} dt, \tag{3.48}$$

and the inverse Fourier transform as

$$\mathcal{E}(t) = \frac{1}{2\pi}\int_{-\infty}^{\infty} \mathcal{E}(\omega)\,\mathrm{e}^{-i\omega t} d\omega. \tag{3.49}$$

In Eq. (3.47), the constant κ_P is the frequency-independent cross-coupling constant between the ring and channel, and is related to the self-coupling constant σ_P through the lossless coupling relation: $\kappa_P^2 + \sigma_P^2 = 1$. The parameter a_P is the amplitude attenuation for the pump in the ring after a single round-trip. It is related to the power attenuation coefficient α_P by $a_P^2 = \exp(-\alpha_P 2\pi R)$. This is the power lost due to scattering only and not coupling. When $a_P = 1$, there is no scattering loss.

The buildup factor is defined as the ratio of the intensity in the ring to the channel and is given by

$$\mathcal{B}(\omega) \equiv \frac{|\mathcal{E}_R(\omega)|^2}{|\mathcal{E}_{CH}(\omega)|^2} = \frac{\kappa_P^2 a_P^2}{1 - 2\sigma_P a_P \cos(\omega T_R) + \sigma_P^2 a_P^2}. \tag{3.50}$$

It contains resonant peaks when the incident light is on resonance with the ring, *i.e.* $\cos(\omega T_R) = 1$, and the buildup is maximized. We choose the central frequency of the pump pulse to be on resonance with the ring, $\omega_P = 2\pi m_P/T_R$, where m_P is a positive integer defining the pump mode number. Inside the ring, the pump field generates signal and idler photons at the frequencies ω_1 and ω_2, via SPDC, such that energy is conserved: $\omega_P = \omega_1 + \omega_2$. The signal and idler fields are also resonant with the ring, $\omega_1 T_R = 2\pi m_1$ and $\omega_2 T_R = 2\pi m_2$, where m_1 and m_2 are the mode numbers for the signal and idler fields, respectively. For simplicity we assume perfect phase matching between the three fields, and that the effective index of refraction is the same for the pump, signal, and idler modes. The latter assumption is experimentally realized in an AlN MRR with a waveguide width of 1.10μm [51], and makes the ring round-trip time the same for each field. Using these assumptions the mode numbers are related by $m_P = m_1 + m_2$.

Generally, signal and idler photons will be generated in a number of different pairs of ring modes, as long as they satisfy energy conservation and phase matching. To simply our theory however, we assume that only the two ring modes m_1 and m_2 are perfectly phased matched, and squeezed light generation in all other modes is neglected.

Since the pump is pulsed, in general it will couple into multiple ring modes depending on how wide its bandwidth is. To ensure that most of the pump light couples into a single mode m_P we require that its duration is longer than the ring round-trip time ($\tau > T_R$). Doing so makes the pulse bandwidth overlap a single resonance peak of the buildup factor and thus the adjacent peaks in the buildup factor do not significantly couple any light into the ring. The buildup factor for the central pump frequency ω_P becomes,

$$\mathcal{B}(\omega_P) = \frac{\kappa_P^2 a_P^2}{(1 - \sigma_P a_P)^2}. \tag{3.51}$$

In all that follows we are only interested in the limit that the buildup factor is large, which only occurs when $(1 - \sigma_P a_P) \ll 1$, such that the denominator of Eq. (3.51) is small. This limit produces the smallest correlation variance in the ring.

Now we need to find an expression for the time-dependent pump field in the ring that we can use to solve for the dynamics of the squeezed state. This is done by taking the inverse Fourier transform of the field component in the ring. As we have shown in our previous work [36], in the limit when $(1 - \sigma_P a_P) \ll 1$ the integral can be approximated very well by

$$\mathcal{E}_R(t) = \frac{\tau\kappa_P a_P \sqrt{\pi} \mathrm{e}^{y(t)^2} \mathrm{erfc}[y(t)]}{\sqrt{8\ln(2)}\, T_R} \mathcal{E}_{CH}(t), \tag{3.52}$$

where

$$y(t) \equiv \frac{(1-\sigma_P a_P)\tau}{\sqrt{8\ln(2)}\, T_R} - \frac{\sqrt{8\ln(2)}\, t}{2\tau}. \tag{3.53}$$

Now to model the evolution of the state in the ring we use the pump field in Eq. (3.52) in the coupled Eqs. (3.26) to (3.28). The pumping strength in the ring defined in Eq. (3.30) becomes

$$g(\tilde{t}\,) = g_0 \frac{\kappa_P a_P \sqrt{\pi} \mathrm{e}^{y(\tilde{t}\,)^2} \mathrm{erfc}[y(\tilde{t}\,)]}{\sqrt{8\ln(2)}} \sqrt{\frac{\tilde{\tau}}{T_R \Gamma_+}} \exp\left(-2\ln(2)\frac{\tilde{t}^2}{\tilde{\tau}^2}\right), \tag{3.54}$$

where we define the dimensionless parameter

$$g_0 \equiv \frac{2|\gamma|\mathcal{E}_0}{\hbar\Gamma_+}, \tag{3.55}$$

which is proportional to the input pump pulse amplitude $\mathcal{E}_0$ divided by the average decay rate of the signal and idler mode Γ_+, where we have used the same parameters defined above, $\tilde{t} = \Gamma_+ t$ and $\tilde{\tau} = \Gamma_+ \tau$. At this point we could simply solve the dynamic Eqs. (3.26) to (3.28) numerically for any desired loss and pump parameters. However, as we shall show, a key parameter that affects the correlation variance is the difference in the loss in the signal and idler modes, ζ. Therefore, to simplify the discussion of our results and to make the pumping strength in Eq. (3.54) dependent only on the pump coupling and loss parameters, we assume that the average of the decay rate of the signal and idler is equal to the pump decay rate, Γ_P, *i.e.*, $\Gamma_+ \equiv \Gamma_P$. When

$(1 - \sigma_P a_P) \ll 1$, the pump decay rate is

$$\Gamma_P = \frac{2(1 - \sigma_P a_P)}{T_R}. \tag{3.56}$$

Then using Eq. (3.56) in Eq. (3.54), the pumping strength in the ring can be written as

$$g(\tilde{t}\,) = \frac{g_0}{2} \frac{\kappa_P a_P}{\sqrt{1 - \sigma_P a_P}} \sqrt{\frac{\tilde{\tau}}{8 \ln(2)}} \exp\left(\frac{-2 \ln(2)\, \tilde{t}^2}{\tilde{\tau}^2} \right) \sqrt{\pi} \mathrm{e}^{y(\tilde{t}\,)^2} \mathrm{erfc}[y(\tilde{t}\,)]. \tag{3.57}$$

This completes the parameterization of our model.

Our focus now is to examine the numerical results for the correlation variance in Eq. (3.36) found by solving the dynamic equations with the pump field given by the expression in Eq. (3.57). To do this, we use a 4th-order Runge-Kutta method which has a run-time of about 1 millisecond on a standard PC. Our model depends on the parameters g_0, κ_P, σ_P, and a_P, and the difference in the loss rates ζ. Thus, our results are effectively independent of the ring radius, pump amplitude, and the nonlinear parameter. However, to make connection to a specific, realistic system, we choose a ring of radius $R = 20\,\mu\mathrm{m}$ made from AlGaAs, with an effective second-order nonlinear susceptibility of $\chi^{(2)} = 11\,\mathrm{pm/V}$ [46]. Additionally, we let the central frequency and amplitude of the pump pulse be $\omega_P = 2\pi \times 128.9\,\mathrm{THz}$ ($\lambda_P = 775\,\mathrm{nm}$) and $\mathcal{E}_0 = 1\,\mathrm{MV/cm}$. The frequencies of the signal and idler fields are $\omega_1 = 2\pi \times 64.68\,\mathrm{THz}$ ($\lambda_1 = 1545\,\mathrm{nm}$) and $\omega_2 = 2\pi \times 64.27\,\mathrm{THz}$ ($\lambda_2 = 1555\,\mathrm{nm}$), respectively. With these parameter choices, $g_0 = 4$.

In our previous work [36], we derived the optimum value for the pulse duration $\tilde{\tau}_{opt}$ by taking the derivative of the pumping strength in Eq. (3.57) with respect to

τ, at the peak value, and set it equal to zero. This results in the following accurate estimate of the optimum pulse duration of

$$\tilde{\tau}_{opt} = 0.684\sqrt{8\ln(2)}. \tag{3.58}$$

The prefactor of 0.684 in this expression arises from the solution of a transcendental equation, and this can be evaluated to arbitrary accuracy. The optimum value for σ_P can be obtained [36] by taking the derivative of the pumping strength with respect to σ_P, at the peak value and $\tilde{\tau} = \tilde{\tau}_{opt}$, and set it equal to zero. For a loss parameter of $a_P = 0.99$, this results in an optimum value of $\sigma_P = 0.868$.

In Fig. 3.2a we plot the correlation variance when the decay rates of the two modes are set to be the same by letting $\zeta = 0$. Since the photons in modes 1 and 2 are scattered from the ring at the same rate, the photon pairs are not separated due to scattering and the state in the ring remains an entangled state with $\Delta^2_{1,2} < 1$.

In Fig. 3.2b we again plot the correlation variance, but let $\zeta = 1/3$, which gives $\Gamma_1 = 2\Gamma_2$ and $\Gamma_2 = 2\Gamma_P/3$. The discrepancy between the two decay rates means that photons are being scattered from mode 1 twice the rate as from mode 2. Effectively, this means that half of the generated entangled state is being traced-out by the scattering; *i.e.*, photon 1 escapes the ring while photon 2 stays inside the ring. Thus, the state in the ring evolves into a thermal state. This is why the correlation variance in Fig. 3.2b goes above 1 after $\tilde{t} \approx 2$. After this time, the correlation variance becomes as large as 60 (not shown in plot) and the state in the ring is essentially a separable two-mode thermal state.

In Fig. 3.3 the minimum of the correlation variance, $\Delta^2_{1,2}(t_{min})$, is shown as a function of $\tilde{\tau}$ and ζ. The first thing to notice is that it is symmetric about $\zeta = 0$.

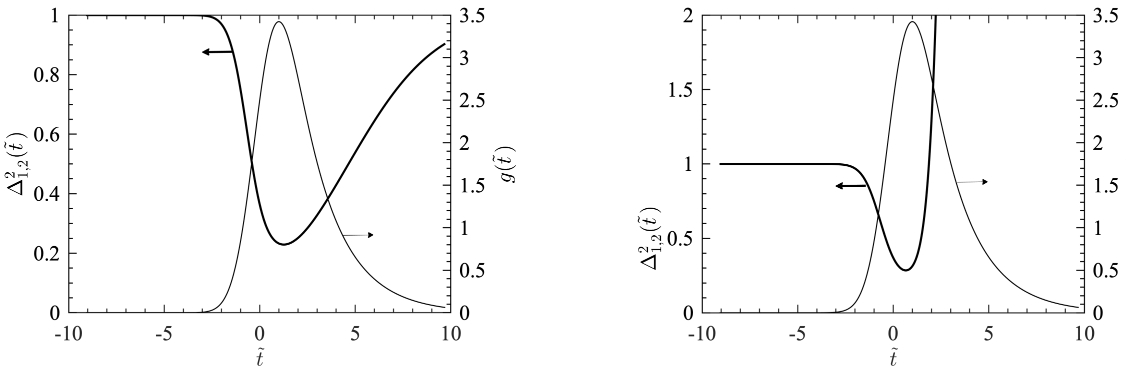

(a) (b)

Figure 3.2: The time-dependent correlation variance for (a) $\zeta = 0$, and (b) $\zeta = 1/3$, pumping strength $g_0 = 4$, using a pulsed pump of duration $\tilde{\tau}_{opt}$, a pump scattering loss of $a_P = 0.99$, and optimum self-coupling constant $\sigma_P = 0.868$. Also shown is the time-dependent pumping strength.

This is because the product $\zeta(n_2 - n_1)$ in Eq. (3.39) is always positive. Next we observe that for a given τ, the smallest $\Delta^2_{1,2}$ is always where $\zeta = 0$, because this makes the numerator of Eq. (3.39) as small as possible (*i.e.*, equal to 1). The global minimum in $\Delta^2_{1,2}(t_{min})$ (indicated by the white cross) occurs with the τ that makes $g(t_{min})$ as large as possible (see Eq. (3.40)), which occurs approximately at $\tilde{\tau}_{opt}$ (black line) given in Eq. (3.58). When we increase or decrease the pulse duration from the optimum value, it causes $\Delta^2_{1,2}(t_{min})$ to increase. This is because the energy of our pulse is independent of its duration, so for long pulses its amplitude scales as $1/\sqrt{\tau}$ and for short pulses the energy is injected over too short a time interval for the intensity to buildup. In both cases, for a long or short pulse, the pumping strength decreases and $\Delta^2_{1,2}$ increases. When $|\zeta| > 0$, the entangled state is degraded by the unequal scattering of its photon pairs, and by increasing τ we observe a rapid increase of $\Delta^2_{1,2}$. Conversely, when $\zeta = 0$ and τ is increased, then the increase of $\Delta^2_{1,2}$ is less rapid, because both photons are scattered at the same rate. However, when the pulse

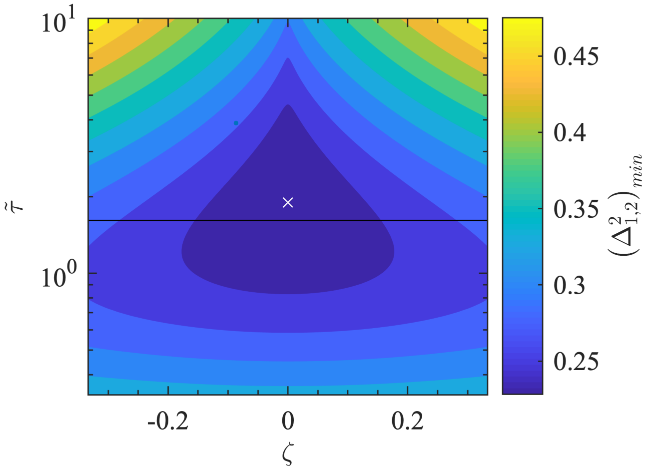

Figure 3.3: The minimum value of the correlation variance $(\Delta^2_{1,2})_{min}$ as a function of the difference between the losses of the two-modes ζ and the pump pulse duration $\tilde{\tau}$. The optimum pulse duration $\tilde{\tau}_{opt}$ given by Eq. (3.58) is shown with the black line, and the global minimum is indicated by the white cross. All other parameters are the same as in Fig. (3.2).

duration is shorter than the optimum, $\Delta^2_{1,2}$ is not very sensitive to $|\zeta|$.

The thermal photon number in mode 1, evaluated at t_{min}, is shown in Fig. 3.4 as a function $\tilde{\tau}$ and ζ for the same parameters as above. A relatively large thermal photon number implies that there is more generation of squeezed light, but if the thermal photon number becomes too large, it destroys the entanglement (see Eq. (3.36)). There is an average thermal photon number of approximately 2 for each mode at the global minimum of the correlation variance. Where the average thermal photon number is 10 there is more generation of squeezed light, but $\Delta^2_{1,2}$ is larger due to the increased thermal noise. The thermal photon number in mode 2 is a mirror reflection, about $\zeta = 0$, of mode 1, which can be shown by letting $\zeta \to -\zeta$ in Eqs. (3.27) and (3.28).

In both Fig. 3.2a and Fig. 3.2b, the minimum value of the correlation variance

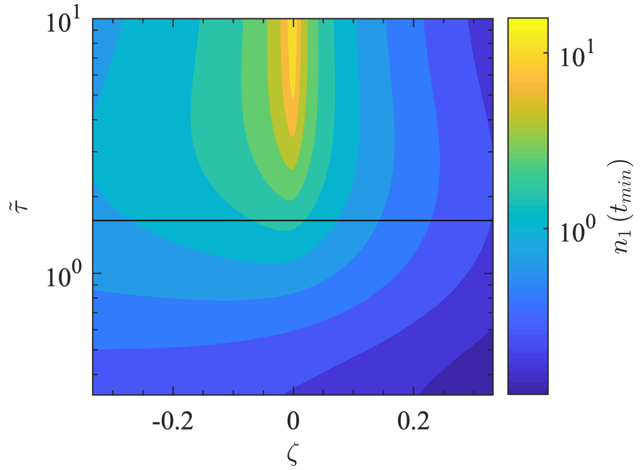

Figure 3.4: The average number of thermal photons in mode 1, evaluated at the time when the correlation variance is minimum, $n_1(t_{min})$, as a function of ζ and $\tilde{\tau}$. All parameters are the same as in Fig. (3.3)

occurs very close to the time when the pumping strength is maximum in the ring (g_{max}). Thus, in Eq. (3.40), which gives the approximate minimum value of the correlation variance, we can let $g(t_{min}) = g_{max}$. In our previous work [36] we showed that this is a valid approximation when the input pulse duration is longer than T_R. Using Eq. (3.57) it can be shown that the pumping strength peaks at $\tilde{t} = 1$ for the optimum pulse duration. Putting $\tilde{t} = 1$ and $\tilde{\tau}_{opt}$ into the pumping strength in Eq. (3.57) gives the following expression for g_{max}:

$$g_{max} = 0.653 g_0 \frac{\kappa_P a_P}{\sqrt{1 - \sigma_P a_P}}. \tag{3.59}$$

Therefore, we can use Eq. (3.59) in Eq. (3.40) in place of $g(t_{min})$ to obtain an expression for the minimum of the correlation variance when $|\zeta| \ll 1$ in terms of the pump parameters g_0, κ_P, σ_P, and a_P only,

$$\left(\Delta_{1,2}^2\right)_{min} = \left[1 + 0.653 g_0 \frac{\kappa_P a_P}{\sqrt{1-\sigma_P a_P}}\right]^{-1}. \tag{3.60}$$

The optimum coupling constant σ_P that minimizes Eq. (3.60) for a fixed g_0 and a_P is,

$$\sigma_P = \frac{1-\sqrt{1-a_P^2}}{a_P}. \tag{3.61}$$

Putting this optimum coupling constant into Eq. (3.60) gives a good approximation to the global minimum in the correlation variance for a given g_0 and loss a_P. In Fig. 3.5, the global minimum in the correlation variance is shown as a function of g_0 for $a_P = 0.99$ (circle) and $a_P = 0.75$ (cross). The solid lines are the expression in Eq. (3.60), and they show excellent agreement with the full numerical simulations across a wide range of g_0 values for the two scattering losses. Also shown is the sum of the thermal photon numbers in the two modes. This shows that the cost associated with decreasing the correlation variance is an increase in the overall thermal noise in the ring. By increasing the scattering loss we observe an increase in $\Delta_{1,2}^2$ and the total thermal photon number. In order to recover the variance we can increase g_0, but this causes an increase in the thermal noise. For example, when $a_P = 0.99$ and $g_0 = 4$, the minimum of the correlation variance is about 0.25 and there are a total of about 4 thermal photons. If we increase the scattering loss to $a_P = 0.75$ and keep $g_0 = 4$, then the variance jumps to about 0.35 and the total thermal photon number decreases to about 2. In order to recover the variance, we would need to increase to $g_0 = 7$, and as a result we would increase the total thermal photon number to about 20.

The expression for the correlation variance in Eq. (3.36) is what one would infer

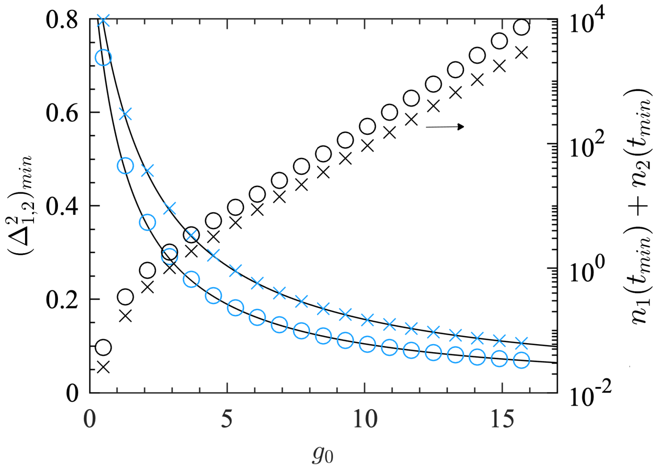

Figure 3.5: The global minimum in the correlation variance as a function of g_0 for pump scattering loss and optimum self-coupling constant of $a_P = 0.99$ and $\sigma_P = 0.868$ (circle) and $a_P = 0.75$ and $\sigma_P = 0.451$ (cross), respectively. Also shown is the total number of thermal photons evaluated at the global minimum for each of these losses.

from measurements in a homodyne detection experiment, if the local oscillators are perfectly phase matched to the squeezing phase $\phi(t)$. It what follows, we will allow for a small angle deviation $\delta\theta$ from perfect phase matching and see how this affects the correlation variance. The correlation variance when there is an angular deviation becomes

$$\Delta^2_{1,2} = (1 + n_1 + n_2)\left[\cosh(2r) - \cos(\delta\theta)\sinh(2r)\right]. \tag{3.62}$$

If $\delta\theta = 0$ we recover the perfect case in Eq. (3.36). In Fig. 3.6a we show the minimum of the correlation variance for an angular deviation of 5 mrad, with $a_P = 0.99$, $\sigma_P = 0.868$, and $g_0 = 4$. This angular deviation was measured in a recent experiment [68]. Overall, the correlation variance is not changed significantly from the ideal case (when there is no offset), but there is a small increase in the global minimum from approximately 0.228 when there is no offset to approximately 0.229. In Fig. 3.6b and Fig. 3.6c the angle offset is increased to $\delta\theta = 20$ mrad and $\delta\theta = 100$ mrad,

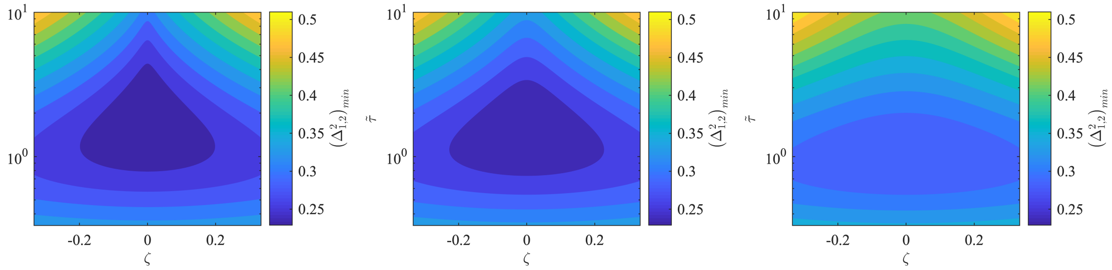

(a) (b) (c)

Figure 3.6: The minimum in the correlation variance as a function of $\tilde{\tau}$ and ζ for homodyning angles of (a) 5 mrad, (b) 20 mrad, and (c) 100 mrad. All other parameters are the same as in Fig. (3.3).

respectively, while keeping all other parameters the same. For these two offsets, the global minimum increases to approximately 0.235 and 0.282, respectively. The general trend created by increasing the angle offset is that the global minimum of the correlation variance shifts to shorter pulse durations and the optimal region flattens out; becoming more sensitive to pulse duration and less sensitive to ζ. Thus, the discrepancy between the two decay rates does not destroy the correlation variance as much when there is an angle offset. Instead, the pulse duration is much more destructive to the correlation variance. When there is an angle offset, it is always better to shorten the optimum pulse duration to decrease the correlation variance.

3.5 Conclusion

In conclusion, we have shown that the solution to the LME for a two-mode cavity pumped with a classical optical pulse is a two-mode squeezed thermal state for all time. We derived a semi-analytic solution for the time-dependent squeezing amplitude, and thermal photon numbers for the two modes, which we then used to derive an expression for the minimum correlation variance in the cavity (see Eq. (3.39)).

The main parameter that affects the correlation variance is the difference in the cavity losses between the two modes ζ. In the ideal case, the losses for the two modes are the same $\zeta = 0$ and the correlation variance just scales inversely proportional to the peak pumping strength in the cavity (see Eq. (3.40)). However, the trade-off is that when the pumping strength is increased the total thermal noise also increases. We also showed that for a continuous pump the steady-state correlation variance can never be less than $1/2$.

We applied our theory to the important example of generating CV entanglement in a ring resonator with different losses for each mode. We derived a semi-analytic expression for the minimum correlation variance in the ring (see Eq. (3.60)) that depends only on the pump scattering loss and coupling parameters. If the two modes have unequal losses we demonstrated that it is always better to decrease the pulse duration from the optimum in order to achieve a smaller correlation variance. We considered the case of a phase offset in a homodyne detection experiment, which would cause a degradation of the measured entanglement, and we showed that the minimum of the correlation variance could be recovered to a high degree by reducing the pulse duration from the optimum. Additionally, when the phase offset is increased, it was shown that the correlation variance is less sensitive to the unequal losses of the two modes.

These results will be of use to researchers that are trying to optimize CV entanglement in lossy cavities when the losses of each mode are different. In future work, we will apply this theory to the generation of two-mode squeezed light in a slab photonic crystal, where a three-mode cavity is side-coupled to a defect waveguide.

Chapter 4

Simple way to incorporate loss when modelling multimode entangled state generation

In this chapter, a numerical method is developed to model the nonlinear generation of light in the modes of multiple lossy coupled nanocavities. In this work, we prove that the density operator for the generated light has the analytic form of an MSTS. Therefore we extend our numerical method for two modes from the previous chapter to systems of multiple modes. We also derive expressions that can be used to test for entanglement in the quadratures of the multimode squeezed state. This work is published as a regular article in Physical Review A [82].

Abstract – We show that the light generated via spontaneous four-wave mixing or parametric down conversion in multiple, coupled, lossy cavities is a multimode squeezed thermal state. Requiring this state to be the solution of the Lindblad master equation results in a set of coupled first-order differential equations for the time-dependent squeezing parameters and thermal photon numbers of the state. The benefit of this semi-analytic approach is that the number of coupled equations scales

linearly with the number of modes and is independent of the number of photons generated. With this analytic form of the state, correlation variances are easily expressed as analytic functions of the time-dependent mode parameters. Thus, our solution makes it computationally tractable and relatively straight forward to calculate the generation and evolution of multimode entangled states in multiple coupled, lossy cavities, even when there are a large number of modes and/or photons.

4.1 Introduction

Multimode squeezed states can be generated via a nonlinear interaction in resonant structures, such as MRRs (see Fig. 4.1a) or coupled-resonator optical waveguides (CROWs) in a photonic crystal (see Fig. 4.1c). They are a source of CV entanglement, since the quadratures of the photons in different modes in the state can be correlated. CV entanglement has applications in boson sampling [83, 84], quantum computing [43, 72, 85], and CV cluster states [34, 81, 86].

The theoretical generation of multimode squeezed states via SFWM or SPDC has been studied extensively for MRRs [54], nonlinear waveguides [87, 88], and CROWs [89, 90]. Photon loss is an important problem in these systems, since it can reduce the squeezing and inseparability of the state.

Loss in MRRs and waveguides due to photon scattering can be handled by introducing reservoir modes that photons can couple in to [54, 91]. The waveguide-reservoir coupling parameters can be estimated with phenomenological values taken from experiment. In contrast, loss in CROWs or coupled-cavities (see Fig. 4.1d) can be handled intrinsically by calculating the complex frequencies of the CROW Bloch modes or cavity modes [89,90]. In this approach, the evolution in these lossy systems is expressed as the non-unitary evolution of the reduced density operator of the generated light, obtained from the solution of the LME. This is the approach that we use in this work.

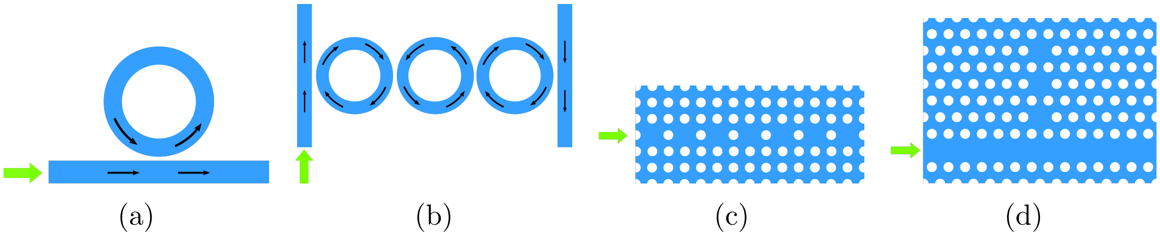

Figure 4.1: Schematics of structures of potential interest. The thick arrow indicates where the pump field is injected. The first structure (a) is an MRR coupled to a waveguide. The second (b) are a series of coupled MRRs coupled to an input and output waveguide. The thin black arrows in (a) and (b) indicate the direction of the field components at the coupling points. The third (c) is a CROW made by periodically removing air holes (shown as white circles) along a row in the crystal. And the fourth (d) is three high-Q cavities that are coupled to a waveguide.

Before discussing our approach, we present in Fig. 4.1, four different lossy coupled-cavity structures in which our theoretical method can be used to determine the quantum state of light generated via SFWM or SPDC. In Fig. 4.1a, an MRR coupled to a waveguide is shown. The pump pulse is injected into the straight waveguide; it then couples into the ring, where it generates multimode entangled light via SFWM or SPDC in the multiple, lossy modes of the ring. In Fig. 4.1b a series of three coupled rings is shown. This structure allows for the generation and propagation of the multimode state in the coupled-rings. Fig. 4.1c shows a CROW in a photonic crystal. The pump pulse propagates in a set of Bloch modes of the CROW and generates signal and idler photons as it propagates. Lastly, Fig. 4.1d shows a three-mode cavity coupled to a waveguide in a photonic crystal. The state is predominantly generated inside the cavity and couples out into the waveguide.

In this work, we prove that the density operator for entangled light generated in multiple lossy modes via SFWM or SPDC takes the form of a multimode squeezed thermal state (MSTS), where the thermal part of the state captures the effects of photon loss. The loss can be handled either phenomenologically or intrinsically, depending on the structure. For M modes, we derive a set of $3M$ coupled first-order differential equations that provide the complete evolution of the squeezing parameters and thermal photon numbers in the density operator. The number of equations is independent of the number of generated photons which is generally many fewer equations than must be solved when using numerical methods that rely on Fock states [92], since in those methods the number of equations can be as large as $(M+N)![M!N!]^{-1}$, where N is the total photon number.

Our solution of the LME applies to the discrete modes of a structure; for example, the modes of the rings in Figs. 4.1a and 4.1b, and the Bloch modes of the CROW in Fig. 4.1c. Our solution can also be applied to the structure in Fig. 4.1d as long as the modes are discretized (*e.g.* by using periodic boundary conditions).

In the limit that the modes are lossless, our formalism reproduces the results for a MSVS given by N. Quesada *et al.* [93]. Also, in the case of only one or two lossy modes, our multimode formalism reproduces the results of previous work [35, 65, 69].

The rest of the paper is organized as follows. In Sec. 4.2 we define the lossy modes of a structure, called quasimodes. In Sec. 4.3 we present the nonlinear Hamiltonian for SFWM, and the LME in the basis of quasimodes. In Sec. 4.4 we show that the analytic solution to the LME is the density operator for a MSTS, and obtain a set of coupled first-order differential equations for the squeezing amplitudes, squeezing phases, and thermal photons numbers. In Sec. 4.5 we give expressions for the correlation variance and the expectation value of the photon number operator. In Sec. 4.6 we show that in the limit when the modes are lossless our coupled equations describe a squeezed vacuum state that agrees with other work, and that they produce results that are consistent with previous work on single- and two- mode squeezed states. In Sec. 4.7 we present our results from solving the coupled differential equations for a squeezing process in the Bloch modes of a four-cavity CROW. Finally, in Sec. 4.8 we conclude.

4.2 Quasimodes

We consider an open dielectric structure with a discrete set of quasimodes that are defined within a computational volume, V_c [9]. The positive frequency part of the electric field in V_c in a quasimode m takes the form

$$\boldsymbol{E}_m^{(+)}(\boldsymbol{r},t) = \boldsymbol{N}_m(\boldsymbol{r})\mathrm{e}^{-i\widetilde{\omega}_m t}, \tag{4.1}$$

where $\boldsymbol{N}_m(\boldsymbol{r})$ is the spatial profile of the quasimode and we define $\widetilde{\omega}_m = \omega_m - i\gamma_m$ the complex frequency with real part ω_m, and the imaginary part γ_m quantifies the energy leakage. The quasimode is a solution to the Helmholtz equation

$$\boldsymbol{\nabla} \times \boldsymbol{\nabla} \times \boldsymbol{N}_m(\boldsymbol{r}) - \frac{\widetilde{\omega}_m^2}{c^2}\epsilon(\boldsymbol{r})\boldsymbol{N}_m(\boldsymbol{r}) = 0, \tag{4.2}$$

with outgoing wave boundary conditions, and $\epsilon(\boldsymbol{r})$ is the relative dielectric function of the structure. The quasimodes are defined in a computational volume V_c that is bounded by perfectly-matched layers to simulate the open boundary conditions. We assume the quasimodes are orthonormal inside V_c in the following sense

$$\int_{V_\mathrm{c}} d^3\boldsymbol{r}\epsilon(\boldsymbol{r})\boldsymbol{N}_m^*(\boldsymbol{r})\cdot\boldsymbol{N}_l(\boldsymbol{r}) = \delta_{ml}, \tag{4.3}$$

where the integral is over V_c only. The orthogonality of the modes is strictly obeyed if there is symmetry in the structure (*e.g.* rotational or translational). For example, the Bloch modes of the CROW in Fig. 4.1c are orthogonal due to the translational symmetry of the CROW, and the modes of the MRR are orthogonal due to the rotational symmetry of the ring. In structures that lack symmetry, such as the cavity coupled to a waveguide in Fig. 4.1d, the orthonormality in Eq. (4.3) is not generally strictly obeyed. However, modes that are separated in frequency by more than their linewidths will be very nearly orthogonal [94]. Therefore, in what follows, we will assume mode orthogonality.

In the next section we present a quantized theory of SFWM and the LME in the basis of these quasimodes.

4.3 The Lindblad master equation for a multimode lossy structure

Before discussing the solution to the LME for multiple lossy modes, we present the system Hamiltonian in the undepleted pump approximation and the LME that we reference throughout the paper.

In a lossy dielectric structure, a discrete basis of orthogonal quasimodes can be used to construct the system Hamiltonian

$$\widehat{H} = \widehat{H}_\mathrm{L} + \widehat{H}_\mathrm{NL}, \tag{4.4}$$

where linear Hamiltonian in the basis of the quasimodes is

$$\widehat{H}_{\mathrm{L}} = \sum_m \hbar\widetilde{\omega}_m \widehat{b}_m^\dagger \widehat{b}_m, \tag{4.5}$$

where $\widehat{b}_m^\dagger$ and $\widehat{b}_m$ are the creation and annihilation operators for photons in the mth quasimode satisfying the standard commutation relation

$$\left[\widehat{b}_m, \widehat{b}_l^\dagger\right] = \delta_{ml}. \tag{4.6}$$

Now we include the SFWM nonlinear interaction where two pump photons p_1 and p_2 are annihilated to create a pair of signal and idler photons m and l. The nonlinear Hamiltonian in the basis of the quasimodes is [95]

$$\widehat{H}_{\mathrm{NL}} = \sum_{m,l,p_1,p_2} G_{mlp_1p_2} \widehat{b}_m^\dagger \widehat{b}_l^\dagger \widehat{b}_{p_1} \widehat{b}_{p_2} + \mathrm{H.c.}, \tag{4.7}$$

where

$$G_{mlp_1p_2} \equiv \frac{9\hbar^2}{16\epsilon_0}\sqrt{\omega_m\omega_l\omega_{p_1}\omega_{p_2}} \sum_{i,j,k,h} \int d^3\boldsymbol{r}\,\chi^{(3)}_{ijkh}(\boldsymbol{r}) N^*_{mi}(\boldsymbol{r}) N^*_{lj}(\boldsymbol{r}) N_{p_1k}(\boldsymbol{r}) N_{p_2h}(\boldsymbol{r}) \tag{4.8}$$

is the effective nonlinear parameter that depends on the spatial overlap of the quasimodes $\boldsymbol{N}_m(\boldsymbol{r})$. The subscripts i, j, k, and h label the Cartesian components of the electric field and the medium nonlinear tensor $\chi^{(3)}$. In deriving this result we have assumed that the imaginary part of the frequencies are small, such that we can neglect them under the square root, so that $\sqrt{\widetilde{\omega}_m} \approx \sqrt{\omega_m}$. This is valid for modes that have a quality factor on the order of 10^3 or higher. For a CROW studied in previous work [96], it was shown that the quality factors of the Bloch modes varied from approximately 10^4 to 10^3. The relative dielectric function does not appear in $\widehat{H}_{\mathrm{NL}}$, because we have constructed it using the electric fields. If we used the displacement fields, then the relative dielectric function would appear in the nonlinear parameter in Eq. (4.8).

The dynamics of the density operator $\widehat{\rho}$ for the pump, signal, and idler light can be modeled using the LME [64]

$$\frac{d\widehat{\rho}}{dt} = -\frac{i}{\hbar}\left[\widehat{H}, \widehat{\rho}\right] + \sum_m \gamma_m \left(2\widehat{b}_m \widehat{\rho} \widehat{b}_m^\dagger - \widehat{b}_m^\dagger \widehat{b}_m \widehat{\rho} - \widehat{\rho} \widehat{b}_m^\dagger \widehat{b}_m\right), \tag{4.9}$$

where $\widehat{H}$ is the Hermitian part of the Hamiltonian in Eq. (4.4), given by

$$\widehat{H} = \sum_m \hbar\omega_m \widehat{b}_m^\dagger \widehat{b}_m + \sum_{m,l,p_1,p_2} G_{mlp_1p_2} \widehat{b}_m^\dagger \widehat{b}_l^\dagger \widehat{b}_{p_1} \widehat{b}_{p_2} + \text{H.c.}. \tag{4.10}$$

General expressions for the Hamiltonian and LME, that are applicable to any lossy structure, can be derived using a set of non-orthogonal quasimodes [97]. The extension from the orthogonal to the non-orthogonal case is not straightforward. All derivations, however, in this paper are done assuming the quasimodes are orthogonal according to Eq. (4.3).

4.3.1 Restrictions on the pump field and nonlinear parameter

The Hamiltonian presented in Eq. (4.10) is valid for a general pump field with a quantum description. However, since we are concerned with generating squeezed states, we let the pump be a classical field and make the undepleted pump approximation. Furthermore, we restrict our analysis to pump fields that can be factored into a function of space multiplied by a function of time. These two restrictions on the pump are shown in Sec. 4.4 to be necessary in order to derive our solution to the LME.

To make the undepleted pump approximation, we let the classical pump field be represented by a lossy multimode coherent state $|\alpha(t)\rangle$, defined as a product of single-mode coherent states $|\alpha_p(t)\rangle$

$$|\alpha(t)\rangle \equiv \prod_p |\alpha_p(t)\rangle \,, \tag{4.11}$$

where the single-mode coherent states are defined as

$$|\alpha_p(t)\rangle = \exp\Big(\alpha_p \mathrm{e}^{-i\widetilde{\omega}_p t} \widehat{b}_p^\dagger - \mathrm{H.c.}\Big) |\mathrm{vac}\rangle \,. \tag{4.12}$$

For a mode p with a frequency in the pump bandwidth we have

$$\widehat{b}_p |\alpha(t)\rangle = \alpha_p \mathrm{e}^{-i\widetilde{\omega}_p t} |\alpha(t)\rangle \,, \tag{4.13}$$

where α_p is the pump amplitude in the pth mode. The average total photon number for the pump is

$$\langle\alpha(t)| \sum_p \widehat{b}_p^\dagger \widehat{b}_p |\alpha(t)\rangle = \sum_p |\alpha_p|^2 \mathrm{e}^{-2\gamma_p t}. \tag{4.14}$$

To obtain the dynamics of the generated light only, the coherent state of the pump is traced-out from the LME in Eq. (4.9). This amounts to replacing the total density operator with the reduced density operator $\langle\alpha(t)|\,\widehat{\rho}(t)\,|\alpha(t)\rangle$ and replacing the nonlinear Hamiltonian in Eq. (4.7) with its form in the undepleted pump approximation [62], given by

$$\widehat{H}_{\rm NL} = \sum_{m,l,p_1,p_2} G_{mlp_1p_2}\alpha_{p_1}\alpha_{p_2}\mathrm{e}^{-i(\widetilde{\omega}_{p_1}+\widetilde{\omega}_{p_2})t}\widehat{b}_m^\dagger\widehat{b}_l^\dagger + \text{H.c.}, \tag{4.15}$$

where the pump operators $\widehat{b}_{p_1}$ and $\widehat{b}_{p_2}$ were replaced with their the expectation value using the coherent state. We now make the crucial assumption that the pump is in a single mode P. Putting $p_1 = p_2 \equiv P$ into Eq. (4.15), we obtain

$$\widehat{H}_{\rm NL} = \alpha^2(t)\sum_{m,l} G_{mlPP}\widehat{b}_m^\dagger\widehat{b}_l^\dagger + \text{H.c.}, \tag{4.16}$$

where

$$\alpha(t) = \alpha_P\mathrm{e}^{-i\widetilde{\omega}_P t}, \tag{4.17}$$

is the time-dependent pump amplitude. For example in the CROW in Fig. 4.1c, this assumption corresponds to the pump being in a single Bloch mode. For some systems, however, this assumption can be relaxed. If, for example, one were to take a Gaussian pump pulse that was normal to the surface of the CROW (as was done in Ref. [89]), then the pump would be in a continuum of free-space modes. However, if the transverse profile of the pump inside the crystal slab does not depend on frequency, then only a single pump mode is important to the nonlinear interaction. Another example is where one considers a pulsed pump in the continuum of modes of the channel waveguide in Fig. 4.1a. If the duration of the pump pulse in the channel is much longer than the ring round-trip time, then the pump fits mostly into a single mode of the ring (as we have shown in Ref. [36]). Since we neglect the nonlinear interaction in the channel and only consider generation in the ring, then only a single pump mode is crucial to the nonlinear interaction in the ring. In both of the last two examples we can replace the constant pump amplitude α_P in Eq. (4.17) with a slowly-varying temporal envelope $\alpha_P(t)$. The crucial point is that the nonlinear Hamiltonian must take the form in Eq. (4.16) in order to derive our solution to the LME.

Note that, although we are using the undepleted pump approximation, this formalism does include linear pump loss, through the imaginary parts of the pump mode frequencies. Note also that one can easily adapt this formalism for SPDC, and all the results below will follow, by just replacing $\alpha^2(t)$ with a single pump amplitude $\alpha(t)$ and using the nonlinear parameter $\chi^{(2)}$ for a second-order nonlinear process [89] in Eq. (4.16) instead.

In the next section we derive a semi-analytic solution to the LME for the Hamiltonian given by Eqs. (4.4) and (4.16) .

4.4 Analytic solution to the Lindblad master equation

In previous work we studied squeezed light generation in two-mode lossy cavities. We showed that the density operator for the generated light in the cavity is a two-mode squeezed thermal state for all time [69]. In this work we show that for a structure with many lossy quasimodes, the density operator for the generated light is the MSTS,

$$\widehat{\rho}(t) = \widehat{S}\,(t)\,\widehat{\rho}_{\text{th}}(t)\widehat{S}^{\dagger}\,(t)\,. \tag{4.18}$$

Here, $S(t)$ is the unitary multimode squeezing operator given by [25]

$$\widehat{S}(t) = \exp\left(\frac{1}{2}\sum_{m,l} z_{ml}(t)\widehat{b}_m^{\dagger}\widehat{b}_l^{\dagger} - \text{H.c.}\right), \tag{4.19}$$

where $z_{ml}(t)$ are the elements of the complex symmetric squeezing matrix $\boldsymbol{z}(t)$. The multimode thermal state $\widehat{\rho}_{\text{th}}(t)$ is a product of single-mode thermal states in each mode [65], such that

$$\widehat{\rho}_{\text{th}}(t) = \prod_m \frac{1}{1+n_m(t)}\left(\frac{n_m(t)}{1+n_m(t)}\right)^{\widehat{b}_m^{\dagger}\widehat{b}_m}, \tag{4.20}$$

where $n_m(t)$ is defined as the average thermal photon number for the mth mode. We stress that the thermal photons are not related to actual thermal effects, but rather capture the process of photon loss. The presence of $n_m(t)$ is due to a scattering process that breaks the entanglement between the generated signal and idler photon pairs. At this point the matrix $\boldsymbol{z}(t)$ and functions $n_m(t)$ are unknown functions of time; in Sec. 4.4.1 and Sec. 4.4.3 we will derive equations of motion for them.

To show that the MSTS in Eq. (4.18) is the solution to the LME in Eq. (4.9), we require that the equality

$$1 = \widehat{\rho}_{\text{th}}^{-1/2}(t)\widehat{S}^{\dagger}(t)\widehat{\rho}(t)\widehat{S}(t)\widehat{\rho}_{\text{th}}^{-1/2}(t) \tag{4.21}$$

is satisfied for all time. Taking the time derivative of Eq. (4.21), it can be shown that

$$0 = -\widehat{\rho}_{\text{th}}^{-1/2}\widehat{S}^{\dagger}\frac{d\widehat{S}}{dt}\widehat{\rho}_{\text{th}}^{1/2} + \widehat{\rho}_{\text{th}}^{1/2}\widehat{S}^{\dagger}\frac{d\widehat{S}}{dt}\widehat{\rho}_{\text{th}}^{-1/2} + \widehat{\rho}_{\text{th}}^{-1/2}\widehat{S}^{\dagger}\frac{d\widehat{\rho}}{dt}\widehat{S}\widehat{\rho}_{\text{th}}^{-1/2} + 2\frac{d\widehat{\rho}_{\text{th}}^{-1/2}}{dt}\widehat{\rho}_{\text{th}}^{1/2}, \tag{4.22}$$

where we drop the time-dependence for convenience.

The majority of the rest of this section is devoted to simplifying the four terms on the right-hand side of Eq. (4.22).

Let the argument of the exponential squeezing operator be

$$\widehat{\sigma} \equiv \frac{1}{2}\sum_{m,l} z_{ml}\widehat{b}_{m}^{\dagger}\widehat{b}_{l}^{\dagger} - \text{H.c.}, \tag{4.23}$$

such that $\widehat{S} = \exp(\widehat{\sigma})$ and $\widehat{S}^{\dagger} = \exp(-\widehat{\sigma})$. In order to simplify Eq. (4.22) we need to know the time derivative of the squeezing operator of Eq. (4.19). This is not straightforward since $\widehat{\sigma}$ does not commute with its time derivative. The derivative of the squeezing operator can be written as

$$\begin{aligned} \frac{d\widehat{S}}{dt} &= \frac{d}{dt}\left(1 + \widehat{\sigma} + \frac{\widehat{\sigma}^2}{2!} + \frac{\widehat{\sigma}^3}{3!} + \dots\right) \\ &= \sum_{n=0}^{\infty}\sum_{k=0}^{\infty}\frac{\widehat{\sigma}^n\dot{\widehat{\sigma}}\widehat{\sigma}^k}{(n+k+1)!}, \end{aligned} \tag{4.24}$$

where $\dot{\widehat{\sigma}} \equiv d\widehat{\sigma}/dt$. The sum in the last line of Eq. (4.24) has the integral representation

$$\sum_{n=0}^{\infty}\sum_{k=0}^{\infty}\frac{\widehat{\sigma}^n\dot{\widehat{\sigma}}\widehat{\sigma}^k}{(n+k+1)!} = \int_0^1 dy\mathrm{e}^{(1-y)\widehat{\sigma}}\dot{\widehat{\sigma}}\mathrm{e}^{y\widehat{\sigma}}. \tag{4.25}$$

To prove this, we expand the exponentials in the integral in a series

$$\begin{aligned}\int_0^1 dy \mathrm{e}^{(1-y)\widehat{\sigma}}\dot{\widehat{\sigma}}\mathrm{e}^{y\widehat{\sigma}} &= \sum_{n=0}^{\infty}\sum_{k=0}^{\infty}\frac{\widehat{\sigma}^n\dot{\widehat{\sigma}}\widehat{\sigma}^k}{n!k!}\int_0^1 dy(1-y)^n y^k \\ &= \sum_{n=0}^{\infty}\sum_{k=0}^{\infty}\frac{\widehat{\sigma}^n\dot{\widehat{\sigma}}\widehat{\sigma}^k}{(n+k+1)!},\end{aligned} \tag{4.26}$$

where the last line follows from the Euler integral of the first kind,

$$\int_0^1 dy(1-y)^n y^k = \frac{n!k!}{(n+k+1)!}. \tag{4.27}$$

Thus, putting Eq. (4.25) into Eq. (4.24) we obtain

$$\frac{d\widehat{S}}{dt} = \int_0^1 dy \mathrm{e}^{(1-y)\widehat{\sigma}}\dot{\widehat{\sigma}}\mathrm{e}^{y\widehat{\sigma}}. \tag{4.28}$$

Using the well-known Baker-Campbell-Hausdorff formula [98] on the integrand in Eq. (4.28) and multiplying the equation by $\widehat{S}^\dagger = \exp(-\widehat{\sigma})$ from the left, we obtain

$$\widehat{S}^\dagger \frac{d\widehat{S}}{dt} = \sum_{k=0}^{\infty}\frac{(-1)^k}{(k+1)!}\widehat{\mathcal{S}}_k, \tag{4.29}$$

where the terms $\widehat{\mathcal{S}}_k$ can be obtained recursively from

$$\widehat{\mathcal{S}}_{k+1} = [\widehat{\sigma}, \widehat{\mathcal{S}}_k], \tag{4.30}$$

for $k = 0, 1, \ldots$, where

$$\widehat{\mathcal{S}}_0 \equiv \dot{\widehat{\sigma}}. \tag{4.31}$$

Each $\widehat{\sigma}$ or $\dot{\widehat{\sigma}}$ that appears in Eqs. (4.30) or (4.31) involves a double sum over the quasimodes (see Eq. (4.23)). Thus, calculating the $k > 0$ terms of $\widehat{\mathcal{S}}_k$ becomes intractable for multiple modes since each term has $2(k + 1)$ sums. However, by introducing a new Schmidt basis via a Takagi factorization of $\widehat{H}_{\mathrm{NL}}$, in which the squeezing operator is diagonal, we are able to calculate the terms $\widehat{\mathcal{S}}_k$ and show that the sum in Eq. (4.29) converges even for the case of a multimode squeezing operator (see Eq. (4.48)). In the next subsection we introduce this new Schmidt basis.

4.4.1 The Schmidt basis and the diagonal multimode squeezing operator

In this subsection we diagonalize the nonlinear Hamiltonian in Eq. (4.16) and the multimode squeezing operator in Eq. (4.19) so that we can simplify the four terms in Eq. (4.22) and prove that the MSTS is the solution to the LME.

We start by performing a Takagi factorization of the nonlinear parameter $\boldsymbol{G}$ in $\widehat{H}_{\mathrm{NL}}$. The Takagi factorization decomposes the complex symmetric square matrix $\boldsymbol{G}$ into the form

$$\boldsymbol{G} = \boldsymbol{U}\boldsymbol{\Lambda}\boldsymbol{U}^{\mathrm{T}}, \tag{4.32}$$

where $\boldsymbol{\Lambda} = \mathrm{diag}(\lambda_1, \lambda_2, \ldots)$ is a diagonal matrix with complex entries, $\boldsymbol{U}$ is a unitary matrix with $\boldsymbol{U}^{\dagger}\boldsymbol{U} = \mathbf{1}$ and $\boldsymbol{U}^{\mathrm{T}}$ is the transpose of $\boldsymbol{U}$. The Takagi factorization is a special case of symmetric singular value decomposition (SVD) [99]. The diagonal matrix $\boldsymbol{\Lambda}$ from the Takagi factorization is just a scaled version of the matrix of singular values obtained from the symmetric SVD (see Appendix C.1).

Putting Eq. (4.32) into Eq. (4.16) we obtain the diagonalized nonlinear Hamiltonian

$$\widehat{H}_{\mathrm{NL}} = \alpha^2(t) \sum_{\mu} \lambda_\mu \widehat{B}_\mu^{\dagger 2} + \text{H.c.}, \tag{4.33}$$

where λ_μ ($\mu = 1, 2, \ldots$) are the diagonal entries of Λ, and we define the new creation and annihilation Schmidt operators

$$\widehat{B}_\mu^\dagger \equiv \sum_m U_{\mu m} \widehat{b}_m^\dagger, \tag{4.34}$$

that have the standard commutation relation

$$\left[\widehat{B}_\mu, \widehat{B}_\nu^\dagger\right] = \delta_{\mu\nu} \tag{4.35}$$

due to the orthogonality of the basis ($\sum_m U_{\mu m}^* U_{\nu m} = \delta_{\mu\nu}$). We call the $\widehat{B}_\mu$ Schmidt operators, since when there is no loss they give the Schmidt decomposition of the multimode squeezed state.

It is clear now why we have to assume the pump is separable into a spatial and temporal part (see $\widehat{H}_{\mathrm{NL}}$ in Eq. (4.16)). This makes the Schmidt mode basis independent of time. Otherwise, a new Takagi factorization would have to be done at each time and the operators $\widehat{B}_\mu$ would become time-dependent. In practice one calculates the nonlinear parameter $\boldsymbol{G}$ for a given structure by first calculating the quasimodes of the structure using a method such as finite-difference time-domain (FDTD) and then calculating the spatial overlap given in Eq. (4.8). Then one performs the Takagi factorization of $\boldsymbol{G}$ to obtain the matrices $\boldsymbol{U}$ and $\boldsymbol{\Lambda}$.

We now make the ansatz for the squeezing parameter matrix $\boldsymbol{z}(t)$,

$$\boldsymbol{z}(t) = \boldsymbol{U}\boldsymbol{r}(t)\mathrm{e}^{i\boldsymbol{\phi}(t)}\boldsymbol{U}^{\mathrm{T}}, \tag{4.36}$$

where $\boldsymbol{r}(t)$ and $\boldsymbol{\phi}(t)$ are real diagonal matrices containing the squeezing amplitudes and squeezing phases of the Schmidt modes, that is $\boldsymbol{r}(t) = \mathrm{diag}(r_1(t), r_2(t), \ldots)$ and $\boldsymbol{\phi}(t) = \mathrm{diag}(\phi_1(t), \phi_2(t), \ldots)$. Putting Eq. (4.36) into Eq. (4.19), we obtain the diagonal multimode squeezing operator

$$\widehat{S}(t) = \prod_{\mu} \widehat{S}_{\mu}(t), \tag{4.37}$$

where $\widehat{S}_{\mu}(t)$ is the single mode squeezing operator for the μth Schmidt mode, given by

$$\widehat{S}_{\mu}(t) \equiv \exp\left(\frac{1}{2} r_{\mu}(t)\mathrm{e}^{i\phi_{\mu}(t)}\widehat{B}_{\mu}^{\dagger 2} - \mathrm{H.c.}\right). \tag{4.38}$$

We show in Sec. 4.4.3 that this is the correct form of the multimode squeezing operator, because when we impose this form, we can derive equations for the $r_{\mu}(t)$ and $\phi_{\mu}(t)$ (see Eqs. (4.69) and (5.10)) that describe an MSTS that is a solution to the LME. Note, one can obtain the squeezing matrix in the quasimode basis $z(t)$, after solving the equations for the $r_{\mu}(t)$ and $\phi_{\mu}(t)$ and putting them into Eq. (4.36).

Before moving to the next subsection, where we take the time derivative of $\widehat{S}(t)$, we present the squeezing transformation for the $\widehat{B}_{\mu}$ and $\widehat{b}_m$ operators. These transformations are necessary when squeezing the terms in Eq. (4.22). Using the squeezing operator in Eq. (4.37), we obtain

$$\begin{aligned}\widehat{S}^{\dagger}\widehat{B}_{\mu}\widehat{S} &= \widehat{S}_{\mu}^{\dagger}\widehat{B}_{\mu}\widehat{S}_{\mu} \\ &= \cosh(r_{\mu})\widehat{B}_{\mu} + \mathrm{e}^{i\phi_{\mu}}\sinh(r_{\mu})\widehat{B}_{\mu}^{\dagger},\end{aligned} \tag{4.39}$$

where the time-dependence is dropped for convenience. All other squeezing transformations involving products of Schmidt operators (such as $\widehat{B}_{\mu}\widehat{B}_{\nu}$) can be derived from Eq. (4.39) and the fact that different Schmidt operators commute. The squeezing transformation of the $\widehat{b}_m$ operators is

$$\widehat{S}^{\dagger}\widehat{b}_{m}\widehat{S} = \sum_{\mu} U_{\mu m}\widehat{S}_{\mu}^{\dagger}\widehat{B}_{\mu}\widehat{S}_{\mu}. \tag{4.40}$$

4.4.2 The time derivative of the multimode squeezing operator

In this subsection we simplify the first two terms in Eq. (4.22) that involve the derivative of the squeezing operator. We show that using the diagonal squeezing operator in Eq. (4.37), we can calculate the sum in Eq. (4.29).

Using Eq. (4.37), along with the fact that the $\widehat{S}_{\mu}$ commute and that $\widehat{S}_{\mu}^{\dagger}\widehat{S}_{\mu} = 1$, the left-hand side of Eq. (4.29) can be written as

$$\widehat{S}^{\dagger}\frac{d\widehat{S}}{dt} = \sum_{\mu}\widehat{S}_{\mu}^{\dagger}\frac{d\widehat{S}_{\mu}}{dt}. \tag{4.41}$$

Each term in the sum in Eq. (4.41) can be expanded using the right-hand side of Eq.

(4.29)

$$\widehat{S}_{\mu}^{\dagger}\frac{d\widehat{S}_{\mu}}{dt} = \sum_{k=0}^{\infty}\frac{(-1)^k}{(k+1)!}\widehat{\mathcal{S}}_{k\mu}. \tag{4.42}$$

Putting Eq. (4.42) into Eq. (4.41), we obtain

$$\widehat{S}^{\dagger}\frac{d\widehat{S}}{dt} = \sum_{\mu}\sum_{k=0}^{\infty}\frac{(-1)^k}{(k+1)!}\widehat{\mathcal{S}}_{k\mu}, \tag{4.43}$$

where the terms $\widehat{\mathcal{S}}_{k\mu}$ in Eq. (4.43) can be obtained recursively from

$$\widehat{\mathcal{S}}_{k+1\mu} = [\widehat{\sigma}_{\mu}, \widehat{\mathcal{S}}_{k\mu}] \tag{4.44}$$

for $k = 0, 1, \ldots$, where the $k = 0$ term is defined as

$$\widehat{\mathcal{S}}_{0\mu} \equiv \dot{\widehat{\sigma}}_{\mu}, \tag{4.45}$$

where

$$\widehat{\sigma}_{\mu} \equiv \frac{1}{2}r_{\mu}\exp(i\phi_{\mu})\widehat{B}_{\mu}^{\dagger 2} - \text{H.c.}. \tag{4.46}$$

Since the definition of $\widehat{\sigma}_{\mu}$ does not contain sums over Schmidt modes, the problem is reduced to just evaluating a series of commutators involving only single mode operators. This is straightforward to do using the commutation relation for the $\widehat{B}_{\mu}$

operators. The odd k and even k terms of the sum are

$$\widehat{\mathcal{S}}_{k\mu} = \begin{cases} -\frac{i}{4}(2r_\mu)^{k+1}\dot{\phi}_\mu\left(2\widehat{B}_\mu^\dagger\widehat{B}_\mu+1\right), & \text{odd}\, k \geq 1 \\ \\ \frac{i}{4}(2r_\mu)^{k+1}\dot{\phi}_\mu\left(\mathrm{e}^{i\phi_\mu}\widehat{B}_\mu^{\dagger 2}+\text{H.c.}\right), & \text{even}\, k \geq 2. \end{cases} \tag{4.47}$$

Putting $\dot{\widehat{\sigma}}_\mu$ and the terms in Eq. (4.47) into Eq. (4.43) and summing over k, we obtain

$$\begin{aligned} \widehat{S}^\dagger\frac{d\widehat{S}}{dt} = \sum_\mu \Bigg(& \frac{i}{2}\sinh^2(r_\mu)\frac{d\phi_\mu}{dt}\left(2\widehat{B}_\mu^\dagger\widehat{B}_\mu+1\right) \\ & + \left(\frac{1}{2}\frac{dr_\mu}{dt}+\frac{i}{4}\sinh(2r_\mu)\frac{d\phi_\mu}{dt}\right)\mathrm{e}^{i\phi_\mu}\widehat{B}_\mu^{\dagger 2} \\ & - \left(\frac{1}{2}\frac{dr_\mu}{dt}-\frac{i}{4}\sinh(2r_\mu)\frac{d\phi_\mu}{dt}\right)\mathrm{e}^{-i\phi_\mu}\widehat{B}_\mu^{2}\Bigg). \end{aligned} \tag{4.48}$$

In order to derive Eq. (4.48) it is necessary that the Schmidt operators are time-independent and have the standard commutator. In the next subsection we put Eq. (4.48) into Eq. (4.22) and derive the set of coupled first-order differential equations for the squeezing amplitudes (r_μ), squeezing phases (ϕ_μ), and thermal photon numbers (n_m).

4.4.3 Differential equations for the squeezing parameters and thermal photon numbers

We are now in a position to simplify the four terms in Eq. (4.22).To make the derivation clearer we redefine the terms in Eq. (4.22) to obtain

$$0 = T1 + T2 + T3, \tag{4.49}$$

where

$$T1 \equiv -\widehat{\rho}_{\text{th}}^{-1/2}\widehat{S}^{\dagger}\frac{d\widehat{S}}{dt}\widehat{\rho}_{\text{th}}^{1/2} + \widehat{\rho}_{\text{th}}^{1/2}\widehat{S}^{\dagger}\frac{d\widehat{S}}{dt}\widehat{\rho}_{\text{th}}^{-1/2}, \tag{4.50}$$

$$T2 \equiv \widehat{\rho}_{\text{th}}^{-1/2}\widehat{S}^{\dagger}\frac{d\widehat{\rho}}{dt}\widehat{S}\widehat{\rho}_{\text{th}}^{-1/2}, \tag{4.51}$$

$$T3 \equiv 2\frac{d\widehat{\rho}_{\text{th}}^{-1/2}}{dt}\widehat{\rho}_{\text{th}}^{1/2}. \tag{4.52}$$

The transformations involving $\widehat{\rho}_{\text{th}}^{\pm 1/2}$ in $T1$ and $T2$ are performed using the identity

$$\widehat{\rho}_{\text{th}}^{\pm 1/2}\widehat{B}_{\mu}\widehat{\rho}_{\text{th}}^{\mp 1/2} = \sum_{m} U_{\mu m}^{*}\widehat{b}_{m}x_{m}^{\mp 1/2}, \tag{4.53}$$

where

$$x_m \equiv \frac{n_m}{1+n_m}. \tag{4.54}$$

It is simple to generalize this identity to transformations involving the product of operators, such as $\widehat{\rho}_{\text{th}}^{\pm 1/2}\widehat{B}_{\mu}\widehat{B}_{\nu}\widehat{\rho}_{\text{th}}^{\mp 1/2}$.

Our strategy is to reduce $T1$, $T2$, and $T3$ to expressions that are a sum of Schrödinger operators multiplied by time-dependent coefficients that depend on the squeezing amplitudes $r_\mu(t)$, squeezing phases $\phi_\mu(t)$, and thermal photon numbers $n_m(t)$, respectively as well as their first derivatives. Then we force these coefficients to be zero, such that Eq. (4.49) is satisfied. The result is a set of coupled first-order differential equations for $\dot{r}_\mu(t)$, $\dot{\phi}_\mu(t)$, and $\dot{n}_m(t)$.

Putting Eq. (4.48) in $T1$ and using Eq. (4.53), we obtain

$$T1 = \sum_{m,l} \left(D_{ml} \widehat{b}_m^\dagger \widehat{b}_l^\dagger + D_{ml}^* \widehat{b}_m \widehat{b}_l + F_{ml} \widehat{b}_m^\dagger \widehat{b}_l \right), \tag{4.55}$$

where the time-dependent coefficients D_{ml} and F_{ml} are

$$D_{ml} = \frac{x_m x_l - 1}{2\sqrt{x_m x_l}} \sum_\mu U_{m\mu} U_{l\mu} \left(\dot{r}_\mu + \frac{i}{2} \sinh(2r_\mu) \dot{\phi}_\mu \right) \mathrm{e}^{i\phi_\mu}, \tag{4.56}$$

and

$$F_{ml} = i \, \frac{x_m - x_l}{\sqrt{x_m x_l}} \sum_\mu U_{m\mu} U_{l\mu}^* \dot{\phi}_\mu \sinh^2(r_\mu). \tag{4.57}$$

Obtaining these coefficients requires many lines of algebra but it is a straightforward exercise.

In order to derive the equations for $\dot{r}_\mu$ and $\dot{\phi}_\mu$, we define new Schrödinger operators

$$\widehat{V}_{ml} \equiv \widehat{b}_m \widehat{b}_l + \widehat{b}_m^\dagger \widehat{b}_l^\dagger, \tag{4.58}$$

$$\widehat{W}_{ml} \equiv -i\widehat{b}_m \widehat{b}_l + i\widehat{b}_m^\dagger \widehat{b}_l^\dagger, \tag{4.59}$$

such that Eq. (4.55) can be written as

$$T1 = \sum_{m,l} \left(\mathrm{Re}\{D_{ml}\} \widehat{V}_{ml} + \mathrm{Im}\{D_{ml}\} \widehat{W}_{ml} + F_{ml} \widehat{b}^{\dagger}_{m} \widehat{b}_{l} \right), \tag{4.60}$$

where $\mathrm{Re}\{D_{ml}\}$ and $\mathrm{Im}\{D_{ml}\}$ are the real and imaginary parts of D_{ml}.

Next we write $T2$ in terms of the operators $\widehat{V}_{ml}$ and $\widehat{W}_{ml}$. The main calculation in $T2$ is the squeezing transformation of $d\widehat{\rho}/dt$. This is the LME in Eq. (4.9). The nonlinear Hamiltonian in the master equation is replaced with its diagonal form in Eq. (4.33). The squeezing transformations are performed using Eq. (4.40). Then by using Eq. (4.53), it can be shown that Eq. (4.51) simplifies to

$$\begin{aligned} T2 = & \sum_{m,l} \left(\mathrm{Re}\{E_{ml}\} \widehat{V}_{ml} + \mathrm{Im}\{E_{ml}\} \widehat{W}_{ml} + K_{ml} \widehat{b}^{\dagger}_{m} \widehat{b}_{l} \right) \\ & + \sum_{\mu,\nu} \Gamma_{\mu\nu} \cosh(r_{\mu}) \cosh(r_{\nu}) \sum_{m} U_{m\mu} U^{*}_{m\nu} x_{m} \\ & - \sum_{\mu} \Gamma_{\mu\mu} \sinh^{2}(r_{\mu}), \end{aligned} \tag{4.61}$$

where

$$\Gamma_{\mu\nu} \equiv 2 \sum_{m} \gamma_{m} U^{*}_{m\mu} U_{m\nu}, \tag{4.62}$$

and the time-dependent coefficients E_{ml} and K_{ml} are

$$\begin{aligned}E_{ml} = &\sum_{\mu,\nu} U_{m\mu}U_{l\nu}\mathrm{e}^{i\phi_\nu}\cosh(r_\mu)\sinh(r_\nu)\left(-i\Omega_{\mu\nu}\frac{x_m x_l - 1}{\sqrt{x_m x_l}} + \frac{1}{2}\Gamma_{\mu\nu}\frac{1 + x_m x_l - 2x_m}{\sqrt{x_m x_l}}\right)\\ &+ \frac{i}{\hbar}\frac{x_m x_l - 1}{\sqrt{x_m x_l}}\sum_{\mu} U_{m\mu}U_{l\mu}\mathrm{e}^{i\phi_\mu}\left(\alpha^2\lambda_\mu\mathrm{e}^{-i\phi_\mu}\cosh^2(r_\mu) + \alpha^{*2}\lambda^*_\mu\mathrm{e}^{i\phi_\mu}\sinh^2(r_\mu)\right),\end{aligned} \tag{4.63}$$

$$\begin{aligned}K_{ml} = &\sum_{\mu,\nu} U_{m\mu}U^*_{l\nu}\cosh(r_\mu)\cosh(r_\nu)\left(i\Omega_{\mu\nu}\frac{x_m - x_l}{\sqrt{x_m x_l}} + \frac{1}{2}\Gamma_{\mu\nu}\frac{2x_m x_l - x_m - x_l}{\sqrt{x_m x_l}}\right)\\ &+ \sum_{\mu,\nu} U_{m\mu}U^*_{l\nu}\mathrm{e}^{i(\phi_\mu - \phi_\nu)}\sinh(r_\mu)\sinh(r_\nu)\left(i\Omega^*_{\mu\nu}\frac{x_m - x_l}{\sqrt{x_m x_l}} + \frac{1}{2}\Gamma^*_{\mu\nu}\frac{2 - x_m - x_l}{\sqrt{x_m x_l}}\right)\\ &- \frac{2}{\hbar}\frac{x_m - x_l}{\sqrt{x_m x_l}}\sum_{\mu} U_{m\mu}U^*_{l\mu}\cosh(r_\mu)\sinh(r_\mu)\left(\alpha^2\lambda_\mu\mathrm{e}^{-i\phi_\mu} + \alpha^{*2}\lambda^*_\mu\mathrm{e}^{i\phi_\mu}\right),\end{aligned} \tag{4.64}$$

where

$$\Omega_{\mu\nu} \equiv \sum_m \omega_m U^*_{m\mu}U_{m\nu}. \tag{4.65}$$

Since the derivative of the thermal state $\widehat{\rho}_{\mathrm{th}}$ in Eq. (4.20) is easy, $T3$ requires no special treatment in order to simplify. Putting Eq. (4.20) into Eq. (4.52) we obtain

$$T3 = \sum_m \left(-\frac{\dot{x}_m}{x_m}\widehat{b}^\dagger_m\widehat{b}_m + \frac{\dot{x}_m}{1 - x_m}\right). \tag{4.66}$$

To form the differential equations for $\dot{r}_\mu$ and $\dot{\phi}_\mu$, we set the sum of the coefficients in front of $\widehat{V}_{ml}$ and $\widehat{W}_{ml}$ in Eqs. (4.60) and (4.61) to zero. This gives

$$\mathrm{Re}\{D_{ml}\} = -\,\mathrm{Re}\{E_{ml}\}, \tag{4.67}$$

$$\mathrm{Im}\{D_{ml}\} = -\,\mathrm{Im}\{E_{ml}\}. \tag{4.68}$$

In Appendix C.2.1, we show that Eq. (4.67) leads to an equation for $\dot{r}_\mu$ and Eq. (4.68) for $\dot{\phi}_\mu$. The resulting differential equations are:

$$\begin{aligned}\dot{r}_\mu &= \frac{1}{i\hbar}\left(\alpha^2\lambda_\mu \mathrm{e}^{-i\phi_\mu} - \text{c.c.}\right) - \frac{1}{2}\sum_{\nu,\sigma}\cosh(r_\nu)\sinh(r_\sigma) \\ &\quad\times\left(\Gamma_{\nu\sigma}\mathrm{e}^{i(\phi_\sigma-\phi_\mu)}\sum_{m,l}\frac{-n_m+n_l+1}{n_m+n_l+1}U_{m\nu}U_{l\sigma}U^*_{m\mu}U^*_{l\mu} + \text{c.c.}\right), \qquad (4.69)\\ \dot{\phi}_\mu &= -2\Omega_{\mu\mu} - \frac{2}{\hbar\tanh(2r_\mu)}\left(\alpha^2\lambda_\mu \mathrm{e}^{-i\phi_\mu} + \text{c.c.}\right) \\ &\quad + \frac{i}{2}\sum_{\nu,\sigma}\frac{\cosh(r_\nu)\sinh(r_\sigma)}{\cosh(r_\mu)\sinh(r_\mu)}\left(\Gamma_{\nu\sigma}\mathrm{e}^{i(\phi_\sigma-\phi_\mu)}\sum_{m,l}\frac{-n_m+n_l+1}{n_m+n_l+1}U_{m\nu}U_{l\sigma}U^*_{m\mu}U^*_{l\mu} - \text{c.c.}\right). \qquad (4.70)\end{aligned}$$

In order to obtain an equation for $\dot{n}_m$, the operators $\widehat{b}^\dagger_m\widehat{b}_l$ in $T1$, $T2$, and $\widehat{b}^\dagger_m\widehat{b}_m$ in $T3$ are expanded in terms of the Schmidt operator $\widehat{B}^\dagger_\mu\widehat{B}_\nu$ using Eq. (4.34). This is necessary since it creates a common operator $\widehat{B}^\dagger_\mu\widehat{B}_\nu$ that is shared between $T1$, $T2$, and $T3$. Then setting the sum of the coefficients in front $\widehat{B}^\dagger_\mu\widehat{B}_\nu$ equal to zero, we show in Appendix C.2.2 that this leads to the following equation for $\dot{n}_m$,

$$\begin{aligned}\dot{n}_m &= (1+n_m)\sum_{\nu,\sigma}U_{m\nu}U^*_{m\sigma}\Gamma^*_{\nu\sigma}\mathrm{e}^{i(\phi_\nu-\phi_\sigma)}\sinh(r_\nu)\sinh(r_\sigma) \\ &\quad - n_m\sum_{\nu,\sigma}U_{m\nu}U^*_{m\sigma}\Gamma_{\nu\sigma}\cosh(r_\nu)\cosh(r_\sigma). \qquad (4.71)\end{aligned}$$

In order to complete the derivation, we have to show that the sum of the coefficients in front of the identity operator in $T2$ (Eq. (4.61)) and $T3$ (Eq. (4.66)) is zero.

Collecting the appropriate terms from Eq. (4.61) and Eq. (4.66), we obtain

$$\begin{aligned} 0 = &\sum_m \frac{\dot{n}_m}{1+n_m} - \sum_\mu \Gamma_{\mu\mu} \sinh^2(r_\mu) \\ &+ \sum_{\mu,\nu} \Gamma_{\mu\nu} \cosh(r_\mu) \cosh(r_\nu) \sum_m U_{m\mu} U^*_{m\nu} \frac{n_m}{1+n_m}. \end{aligned} \tag{4.72}$$

Putting Eq. (4.71) into Eq. (4.72) and summing over m, it is easily shown that the right-hand side is equal to zero, where we use the fact that $\sum_m U_{m\nu} U^*_{m\sigma} = \delta_{\nu\sigma}$, and $\Gamma^*_{\mu\mu} = \Gamma_{\mu\mu}$. This completes the derivation since we have shown that the coefficients in front of the operators $\widehat{V}_{ml}$, $\widehat{W}_{ml}$, $\widehat{B}^\dagger_\mu \widehat{B}_\nu$, and the identity operator sum to zero.

The key result of this work are Eqs. (4.69) - (4.71), which describe the time-dependence of the squeezing amplitudes, squeezing phases, and thermal photon numbers of the MSTS. For a system of M quasimodes, they form a set of $3M$ coupled first-order differential equations, which can be easily solved on a standard PC. The benefit of having these equations is that once they are solved, we have the time-dependent density operator of the MSTS and with it we can calculate any observables such as the correlation variance and photon number. Note that the number of equations does not depend on the number of photons at all. In contrast, numerical techniques for calculating the density operator often require solving a large number of coupled equations that depend on the photon number [92]. Therefore our approach can greatly reduce the number of coupled equations, making it more feasible to study large, multimode, lossy structures.

We note that the coupled equations as formulated apply only to a set of discrete modes. If one has a continuum of modes, such as for the Bloch modes of a CROW, one needs to simply discritize the modes by applying the appropriate (*e.g.*

periodic) boundary conditions. Otherwise, the equations become a set of coupled integro-differential equations, which become difficult to solve computationally without discretization. In Sec. 4.7 we solve these equations for a CROW with four cavities, where we use periodic boundary conditions to quantize the allowed Bloch vectors. In Appendix C.3 we discuss how to solve Eqs. (4.69) - (4.71) when the initial state is the vacuum state.

In the next section we derive expressions for the expectation value of the photon number operator and the same-time correlation variance between different quasimodes using the MSTS.

4.5 Expectation values and the correlation variance

In this section we use the MSTS to evaluate the expectation value of the quasimode number operator and to calculate the same-time correlation variance between pairs of quasimodes. Let $\widehat{X}_{ml}$ and $\widehat{Y}_{ml}$ be linear combinations of the quasimode quadrature operators

$$\widehat{X}_{ml} = \frac{\widehat{b}_m \mathrm{e}^{-i\theta_m} + \widehat{b}_m^\dagger \mathrm{e}^{i\theta_m}}{2} - \frac{\widehat{b}_l \mathrm{e}^{-i\theta_l} + \widehat{b}_l^\dagger \mathrm{e}^{i\theta_l}}{2}, \tag{4.73}$$

$$\widehat{Y}_{ml} = \frac{\widehat{b}_m \mathrm{e}^{-i\theta_m} - \widehat{b}_m^\dagger \mathrm{e}^{i\theta_m}}{2i} + \frac{\widehat{b}_l \mathrm{e}^{-i\theta_l} - \widehat{b}_l^\dagger \mathrm{e}^{i\theta_l}}{2}, \tag{4.74}$$

where θ_m and θ_l are angles in phase space. In order to quantify the inseparability of the MSTS, the correlation variance [41] between two quasimodes m and l is defined as

$$\Delta_{ml}^2(t) = \left\langle \left(\Delta \widehat{X}_{ml}\right)^2 \right\rangle + \left\langle \left(\Delta \widehat{Y}_{ml}\right)^2 \right\rangle, \tag{4.75}$$

where

$$\left\langle \left(\Delta \widehat{X}_{ml}\right)^2 \right\rangle \equiv \mathrm{Tr}\left(\widehat{\rho}(t)\widehat{X}_{ml}^2\right), \tag{4.76}$$

$$\left\langle \left(\Delta \widehat{Y}_{ml}\right)^2 \right\rangle \equiv \mathrm{Tr}\left(\widehat{\rho}(t)\widehat{Y}_{ml}^2\right), \tag{4.77}$$

is defined as the variance of the operator and $\widehat{\rho}(t)$ is the density operator for the MSTS. Here we have used the fact that $\left\langle \widehat{X}_{ml} \right\rangle = \left\langle \widehat{Y}_{ml} \right\rangle = 0$. It can be proved [22, 23] that the MSTS is inseparable, and thus contains entanglement, iff $\Delta_{ml}^2 < 1$.

In order to calculate the correlation variances one needs to know the expectation values $\left\langle \widehat{b}_m^\dagger \widehat{b}_l \right\rangle$ and $\left\langle \widehat{b}_m \widehat{b}_l \right\rangle$. Using the Schmidt operators, we obtain

$$\left\langle \widehat{b}_m^\dagger \widehat{b}_l \right\rangle = \sum_{\mu,\nu} U_{\mu m}^* U_{\nu l} \left\langle \widehat{B}_\mu^\dagger \widehat{B}_\nu \right\rangle, \tag{4.78}$$

$$\left\langle \widehat{b}_m \widehat{b}_l \right\rangle = \sum_{\mu,\nu} U_{\mu m} U_{\nu l} \left\langle \widehat{B}_\mu \widehat{B}_\nu \right\rangle, \tag{4.79}$$

where the expectation values of the Schmidt operators are

$$\left\langle \widehat{B}_\mu^\dagger \widehat{B}_\nu \right\rangle = \mathrm{Tr}\left[\widehat{\rho}_{\mathrm{th}}(t)\widehat{S}^\dagger(t)\widehat{B}_\mu^\dagger \widehat{B}_\nu \widehat{S}(t)\right], \tag{4.80}$$

$$\left\langle \widehat{B}_\mu \widehat{B}_\nu \right\rangle = \mathrm{Tr}\left[\widehat{\rho}_{\mathrm{th}}(t)\widehat{S}^\dagger(t)\widehat{B}_\mu \widehat{B}_\nu \widehat{S}(t)\right]. \tag{4.81}$$

These can be simplified using the squeezing transformation in Eq. (4.39) followed by the thermal state transformation in Eq. (4.53). Doing this, Eq. (4.78) and Eq. (4.79) become

$$\begin{aligned}\left\langle \widehat{b}_m^\dagger \widehat{b}_l \right\rangle &= \sum_{\mu,\nu} \left(U_{\mu m}^* U_{\nu l} \cosh(r_\mu)\cosh(r_\nu) + U_{\nu m}^* U_{\mu l} \sinh(r_\mu)\sinh(r_\nu) \mathrm{e}^{i(\phi_\mu - \phi_\nu)} \right) \eta_{\mu\nu} \\ &+ \sum_{\mu} U_{\mu m}^* U_{\mu l} \sinh^2(r_\mu), \qquad (4.82) \\ \left\langle \widehat{b}_m \widehat{b}_l \right\rangle &= \sum_{\mu,\nu} \left(U_{\mu m} U_{\nu l} + U_{\nu m} U_{\mu l} \right) \sinh(r_\mu)\cosh(r_\nu) \mathrm{e}^{i\phi_\mu} \eta_{\mu\nu} \\ &+ \sum_{\mu} U_{\mu m} U_{\nu l} \cosh(r_\mu)\sinh(r_\mu) \mathrm{e}^{i\phi_\mu}, \qquad (4.83)\end{aligned}$$

where

$$\eta_{\mu\nu}(t) \equiv \sum_m U_{\mu m} U_{\nu m}^* n_m(t). \qquad (4.84)$$

The time-dependent expectation value of the photon number operator for the mth quasimode $\left\langle \widehat{b}_m^\dagger \widehat{b}_m \right\rangle$ can be obtained by letting $m = l$ in Eq. (4.82). Also, putting Eq. (4.82) and Eq. (4.83) into Eq. (4.75) one can calculate the time-dependent correlation variance between any two modes and quantify the inseparability of the MSTS.

4.6 Limiting cases and comparison to other work

In this section we discuss three limiting cases to our multimode theory presented above and compare the results to other work. The first limit is when the modes are all *lossless*, such that the imaginary part of every quasimode is equal to zero ($\gamma_m = 0$). In this limit we show that our theory gives a MSVS, and show that the squeezing parameter and squeezing phase we obtain agree with other work [93]. The second limit we consider is when there is only a single *lossy* mode that holds the squeezed light. We show that in this limit our multimode theory gives a single-mode squeezed state in agreement with previous work [35]. In the third limit we allow two *lossy* modes for the squeezed light and show that our theory gives a two-mode squeezed thermal state in agreement with our previous work [69].

4.6.1 Lossless modes

If the modes are lossless, then the thermal photon number n_m of each mode is equal to zero and the thermal state in Eq. (4.18) gets replaced with the vacuum state $|0\rangle \langle 0|$. Furthermore, the terms proportional to γ_m are dropped in the LME, so it becomes the quantum Liouville equation. Therefore the density operator becomes

$$\widehat{\rho}(t) = \widehat{S}(t) |0\rangle \langle 0| \widehat{S}^{\dagger}(t), \tag{4.85}$$

which is the density operator for a MSVS. One can determine the squeezing parameter r_μ and squeezing phase ϕ_μ for this state by letting $\gamma_m = 0$ in Eq. (4.69) and Eq. (5.10). Doing this we obtain

$$\dot{r}_\mu = \frac{1}{i\hbar} \left(\alpha^2 \lambda_\mu \mathrm{e}^{-i\phi_\mu} - \text{c.c.} \right), \tag{4.86}$$

$$\dot{\phi}_\mu = -2\Omega_{\mu\mu} - \frac{2\left(\alpha^2 \lambda_\mu \mathrm{e}^{-i\phi_\mu} + \text{c.c.} \right)}{\hbar \tanh(2r_\mu)}. \tag{4.87}$$

Assuming that the system starts initially in vacuum at $t = t_i$ with $r_\mu(t_i) = 0$, the second term in Eq. (4.87) goes to infinity. To prevent this we force the numerator to be zero initially and also at all later times. Thus to obtain our final solution we put

$$\mathrm{Re}\left\{\alpha^2\lambda_\mu \mathrm{e}^{-i\phi_\mu}\right\} = 0. \tag{4.88}$$

Writing $\alpha^2(t) = |\alpha(t)|^2 \exp(-i\chi(t))$ and $\lambda_\mu = |\lambda_\mu| \exp(i\theta_\mu)$, where $\chi(t)$ is a time-dependent phase and θ_μ is a time-independent phase, we obtain from Eq. (4.88) the phase condition

$$-\chi(t) + \theta_\mu - \phi_\mu(t) = \pi/2. \tag{4.89}$$

Putting Eq. (4.89) into Eq. (4.86) and Eq. (4.87) and integrating gives

$$r_\mu(t) = \frac{2|\lambda_\mu|}{\hbar}\int_{t_i}^{t} dt' |\alpha(t')|^2, \tag{4.90}$$

$$\phi_\mu(t) = -2(t - t_i)\Omega_{\mu\mu} + \phi_\mu(t_i). \tag{4.91}$$

Therefore the multimode squeezing operator can be written as

$$\widehat{S}(t) = \prod_\mu \exp\left(\frac{|\lambda_\mu|}{\hbar} r_\mu(t) \mathrm{e}^{-2i\Omega_{\mu\mu}t}\widehat{B}_\mu^{\dagger 2} - \mathrm{H.c.}\right), \tag{4.92}$$

where we let $\phi_\mu(t_i) = 2\Omega_{\mu\mu}t_i$. The MSVS we obtain is given by $\widehat{S}(t)\left|0\right\rangle$. This is the same state obtained by Quesada N. *et al.*, following a similar procedure that uses the Takagi factorization (see Eq. (204) and Eqs. (237) - (238) in Ref. [93]). We note that this state has the same form one obtains in the weak pump limit (*i.e.* $\alpha \ll 1$) by keeping only the first-order terms in the Dyson or Magnus expansion of the evolution operator, a result that is also noted by Quesada N. *et al.* [93]. For lossless modes the expectation values of Eq. (4.82) and Eq. (4.83) become

$$\left\langle \widehat{b}_m^\dagger \widehat{b}_l \right\rangle = \sum_\mu U_{\mu m}^* U_{\mu l} \sinh^2(r_\mu), \tag{4.93}$$

$$\left\langle \widehat{b}_m \widehat{b}_l \right\rangle = \sum_\mu U_{\mu m} U_{\mu l} \cosh(r_\mu) \sinh(r_\mu) \mathrm{e}^{i\phi_\mu}. \tag{4.94}$$

These are the same results that were derived by Quesada N. *et al.* (see Eqs. (234) - (235) in Ref. [93]).

4.6.2 Lossy single-mode squeezed states

In this subsection we show that for a single lossy mode the coupled differential equations Eqs. (4.69) - (5.11) give a squeezing amplitude, squeezing phase, and thermal photon number that agrees with previous work on single-mode squeezed thermal states [35]. In this case, the Takagi factorization of the nonlinear parameter is trivial since there is only one mode. The matrix $\boldsymbol{U}$ has only a single entry $U_{11} = 1$. The single-mode squeezing operator can be written as

$$\widehat{S}(z(t)) = \exp\left(\frac{1}{2} z_{11}(t) \widehat{b}_1^{\dagger 2} - \text{H.c.}\right), \tag{4.95}$$

where the single squeezing parameter $z_{11}(t)$ is given simply by

$$z_{11}(t) = r_1(t) \mathrm{e}^{i\phi_1(t)}. \tag{4.96}$$

Thus, using Eq. (4.39) the quasimode and Schmidt operators are identical $\widehat{b} = \widehat{B}$. Only keeping the $m = l = \mu = \nu = 1$ terms in Eqs. (4.69) - (5.11) and putting

$U_{11} = 1$ we obtain

$$\dot{r}_1 = \frac{2|\alpha|^2|\lambda|}{\hbar} - \frac{2\gamma_1}{2n_1+1}\cosh(r_1)\sinh(r_1), \tag{4.97}$$

$$\dot{\phi}_1 = -2\omega_1, \tag{4.98}$$

$$\dot{n}_1 = 2\gamma_1\left(\sinh^2(r_1) - n_1\right), \tag{4.99}$$

where we have used the phase condition in Eq. (4.89) again to simplify the equations. These equations are derived for SFWM, but they can be easily adapted for SPDC. The only things that need to change are in Eq. (4.97), $|\lambda|$ has to be redefined for SPDC, and $|\alpha|^2$ becomes $|\alpha|$. Therefore, the structure of the equations is unchanged for SPDC. In light of this, these equations are seen to agree with previous work for single-mode squeezed states in a lossy cavity [35].

For a single lossy mode, the expectation values in Eq. (4.82) and Eq. (4.83) become

$$\left\langle \widehat{b}_1^\dagger \widehat{b}_1 \right\rangle = n_1\cosh(2r_1) + \sinh^2(r_1), \tag{4.100}$$

$$\left\langle \widehat{b}_1 \widehat{b}_1 \right\rangle = (2n_1+1)\cosh(r_1)\sinh(r_1). \tag{4.101}$$

These are the same equations that were derived in previous work [65].

4.6.3 Lossy two-mode squeezed states

In this subsection, we show that for two lossy modes the coupled equations give results that agree with our previous work on two-mode squeezed states. For two modes, the nonlinear parameter is a 2×2 symmetric matrix and its Takagi factorization is

$$\begin{bmatrix} 0 & G_{12} \\ G_{12} & 0 \end{bmatrix} = \boldsymbol{U} \begin{bmatrix} G_{12} & 0 \\ 0 & G_{12} \end{bmatrix} \boldsymbol{U}^{\mathrm{T}}, \tag{4.102}$$

where we neglect generation of squeezed light in single modes by letting $G_{11} = G_{22} = 0$. The unitary matrix $\boldsymbol{U}$ is given by

$$\boldsymbol{U} = \frac{1}{2} \begin{bmatrix} 1-i & 1+i \\ 1+i & 1-i \end{bmatrix}. \tag{4.103}$$

Using Eq. (4.36), the squeezing parameter is given by

$$\begin{bmatrix} 0 & z_{12}(t) \\ z_{12}(t) & 0 \end{bmatrix} = \boldsymbol{U} \begin{bmatrix} r(t)\mathrm{e}^{i\phi(t)} & 0 \\ 0 & r(t)\mathrm{e}^{i\phi(t)} \end{bmatrix} \boldsymbol{U}^{\mathrm{T}}, \tag{4.104}$$

where $z_{12} \equiv r\exp(i\phi)$. There is a single squeezing amplitude ($r(t)$) and squeezing phase ($\phi(t)$), but the thermal photon number for the two modes, $n_1(t)$ and $n_2(t)$, are allowed to be different. This means that the photon loss rates are different for each mode. Putting this $\boldsymbol{U}$ into Eqs. (4.69) - (5.11) and letting $\lambda = G_{12}$, we obtain

$$\dot{r} = \frac{2|\alpha|^2|\lambda|}{\hbar} - \frac{\cosh(r)\sinh(r)}{1+n_1+n_2}\left[\gamma_1 + \gamma_2 + (\gamma_1 - \gamma_2)(n_2 - n_1)\right], \tag{4.105}$$

$$\dot{\phi} = -(\omega_1 + \omega_2), \tag{4.106}$$

$$\dot{n}_1 = 2n_1\left[\gamma_2\sinh^2(r) - \gamma_1\cosh^2(r)\right] + 2\gamma_2\sinh^2(r), \tag{4.107}$$

$$\dot{n}_2 = 2n_2\left[\gamma_1\sinh^2(r) - \gamma_2\cosh^2(r)\right] + 2\gamma_1\sinh^2(r). \tag{4.108}$$

These equations have the same form as those that were derived in our previous work on two-mode squeezed states (see Eqs. (19) - (22) in Ref. [69]) generated via SPDC. As mentioned in the previous subsection, we can adapt Eqs. (4.105) - (4.108) for SPDC by replacing $|\alpha|^2$ and λ with $|\alpha|$ and the nonlinear parameter for SPDC.

4.7 Results for a four-cavity CROW

In this section we present our results from solving the coupled equations Eqs. (4.69) - (4.71) for SFWM in a system of four coupled-cavities. The structure is the CROW in Fig. 4.1c, but we take the structure to have only four cavities and we enforce periodic boundary conditions at the two ends of the four-cavity system. Thus, the quasimodes are Bloch modes, but the allowed Bloch vectors, k, are quantized, such that there are only four allowed values. Although such boundary conditions are not physically realizable, we choose this system because it is simple and gives analytic expressions for the complex mode frequencies and the effective nonlinear parameters. This toy-model is intended to demonstrate how to go about solving the system of equations when there are more than the two modes that have been modeled in previous work [69].

To obtain our results we use parameters from a CROW studied in previous work. The photonic crystal slab that contains the coupled-cavities has a refractive index of $n = 3.4$ and a second-order refractive index of $n^{(2)} = 4.5 \times 10^{-18}\,\mathrm{m}^2/\mathrm{W}$, corresponding to Si at telecom wavelengths [100]. The photonic crystal is a square lattice with lattice constant, d. The slab thickness is $0.8d$ and the air-hole radius is $0.4d$. Using these parameters, with find from finite-difference time domain calculations that each individual cavity contains a single mode at the frequency $\widetilde{\omega}_0 = (0.305 - i7.71 \times$

$10^{-6})2\pi c/d$, resulting in a quality factor $Q_0 = 19800$ [96]. The Bloch modes and their frequencies are obtained using a nearest-neighbour tight-binding model, where the individual cavity modes form a basis [90]. The computed frequencies of the 4 Bloch modes at $kD = \{-\pi/2, 0, \pi/2, \pi\}$ are shown in Tab. 4.1a, where $D \equiv 2d$ is the periodicity of the CROW. Since the CROW is effectively a one-dimensional system, we do not consider transverse wavevector components. The expression for the CROW dispersion is approximately given by [89]

$$\widetilde{\omega}_k \approx \widetilde{\omega}_0 \left(1 - \widetilde{\beta}_1 \cos(kD)\right), \tag{4.109}$$

where $\widetilde{\beta}_1 = 9.87 \times 10^{-3} - i1.97 \times 10^{-5}$ is the complex coupling parameter between individual nearest-neighbour cavity modes [96]. This expression gives the loss dispersion of the CROW as well, it can be obtained by $-2\,\mathrm{Im}\{\widetilde{\omega}_k\}$.

We let the pump be a *continuous-wave* with frequency ω_P, modelled by a coherent state with amplitude

$$\alpha(t) = |\alpha|\, \mathrm{e}^{-i\omega_P t}, \tag{4.110}$$

where $|\alpha|^2$ is the average pump photon number. The pump is in the single Bloch mode with wavevector $k_P = \pi/(2D)$ and frequency $\omega_P = 0.305(2\pi c/d)$. Signal and idler photons are generated via SFWM into modes with wavevectors k_1 and k_2, respectively. The effective nonlinear parameter for this process (see Eq. (4.8)) has been shown to be approximately given by [90]

$$G_{k_1 k_2 k_P k_P} \approx G_0 \mathrm{e}^{-i\Delta k D/2} \frac{\mathrm{sinc}\,(M\Delta k D/2)}{\mathrm{sinc}\,(\Delta k D/2)}, \tag{4.111}$$

Table 4.1: (a) Bloch mode wavevectors k and their complex frequencies $\widetilde{\omega}_k$ for a CROW with 4 cavities. Here $D \equiv 2d$ is twice the lattice spacing d. (b) Diagonal values λ_μ and Schmidt frequencies $\Omega_{\mu\mu}$ for the μth Schmidt mode. The four Schmidt modes are obtained by taking the Takagi factorization of the nonlinear parameter in Eq. (4.111).

(a)

kD	$\widetilde{\omega}_k d/(2\pi c)$
π	$0.308010 - i1.38 \times 10^{-5}$
$\pm\pi/2$	$0.305000 - i7.71 \times 10^{-6}$
0	$0.301990 - i1.63 \times 10^{-6}$

(b)

μ	λ_μ	$\Omega_{\mu\mu} d/(2\pi c)$
1	1.21	0.304877
2	1.16	0.304999
3	0.742	0.304953
4	0.665	0.305170

where $\Delta k \equiv k_1 + k_2 - 2k_P$ is the phase mismatch between the different Bloch modes, M is the total number of cavities, and

$$G_0 \equiv \frac{\hbar^2 \omega_0^2 \chi_{\text{eff}}^{(3)}}{16\epsilon_0 M V_{\text{eff}}}, \tag{4.112}$$

where $\chi_{\text{eff}}^{(3)}$ is the effective nonlinear coefficient, and V_{eff} is the effective mode volume of the individual cavity mode.

Now we perform a Takagi factorization of the nonlinear parameter in Eq. (4.111). The resulting diagonal values λ_μ and Schmidt mode frequencies $\Omega_{\mu\mu}$ (see Eq. (4.65)) are shown in Tab. 4.1b. We note that the λ_μ do not add to one, since these are not the eigenvalues of the density operator. The frequencies $\Omega_{\mu\mu}$ are all within 0.06% of the pump frequency ω_P. This is due to the dispersion of the Bloch mode frequencies having a small bandwidth and choosing the pump to be at the center of the band. This will not be the case for a general structure. As we show below, however, the Schmidt modes with frequencies that are nearly on resonance with the pump have larger squeezing amplitudes than those that are off resonance.

To obtain a particular solution, we initially let the system be in the vacuum state by setting all the squeezing amplitudes and thermal photon numbers equal to zero. In Appendix C.3 we discuss how to solve the coupled equations starting from the vacuum (see Eqs. (C.22) and (C.23)), particularly how to choose the initial squeezing phase. At time $t = 0$ the pump is put into the Bloch mode $k_P = \pi/(2D)$ and then it generates signal and idler photons in the Bloch modes k_1 and k_2, respectively. Using these initial conditions, we solve Eqs. (4.69) - (5.11) numerically using a Runge-Kutta method (such as the ode45 function in MATLAB). For 4 modes it takes on the order of 10 seconds to solve the equations using a standard PC.

In what follows, we use t_{c} as our unit of time, where t_{c} is defined as the time it takes a pulse of light with group velocity v to propagate the total distance, L, of the coupled-cavity structure:

$$t_{\mathrm{c}} \equiv \frac{L}{v}. \tag{4.113}$$

For 4 cavities with a lattice constant of $d = 480\mathrm{nm}$, the length of the structure is $L = 2.9\mu\mathrm{m}$. If the pulse is centered at $kD = \pi/2$, and assuming linear dispersion in Eq. (4.109), then the group velocity of the pulse is approximately $v = c/26.6$. Therefore, we obtain $t_{\mathrm{c}} = 0.25\mathrm{ps}$. Additionally, we define the pumping strength dimensionless parameter,

$$g \equiv \frac{4G_0 \left|\alpha\right|^2 t_{\mathrm{c}}}{\hbar}, \tag{4.114}$$

which scales the squeezing amplitude in all the Schmidt modes. In all that follows, we set $g = 1/12$. This value of g can be achieved with an average pump photon number of $|\alpha|^2 = 4.6 \times 10^7$ and an effective mode volume of $V_{\text{eff}} = 3(\mu\text{m})^3$ for the cavity mode with frequency $\widetilde{\omega}_0$. It gives squeezing amplitudes in the Schmidt modes that are on the order of one, while keeping the thermal photon number many orders of magnitude below the number of photons in the pump.

We start by considering the Schmidt mode squeezing amplitudes in Fig. 4.2a. At $t = 0$ the pump is turned on and the r_μ initially increase linearly with time, where it can be shown using Eq. (4.69) that the slope is approximately given by $\dot{r}_\mu \approx g|\lambda_\mu|/2$ (see also Eq. (D.79)). This is because for short times the thermal noise and detuning $|\Omega_{\mu\mu} - \omega_P|$ can be neglected. The Schmidt modes that are detuned from the pump will have oscillations in their r_μ and an r_μ that is smaller than that of the modes that are on resonance with the pump. The oscillations exist for Schmidt modes that have a detuning from the pump frequency that satisfies $|\Omega_{\mu\mu} - \omega_P|t_{\text{c}} > g|\lambda_\mu|/2$. Thus, these oscillations will disappear if we increase the pumping strength g. If, however, g is small, then the period of the oscillations are approximately given by $\pi(|\Omega_{\mu\mu} - \omega_P|t_{\text{c}})^{-1}$. For example, using this expression, the squeezing amplitude in the $\mu = 1$ and $\mu = 4$ Schmidt modes have periods of approximately $26t_{\text{c}}$ and $19t_{\text{c}}$, respectively. As time increases, the amplitude of the oscillations are dampened due to the intrinsic losses of the Bloch modes.

Next, we consider the derivative of the Schmidt mode squeezing phases, $\dot{\phi}_\mu$, in Fig. 4.2b. Initially the derivative is approximately constant, corresponding to the phases increasing linearly with time. In Appendix C.3 we show that for short times $\dot{\phi}_\mu(t) \approx \Omega_{\mu\mu} + \omega_P$. The modes $\mu = 2$ and $\mu = 3$ that are close to resonance with the pump have an approximately constant phase derivative approaching $2\omega_P$. The detuned modes $\mu = 1$ and $\mu = 4$ have peaks in their phase derivatives whenever the squeezing amplitude is close to zero. This is because in Eq. (5.10) the term proportional to $1/\tanh(2r_\mu)$ is large when $r_\mu \ll 1$, which causes $\dot{\phi}_\mu$ to increase.

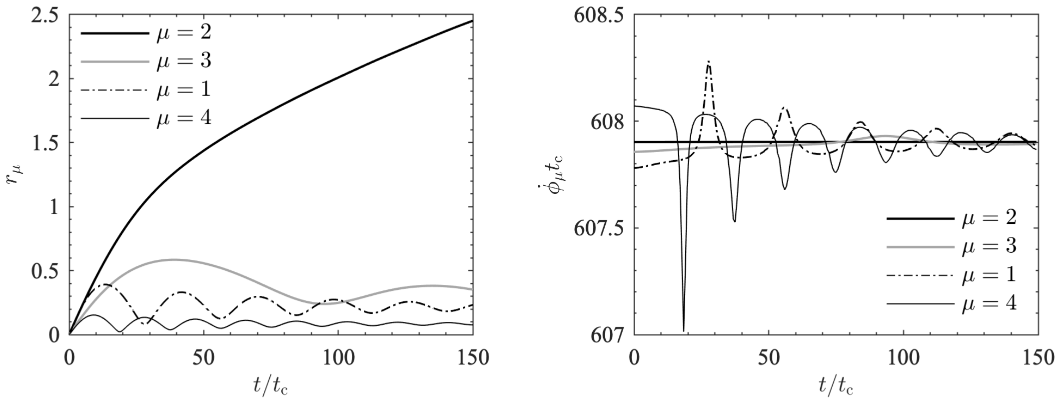

(a) (b)

Figure 4.2: (a) Squeezing amplitudes r_μ and (b) derivatives of the squeezing phases $\dot{\phi}_\mu$ in the four Schmidt modes of four coupled-cavities. Here $t_c = 0.25$ps is the time for a light pulse to cross the length of the structure.

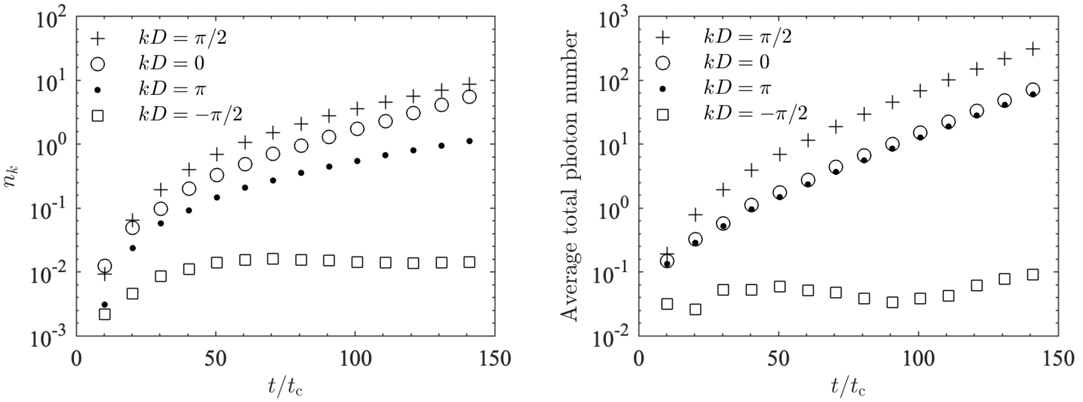

(a) (b)

Figure 4.3: (a) Thermal photon number n_k and (b) average total photon number in the Bloch modes of four coupled-cavities.

Now, we present the average thermal photon numbers in the Bloch modes, n_k, in

Fig. 4.3a. At short times $t < 10t_c$ the n_k are negligible. The n_k do not go above approximately 10 for the pumping strength $g = 1/12$. The majority of the thermal noise is generated in the Bloch modes with positive wavevectors. The n_k in the Bloch mode with $kD = -\pi/2$ is only approximately 0.01.

In Fig. 4.3b we calculate the average total photon number using Eq. (4.79). There are on the order of approximately 10^3 total photons generated by the nonlinear process. The majority are generated in the forward-propagating Bloch mode, $kD = \pi/2$ and $kD = \pi$ and $k = 0$. Only approximately 0.1 photons, on average, are generated in the backward-propagating Bloch mode, $kD = -\pi/2$.

4.8 Conclusion

The key finding in this paper is that the solution to the LME for a set of lossy quasimodes is the density operator for a MSTS (see Eq. (4.18)). In order to prove this we introduce an orthogonal Schmidt basis via the Takagi factorization in Sec. 4.4.1 to diagonalize the nonlinear Hamiltonian and squeezing operator. The main result is a set of coupled first-order differential equations that the squeezing amplitude, squeezing phase, and thermal photon numbers must obey in order for the MSTS to be a solution (see Eqs. (4.69) - (4.71)).

In order to derive the solution, we make the undepleted pump approximation on the nonlinear Hamiltonian and assume that the nonlinear parameter is essentially the same for all pump modes in the pump bandwidth and neglect its dependence on the pump frequencies (see Sec. 4.3.1). The latter assumption is valid for a pump pulse in a waveguide or free space as long as the pulse is long in duration.

Our theory is applicable to the orthogonal set of discrete lossy modes in structures, such as MRRs, coupled-MRRs, CROWs, and high-Q cavities coupled to a waveguide in a photonic crystal (see Fig. 4.1).

Our results are consistent with previous work done on single-mode and two-mode squeezed thermal states (see Refs. [35] and [69]) as presented in Sec. 4.6. Also in the limit where the quasimodes become lossless, our solution reduces to a MSVS, and it agrees with other work [93] that used a similar approach also using a Takagi factorization.

To our knowledge, this is the first time the analytic solution for the quantum state of light generated via nonlinear processes in $M > 2$ lossy modes has been derived. Not only is the solution of theoretical importance, it can greatly reduce the number of coupled differential equations required to solve for the density operator. One alternative way to determine the density operator numerically, is by calculating its matrix elements using Fock states. The number of possible states for N photons in M quasimodes is $\sum_{j=0}^{N} \binom{j+M-1}{j} = (M+N)!/(M!N!)$ [92], where $\binom{n}{k} = n!/[k!(n-k)!]$ is the binomial coefficient. In order to find the matrix elements, the number of coupled equations one has to solve is the square of this. However, using our results one can determine the density operator by solving only $3M$ coupled first-order differential equations that are independent of N. For example if $N = 20$ and $M = 4$ there are 10626 basis states and thus $(10626)^2$ coupled equations. But our theory would only require solving 12 coupled equations.

The expressions we derive for the correlation variances (see Sec. 4.5) only contain double sums over the Schmidt modes and do not require one to solve any additional coupled equations. Thus, the differential equations only need to be solved once and then any same-time correlation variances of interest can be quickly calculated.

We believe that our new solution to this important problem will make it more feasible to study large multimode lossy structures and to optimize them for a wide variety of quantum information applications. In future work, we will apply our theory to more physically realistic structures, such as many-cavity CROWs and MRRs. We then hope to show that the generated MSTS is an approximate Gaussian cluster state [34, 101]. To do this, one needs to determine under what conditions on the nonlinear parameter and/or the squeezing matrix, does the state satisfy nullifier equations. If it is possible to determine these conditions for the MSTS we derived, then it can be used as a cluster state resource for quantum computations [81].

Chapter 5

Nonlinear optical generation of entangled squeezed states in lossy nonorthogonal quasimodes: an analytic solution

In the previous chapter, we proved that the nonlinearly-generated light in the lossy modes of resonant cavities has the density operator of an MSTS. However, we assumed that the lossy modes were orthogonal in order to derive the solution. This assumption means that our solution could only be applied to idealized structures that have high-symmetry. In this chapter, we remove this assumption and consider the general case of *nonorthogonal* lossy mode, and prove that the density operator still has the analytic form of an MSTS in this most general case. This manuscript was submitted to Physical Review Letters on the 13th of October, 2022.

Abstract – We prove that the density operator for the nonlinearly-generated quantum state of light in the M lossy nonorthogonal quasimodes of a nanocavity system has the analytic form of a multimode squeezed thermal state, where the time-dependence of the squeezing and thermal photon parameters are given by a set of $3M$ coupled differential equations. We apply our approach to a system with two highly

nonorthogonal quasimodes and obtain good agreement with simulations using a basis of Fock states. Our approach provides an efficient way to model and optimize the generation of mixed Gaussian cluster states.

5.1 Introduction

Squeezed states of light are the fundamental states used to generate multimode entangled states for CV quantum computing [102]. Multimode entangled states can be made by propagating a series of squeezed states through an array of linear optical elements, which together entangle the modes in both frequency and time [86,103–105]. Alternatively, they can be generated directly in multimode nanocavity systems using the nonlinear optical processes of SFWM or SPDC [106]. Using the first approach, it has been demonstrated experimentally that three-dimensional cluster states can be generated, which can be used to make a universal quantum computer [81]. Using the second approach, universal CV cluster states have been created using an OPO, where the quantum information is encoded in the quadratures of the optical frequency comb of the OPO [107,108]. Also, cluster states have been generated using an MRR [109], where the squeezed modes are simultaneously entangled in frequency and time. In this paper, we use the second approach and theoretically study the generation of multimode entangled states via SFWM in general lossy multimode structures.

Theoretical studies on CV cluster states have largely focused on the generation of an MSVS, a pure Gaussian state, where the scattering losses are neglected during its generation [34, 86, 106]. However, the nonlinear nanophotonic structures used to generate the light have lossy modes that leak energy into the surrounding environment. Therefore, the generated light in the lossy modes cannot be in a pure state.

We refer to the lossy modes of a structure as *quasimodes*, which are eigenstates of the non-Hermitian linear Hamiltonian, with complex frequencies, $\widetilde{\omega}_m = \omega_m - i\gamma_m$, that have a real part, ω_m, as well as an imaginary part, γ_m, that quantifies the energy leakage.

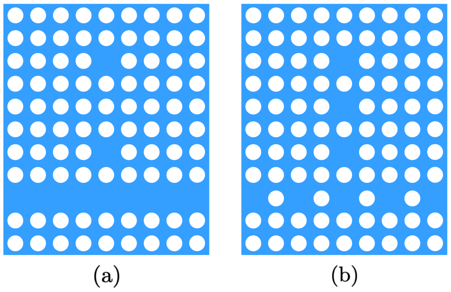

Figure 5.1: Schematics of two different square lattice photonic crystal slab structures of interest (the white circles are air-holes). The first structure (a) consists of two coupled cavities side-coupled to a defect-waveguide. The second structure (b) consists of three coupled high-Q cavities, side-coupled to a coupled-resonator optical waveguide.

Theoretical work including the effects of scattering loss has been done on the generation of entangled states and squeezed states via SFWM or SPDC in MRRs [36, 53, 69], nonlinear waveguides [110], and coupled-cavities in a photonic crystal slab [89, 90]. Recently, it was proven that the generated light in the quasimodes in such systems takes the form of a MSTS [82], where the thermal part of the state captures the photon loss. It was demonstrated that the amount of squeezing in the MSTS is less than it is in a MSVS with the same squeezing parameter, due to an increase in quadrature noise arising from scattering loss during the generation and propagation processes. Although these studies have not focused on generating cluster states, the MSTS solution opens up a path to study cluster states generated by SFWM in lossy structures.

The MSTS solution has thus far only been proven for the case when the quasimodes are orthogonal, which will only occur for the modes in structures that have high symmetry, such as the ring modes of an MRR or the Bloch modes of a defect waveguide in a photonic crystal slab. In these structures, the quasimodes are eigenmodes of symmetry operators (*e.g.* rotational or translational) that make quasimodes of different frequency orthogonal. As a result, their spatial overlap integral is zero. The quasimodes of general lossy structures are not orthogonal and thus the MSTS solution has only been shown to be valid for a restricted set of idealized high-symmetry structures.

There are many structures of interest that have quasimodes that are highly nonorthogonal; two examples are shown in Fig. 5.1. In Fig. 5.1(a), pairs of signal and idler photons can be generated in the quasimodes of the two coupled cavities by pumping them from above with a Gaussian beam. The defect CROW couples the generated light out the of cavities, but it also breaks the symmetry of the lattice, causing the modes to be nonorthogonal. The structure in Fig. 5.1(b) incorporates a CROW for the pump, which resonantly couples to side-coupled nonlinear resonant cavities, where it generates pairs of signal and idler photons. There are three modes in the side-coupled cavities, one for the pump and one each for the generated signal and idler photons. We have calculated the quasimodes for the structure in Fig. 5.1 (b) and found that the overlap between some of the modes can be as high as 10%. This system is of particular interest as it incorporates the pump, signal, and idler channel as well as the nonlinear resonant structure all in one integrated system. Therefore, it is important to find an efficient and accurate way to model the nonlinear generation in such systems.

In this work, we prove that the density operator for the generated light in a lossy system with a set of quasimodes takes the form of a MSTS, even when the quasimodes are nonorthogonal, but the thermal portion of the density operator is not diagonal in the quasimode basis, but in a new orthogonalized basis. We apply our theory to a simplified version of the structure in Fig. 5.1(a) to generate a two-mode squeezed thermal state in the two nonorthogonal quasimodes of the resonant structure which have an overlap of about 80%, and demonstrate agreement with numerical approaches as well as the strong effect of the nonorthogonality.

The nonorthogonality of the quasimodes prevent the usual quantization procedure, but there are two approaches to quantizing them. The first approach is based on a Green's function quantization method, and is applicable to general absorptive and lossy media [111]. The second approach is to quantize the electric field in the standard way using the lossless normal modes, and then to project onto the lossy quasimodes by a non-Hermitian projection operator [9]. The projection approach is an approximate approach that is applicable to non-absorptive media with scattering losses through the open boundaries, and is the one that we use in this paper. In Appendix D.2 we show that for the case of SFWM or SPDC in a non-absorptive medium with scattering loss, both approaches give the exact same form for the LME for the density operator, $\widehat{\rho}(t)$, of the generated light:

$$\frac{d\widehat{\rho}}{dt} = \frac{-i}{\hbar}\left[\widehat{H}, \widehat{\rho}\right] + \sum_{m,l} \chi^{(-)}_{ml}\left(2\widehat{a}_l\widehat{\rho}\widehat{a}^\dagger_m - \widehat{\rho}\widehat{a}^\dagger_m\widehat{a}_l - \widehat{a}^\dagger_m\widehat{a}_l\widehat{\rho}\right). \tag{5.1}$$

Therefore the form of $\widehat{\rho}(t)$ is independent of the quantization approach used. Here $\widehat{H}$ is the Hermitian Hamiltonian, which includes the linear Hamiltonian as well as the nonlinear interaction, and $\widehat{a}_m$ and $\widehat{a}^\dagger_m$ are the annihilation and creation operator for photons in the symmetrized mode m, with $[\widehat{a}_m, \widehat{a}_l^\dagger] = \delta_{ml}$. The symmetrized modes are linear combinations of the nonorthogonal quasimodes, chosen so that the symmetrized modes are orthogonal, but are no longer eigenstates of the non-Hermitian linear Hamiltonian (see Appendix D.2). We define $\boldsymbol{\chi}^{(-)} \equiv \frac{i}{2}\left(\boldsymbol{\chi} - \boldsymbol{\chi}^\dagger\right)$, where $\boldsymbol{\chi}$ is the quasimode coupling matrix. The off-diagonal coupling terms in $\boldsymbol{\chi}$ come from the quasimode nonorthogonality, and have been shown to contribute to the spontaneous emission rate of a quantum dot in a cavity [94, 112]. In our approach, the quasimode coupling matrix is related to the quasimode overlap and the quasimode frequencies with $\boldsymbol{\chi} \equiv \boldsymbol{O}^{1/2}\widetilde{\boldsymbol{\omega}}\boldsymbol{O}^{-1/2}$, where $\boldsymbol{O}$ is a matrix of the mode overlaps and $\widetilde{\boldsymbol{\omega}} \equiv \mathrm{diag}(\widetilde{\omega}_1, \ldots)$ is a diagonal matrix of the quasimode frequencies.

The generation of the light in the cavity system can be modelled with Eq. (5.1). Numerical solutions to Eq. (5.1) for the density operator can be obtained by expanding the operators in a basis of Fock states and then integrating the resulting set of coupled differential equations [113]. The number of equations is the square of the dimension of the basis. For example, for a state with M modes and a maximum photon number of N, the number of possible Fock states is at least $(M + N)!/(M!N!)$ [92], and the number of equations is the square of this. Thus, for multimode states with many photons there can be an impractical number of equations to solve in order to obtain accurate results for the density matrix, unless dimension reduction techniques are used. Alternatively, instead of solving for the time-dependent density operator, one might be able to calculate the time-dependent expectation value of any mode operators, with only the initial state, using a Heisenberg – Langevin approach generalized to nonorthogonal modes. If one knows beforehand that the state is Gaussian at all times, then it is fully determined by its covariance matrix. Calculating the covariance matrix using this approach only requires solving on the order of M^2 coupled differential equations. However, as we shall show, our method only requires one to solve the $3M$ coupled first-order differential equations for the MSTS parameters. We now present the derivation of our analytic solution to the LME.

5.2 Analytic solution to the Lindblad master equation

We consider a general lossy resonant structure that has a set of discrete nonorthogonal quasimodes, and we let the initial state of the system to be the vacuum state. The squeezed light is generated in the quasimodes by a SFWM interaction, where pairs of signal and idler photons are generated by the annihilation of pairs of pump photons. We take the pump to be a classical electric field that is modelled as a coherent state. Our analytic solution requires that the signal and idler modes are effectively coupled to a single pump mode, such that we can factorize the nonlinear parameter, for the SFWM interaction, into a part that only depends on the pump and a separate part that only depends on the signal and idler modes. One way to achieve this is to require the pump be in a coherent state, $|\alpha(t)\rangle$, in a single quasimode, P, with a time-dependent coherent state parameter given by $\alpha(t) = \alpha_P(t)\exp(-i\omega_P t)$, where $\alpha_P(t)$ is slowly-varying complex temporal envelope and ω_P is the pump frequency. Alternatively, this can be achieved in a setup where the structure is pumped from above, *e.g.* with a Gaussian beam in the free-space continuous modes, but the pump beam modes all have essentially the same nonlinear overlap with a given pair of signal and idler modes (see Ref. [89] and Appendix D.5). Using the undepleted pump approximation, the nonlinear Hamiltonian for the interaction takes the form

$$\widehat{H}_{\mathrm{NL}} = \hbar\alpha^2(t)\sum_{m,l} S_{ml}\widehat{a}_m^\dagger\widehat{a}_l^\dagger + \mathrm{H.c.}, \tag{5.2}$$

where the matrix $\boldsymbol{S}$ is the nonlinear parameter for SFWM (see Appendix D.2).

The generated light satisfies the LME (Eq. (5.1)), where the system Hamiltonian is defined as, $\widehat{H} \equiv \widehat{H}_{\mathrm{L}} + \widehat{H}_{\mathrm{NL}}$, where the linear Hamiltonian is given by

$$\widehat{H}_L = \hbar\sum_{m,l} \chi_{ml}^{(+)}\widehat{a}_m^\dagger\widehat{a}_l, \tag{5.3}$$

with $\boldsymbol{\chi}^{(+)} \equiv \frac{1}{2}\left(\boldsymbol{\chi} + \boldsymbol{\chi}^\dagger\right)$. The main result of this work is that the analytic solution to Eq. (5.1) can be written in the form of an MSTS, defined as

$$\widehat{\rho}(t) = \widehat{S}(t)\widehat{\rho}_{\mathrm{th}}(t)\widehat{S}^\dagger(t), \tag{5.4}$$

where $\widehat{S}(t)$ is a unitary multimode squeezing operator and $\widehat{\rho}_{\mathrm{th}}(t)$ is a density operator describing a multimode thermal state. As we will show, with the right basis choice, $\widehat{S}(t)$ can be expressed as a product of single-mode squeezing operators, and $\widehat{\rho}_{\mathrm{th}}(t)$ can be expressed as a product of single-mode thermal density operators, but the basis required for thermal-state factorization is different than that used to factorize the squeezing operator. Expressing them in this way allows us to derive a set of coupled differential equations that the squeezing parameters and thermal photon numbers for the state must obey in order for $\widehat{\rho}(t)$ to be the solution. To express $\widehat{S}(t)$ as a product of single-mode squeezing operators, we perform a symmetric singular value decomposition of the nonlinear parameter in Eq. (5.2), $\boldsymbol{S} = \boldsymbol{U}\boldsymbol{\lambda}\boldsymbol{U}^{\mathrm{T}}$, where $\boldsymbol{U}\boldsymbol{U}^\dagger = 1$

and $\boldsymbol{\lambda} \equiv \mathrm{diag}(\lambda_1, \ldots)$ is a diagonal matrix of the singular values. Putting this into Eq. (5.2), we obtain

$$\widehat{H}_{\mathrm{NL}} = \hbar\alpha^2(t) \sum_{\mu} \lambda_\mu \widehat{B}_\mu^{\dagger 2} + \mathrm{H.c.}, \tag{5.5}$$

where we define the *Schmidt mode creation operators* as $\widehat{B}_\mu^\dagger \equiv \sum_m U_{\mu m} \widehat{a}_m^\dagger$, with $[\widehat{B}_\mu, \widehat{B}_\nu^\dagger] = \delta_{\mu\nu}$. In order to write $\widehat{\rho}_{\mathrm{th}}(t)$ as a product of single-mode thermal density operators, we perform a singular value decomposition of $\boldsymbol{\chi}^{(+)}$ (see Eq. (5.3)), $\boldsymbol{\chi}^{(+)} = \boldsymbol{M}^{(+)} \boldsymbol{\omega}^{\mathrm{s}} \boldsymbol{M}^{(+)\dagger}$, where $\boldsymbol{M}^{(+)} \boldsymbol{M}^{(+)\dagger} = 1$ and $\boldsymbol{\omega}^{\mathrm{s}} \equiv \mathrm{diag}(\omega_1^{\mathrm{s}}, \ldots)$ is a diagonal matrix of the singular values. Putting this into Eq. (5.3), we obtain

$$\widehat{H}_{\mathrm{L}} = \hbar \sum_{\kappa} \omega_\kappa^{\mathrm{s}} \widehat{C}_\kappa^\dagger \widehat{C}_\kappa, \tag{5.6}$$

where we define the *thermal mode creation operators* as $\widehat{C}_\kappa^\dagger \equiv \sum_m M_{\kappa m}^{(+)} \widehat{a}_m^\dagger$, with $[\widehat{C}_\kappa, \widehat{C}_{\kappa'}^\dagger] = \delta_{\kappa\kappa'}$.

Now in the Schmidt mode basis, $\widehat{S}(t)$ can be written simply as [82]

$$\widehat{S}(t) = \prod_{\mu} \exp\left(\frac{1}{2} r_\mu(t) \mathrm{e}^{i\phi_\mu(t)} \widehat{B}_\mu^{\dagger 2} - \mathrm{H.c.}\right), \tag{5.7}$$

where $r_\mu(t)$ and $\phi_\mu(t)$ are the squeezing amplitude and the squeezing phase of the μth Schmidt mode. In the thermal mode basis, $\widehat{\rho}_{\mathrm{th}}(t)$ can be written simply as

$$\widehat{\rho}_{\mathrm{th}}(t) = \prod_{\kappa} \frac{1}{1 + n_\kappa(t)} \left(\frac{n_\kappa(t)}{1 + n_\kappa(t)}\right)^{\widehat{C}_\kappa^\dagger \widehat{C}_\kappa}, \tag{5.8}$$

where $n_\kappa(t) \equiv \mathrm{Tr}\left[\widehat{\rho}_{\mathrm{th}}(t) \widehat{C}_\kappa^\dagger \widehat{C}_\kappa\right]$ is the average thermal photon number of the thermal mode, κ. The average thermal photon number is not related to thermal effects, but rather captures the process of photon loss due to scattering.

We show in Appendix D.3 that requiring that Eq. (5.4) is the solution to the LME leads to the following coupled differential equations for $r_\mu(t)$, $\phi_\mu(t)$, and $n_\kappa(t)$:

$$\frac{dr_\mu}{dt} = \frac{2}{\hbar}\operatorname{Im}\left[\alpha^2(t)\lambda_\mu \mathrm{e}^{-i\phi_\mu}\right] - 2\sum_{\nu,\sigma}\cosh\left(r_\nu\right)\sinh\left(r_\sigma\right)\operatorname{Re}\left[\mathcal{N}_{\mu\nu\sigma}\right], \tag{5.9}$$

$$\frac{d\phi_\mu}{dt} = -2\Omega_{\mu\mu} - \frac{4}{\hbar\tanh(2r_\mu)}\operatorname{Re}\left[\alpha^2(t)\lambda_\mu \mathrm{e}^{-i\phi_\mu}\right] - 2\sum_{\nu,\sigma}\frac{\cosh\left(r_\nu\right)\sinh\left(r_\sigma\right)}{\cosh\left(r_\mu\right)\sinh\left(r_\mu\right)}\operatorname{Im}\left[\mathcal{N}_{\mu\nu\sigma}\right], \tag{5.10}$$

$$\begin{aligned}\frac{dn_\kappa}{dt} &= -2n_\kappa\sum_{\nu,\sigma}Y_{\kappa\nu}Y^*_{\kappa\sigma}\Gamma_{\sigma\nu}\cosh(r_\nu)\cosh(r_\sigma)\\ &\quad + 2(1+n_\kappa)\sum_{\nu,\sigma}Y_{\kappa\nu}Y^*_{\kappa\sigma}\Gamma_{\nu\sigma}\sinh(r_\nu)\sinh(r_\sigma)\mathrm{e}^{i(\phi_\nu-\phi_\sigma)},\end{aligned} \tag{5.11}$$

where $\Omega_{\mu\mu}$ is the μth Schmidt mode frequency, where $\boldsymbol{\Omega} \equiv \boldsymbol{Y}^\dagger\boldsymbol{\omega}^{\mathrm{s}}\boldsymbol{Y}$, with $\boldsymbol{Y} \equiv \boldsymbol{M}^{(+)\dagger}\boldsymbol{U}$, and $\boldsymbol{\Gamma} \equiv \boldsymbol{V}^\dagger\boldsymbol{\gamma}^{\mathrm{s}}\boldsymbol{V}$, where $\boldsymbol{V} \equiv \boldsymbol{M}^{(-)\dagger}\boldsymbol{U}$. Here $\boldsymbol{M}^{(-)}$ is obtained from a singular value decomposition of $\boldsymbol{\chi}^{(-)}$ (found in the LME, Eq. (5.1)), $\boldsymbol{\chi}^{(-)} = \boldsymbol{M}^{(-)}\boldsymbol{\gamma}^{\mathrm{s}}\boldsymbol{M}^{(-)\dagger}$, where $\boldsymbol{M}^{(-)}\boldsymbol{M}^{(-)\dagger} = 1$ and $\boldsymbol{\gamma}^{\mathrm{s}} \equiv \operatorname{diag}(\gamma^{\mathrm{s}}_1, \ldots)$ is a diagonal matrix of the singular values. For convenience we have also defined

$$\mathcal{N}_{\mu\nu\sigma} \equiv \Gamma_{\sigma\nu}\mathrm{e}^{i(\phi_\sigma-\phi_\mu)}\sum_{\kappa,\kappa'}Y_{\kappa\sigma}Y_{\kappa'\nu}Y^*_{\kappa\mu}Y^*_{\kappa'\mu}\frac{n_\kappa - n_{\kappa'} + 1}{n_\kappa + n_{\kappa'} + 1}. \tag{5.12}$$

The coupled equations Eqs. (5.9) - (5.11) can be solved numerically for the parameters $r_\mu(t)$, $\phi_\mu(t)$, and $n_\kappa(t)$ using a Runge Kutta method. For M modes, there are only $3M$ coupled equations that need to be solved. Using these parameters in Eqs. (5.4), (5.7), and (5.8), the density operator of the MSTS is obtained for all times

5.3 Quadrature squeezing of the Schmidt modes

With the MSTS one can derive simple analytic expressions for the expectation value of observables written in terms of the Schmidt mode operators. As an example, we derive an analytic expression for the quadrature squeezing of the Schmidt modes. We define the quadrature operator

$$\widehat{Q}_\mu \equiv \mathrm{e}^{i(\omega_P t+\beta_\mu)}\widehat{B}_\mu + \mathrm{e}^{-i(\omega_P t+\beta_\mu)}\widehat{B}_\mu^\dagger, \tag{5.13}$$

where β_μ is the initial phase at $t = 0$. The quantum noise in the quadrature is defined as the variance of the quadrature operator, $\langle \widehat{Q}_\mu^2 \rangle \equiv \mathrm{Tr}(\widehat{Q}_\mu^2 \widehat{\rho}(t))$. Using the MSTS in Eq. (5.4) it can be shown that the quadrature noise is simply given by

$$\begin{aligned}\langle \widehat{Q}_\mu^2 \rangle = {}& (1+2\eta_{\mu\mu})\sin^2(\phi_\mu/2+\omega_P t+\beta_\mu)\,\mathrm{e}^{2r_\mu} \\ & + (1+2\eta_{\mu\mu})\cos^2(\phi_\mu/2+\omega_P t+\beta_\mu)\,\mathrm{e}^{-2r_\mu},\end{aligned} \tag{5.14}$$

where we define $\eta_{\mu\nu}(t) \equiv \sum_\kappa Y_{\mu\kappa} n_\kappa(t) Y_{\nu\kappa}^*$. It can be shown that for the Schmidt mode frequencies, $\Omega_{\mu\mu}$, that are on resonance with twice the pump frequency, the squeezing phase solution is approximately given by, $\phi_\mu(t) \simeq -2\omega_P t - 2\beta_\mu$, and the amplitude of the oscillations in Eq. (5.14) are greatly diminished. Thus, close to resonance we obtain the approximate expression, $\langle \widehat{Q}_\mu^2 \rangle \simeq (1+2\eta_{\mu\mu})\,\mathrm{e}^{-2r_\mu}$, which only contains the exponential squeezing factor. The quadrature noise is squeezed below the vacuum noise whenever $\langle \widehat{Q}_\mu^2 \rangle < 1$. The thermal factor $(1+2\eta_{\mu\mu})$ increases the noise, and thus the squeezing level is less than it is in a pure MSVS with the same squeezing parameter.

5.4 Two-mode squeezed thermal state generated in two coupled-cavities in a finite photonic crystal slab

We now apply our theory to study the generation of a two-mode squeezed thermal state in two coupled defect cavities, that are embedded asymmetrically in a finite square lattice photonic crystal slab with the period d (see Fig. 5.2(a)). This structure has been studied in Refs. [9] and [97] in a different context, and we use the same parameters for the photonic crystal slab here (see Appendix D.5). We have chosen the system to be asymmetric so that (as we shall see) the two confined quasimodes of the system are nonorthogonal. The individual cavity modes and their frequencies are obtained from finite-difference time-domain (FDTD) calculations using Lumerical. The two confined quasimodes are obtained with a tight-binding model [9], where the individual cavity modes form the basis.

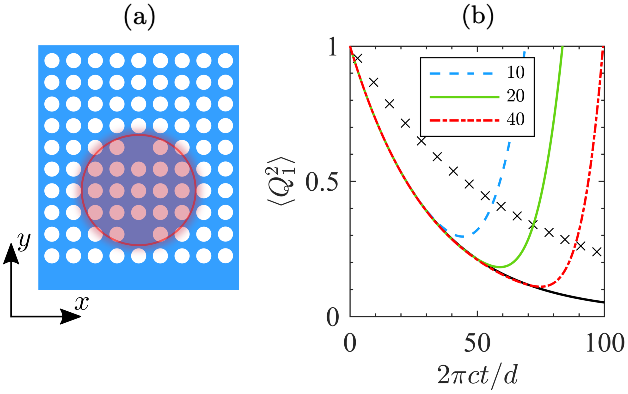

Figure 5.2: (a) Schematic of the structure we model to obtain our results. This is a simplified version of Fig. 5.1 (b). It consists of two coupled-cavities in a finite photonic crystal slab that are embedded asymmetrically in a square lattice. The cavities are pumped from above with a Gaussian pulse. Its transverse profile is shown as the large shaded circle (where the solid line circle is its full width at half maximum). (b) Quadrature noise, $\langle Q_1^2 \rangle$, calculated using the two-mode squeezed thermal state (solid black line), and using QuTiP with 10, 20, and 40 Fock basis states in each mode. Also, we plot the quadrature noise when the overlap is excluded ($O_{12} = O_{21} = 0$) (crosses).

The overlap matrix (see Appendix D.1) for the two quasimodes for the structure in Fig. 5.2(a) is

$$\boldsymbol{O} = \begin{bmatrix} 1 & 0.76 - i0.44 \\ 0.76 + i0.44 & 1 \end{bmatrix}, \tag{5.15}$$

which shows that the quasimodes of different frequency are highly nonorthogonal with a large overlap, $|O_{12}| = |O_{21}| = 0.88$. The theoretical upper limit of the overlap is 0.90 (see Appendix D.1). Thus, our calculation shows that the nonorthogonality between the two modes is nearly at its maximum.

To generate the squeezed state in the coupled-cavities, we take the system to be pumped from above with a 0.43mW Gaussian beam polarized in the y direction that is continuous-wave in time, with frequency $\omega_P d/(2\pi c) = 0.3027$ (its profile is illustrated by the large shaded circle in Fig. 5.2(a)). We let its full width at half maximum be $5d$ (solid line circle). The details of the derivation of the nonlinear parameter $\boldsymbol{S}$ using this Gaussian pump pulse are given in Appendix D.5.

We solve the coupled-equations Eqs. (5.9) - (5.11) using a fourth-order Runge-Kutta method. For $t < 0$ the state is the vacuum state, and then at $t = 0$ the continuous-wave pump is turned on and the generation process begins. For the two-mode system, it takes about 0.5 seconds on a standard PC to solve the coupled-equations.

In order to demonstrate the validity and efficiency of our results, we compare them with numerical calculations done using QuTiP [114], which is a software package that can solve the LME numerically (even for nonorthogonal quasimodes) by expanding operators in a Fock basis. In Fig. 5.2(b) we plot the quadrature noise in the first quasimode, $\langle Q_1^2 \rangle$, calculated using Eq. (5.14) and QuTiP. The quadrature noise is squeezed below the vacuum noise, $\langle Q_1^2 \rangle < 1$, for all times. In the plot, the oscillations in the noise shown in Eq. (5.14) are not evident, because the pump is resonant, such that the squeezing phase is approximately given by $\phi_1(t) \simeq -2\omega_P t - \pi$. The Fock basis results converge to the MSTS result when the number of Fock basis states in each quasimode is increased sufficiently. For our system, we see convergence for $t < 70d/(2\pi c)$ using 40 Fock states in each mode. With this number of states, the density operator is represented as a 1600×1600 matrix in the Fock basis, and thus one needs to solve as many as 2.56 million coupled equations (*i.e.*, one for each element of the density matrix). However, with our approach we only need to solve 6 equations. At $t = 70d/(2\pi c)$ there are about 3 total photons generated on average, and at $t = 100d/(2\pi c)$ there are 9.

Finally, we demonstrate that the non-zero overlap between the quasimodes in Eq. (5.15) has a significant effect on the quadrature squeezing. We do this by excluding the overlap between the two quasimodes, *i.e.* $O_{12} = O_{21} = 0$, while keeping all other values the same. This quantifies the effect that the overlap has on the results, but it is not intended to represent a physical situation for the structure. In Fig. 5.2(b) we plot $\langle Q_1^2 \rangle$ without the overlap (crosses); as can be seen, for $t = 100d/(2\pi c)$ there is an increase in the noise of 6.3 dB above the correct value.

In this section we have shown that 1) the numerical results using our method agree with those using a Fock basis, as long as enough states are included; 2) when the photon number becomes large, the simulations using a Fock basis take a prohibitively long time to run; and 3) our approach remains accurate and fast even when the effects of the mode nonorthogonality is large.

5.5 Conclusion

We have proven that the analytic solution to the LME for light generated by a nonlinearity in the quasimodes of a general multimode structure is the density operator for an MSTS, even when the mode nonorthogonality is included. Our approach can make it more feasible to study the important problem of nonlinear optical generation of entangled squeezed states in multimode lossy nanocavities, since the number of equations to solve depends only linearly on the total number of system modes. Our analytic solution opens up a path to investigate and optimize the generation and evolution of cluster states made from a general mixed Gaussian state.

Chapter 6

Squeezing criterion to generate any mixed Gaussian continuous-variable cluster state

In the previous chapters, I showed that the MSTS is the state produced by non-linear optics in lossy coupled-cavities. In this chapter, I show that the MSTS is an approximate CV cluster state, provided squeezing criterion (that I will derive) are obeyed. Recent work has showed that any squeezed vacuum state (a pure Gaussian state) can be considered a cluster state [101], however I believe this is the first time that a condition has been derived for a mixed Gaussian state to be considered a cluster state. This work is unpublished and is intended to be a regular chapter of this thesis.

6.1 Introduction

The cluster state was originally introduced as a maximally entangled state of qubits with a high persistency of entanglement [20]. It was shown that the cluster state contains all the entanglement necessary for any quantum computation, such that any quantum circuit can be imprinted on the cluster state by measuring the qubits in a particular basis and a particular order. Thus, a scheme of one-way, measurement-based quantum computation was presented consisting of doing single qubit measurements on the cluster state [19] and it was experimentally verified using a four-qubit cluster state [115].

S. Lloyd and S. L. Braunstein [102] extended quantum computation from qubits to CVs. They proved that for universal quantum computation with CVs, one only needs linear operations and a single nonlinear operation (such as photon counting). It was then shown that cluster states can be extended to CVs, where instead of the state being made from qubits, it is made from eigenstates of the quadrature operator [28]. Eigenstates of the quadrature operator are not physical, however an approximation to them are squeezed states that have a large but finite squeezing amplitude. Due to finite squeezing, the practical CV cluster states are only approximations of the ideal ones made with infinitely squeezed states. CV cluster states have the advantage that they are simple to create since they only require linear operations and photon counting, making them an experimentally viable option for quantum computing [102]. Although, one of the challenges with CV cluster states is the presence of finite squeezing and photon scattering noise, which leads to imperfect quantum computation [116]. However, a theoretical finite squeezing threshold of about 17dB has been established that the CV cluster state must obey in order for fault-tolerant quantum computation [42, 117].

An approximate CV cluster state can be written as a pure Gaussian state that has the form of an MSVS. Experimentally, there are mainly two methods to generate CV cluster states. The first method consists of generating a series of single-mode squeezed states (*e.g.* with an MRR), then entangling the modes with beamsplitters and phase shifters [105,118]. Collectively, these operations perform a multimode squeezing transformation on the vacuum that results in the MSVS. The second method generates the MSVS all at once using a nonlinear process in a resonant structure [106]. One method to nonlinearly generate the MSVS is to generate signal and idler photons with spontaneous four-wave mixing in the frequency comb of an MRR, where the quadratures of the ring-modes are entangled [109,119,120]. However, as I have shown in Chapters 4 and 5, nonlinear optics produces a MSTS, not an MSVS. Therefore, the theory of generating cluster states should incorporate *mixed Gaussian states* rather than pure Gaussian states.

Theoretically, it was recently shown that any multimode squeezing transformation on the *vacuum* creates a pure Gaussian cluster state [101]. These are approximate CV cluster states since they satisfy a nullifier equation in the limit of infinite squeezing. Using the nullifier equation it is possible to mathematically relate the squeezing parameters of the MSVS to the adjacency matrix of the cluster state [106]. This opens up the possibility of engineering the squeezing parameters of the MSVS to generate any cluster state.

There has been some preliminary work in the literature on how to generalize pure Gaussian cluster states to mixed Gaussian cluster states [34]. The idea is to replace the vacuum state with a thermal state, such that instead of the MSVS, one works with a MSTS. The MSTS also must satisfy a nullifier equation in the limit of infinite squeezing in order for it to be an approximate cluster state. However, it has not been proved yet if the MSTS does satisfy the nullifier equation for perfect squeezing, nor has a mathematical connection been derived between the parameters of the MSTS and the adjacency matrix of the cluster state. This is an important generalization, since the resonant structures that are used to generated the squeezed states that make the cluster state, are inherently lossy. Thus, the cluster state cannot be a pure state and it must be a mixed state. Also, when the scattering loss is included, the quadrature noise is increased and the amount of squeezing in the state is reduced. As we will show, the loss can prevent the state from satisfying the nullifier equation and thus prevent it from being characterized as a cluster state. Therefore, the loss should not be neglected when considered the practical use of CV cluster states.

In this chapter, I derive squeezing criterion that the MSTS must satisfy in order for it to be considered an approximate CV cluster state, I demonstrate that the MSTS can be generated with a linear optics circuit, and I derive the adjacency matrix for the cluster state, written in terms of the linear operations of the circuit.

6.2 M-mode squeezed thermal state

We consider a mixed Gaussian state with M modes. Let $\widehat{\boldsymbol{a}}^\dagger$ and $\widehat{\boldsymbol{a}}$ be $M \times 1$ column vectors

$$\widehat{\boldsymbol{a}}^\dagger \equiv \left(\widehat{a}_1^\dagger, \ldots, \widehat{a}_M^\dagger\right)^{\mathrm{T}}, \tag{6.1}$$

$$\widehat{\boldsymbol{a}} \equiv \left(\widehat{a}_1, \ldots, \widehat{a}_M\right)^{\mathrm{T}}, \tag{6.2}$$

where $\widehat{a}_m^\dagger$ and $\widehat{a}_m$ are the creation and annihilation operator for the mth mode, and $(\widehat{\boldsymbol{a}}^\dagger)^{\mathrm{T}}$ denotes the transpose of the vector. We assume that the modes are orthogonal, such that these operators satisfy the commutation relation $[\widehat{\boldsymbol{a}}, (\widehat{\boldsymbol{a}}^\dagger)^{\mathrm{T}}] = \mathbf{1}$, where $\mathbf{1}$ is the $M \times M$ identity matrix. For example, if the system that generates the MSTS has nonorthogonal quasimodes (as was the case in Chapter 5), then here $\widehat{a}_m^\dagger$ are the operators for the orthogonal symmetrized modes, that are linear combinations of the nonorthgonal quasimodes (see Eq. (D.24)). On the other hand, if the system has orthogonal quasimodes, then $\widehat{a}_m^\dagger$ are quasimode operators. The vector of quadrature operators are defined as $\widehat{\boldsymbol{Y}} \equiv \left(\widehat{Y}_1, \ldots, \widehat{Y}_M\right)^{\mathrm{T}}$ and $\widehat{\boldsymbol{X}} \equiv \left(\widehat{X}_1, \ldots, \widehat{X}_M\right)^{\mathrm{T}}$, where

$$\widehat{Y}_m = -i(\widehat{a}_m \mathrm{e}^{i\theta_m} - \widehat{a}_m^\dagger \mathrm{e}^{-i\theta_m}), \tag{6.3}$$

and

$$\widehat{X}_m = \widehat{a}_m \mathrm{e}^{i\theta_m} + \widehat{a}_m^\dagger \mathrm{e}^{-i\theta_m}, \tag{6.4}$$

are conjugate quadrature operators for the mth mode, where the phase θ_m is a real number parameter, and they satisfy the commutation relation $[\widehat{\boldsymbol{X}}, \widehat{\boldsymbol{Y}}^{\mathrm{T}}] = 2i\mathbf{1}$. We let the density operator for the mixed Gaussian state take the form of a squeezed, thermal state

$$\widehat{\rho} = \widehat{S}(\boldsymbol{z})\widehat{\rho}_{\mathrm{th}}(\boldsymbol{\beta})\widehat{S}^\dagger(\boldsymbol{z}), \tag{6.5}$$

where $\widehat{S}(\boldsymbol{z})$ is an M-mode squeezing operator defined by

$$\widehat{S}(\boldsymbol{z}) = \exp\left(\frac{\mathrm{z}}{2}\left(\widehat{\boldsymbol{a}}^\dagger\right)^{\mathrm{T}} \boldsymbol{z}\widehat{\boldsymbol{a}}^\dagger - \frac{\mathrm{z}}{2}\left(\widehat{\boldsymbol{a}}\right)^{\mathrm{T}} \boldsymbol{z}^\dagger\widehat{\boldsymbol{a}}\right), \tag{6.6}$$

where $\boldsymbol{z}$ is an $M \times M$ symmetric matrix ($\boldsymbol{z}^{\mathrm{T}} = \boldsymbol{z}$) of complex squeezing parameters, z is a real positive number that sets the squeezing strength, and $\widehat{\rho}_{\mathrm{th}}(\boldsymbol{\beta})$ is the density operator for a thermal state, defined by

$$\widehat{\rho}_{\mathrm{th}}(\boldsymbol{\beta}) = \frac{1}{\mathrm{Tr}\left(\exp\Big(-\left(\widehat{\boldsymbol{a}}^{\dagger}\right)^{\mathrm{T}}\boldsymbol{\beta}\widehat{\boldsymbol{a}}\Big)\right)}\exp\Big(-\left(\widehat{\boldsymbol{a}}^{\dagger}\right)^{\mathrm{T}}\boldsymbol{\beta}\widehat{\boldsymbol{a}}\Big), \tag{6.7}$$

where $\boldsymbol{\beta}$ is an $M \times M$ Hermitian matrix.

It is convenient to decompose the squeezing parameter matrix, $\boldsymbol{z}$, using the polar decomposition

$$\boldsymbol{z} = \boldsymbol{u}\mathrm{e}^{i\boldsymbol{\zeta}}, \tag{6.8}$$

where $\boldsymbol{u}$ is an $M \times M$ Hermitian matrix ($\boldsymbol{u}^{\mathrm{T}} = \boldsymbol{u}^{*}$) of squeezing amplitudes, and $\boldsymbol{\zeta}$ is an $M \times M$ real symmetric matrix ($\boldsymbol{\zeta}^{*} = \boldsymbol{\zeta}$ and $\boldsymbol{\zeta}^{\mathrm{T}} = \boldsymbol{\zeta}$) of squeezing phases.

In the next subsection we derive the conditions that the squeezed thermal state in Eq. (6.5) must obey in order for it to be a Gaussian cluster state.

6.3 Conditions for the mixed Gaussian state to be a Gaussian cluster state

A cluster state can be related to a weighted graph. Each node of the graph is assigned to a mode of the state. A real symmetric adjacency matrix, $\boldsymbol{A}$, gives the weights between the nodes of the graph, whose (m, n)th element is defined as the interaction strength between the modes m and n in the cluster state. For a given $\boldsymbol{A}$, the state with density operator $\widehat{\rho}$, that is parameterized by an overall squeezing strength z, is a cluster state only if its covariance matrix of the nullifier operator

$(\widehat{\boldsymbol{Y}} - \boldsymbol{A}\widehat{\boldsymbol{X}})$ goes to zero, in the limit of infinite z [34],

$$\lim_{\mathrm{z}\to\infty} \operatorname{cov}\left(\widehat{\boldsymbol{Y}} - \boldsymbol{A}\widehat{\boldsymbol{X}}\right) = 0. \tag{6.9}$$

The covariance of a vector operator $\widehat{\boldsymbol{O}}$ is defined as [34]

$$\operatorname{cov}\left(\widehat{\boldsymbol{O}}\right) \equiv \frac{1}{2}\left\langle \widehat{\boldsymbol{O}}\widehat{\boldsymbol{O}}^{\mathrm{T}} + \left(\widehat{\boldsymbol{O}}\widehat{\boldsymbol{O}}^{\mathrm{T}}\right)^{\mathrm{T}} \right\rangle. \tag{6.10}$$

The central result of this chapter is that the squeezed thermal state in Eq. (6.5) obeys the nullifier equation (Eq. (6.9)) and can be classified as an approximate CV cluster state, with adjacency matrix $\boldsymbol{A}$. As I will show, the nullifier equation (Eq. (6.9)) is satisfied only if the squeezing phases $\boldsymbol{\zeta}$ of the squeezing operator satisfy the equation

$$\mathrm{e}^{-i\boldsymbol{\zeta}} = \mathrm{e}^{i\boldsymbol{\theta}} \left(i\mathbf{1} - \boldsymbol{A}\right)^{-1} \left(i\mathbf{1} + \boldsymbol{A}\right) \mathrm{e}^{i\boldsymbol{\theta}}, \tag{6.11}$$

where $\boldsymbol{\theta} = \operatorname{diag}(\theta_1, \ldots, \theta_M)$, and if the following squeezing criterion are met

$$\lim_{\mathrm{z}\to\infty} \mathrm{e}^{-\mathrm{z}\boldsymbol{u}} \sqrt{2\boldsymbol{\eta}^{\mathrm{T}} + \mathbf{1}} = 0, \tag{6.12}$$

where

$$\boldsymbol{\eta}^{\mathrm{T}} \equiv \operatorname{Tr}\left((\widehat{\boldsymbol{a}}^{\dagger}\widehat{\boldsymbol{a}}^{\mathrm{T}})^{\mathrm{T}} \widehat{\rho}_{\mathrm{th}}(\boldsymbol{\beta}) \right), \tag{6.13}$$

is an $M \times M$ Hermitian matrix with thermal photon numbers along the diagonal (that quantify photon scattering loss) and the nonzero off-diagonal elements are due to coupling between the modes. The limit in Eq. (6.12) is not trivial to evaluate, because both $\boldsymbol{u}$ and $\boldsymbol{\eta}$ have nontrivial dependence on z. As z → ∞, the noise is squeezed by the factor $\mathrm{e}^{-\mathrm{z}\boldsymbol{u}}$ and simultaneously increased by the thermal noise factor $(2\boldsymbol{\eta}^{\mathrm{T}}+\mathbf{1})$. Thus, the noise will approach zero only if the squeezing factor can overcome the thermal noise.

Now I will prove the central result in Eq. (6.11). It is useful to express the nullifier operator in terms of the mode operators instead. Let

$$\widehat{\boldsymbol{v}} \equiv \begin{pmatrix} \widehat{\boldsymbol{a}} \\ \widehat{\boldsymbol{a}}^{\dagger} \end{pmatrix}, \tag{6.14}$$

such that the nullifier operator can be written as

$$\widehat{\boldsymbol{Y}} - \boldsymbol{A}\widehat{\boldsymbol{X}} = \boldsymbol{Q}\widehat{\boldsymbol{v}}, \tag{6.15}$$

where the matrix $\boldsymbol{Q}$ is defined by

$$\boldsymbol{Q} \equiv \left(-i\mathrm{e}^{i\boldsymbol{\theta}} - \boldsymbol{A}\mathrm{e}^{i\boldsymbol{\theta}}, i\mathrm{e}^{-i\boldsymbol{\theta}} - \boldsymbol{A}\mathrm{e}^{-i\boldsymbol{\theta}}\right). \tag{6.16}$$

Taking the covariance of Eq. (6.15) with $\widehat{\rho}$ in Eq. (6.5), we obtain [34]

$$\mathrm{cov}(\widehat{\boldsymbol{Y}} - \boldsymbol{A}\widehat{\boldsymbol{X}}) = \boldsymbol{Q}\mathrm{Tr}\left(\widehat{S}^{\dagger}(\boldsymbol{z})\frac{\widehat{\boldsymbol{v}}\widehat{\boldsymbol{v}}^{\mathrm{T}} + (\widehat{\boldsymbol{v}}\widehat{\boldsymbol{v}}^{\mathrm{T}})^{\mathrm{T}}}{2}\widehat{S}(\boldsymbol{z})\widehat{\rho}_{\mathrm{th}}(\boldsymbol{\beta})\right)\boldsymbol{Q}^{\mathrm{T}}. \tag{6.17}$$

The squeezing transformation of the $\widehat{\boldsymbol{v}}$ operators is [25]

$$\widehat{S}^{\dagger}(\boldsymbol{z})\widehat{\boldsymbol{v}}\widehat{S}(\boldsymbol{z}) = \boldsymbol{B}\widehat{\boldsymbol{v}}, \tag{6.18}$$

where

$$\boldsymbol{B} \equiv \begin{pmatrix} \cosh(\mathrm{z}\boldsymbol{u}) & \sinh(\mathrm{z}\boldsymbol{u})\mathrm{e}^{i\boldsymbol{\zeta}} \\ \sinh(\mathrm{z}\boldsymbol{u}^{*})\mathrm{e}^{-i\boldsymbol{\zeta}} & \cosh(\mathrm{z}\boldsymbol{u}^{*}) \end{pmatrix}. \tag{6.19}$$

Putting Eq. (6.18) into Eq. (6.17), we obtain

$$\mathrm{cov}(\widehat{\boldsymbol{Y}} - \boldsymbol{A}\widehat{\boldsymbol{X}}) = \frac{1}{2}\boldsymbol{Q}\boldsymbol{B}\boldsymbol{K}\boldsymbol{B}^{\mathrm{T}}\boldsymbol{Q}^{\mathrm{T}}, \tag{6.20}$$

where $\boldsymbol{K}$ is a symmetric matrix related to the photon scattering loss, given by

$$\boldsymbol{K} = \begin{pmatrix} \boldsymbol{0} & 2\boldsymbol{\eta}^{\mathrm{T}} + \boldsymbol{1} \\ 2\boldsymbol{\eta} + \boldsymbol{1} & \boldsymbol{0} \end{pmatrix}. \tag{6.21}$$

To show that the covariance given in Eq. (6.20) goes to zero as $\mathrm{z} \to \infty$, define

$$\boldsymbol{Q}\boldsymbol{B} \equiv (\boldsymbol{F}, \boldsymbol{F}^{*}), \tag{6.22}$$

where

$$\begin{aligned} \boldsymbol{F} &\equiv -(i\boldsymbol{1} + \boldsymbol{A})\mathrm{e}^{i\boldsymbol{\theta}}\cosh(\mathrm{z}\boldsymbol{u}) + (i\boldsymbol{1} - \boldsymbol{A})\mathrm{e}^{-i\boldsymbol{\theta}}\sinh(\mathrm{z}\boldsymbol{u}^{*})\mathrm{e}^{-i\boldsymbol{\zeta}} \\ &= -(i\boldsymbol{1} + \boldsymbol{A})\mathrm{e}^{i\boldsymbol{\theta}}\cosh(\mathrm{z}\boldsymbol{u}) + (i\boldsymbol{1} - \boldsymbol{A})\mathrm{e}^{-i\boldsymbol{\theta}}\mathrm{e}^{-i\boldsymbol{\zeta}}\sinh(\mathrm{z}\boldsymbol{u}), \end{aligned} \tag{6.23}$$

where to get the last line we used the fact that $\boldsymbol{u}^{*}\exp(-i\boldsymbol{\zeta}) = \exp(-i\boldsymbol{\zeta})\boldsymbol{u}$ [25], which follows from $\boldsymbol{z}$ being symmetric, and $\boldsymbol{u}$ and and $\boldsymbol{\zeta}$ being Hermitian. Expanding the hyperbolic functions as, $\cosh(\mathrm{z}\boldsymbol{u}) = (\exp(\mathrm{z}\boldsymbol{u}) + \exp(-\mathrm{z}\boldsymbol{u}))/2$ and $\sinh(\mathrm{z}\boldsymbol{u}) =$

$(\exp(\mathrm{z}\boldsymbol{u}) - \exp(-\mathrm{z}\boldsymbol{u}))/2$, and putting these into Eq. (6.23), we obtain

$$\begin{aligned}\boldsymbol{F} &= -\frac{1}{2}(i\mathbf{1}+\boldsymbol{A})\mathrm{e}^{i\boldsymbol{\theta}}(\mathrm{e}^{\mathrm{z}\boldsymbol{u}}+\mathrm{e}^{-\mathrm{z}\boldsymbol{u}}) + \frac{1}{2}(i\mathbf{1}-\boldsymbol{A})\mathrm{e}^{-i\boldsymbol{\theta}}\mathrm{e}^{-i\boldsymbol{\zeta}}(\mathrm{e}^{\mathrm{z}\boldsymbol{u}}-\mathrm{e}^{-\mathrm{z}\boldsymbol{u}})\\ &= \frac{1}{2}\left((i\mathbf{1}-\boldsymbol{A})\mathrm{e}^{-i\boldsymbol{\theta}}\mathrm{e}^{-i\boldsymbol{\zeta}} - (i\mathbf{1}+\boldsymbol{A})\mathrm{e}^{i\boldsymbol{\theta}}\right)\mathrm{e}^{\mathrm{z}\boldsymbol{u}} - \frac{1}{2}\left((i\mathbf{1}-\boldsymbol{A})\mathrm{e}^{-i\boldsymbol{\theta}}\mathrm{e}^{-i\boldsymbol{\zeta}} + (i\mathbf{1}+\boldsymbol{A})\mathrm{e}^{i\boldsymbol{\theta}}\right)\mathrm{e}^{-\mathrm{z}\boldsymbol{u}}.\end{aligned} \tag{6.24}$$

Therefore, Eq. (6.20) can be written as

$$\begin{aligned}\mathrm{cov}(\widehat{\boldsymbol{Y}} - \boldsymbol{A}\widehat{\boldsymbol{X}}) &= \frac{1}{2}\boldsymbol{F}(2\boldsymbol{\eta}^{\mathrm{T}}+\mathbf{1})\boldsymbol{F}^{\dagger} + \frac{1}{2}\left(\boldsymbol{F}(2\boldsymbol{\eta}^{\mathrm{T}}+\mathbf{1})\boldsymbol{F}^{\dagger}\right)^{\mathrm{T}}\\ &= \frac{1}{2}\boldsymbol{F}\sqrt{2\boldsymbol{\eta}^{\mathrm{T}}+\mathbf{1}}\left(\boldsymbol{F}\sqrt{2\boldsymbol{\eta}^{\mathrm{T}}+\mathbf{1}}\right)^{\dagger} + (\text{transpose}),\end{aligned} \tag{6.25}$$

where we used the fact that $(\boldsymbol{\eta}^{\mathrm{T}})^{\dagger} = \boldsymbol{\eta}^{\mathrm{T}}$. Therefore, the equivalent requirement of Eq. (6.9) for $\widehat{\rho}$ to be a cluster state is

$$\lim_{\mathrm{z}\to\infty} \boldsymbol{F}\sqrt{2\boldsymbol{\eta}^{\mathrm{T}}+\mathbf{1}} = 0. \tag{6.26}$$

Putting Eq. (6.24) into Eq. (6.26), there are two terms in Eq. (6.26) that both need to approach zero. The first term is

$$\left((i\mathbf{1}-\boldsymbol{A})\mathrm{e}^{-i\boldsymbol{\theta}}\mathrm{e}^{-i\boldsymbol{\zeta}} - (i\mathbf{1}+\boldsymbol{A})\mathrm{e}^{i\boldsymbol{\theta}}\right)\lim_{\mathrm{z}\to\infty}\mathrm{e}^{\mathrm{z}\boldsymbol{u}}\sqrt{2\boldsymbol{\eta}^{\mathrm{T}}+\mathbf{1}} = 0, \tag{6.27}$$

which does not approach zero as $\mathrm{z} \to \infty$ because of the exponential factor $\mathrm{e}^{\mathrm{z}\boldsymbol{u}}$. Thus, we force Eq. (6.27) to be zero by making the matrix multiplying the limit $\left((i\mathbf{1}-\boldsymbol{A})\mathrm{e}^{-i\boldsymbol{\theta}}\mathrm{e}^{-i\boldsymbol{\zeta}} - (i\mathbf{1}+\boldsymbol{A})\mathrm{e}^{i\boldsymbol{\theta}}\right)$ be equal to the null matrix $\mathbf{0}$, which is achieved by requiring that $\boldsymbol{\zeta}$ satisfies Eq. (6.11). The second term in Eq. (6.26) is

$$\left((i\mathbf{1}-\boldsymbol{A})\mathrm{e}^{-i\boldsymbol{\theta}}\mathrm{e}^{-i\boldsymbol{\zeta}}+(i\mathbf{1}+\boldsymbol{A})\mathrm{e}^{i\boldsymbol{\theta}}\right)\lim_{\mathrm{z}\to\infty}\mathrm{e}^{-z\boldsymbol{u}}\sqrt{2\boldsymbol{\eta}^{\mathrm{T}}+\mathbf{1}}=0, \tag{6.28}$$

which approaches zero only if the squeezing criterion in Eq. (6.12) are satisfied. Therefore, we have proven that $\widehat{\rho}$ is a Gaussian cluster state only if it satisfies Eqs. (6.11) and (6.12).

6.4 Cluster state for a given multimode squeezed thermal state

For a given multimode squeezed thermal state (Eq. (6.5)), Eq. (6.11) can be inverted to solve for the adjacency matrix $\boldsymbol{A}$ for the cluster state in terms of the squeezing phases $\boldsymbol{\zeta}$ and phases $\boldsymbol{\theta}$

$$\boldsymbol{A}=-i\left(\mathbf{1}-\mathrm{e}^{-i\boldsymbol{\theta}}\mathrm{e}^{-i\boldsymbol{\zeta}}\mathrm{e}^{-i\boldsymbol{\theta}}\right)\left(\mathbf{1}+\mathrm{e}^{-i\boldsymbol{\theta}}\mathrm{e}^{-i\boldsymbol{\zeta}}\mathrm{e}^{-i\boldsymbol{\theta}}\right)^{-1}. \tag{6.29}$$

Since $\exp(-i\boldsymbol{\theta})\exp(-i\boldsymbol{\zeta})\exp(-i\boldsymbol{\theta})$ is a unitary matrix, it can be written as $\exp(i\boldsymbol{\kappa})$, where $\boldsymbol{\kappa}$ is a real symmetric matrix. Putting this into Eq. (6.29), results in

$$\begin{aligned}\boldsymbol{A}&=-i\left(\mathbf{1}-\mathrm{e}^{i\boldsymbol{\kappa}}\right)\left(\mathbf{1}+\mathrm{e}^{i\boldsymbol{\kappa}}\right)^{-1}\\&=\sin(\boldsymbol{\kappa}/2)\left(\cos(\boldsymbol{\kappa}/2)\right)^{-1},\end{aligned} \tag{6.30}$$

which shows that the adjacency matrix is real.

In Chapter 4, we showed that the multimode squeezed thermal state can be produced via nonlinear optics, and we derived coupled-equations for the squeezing amplitudes, squeezing phases, and thermal photon numbers for the state (see Eqs. (4.69)

- (4.71)). From the solution of these equations, the squeezing phases of the state can be obtained, and putting them into Eq. (6.29) the adjacency matrix for the resulting cluster state is obtained. Therefore, the cluster state can be generated all at once with a nonlinear interaction, and its adjacency matrix (given in Eq. (6.29)) can be calculated using the MSTS squeezing phases obtained from solving Eqs. (4.69) - (4.71). In the next section, I show that the cluster state can be alternatively generated using a linear optics circuit.

6.5 Generating a cluster state with a linear optics circuit

In this section, I consider the generation of an M-mode cluster state using a linear optics circuit. Typically, the theoretical input state to the circuit is a set of uncoupled single-mode squeezed vacuum states. However, I consider the input state to be M uncoupled single-mode squeezed thermal states. Using a circuit consisting of linear operations such as beam splitters and phase shifters the single-mode squeezed thermal states are subsequently mixed and the output state of the circuit contains correlations between the quadratures of the modes. There are a set of M uncoupled input ports to the circuit and in each input port a single-mode squeezed thermal state is injected. The separable input state can be written as a product of M single-mode squeezed thermal states, defined as

$$\begin{aligned}\widehat{\rho}_{\text{in}} &= \prod_{\mu=1}^{M} \exp\Big(\frac{\mathrm{z}}{2} r_\mu \left(\mathrm{e}^{i\phi_\mu} \widehat{B}_\mu^{\dagger 2} - \mathrm{e}^{-i\phi_\mu} \widehat{B}_\mu^{2}\right)\Big) \frac{1}{\mathcal{Z}} \exp\Big(-\widetilde{\beta}_\mu \widehat{B}_\mu^\dagger \widehat{B}_\mu\Big) \exp\Big(-\frac{\mathrm{z}}{2} r_\mu \left(\mathrm{e}^{i\phi_\mu} \widehat{B}_\mu^{\dagger 2} - \mathrm{e}^{-i\phi_\mu} \widehat{B}_\mu^{2}\right)\Big) \\ &= \exp\Big(\frac{\mathrm{z}}{2} \left((\widehat{\boldsymbol{B}}^\dagger)^{\mathrm{T}} \boldsymbol{r} \mathrm{e}^{i\boldsymbol{\phi}} \widehat{\boldsymbol{B}}^\dagger - \widehat{\boldsymbol{B}}^{\mathrm{T}} \boldsymbol{r} \mathrm{e}^{-i\boldsymbol{\phi}} \widehat{\boldsymbol{B}}\right)\Big) \frac{1}{\mathcal{Z}} \exp\Big(-\widehat{\boldsymbol{B}}^{\dagger \mathrm{T}} \widetilde{\boldsymbol{\beta}} \widehat{\boldsymbol{B}}\Big) \\ &\times \exp\Big(-\frac{\mathrm{z}}{2} \left((\widehat{\boldsymbol{B}}^\dagger)^{\mathrm{T}} \boldsymbol{r} \mathrm{e}^{i\boldsymbol{\phi}} \widehat{\boldsymbol{B}}^\dagger - \widehat{\boldsymbol{B}}^{\mathrm{T}} \boldsymbol{r} \mathrm{e}^{-i\boldsymbol{\phi}} \widehat{\boldsymbol{B}}\right)\Big), \end{aligned} \tag{6.31}$$

where $\widehat{B_\mu}$ destroys a photon in the port μ, r_μ and ϕ_μ are the squeezing amplitude and squeezing phase for the port μ, $\mathcal{Z}$ is a normalization constant (partition function) for the thermal state density operator, and $\widetilde{\beta}_\mu$ is real parameter that is related to the thermal photon number for the input port μ, n_μ, given by

$$n_\mu = \left(\exp\left(\widetilde{\beta}_\mu\right) - 1\right)^{-1}. \tag{6.32}$$

In Eq. (6.31), $\boldsymbol{r} = \mathrm{diag}(r_1, \ldots, r_M)$ and $\boldsymbol{\phi} = \mathrm{diag}(\phi_1, \ldots, \phi_M)$ are real diagonal matrices. There are M output ports at the output of the circuit. It is assumed that the destruction operators for each output port, $\widehat{a}_m$, are related to the input operators $\widehat{B}_\mu$ by the unitary transformation, $\boldsymbol{U}$, that is enacted by the circuit. Thus, the vector of output operators $\widehat{\boldsymbol{a}}$ can be written as

$$\widehat{\boldsymbol{a}} = \boldsymbol{U}\widehat{\boldsymbol{B}}, \tag{6.33}$$

where $\boldsymbol{U}^\dagger\boldsymbol{U} = \mathbf{1}$. In Fig. 6.1 we show an illustration of the linear optics circuit. The horizontal black lines represent the input and output modes to the circuit, $\widehat{\boldsymbol{B}}$ and $\widehat{\boldsymbol{a}}$, respectively. The rectangle represents a sequence of beamsplitters and phase shifters that perform a unitary transformation $\boldsymbol{U}$ on the input modes.

Putting Eq. (6.33) into Eq. (6.31), the output density operator is given by

$$\widehat{\rho}_{\mathrm{out}} = \exp\Big(\frac{\mathrm{z}}{2}\left(\widehat{\boldsymbol{a}}^\dagger\right)^{\mathrm{T}}\boldsymbol{z}\widehat{\boldsymbol{a}}^\dagger - \frac{\mathrm{z}}{2}\left(\widehat{\boldsymbol{a}}\right)^{\mathrm{T}}\boldsymbol{z}^\dagger\widehat{\boldsymbol{a}}\Big)\frac{1}{\mathcal{Z}}\exp\left(-\widehat{\boldsymbol{a}}^{\dagger\mathrm{T}}\boldsymbol{\beta}\widehat{\boldsymbol{a}}\right)\exp\Big(-\frac{\mathrm{z}}{2}\left(\widehat{\boldsymbol{a}}^\dagger\right)^{\mathrm{T}}\boldsymbol{z}\widehat{\boldsymbol{a}}^\dagger - \frac{\mathrm{z}}{2}\left(\widehat{\boldsymbol{a}}\right)^{\mathrm{T}}\boldsymbol{z}^\dagger\widehat{\boldsymbol{a}}\Big), \tag{6.34}$$

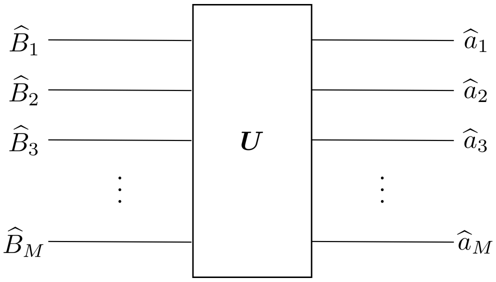

Figure 6.1: Illustration of a linear optics circuit, $\boldsymbol{U}$, that transforms the M input modes $\widehat{B}_\mu$ to the M output modes $\widehat{a}_m$.

where

$$\boldsymbol{z} = \boldsymbol{U}\boldsymbol{r}\mathrm{e}^{i\boldsymbol{\phi}}\boldsymbol{U}^{\mathrm{T}}. \tag{6.35}$$

and

$$\boldsymbol{\beta} = \boldsymbol{U}\widetilde{\boldsymbol{\beta}}\boldsymbol{U}^{\dagger} \tag{6.36}$$

Since $\boldsymbol{z}$ and $\boldsymbol{\beta}$ are nondiagonal matrices the output state $\widehat{\rho}_{\text{out}}$ is inseparable to some degree and it will contain correlations between the quadratures of the different output ports. The output state $\widehat{\rho}_{\text{out}}$ has the same form as the density operator in Eq. (6.5) and thus the same squeezing criterion that we derived in Eq. (6.12) can be used on $\widehat{\rho}_{\text{out}}$ to test if it is a cluster state. Therefore if $\widehat{\rho}_{\text{out}}$ satisfies the squeezing criterion in Eq. (6.12) then it is a cluster state.

The squeezing criterion is written in terms of the squeezing amplitudes $\boldsymbol{u}$ and squeezing phases $\boldsymbol{\zeta}$, that were obtained from the polar decomposition of $\boldsymbol{z}$ (*i.e.*, $\boldsymbol{z} = \boldsymbol{u}\exp(i\boldsymbol{\zeta})$). We can relate $\boldsymbol{u}$ to the input squeezing amplitudes $\boldsymbol{r}$, and $\boldsymbol{\zeta}$ to the input squeezing phases $\boldsymbol{\phi}$ using

$$\boldsymbol{u} = \boldsymbol{U}\boldsymbol{r}\boldsymbol{U}^{\dagger}, \tag{6.37}$$

and

$$\mathrm{e}^{i\boldsymbol{\zeta}} = \boldsymbol{U}\mathrm{e}^{i\boldsymbol{\phi}}\boldsymbol{U}^{\mathrm{T}}, \tag{6.38}$$

such that with these choices, the polar decomposition of $\boldsymbol{z}$ and its symmetric singular value decomposition in Eq. (6.35) are equivalent. Putting Eq. (6.37) into the squeezing criterion in Eq. (6.12) results in

$$\lim_{\mathrm{z}\to\infty} \mathrm{e}^{-\mathrm{z}\boldsymbol{U}\boldsymbol{r}\boldsymbol{U}^{\dagger}} \sqrt{2\boldsymbol{\eta}^{\mathrm{T}} + \mathbf{1}} = 0. \tag{6.39}$$

The exponential in Eq. (6.39) can be written as

$$\begin{aligned}
\mathrm{e}^{-\mathrm{z}\boldsymbol{U}\boldsymbol{r}\boldsymbol{U}^{\dagger}} &= \sum_{n=0}^{\infty} \frac{(-1)^n}{n!} \left(\boldsymbol{U}\mathrm{z}\boldsymbol{r}\boldsymbol{U}^{\dagger}\right)^n \\
&= \boldsymbol{U} \sum_{n=0}^{\infty} \frac{(-\mathrm{z}\boldsymbol{r})^n}{n!} \boldsymbol{U}^{\dagger} \\
&= \boldsymbol{U}\mathrm{e}^{-\mathrm{z}\boldsymbol{r}}\boldsymbol{U}^{\dagger},
\end{aligned} \tag{6.40}$$

where I have used the fact that $\boldsymbol{U}\boldsymbol{U}^{\dagger} = \mathbf{1}$. Putting Eq. (6.40) into Eq. (6.39) results in

$$\boldsymbol{U} \lim_{\mathrm{z}\to\infty} \mathrm{e}^{-\mathrm{z}\boldsymbol{r}}\boldsymbol{U}^{\dagger}\sqrt{2\boldsymbol{\eta}^{\mathrm{T}} + \mathbf{1}} = 0, \tag{6.41}$$

where the matrix $\boldsymbol{U}$ was put in front of the limit, since it does not depend on z. Multiplying Eq. (6.41) from the left with $\boldsymbol{U}^\dagger$ and from the right with $\boldsymbol{U}$ results in

$$\lim_{\mathrm{z}\to\infty} \mathrm{e}^{-\mathrm{z}\boldsymbol{r}} \boldsymbol{U}^\dagger \sqrt{2\boldsymbol{\eta}^{\mathrm{T}} + \boldsymbol{1}}\boldsymbol{U} = 0, \tag{6.42}$$

where I have used the fact that $\boldsymbol{U}\boldsymbol{U}^\dagger = \boldsymbol{1}$. To simplify the square-root factor in Eq. (6.42), consider its square

$$\begin{aligned} \left(\boldsymbol{U}^\dagger \sqrt{2\boldsymbol{\eta}^{\mathrm{T}} + \boldsymbol{1}}\boldsymbol{U}\right)^2 &= \boldsymbol{U}^\dagger \left(2\boldsymbol{\eta}^{\mathrm{T}} + \boldsymbol{1}\right)\boldsymbol{U} \\ &= 2\boldsymbol{U}^\dagger\boldsymbol{\eta}^{\mathrm{T}}\boldsymbol{U} + \boldsymbol{1}, \end{aligned} \tag{6.43}$$

Putting Eq. (6.43) into Eq. (6.42) results in

$$\lim_{\mathrm{z}\to\infty} \mathrm{e}^{-\mathrm{z}\boldsymbol{r}} \sqrt{2\boldsymbol{n} + \boldsymbol{1}} = 0, \tag{6.44}$$

where $\boldsymbol{n}$ is simply a diagonal matrix of the thermal photon numbers for the input ports, defined by

$$\begin{aligned} \boldsymbol{n} &\equiv \boldsymbol{U}^\dagger\boldsymbol{\eta}^{\mathrm{T}}\boldsymbol{U} \\ &= \frac{1}{\mathcal{Z}} \mathrm{Tr}\left((\widehat{\boldsymbol{B}}^\dagger \widehat{\boldsymbol{B}}^{\mathrm{T}})^{\mathrm{T}} \exp\left(-\widehat{\boldsymbol{B}}^{\dagger\mathrm{T}} \widetilde{\boldsymbol{\beta}} \widehat{\boldsymbol{B}}\right)\right). \end{aligned} \tag{6.45}$$

Note that Eq. (6.45) is a diagonal matrix because the off-diagonal elements, such as $\mathrm{Tr}\left(\widehat{B}_1^\dagger \widehat{B}_2 \exp\left(-\widehat{\boldsymbol{B}}^{\dagger\mathrm{T}} \widetilde{\boldsymbol{\beta}} \widehat{\boldsymbol{B}}\right)\right)$, are zero.

The squeezing criterion in Eq. (6.44) is the the same as requiring that the quadrature noise in each input port μ is sufficiently squeezed. To show this connection, I define the quadrature operator for the input port μ as

$$\widehat{X}_\mu \equiv \widehat{B}_\mu \mathrm{e}^{-i\phi_\mu/2} + \widehat{B}_\mu^\dagger \mathrm{e}^{i\phi_\mu/2}. \tag{6.46}$$

It can be shown using Eq. (1.8), that the quadrature noise in $\widehat{X}_\mu$ using $\widehat{\rho}_{\text{in}}$ in Eq. (6.31) is given by

$$(\Delta X_\mu)^2 = \mathrm{e}^{-2r_\mu}\left(2n_\mu + 1\right). \tag{6.47}$$

Taking the limit of Eq. (6.47) as r_μ goes to infinity, for all μ, gives the same criterion as Eq. (6.44). That is, if the quadrature noise in the input port μ satisfies the condition

$$\lim_{r_\mu \to \infty} \Delta X_\mu = 0 \quad \text{for all } \mu, \tag{6.48}$$

then the output state $\widehat{\rho}_{\text{out}}$ is a cluster state. Remarkably, one only needs to check that the quadrature noise is sufficiently squeezed at each input port in order to show that the output state is a valid cluster state. There is no measurement of the output state required at the output ports to determine if it is a cluster state.

Assuming that the criterion in Eq. (6.48) are satisfied, the adjacency matrix, $\boldsymbol{A}$, for the cluster state at the output can be written in terms of $\boldsymbol{U}$ and $\boldsymbol{\phi}$. Putting Eq. (6.38) into Eq. (6.29) we obtain

$$\boldsymbol{A} = -i\left(\boldsymbol{1} - \mathrm{e}^{-i\boldsymbol{\theta}}\boldsymbol{U}^*\mathrm{e}^{-i\boldsymbol{\phi}}\boldsymbol{U}^\dagger\mathrm{e}^{-i\boldsymbol{\theta}}\right)\left(\boldsymbol{1} + \mathrm{e}^{-i\boldsymbol{\theta}}\boldsymbol{U}^*\mathrm{e}^{-i\boldsymbol{\phi}}\boldsymbol{U}^\dagger\mathrm{e}^{-i\boldsymbol{\theta}}\right)^{-1}. \tag{6.49}$$

Any linear optics circuit $\boldsymbol{U}$ can be put into Eq. (6.49) to obtain the resulting $\boldsymbol{A}$ for the cluster state at the output of the circuit. There can be many different circuits $\boldsymbol{U}$ that produce the same $\boldsymbol{A}$. It was proved by M. Reck and A. Zeillinger [121] that any $M \times M$ unitary transformation $\boldsymbol{U}$ can be constructed experimentally with a sequence of at most $M(M-1)/2$ general beamsplitter transformations. It is difficult to work out analytically what the phase and reflectivity of each beamsplitter in the sequence should be in order to produce a particular $\boldsymbol{U}$. However, the decomposition of $\boldsymbol{U}$ into the correct sequence of operations can be guessed for simple circuits or obtained algorithmically in more complex circuits. In the following subsections, we give examples of the adjacency matrix obtained with Eq. (6.49) for 2- and 4-mode cluster states that are made using simple circuits of 50/50 beamsplitters and phase shifters.

6.5.1 2-mode cluster state

In this subsection, I show that the adjacency matrix of a 2-mode cluster state can be created with a circuit consisting of a beamsplitter and two phase shifters on the second mode. An illustration of the circuit is shown in Fig. 6.2(a) and the resulting cluster state graph representation in Fig. 6.2(b).

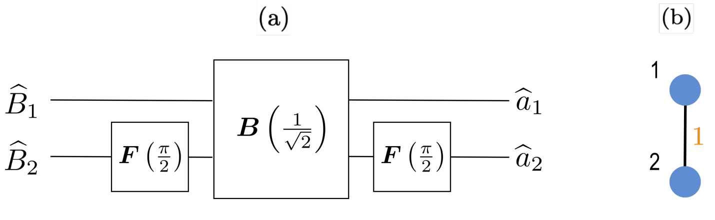

Figure 6.2:]
(a) Illustration of a linear optics circuit consisting of two $\pi/2$ phase shifters $\boldsymbol{F}(\pi/2)$ that act on the second mode and a 50/50 beamsplitter $\boldsymbol{B}(1/\sqrt{2})$, and (b) a graph that illustrates the adjacency matrix for the output 2-mode cluster state made by the circuit, with a single edge of weight 1 connecting the two nodes of the graph.

The input state to the circuit, $\widehat{\rho}_{\text{in}}$, is a product of two single-mode squeezed thermal states (one for each of the two input ports), which is obtained by letting $M = 2$ in Eq. (6.31). For simplicity we assume that the squeezing amplitudes and squeezing phases of both squeezing operators are equal, $r_1 = r_2 = r$ and $\phi_1 = \phi_2 = \phi$. The thermal photon numbers for the two input ports are n_1 and n_2, respectively.

The circuit $\boldsymbol{U}(2)$ can be decomposed as

$$\boldsymbol{U}(2) = \boldsymbol{F}_2\left(\frac{\pi}{2}\right)\boldsymbol{B}_{12}\left(\frac{1}{\sqrt{2}}\right)\boldsymbol{F}_2\left(\frac{\pi}{2}\right), \tag{6.50}$$

where the $\pi/2$ phase shifter transformation of the second mode is given by

$$\boldsymbol{F}_2\left(\frac{\pi}{2}\right) = \begin{pmatrix} 1 & 0 \\ 0 & i \end{pmatrix}, \tag{6.51}$$

and the beam splitter transformation is given by

$$\boldsymbol{B}_{12}\left(\frac{1}{\sqrt{2}}\right) = \frac{1}{\sqrt{2}}\begin{pmatrix} 1 & 1 \\ 1 & -1 \end{pmatrix}. \tag{6.52}$$

The beamsplitter mixes the two single-mode squeezed thermal states, effectively creating correlations between their quadratures. Putting Eqs. (6.51) and (6.52) into Eq. (6.50), $\boldsymbol{U}(2)$ can be written as

$$\boldsymbol{U}(2) = \frac{1}{\sqrt{2}}\begin{pmatrix} 1 & i \\ i & 1 \end{pmatrix}. \tag{6.53}$$

Now I put Eq. (6.53) into Eq. (6.49) to obtain the adjacency matrix $\boldsymbol{A}$ for the circuit

$\boldsymbol{U}(2)$. Doing this, we obtain

$$\boldsymbol{A} = \begin{pmatrix} 0 & 1 \\ 1 & 0 \end{pmatrix}. \tag{6.54}$$

In Fig. 6.2(b) we show a graph representation of the cluster state created by $\boldsymbol{U}(2)$. The weight of the edge connecting node 1 and node 2 is given by the element A_{12} in the adjacency matrix in Eq. (6.54). The phases θ_1 and θ_2 are applied to the output modes $\widehat{a}_1$ and $\widehat{a}_2$, repsectively, and they are parameters that can be freely chosen. To obtain the adjacency matrix in Eq. (6.54) we chose $\theta_1 = \theta_2 = -\phi$, such that all the phases in Eq. (6.49) cancel.

The output state of the circuit, $\widehat{\rho}_{\mathrm{out}}$, is given by letting $M = 2$ in Eq. (6.34). The squeezing parameter matrix $\boldsymbol{z}$ for the squeezing operator in $\widehat{\rho}_{\mathrm{out}}$ is obtained by putting Eq. (6.53) into Eq. (6.35). Doing this, I obtain

$$\boldsymbol{z} = ir\mathrm{e}^{i\phi}\boldsymbol{A}, \tag{6.55}$$

which gives the two-mode squeezing operator $\exp\Big(i(r/2)\mathrm{e}^{i\phi}\widehat{a}_1^\dagger\widehat{a}_2^\dagger - \mathrm{H.c.}\Big)$. Both diagonal elements of $\boldsymbol{A}$ are zero, which means that there is no self-coupling in the squeezing operator. For this simple circuit, the squeezing amplitude for the output state is simply proportional to the adjacency matrix. The thermal photon matrix, $\boldsymbol{\eta}$ in Eq. (6.13), for the output state is obtained by putting Eq. (6.53) into Eq. (6.45)

$$\boldsymbol{\eta} = \frac{1}{2}\begin{pmatrix} n_1 + n_2 & i(n_1 - n_2) \\ -i(n_1 - n_2) & n_1 + n_2 \end{pmatrix}. \tag{6.56}$$

The diagonal elements in Eq. (6.56) are the thermal photon numbers for each output port, which shows that the number of thermal photons at both output ports is the average of the thermal photon numbers for the input ports. The off-diagonal elements are proportional to the difference of the input photon numbers and they capture the coupling between the thermal noise of each output port. When the thermal photon numbers at the input are equal $n_1 = n_2$, then the thermal noises at the two output ports are not coupled.

6.5.2 4-mode cluster state

In this subsection, I show that the adjacency matrix of a 4-mode cluster state can be created using the circuit shown in Fig. 6.2(a). The resulting graph representation of the cluster state is shown in Fig. 6.2(b).

The input state to the circuit, $\widehat{\rho}_{\text{in}}$, is a product of four single-mode squeezed thermal states (one for each of the four input ports), which is obtained by letting $M = 4$ in Eq. (6.31). For simplicity we assume that the squeezing amplitudes and squeezing phases of all four squeezing operators are equal and each of them are given by r and ϕ, respectively ($\boldsymbol{r} = r\mathbf{1}$ and $\boldsymbol{\phi} = \phi\mathbf{1}$). The thermal photon numbers for the four input ports are allowed to be different.

The circuit $\boldsymbol{U}(4)$ can be decomposed as

$$\begin{aligned}\boldsymbol{U}(4) = &\left[\boldsymbol{F}_4\left(\frac{\pi}{2}\right)\boldsymbol{B}_{24}\left(\frac{1}{\sqrt{2}}\right)\boldsymbol{F}_4\left(\frac{\pi}{2}\right)\right]\left[\boldsymbol{F}_3\left(\frac{\pi}{2}\right)\boldsymbol{B}_{23}\left(\frac{1}{\sqrt{2}}\right)\boldsymbol{F}_3\left(\frac{\pi}{2}\right)\right]\\ &\times\left[\boldsymbol{F}_2\left(\frac{\pi}{2}\right)\boldsymbol{B}_{12}\left(\frac{1}{\sqrt{2}}\right)\boldsymbol{F}_2\left(\frac{\pi}{2}\right)\right],\end{aligned} \tag{6.57}$$

where $\boldsymbol{F}_\mu(\pi/2)$ is the 4×4 identity matrix except the element (μ,μ) is replaced with i,

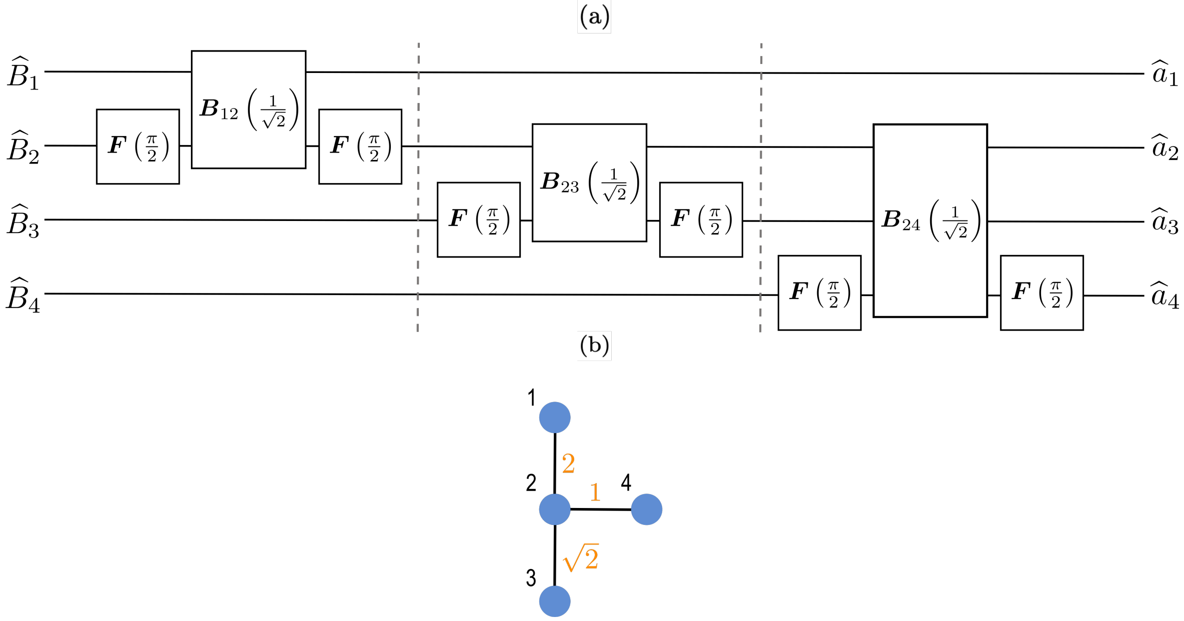

Figure 6.3: (a) Illustration of a linear optics circuit that generates a 4-mode cluster state with similar operations to those in Fig. 6.2, and (b) a graph that illustrates the adjacency matrix for the cluster state, with weighted edges shown.

that is $[\boldsymbol{F}_\mu(\pi/2)]_{\mu\mu} = i$, and where $\boldsymbol{B}_{\mu\nu}\left(1/\sqrt{2}\right)$ is the 4×4 identity matrix except the elements (μ,μ), (μ,ν), (ν,μ), and (ν,ν) are replaced with the corresponding elements from the 2×2 beamsplitter in Eq. (6.52). The first beamsplitter operation in Eq. (6.57) mixes the input modes 1 and 2, creating a two-mode cluster state (as shown above). The second beamsplitter mixes the modes 2 and 3, creating a one-dimensional chain cluster state of the modes $1-3$. The third beamsplitter mixes the modes 4 and 2, linking mode 4 to mode 2 in the chain. Putting these definitions into Eq. (6.57),

$\boldsymbol{U}(4)$ can be written as

$$\boldsymbol{U}(4) = \frac{1}{\sqrt{2}} \begin{pmatrix} 1 & i & 0 & 0 \\ i/2 & 1/2 & i/\sqrt{2} & i \\ -1/\sqrt{2} & i/\sqrt{2} & 1 & 0 \\ -1/2 & i/2 & -1/\sqrt{2} & 1 \end{pmatrix}. \tag{6.58}$$

Now I put Eq. (6.53) into Eq. (6.49) to obtain the adjacency matrix $\boldsymbol{A}$ for the circuit $\boldsymbol{U}$. Doing this, I obtain

$$\boldsymbol{A} = \begin{pmatrix} 0 & 2 & 0 & 0 \\ 2 & 0 & \sqrt{2} & 1 \\ 0 & \sqrt{2} & 0 & 0 \\ 0 & 1 & 0 & 0 \end{pmatrix}. \tag{6.59}$$

This cluster state is represented as a graph in Fig. 6.3(b), where the weights of the edges connecting pairs of nodes are given by the adjacency matrix in Eq. (6.59). Similar to the previous subsection, we also let $\boldsymbol{\theta} = \theta\mathbf{1}$ and $\theta = -\phi$ in Eq. (6.49) to obtain the $\boldsymbol{A}$ in Eq. (6.59).

The output state of the circuit, $\widehat{\rho}_{\text{out}}$, is obtained by putting $M = 4$ in Eq. (6.34). The squeezing parameter matrix $\boldsymbol{z}$ for the squeezing operator in $\widehat{\rho}_{\text{out}}$ is obtained by putting Eq. (6.58) into Eq. (6.35). The result of this is not a simple expression where $\boldsymbol{z}$ is proportional to $\boldsymbol{A}$, such as the one we derived in the case for 2-modes (see Eq. (6.55)). However, for this case $\boldsymbol{z}$ can be written in terms of $\boldsymbol{A}$ as

$$\boldsymbol{z} = r\mathrm{e}^{i\phi} \left(i\mathbf{1} + \boldsymbol{A}\right)^{-1} \left(i\mathbf{1} - \boldsymbol{A}\right). \tag{6.60}$$

6.6 Conclusion

In conclusion, I showed that the multimode squeezed thermal state can be classified as an approximate CV cluster state, as long as certain squeezing criterion are obeyed, that take into account the noise due to scattered photons. I derived an expression for the adjacency matrix of the cluster state that is written in terms of the squeezing phases of the squeezed thermal state and the phase-space angles of the quadrature operators, as well as calculated the adjacency matrix for 2- and 4-mode cluster states made from simple linear optics circuits. The cluster state can also be generated all at once with a nonlinear interaction, and the adjacency matrix can be calculated using the coupled-equations for the multimode squeezed thermal state that we derived in Chapter 4. In the future, it would be interesting to develop more complex linear optics circuits to generate larger cluster states, that incorporate squeezed thermal states.

Chapter 7

Conclusion

In this thesis, I ultimately showed that the density operator for an MSTS is the solution to the LME for the nonlinearly generated light in M coupled, lossy cavities. I showed this for a general system with lossy nonorthogonal quasimodes, under the assumptions that the dielectric function of the system is real, such that the dielectric material is non-absorptive but can still scatter photons and the pump is classical field in a single mode. I derived a set of $3M$ coupled first-order differential equations for the squeezing amplitudes, squeezing phases, and thermal photon numbers of the MSTS. These equations can make it much faster to numerically calculate the density operator of the MSTS, since the number of equations to solve increases proportionally to M; compared to other numerical techniques that use a basis of Fock states to calculate the density operator, where the dimension of the problem can grow exponentially with the size of the system. Therefore, the MSTS solution makes it more feasible to study the nonlinear generation and propagation of nonclassical light in systems with multiple, coupled lossy cavities. Using the simple expressions that were derived for the variances and covariances of the quadrature operators using the MSTS, the generated state of light in the cavities can be characterized, allowing one to detemine the amount of squeezing in its modes and/or its inseparability.

In Chapters 2 and 3, the MSTS solution was applied to a MRR to study the nonlinear optical generation of squeezed states in the ring. Using the MSTS, an analytic expression was derived for the minimum quadrature noise (maximum squeezing) in the ring, which was written in terms of the ring-coupling parameter and scattering loss (see Eq. (2.39)). Also, an analytic expression for the minimum correlation variance in a two-mode squeezed state in the ring was derived (see Eq. (3.60)). These simple equations can be used to inform researchers as to what is the optimal ring-coupling parameter in the presence of scattering loss, in order to generate highly inseparable two-mode squeezed states in the ring, or to generate squeezed states in the ring that are maximally squeezed.

In the coupled-cavity structures that were studied in this thesis, scattering loss causes the quasimodes to be nonorthogonal, unless the structure has high-symmetry and the modes are eigenstates of symmetry operators. In Chapter 5, I showed that the MSTS solution to the Lindblad master equation is valid, even when the nonorthogonality of the quasimodes is included. This extends the applicability of the theory to a general system of lossy coupled-cavities, including systems that have no symmetry. I showed that in one of the simplest systems for squeezed light generation, just two coupled defect-cavities that are asymmetrically placed in a photonic crystal slab, the spatial overlap of the two nonorthogonal quasimodes is over 80% and it led to a non-negligible detrimental effect on the squeezing level in the cavities.

Another application of the MSTS is for the generation of CV cluster states via nonlinear optics. Theoretical studies of CV cluster states have largely focussed on pure Gaussian states generated by a multimode squeezing transformation on the vacuum. However, this approach does not take into account the photon loss due to scattering during the generation process. This loss can prevent the generated squeezed state from being classified as a cluster state and thus it should be included. The MSTS solution provides a simple way to incorporate loss during the generation of the cluster state and it opens a path to extend the theory of pure Gaussian cluster states to mixed Gaussian cluster states. In Chapter 6, I showed that the MSTS can be classified as an approximate CV cluster state, provided squeezing criterion are obeyed by the state that take into account the noise due to photon scattering. Also, I derived the adjacency matrix for the cluster state in terms of the squeezing phase parameters of the MSTS. Additionally, using the coupled-equations that were derived for the parameters of the MSTS, one can easily calculate the adjacency matrix of the nonlinearly generated cluster state.

There is ongoing work in the group that I will be apart of, at least for the next few months, that is investigating the nonlinear generation of multimode squeezed states in large systems of nonorthogonal quasimodes, such as a photonic crystal slab with a three-mode defect-cavity side-coupled to a defect-waveguide. This system is of interest since it can incorporate the generation and propagation of the MSTS on a chip, and using the coupled-equations we derived we are able to characterize the state at all times and at any point in the crystal. This work will help make it practical to study nonclassical light in integrated circuits made from coupled-cavities in photonic crystals.

Systems of coupled-cavities in a photonic crystal slab may also be of interest for cluster state generation. In general, an MSTS can be generated in the coupled-cavities by pumping the slab from above with a laser beam, where each individual cavity supports a single mode of the MSTS. The squeezing parameters in the MSTS will depend on the coupling strength between the modes of the individual cavities (via the mode overlaps in the nonlinear parameter), and thus the adjacency matrix for the corresponding cluster state will have elements that also depend on the coupling strengths. Theoretically, it may be possible to engineer the coupling strengths to obtain any cluster state. One of the challenges with this approach is that the generated MSTS can have many modes that do not contain a sufficient enough squeezing level to obey the squeezing criterion that we derived, and thus is will not be considered a valid cluster state. It will take some effort to engineer the nonlinear interaction in large systems of lossy coupled-cavities to create sufficiently squeezed light in all the modes. However, I remain optimistic that if the appropriate structure were to be discovered, then one can nonlinearly generate large cluster states all at once. I hope that this line of work will continue in the group and that the theory I developed in Chapters 5 and 6 will serve as a valuable foundation for this future work.

MRRs are a platform that have proven to be useful for cluster state generation. They offer an opportunity to engineer the interaction between the resonant modes of the ring, and it is easy to show using our theory that there is sufficiently squeezed light in each ring mode (even after photon loss is included), such that the squeezing criterion are obeyed. Using the theory in Chapter 4, one could model a system where a MRR is pumped in a single mode of the ring and it generates pairs of entangled signal and idler photons in pairs of ring-modes that conserve energy and momentum with respect to the pump mode. This should result in the generation of a sequence of uncoupled, two-mode cluster states. The sequence of two-mode cluster states would then couple out of the ring and into a channel waveguide, where from there they can become the input to a linear optics circuit that mixes the two-mode cluster states with beamsplitters and phase shifters to form a larger cluster state (similar to what I showed in Chapter 6). This hybrid approach uses the theory developed in Chapters 4 and 6 to nonlinearly generate sequences of smaller cluster states that are subsequently mixed using a linear optics circuit to produce a larger cluster sate.

The future of the applications of nonlinear optics to generate CV cluster states is very bright. The work presented in this thesis opens a path to investigate CV cluster states that are generated in lossy systems by a combination of nonlinear and linear optics, and will help researchers optimize CV quantum computation in the presence of photon scattering loss.

Bibliography

[1] G. Plunien, B. Müller, and W. Greiner. The Casimir effect. *Phys. Rep*, 134:87, 1986.

[2] Roman Schnabel. Squeezed states of light and their applications in laser interferometers. *Phys. Rep.*, 684:1–51, 2016.

[3] C. Couteau. Spontaneous parametric down-conversion. *Contemp. Phys*, 59:291, 2018.

[4] T. Hao, Q. Cen, S. Guan, W. Li, Y. Dai, N. Zhu, and M. Li. Optoelectronic parametric oscillator. *Light Sci. Appl*, 9:102, 2020.

[5] T. J. Steiner, J. E. Castro, L. Chang, Q. Dang, W. Xie, J. Norman, J. E. Bowers, and G. Moody. Ultrabright entangled-photon-pair generation from an AlGaAs-on-insulator microring resonator. *PRX Quantum*, 2:010337, 2021.

[6] J. Carpenter, C. Xiong, M. J. Collins, J. Li, T. F. Krauss, B. J. Eggleton, A. S. Clark, and J. Schröder. Mode multiplexed single-photon and classical channels in a few-mode fiber. *Opt. Express*, 21:28794, 2013.

[7] P. T. Kristensen, J. Rosenkrantz de Lasson, and N. Gregersen. Calculation, normalization, and perturbation of quasinormal modes in coupled cavity-waveguide systems. *Opt. Lett.*, 39:6359, 2014.

[8] S. Ek, P. Lunnemann, Y. Chen, E. Semenova, K. Yvind, and J. Mork. Slow-light-enhanced gain in active photonic crystal waveguides. *Nat. Commun*, 5:5039, 2014.

[9] D P Fussell and M M Dignam. Quasimode-projection approach to quantum-dot–photon interactions in photonic-crystal-slab coupled-cavity systems. *Phys. Rev. A*, 77:053805, 2008.

[10] P. T. Kristensen and Stephen Hughes. Modes and mode volumes of leaky optical cavities and plasmonic nanoresonators. *ACS Photonics*, 1:2, 2014.

[11] J. D. Joannopoulos, S. G. Johnson, J. N. Winn, and R. D. Meade. *Photonic crystals: Molding the flow of light.* Princeton University Press, 2008.

[12] A. Einstein, B. Podolsky, and N. Rosen. Can quantum-mechanical description of physical reality be considered complete? *Phys. Rev.*, 47:777, 1935.

[13] J. S. Bell. On the Einstein Podolsky Rosen paradox. *Physics Physique Fizika*, 1:195, 1964.

[14] Alain Aspect, Philippe Grangier, and Gérard Roger. Experimental realization of Einstein-Podolsky-Rosen-Bohm Gedankenexperiment: A new violation of Bell's inequalities. *Phys. Rev. Lett.*, 49:91, 1982.

[15] S. Pirandola, J. Eisert, C. Weedbrook, A. Furusawa, and S. L. Braunstein. Advances in quantum teleportation. *Nat. Ph.*, 9:641, 2015.

[16] Thomas Jennewein, Christoph Simon, Gregor Weihs, Harald Weinfurter, and Anton Zeilinger. Quantum Cryptography with Entangled Photons. *Phys. Rev. Lett.*, 84:4729, 2000.

[17] Pieter Kok, W. J. Munro, Kae Nemoto, T. C. Ralph, Jonathan P. Dowling, and G. J. Milburn. Linear optical quantum computing with photonic qubits. *Rev. Mod. Phys.*, 79:135, 2007.

[18] W. Dür, G. Vidal, and J. I. Cirac. Three qubits can be entangled in two inequivalent ways. *Phys. Rev. A*, 62:062314, 2000.

[19] R. Raussendorf and H. Briegel. A one-way quantum computer. *Phys. Rev. Lett.*, 86:5188, 2001.

[20] H. Briegel and R. Raussendorf. Persistent entanglement in arrays of interacting particles. *Phys. Rev. Lett.*, 86:910, 2001.

[21] L. S. Madsen, F. Laudenbach, M. F. Askarani, et al. Quantum computational advantage with a programmable photonic processor. *Nature*, 606:75, 2022.

[22] Lu-Ming Duan, G Giedke, J I Cirac, and P Zoller. Inseparability Criterion for Continuous Variable Systems. *Phys. Rev. Lett.*, 84:2722, 2000.

[23] R Simon. Peres-Horodecki Separability Criterion for Continuous Variable Systems. *Phys. Rev. Lett.*, 84:2726, 2000.

[24] C. F. Lo and R. Sollie. Generalized multimode squeezed states. *Phys. Rev. A*, 47:733, 1993.

[25] Xin Ma and W Rhodes. Multimode squeeze operators and squeezed states. *Phys. Rev. A*, 41:4625, 1990.

[26] Peter van Loock and Akira Furusawa. Detecting genuine multipartite continuous-variable entanglement. *Phys. Rev. A*, 67:052315, 2003.

[27] R. Raussendorf, D. E. Browne, and H. Briegel. Measurement-based quantum computation on cluster states. *Phys. Rev. A*, 68:022312, 2003.

[28] N. C. Menicucci, P. van Loock, M. Gu, C. Weedbrook, T. C. Ralph, and M. A. Nielsen. Universal quantum computation with continuous-variable cluster states. *Phys. Rev. Lett.*, 97:110501, 2006.

[29] J. Zhang and S. L. Braunstein. Continuous-variable Gaussian analog of cluster states. *Phys. Rev. A*, 73:032318, 2006.

[30] N. C. Menicucci, S. T. Flammia, H. Zaidi, and O. Pfister. Ultracompact generation of continuous-variable cluster states. *Phys. Rev. A*, 76:010302(R), 2007.

[31] P. van Loock, C. Weedbrook, and M Gu. Building Gaussian cluster states by linear optics. *Phys. Rev. A*, 76:032321, 2006.

[32] M. Gu, C. Weedbrook, N. C. Menicucci, T. C. Ralph, and P. van Loock. Quantum computing with continuous-variable clusters. *Phys. Rev. A*, 79:062318, 2009.

[33] J. Zhang. Graphical description of local Gaussian operations for continuous-variable weighted graph states. *Phys. Rev. A*, 78:052307, 2008.

[34] N. C. Menicucci, S. T. Flammia, and P. van Loock. Graphical calculus for Gaussian pure states. *Phys. Rev. A*, 83:042335, 2011.

[35] Hossein Seifoory, Sean Doutre, Marc Dignam, and J E Sipe. Squeezed thermal states: the result of parametric down conversion in lossy cavities. *J. Opt. Soc. Am. B*, 34:1587, 2017.

[36] C Vendromin and M M Dignam. Optimization of a lossy microring resonator system for the generation of quadrature-squeezed states. *Phys. Rev. A*, 102:023705, 2020.

[37] Radan Slavík, Francesca Parmigiani, Joseph Kakande, et al. All-optical phase and amplitude regenerator for next-generation telecommunications systems. *Nat. Ph.*, 4:690–695, 2010.

[38] Qing Shou Tan, Jie Qiao Liao, Xiaoguang Wang, and Franco Nori. Enhanced interferometry using squeezed thermal states and even or odd states. *Phys. Rev. A*, 89:053822, 2014.

[39] J. Aasi, J. Abadie, B. Abbott, et al. (The LIGO Scientific Collaboration), Enhanced sensitivity of the LIGO gravitational wave detector by using squeezed states of light. *Nature Photonics*, 7:613–619, 2013.

[40] Benjamin J. Metcalf, Justin B. Spring, Peter C. Humphreys, Nicholas Thomas-Peter, Marco Barbieri, W. Steven Kolthammer, Xian Min Jin, Nathan K. Langford, Dmytro Kundys, James C. Gates, et al. Quantum teleportation on a photonic chip. *Nat. Ph.*, 8:770, 2014.

[41] G Masada, K Miyata, A Politi, T Hashimoto, J L O'Brien, and A Furusawa. Continuous-variable entanglement on a chip. *Nat. Ph.*, 9:316–319, 2015.

[42] Nicolas C. Menicucci. Fault-tolerant measurement-based quantum computing with continuous-variable cluster states. *Phys. Rev. Lett.*, 112:120504, 2014.

[43] Samuel L. Braunstein and Peter van Loock. Quantum information with continuous variables. *Rev. Mod. Phys.*, 77:513–577, 2005.

[44] Samuel L. Braunstein and H. J. Kimble. Teleportation of continuous quantum variables. *Phys. Rev. Lett.*, 80:869–872, 1998.

[45] Ling-An Wu, H. Kimble, John Hall, and Huifa Wu. Generation of squeezed states by parametric down conversion. *Phys. Rev. Lett.*, 57:2520–2523, 1986.

[46] Zhenshan Yang, Philip Chak, Alan D Bristow, Henry M Van Driel, Rajiv Iyer, J Stewart Aitchison, Arthur L Smirl, and J E Sipe. Enhanced second-harmonic generation in AlGaAs microring resonators. *Opt. Lett.*, 32:826, 2007.

[47] Xiyuan Lu, Qing Li, Daron A. Westly, et al. Chip-integrated visible–telecom entangled photon pair source for quantum communication. *Nat. Phys.*, 15:373–381, 2019.

[48] Z. Vernon, N. Quesada, M. Liscidini, et al. Scalable squeezed-light source for continuous-variable quantum sampling. *Phys. Rev. Appl.*, 12:064024, 2019.

[49] V. D. Vaidya, B. Morrison, L. G. Helt, et al. Broadband quadrature-squeezed vacuum and nonclassical photon number correlations from a nanophotonic device. e-print arXiv:1904.07833, 2019.

[50] Farid Samara, Anthony Martin, Claire Autebert, et al. High-Rate Photon Pairs and Sequential Time-Bin Entanglement with Si3N4 Ring Microresonators. *Opt. Express*, 27:19309–19318, 2019.

[51] Xiang Guo, Chang Ling Zou, Carsten Schuck, Hojoong Jung, Risheng Cheng, and Hong X. Tang. Parametric down-conversion photon-pair source on a nanophotonic chip. *Light Sci. Appl.*, 6:e16249, 2017.

[52] Zhenshan Yang and J. E. Sipe. Generating entangled photons via enhanced spontaneous parametric downconversion in AlGaAs microring resonators. *Opt. Lett.*, 32:3296, 2007.

[53] Z. Vernon and J. E. Sipe. Spontaneous four-wave mixing in lossy microring resonators. *Phys. Rev. A*, 91:053802, 2015.

[54] Z. Vernon and J. E. Sipe. Strongly driven nonlinear quantum optics in microring resonators. *Phys. Rev. A*, 92:033840, 2015.

[55] Paul M. Alsing and Edwin E. Hach. Photon-pair generation in a lossy microring resonator. ii. entanglement in the output mixed Gaussian squeezed state. *Phys. Rev. A*, 96:033848, 2017.

[56] Avik Dutt, Kevin Luke, Sasikanth Manipatruni, et al. On-Chip Optical Squeezing. *Phys. Rev. Appl.*, 3:044005, 2015.

[57] A Dutt, S Miller, K Luke, J Cardenas, A L Gaeta, P Nussenzveig, and M Lipson. Tunable squeezing using coupled ring resonators on a silicon nitride chip. *Opt. lett.*, 41:223, 2016.

[58] John E Heebner, Philip Chak, Suresh Pereira, et al. Distributed and localized feedback in microresonator sequences for linear and nonlinear optics. *J. Opt. Soc. Am. B*, 21:1818–1832, 2004.

[59] D Duchesne, K A Rutkowska, M Volatier, et al. Second Harmonic Generation in AlGaAs Nanowaveguides. *Opt. Express*, 19:12408–12417, 2011.

[60] John Heebner, Rohit Grover, and Tarek Ibrahim. *Optical Microresonators: Theory, Fabrication, and Applications.* Springer New York, 2008.

[61] S. Biasi, P. Guillemé, A. Volpini, G. Fontana, and L. Pavesi. Time response of a microring resonator to a rectangular pulse in different coupling regimes. *J. Light Technol.*, 37:5091–5099, 2019.

[62] J. C. Garrison and R. Y. Chiao. *Quantum Optics.* Oxford University Press, 2008.

[63] Hossein Seifoory, Lukas G Helt, and Marc M Dignam. Counterpropagating continuous variable entangled states in lossy coupled-cavity optical waveguides. *Phys. Rev. A*, 100:033839, 2019.

[64] H. P. Breuer and F. Petruccione. *The Theoy of Open Quantum Systems.* Oxford University Press, 2002.

[65] M. S. Kim, F. A. M. de Oliveira, and P. L. Knight. Properties of squeezed number states and squeezed thermal states. *Phys. Rev. A*, 40:2494–2503, 1989.

[66] Henning Vahlbruch, Moritz Mehmet, Karsten Danzmann, and Roman Schnabel. Detection of 15 db squeezed states of light and their application for the absolute

calibration of photoelectric quantum efficiency. *Phys. Rev. Lett.*, 117:110801, 2016.

[67] E Knill. Quantum computing with realistically noisy devices. *Nature*, 434:39–44, 2005.

[68] Shaoping Shi, Yajun Wang, Wenhai Yang, et al. Detection and perfect fitting of 13.2db squeezed vacuum states by considering green-light-induced infrared absorption. *Opt. Lett.*, 43:5411–5414, 2018.

[69] C Vendromin and M M Dignam. Continuous-variable entanglement in a two-mode lossy cavity: An analytic solution. *Phys. Rev. A*, 103:022418, 2021.

[70] Charles H Bennett, Gilles Brassard, Claude Crepeau, Richard Jozsa, Asher Peres, and William K Wootters. Teleporting an unknown quantum state via dual classical and Einstein-Podolsky-Rosen channels. *Phys. Rev. Lett.*, 70:1895, 1993.

[71] Mark Hillery. Quantum cryptography with squeezed states. *Phys. Rev. A*, 61:022309, 2000.

[72] S. Takeda and A. Furusawa. Toward large-scale fault-tolerant universal photonic quantum computing. *APL Photonics*, 4:060902, 2019.

[73] A. S. Villar, L. S. Cruz, K. N. Cassemiro, M. Martinelli, and P. Nussenzveig. Generation of bright two-color continuous variable entanglement. *Phys. Rev. Lett.*, 95:243603, 2005.

[74] M D Reid. Demonstration of the Einstein-Podolsky-Rosen paradox using non-degenerate parametric amplification. *Phys. Rev. A*, 40:913, 1989.

[75] Xianwen Liu, Alexander W. Bruch, Zheng Gong, Juanjuan Lu, Joshua B. Surya, Liang Zhang, Junxi Wang, Jianchang Yan, and Hong X. Tang. Ultra-high-Q UV microring resonators based on a single-crystalline AlN platform. *Optica*, 5:1279, 2018.

[76] J. W. Silverstone, R. Santagati, D. Bonneau, M. J. Strain, M. Sorel, J. L. O'Brien, and M. G. Thompson. Qubit entanglement between ring-resonator photon-pair sources on a silicon chip. *Nat. Commun.*, 6:7948, 2015.

[77] Although the phase with a positive sign in front of the $\pi/2$ term is also a solution, that solution gives $du(t_i)/dt < 0$, which results in a negative u, which is not allowed, since by definition u is a positive amplitude.

[78] Y Zhao, Y Okawachi, J K Jang, X Ji, M Lipson, and A L Gaeta. Near-degenerate quadrature-squeezed vacuum generation on a silicon-nitride chip. *Phys. Rev. Lett.*, 124:193601, 2020.

[79] F Mondain, T Lunghi, A Zavatta, E Gouzien, F Doutre, M De Micheli, S Tanzilli, and V D'Auria. Chip-based squeezing at a telecom wavelength. *Photonics res.*, 7:A37, 2019.

[80] Z Vernon, N Quesada, M Liscidini, B Morrison, M Menotti, K Tan, and J E Sipe. Scalable squeezed-light source for continuous-variable quantum sampling. *Phys. Rev. Appl.*, 12:064024, 2019.

[81] B H Wu, R N Alexander, S Liu, and Z Zhang. Quantum computing with multi-dimensional continuous-variable cluster states in a scalable photonic platform. *Phys. Rev. Res.*, 2:023138, 2020.

[82] C Vendromin and M M Dignam. Simple way to incorporate loss when modeling multimode-entangled-state generation. *Phys. Rev. A*, 105:063707, 2022.

[83] C S Hamilton, R Kruse, L Sansoni, S Barkhofen, C Silberhorn, and I Jex. Gaussian boson sampling. *Phys. Rev. Lett.*, 119:170501, 2017.

[84] R Kruse, C S Hamilton, L Sansoni, S Barkhofen, C Silberhorn, and I Jex. Detailed study of Gaussian boson sampling. *Phys. Rev. A*, 100:032326, 2019.

[85] O. Pfister. Continuous-variable quantum computing in the quantum optical frequency comb. *J. Phys. B: At. Mol. Opt. Phys.*, 53:012001, 2020.

[86] J Zhang and S L Braunstein. Continuous-variable Gaussian analog of cluster states. *Phys. Rev. A*, 73:032318, 2006.

[87] Z Yang, M Liscidini, and J E Sipe. Spontaneous parametric down-conversion in waveguides: A backward Heisenberg picture approach. *Phys. Rev. A*, 77:033808, 2008.

[88] P R Sharapova, G Frascella, M Riabinin, A M Pérez, O V Tikhonova, S Lemieux, R W Boyd, G Leuchs, and M V Chekhova. Properties of bright squeezed vacuum at increasing brightness. *Phys. Rev. Res.*, 2:013371, 2020.

[89] Hossein Seifoory, L G Helt, J E Sipe, and Marc M Dignam. Counterpropagating continuous-variable entangled states in lossy coupled-cavity optical waveguides. *Phys. Rev. A*, 100:033839, 2019.

[90] M. K. Dezfouli and M. M. Dignam. Photon-pair generation in lossy coupled-resonator optical waveguides via spontaneous four-wave mixing. *Phys. Rev. A*, 95:033815, 2017.

[91] L. Helt and N. Quesada. Degenerate squeezing in waveguides: A unified theoretical approach. *J. Phys. Photonics*, 2:035001, 2020.

[92] M Gregg and M Richter. Efficient and exact numerical approach for many multi-level systems in open system CQED. *New J. Phys.*, 18:043037, 2016.

[93] N Quesada, L. G. Helt, M Menotti, M Liscidini, and J. E. Sipe. Beyond photon pairs: Nonlinear quantum photonics in the high-gain regime. *arXiv:2110.04340*, 2021.

[94] M M Dignam, D P Fussell, M J Steel, C Martijn de Sterke, and R C McPhedran. Spontaneous emission suppression via quantum path interference in coupled microcavities. *Phys. Rev. Lett.*, 96:103902, 2006.

[95] N Quesada, G Triginer, M D Vidrighin, and J E Sipe. Theory of high-gain twin-beam generation in waveguides: From Maxwell's equations to efficient simulation. *Phys. Rev. A*, 102:033519, 2020.

[96] D P Fussell and M M Dignam. Engineering the quality factors of coupled-cavity modes in photonic crystal slabs. *Appl. Phys. Lett.*, 90:183121, 2007.

[97] M. M. Dignam and M. K. Dezfouli. Photon-quantum-dot dynamics in coupled-cavity photonic crystal slabs. *Phys. Rev. A*, 85:013809, 2012.

[98] The formula we use is $\mathrm{e}^{-A}B\mathrm{e}^{A} = B-[A,B]+\frac{1}{2!}[A,[A,B]]-\frac{1}{3!}[A,[A,[A,B]]]+\ldots$, where A and B are general operators.

[99] A Bunse-Gerstner and W B Gragg. Singular value decompositions of complex symmetric matrices. *JCAM*, 21:41, 1988.

[100] M Dinu, F Quochi, and H Garcia. Third-order nonlinearities in silicon at telecom wavelengths. *Appl. Phys. Lett.*, 82:2954, 2003.

[101] S Zippilli and D Vitali. Possibility to generate any Gaussian cluster state by a multimode squeezing transformation. *Phys. Rev. A*, 102:052424, 2020.

[102] Seth Lloyd and Samuel L Braunstein. Quantum computation over continuous variables. *Phys. Rev. Lett.*, 82:1784, 1999.

[103] Peter van Loock, Christian Weedbrook, and Mile Gu. Building Gaussian cluster states by linear optics. *Phys. Rev. A*, 76:032321, 2007.

[104] Shota Yokoyama, Ryuji Ukai, Seiji C Armstrong, Chanond Sornphiphatphong, Toshiyuki Kaji, Shigenari Suzuki, J Yoshikawa, Hidehiro Yonezawa, Nicolas C Menicucci, and Akira Furusawa. Ultra-large-scale continuous-variable cluster states multiplexed in the time domain. *Nat. Photonics*, 7:982, 2013.

[105] Mikkel V Larsen, Xueshi Guo, Casper R Breum, Jonas S Neergaard-Nielsen, and Ulrik L Andersen. Deterministic generation of a two-dimensional cluster state. *Science*, 366:369, 2019.

[106] Nicolas C Menicucci, Steven T Flammia, Hussain Zaidi, and Olivier Pfister. Ultracompact generation of continuous-variable cluster states. *Phys. Rev. A*, 76:010302, 2007.

[107] Nicolas C Menicucci, Steven T Flammia, and Olivier Pfister. One-way quantum computing in the optical frequency comb. *Phys. Rev. Lett.*, 101:130501, 2008.

[108] Jonathan Roslund, R Medeiros de Araújo, Shifeng Jiang, Claude Fabre, and Nicolas Treps. Wavelength-multiplexed quantum networks with ultrafast frequency combs. *Nat. Photonics*, 8:109, 2014.

[109] Christian Reimer, Stefania Sciara, Piotr Roztocki, Mehedi Islam, Luis Romero Cortés, Yanbing Zhang, Bennet Fischer, Sebastien Loranger, Raman Kashyap, Alfonso Cino, Sai T Chu, Brent E Little, David J Moss, Lucia Caspani, William J Munro, Jose Azaña, Michael Kues, and Roberto Morandotti. High-dimensional one-way quantum processing implemented on d-level cluster states. *Nat. Phys.*, 15:148, 2019.

[110] L G Helt, M J Steel, and J E Sipe. Spontaneous parametric downconversion in waveguides: What's loss got to do with it? *New J. Phys.*, 17:013055, 2014.

[111] Sebastian Franke, Stephen Hughes, Mohsen Kamandar Dezfouli, Philip Trost Kristensen, Kurt Busch, Andreas Knorr, and Marten Richter. Quantization of quasinormal modes for open cavities and plasmonic cavity quantum electrodynamics. *Phys. Rev. Lett.*, 122:213901, 2019.

[112] Juanjuan Ren, Sebastian Franke, and Stephen Hughes. Connecting classical and quantum mode theories for coupled lossy cavity resonators using quasinormal modes. *ACS Photonics*, 9:138, 2022.

[113] Daniel Manzano. A short introduction to the Lindblad master equation. *AIP Advances*, 10:025106, 2020.

[114] J R Johansson, P D Nation, and F Nori. Qutip: An open-source Python framework for the dynamics of open quantum systems. *Comp. Phys. Comm.*, 183:1760, 2012.

[115] P. Walther, K. J. Resch, T. Rudolph, E. Schenck, H. Weinfurter, V. Vedral, M. Aspelmeyer, and A. Zeilinger. Experimental one-way quantum computing. *Nature*, 434:169, 2005.

[116] S. L. Braunstein. Quantum error correction for communication with linear optics. *Nature*, 394:47, 1998.

[117] Blayney W. Walshe, Lucas J. Mensen, Ben Q. Baragiola, and Nicolas C. Menicucci. Robust fault tolerance for continuous-variable cluster states with excess antisqueezing. *Phys. Rev. A*, 100:010301, 2019.

[118] Peter van Loock, Christian Weedbrook, and Mile Gu. Building Gaussian cluster states by linear optics. *Phys. Rev. A*, 76:032321, 2007.

[119] Moran Chen, Nicolas C. Menicucci, and Olivier Pfister. Experimental realization of multipartite entanglement of 60 modes of a quantum optical frequency comb. *Phys. Rev. Lett.*, 112:120505, 2014.

[120] Bo-Han Wu, Rafael N. Alexander, Shuai Liu, and Zheshen Zhang. Quantum computing with multidimensional continuous-variable cluster states in a scalable photonic platform. *Phys. Rev. Research*, 2:023138, 2020.

[121] Michael Reck, Anton Zeilinger, Herbert J. Bernstein, and Philip Bertani. Experimental realization of any discrete unitary operator. *Phys. Rev. Lett.*, 73:58, 1994.

[122] *NIST Digital Library of Mathematical Functions.* http://dlmf.nist.gov/, Release 1.0.26 of 2020-03-15. F. W. J. Olver, A. B. Olde Daalhuis, D. W. Lozier, B. I. Schneider, R. F. Boisvert, C. W. Clark, B. R. Miller, B. V. Saunders, H. S. Cohl, and M. A. McClain, eds.

[123] Nick K Hon, Richard Soref, and Bahram Jalali. The third-order nonlinear optical coefficients of si, ge, and $\mathrm{Si}_{1-x}\mathrm{Ge}_x$ in the midwave and longwave infrared. 110:011301, 2011.

Appendix A

Supplemental material for Chapter 2

A.1 Derivation of the time-dependent pump pulse in the ring

In this section we derive an approximate expression for the pump field in the ring, $E_3\left(\tilde{t}\right)$. We start with Eq. (2.13). To simplify this, we define

$$\chi(\Omega) \equiv \frac{1}{\exp(-i\Omega) - \sigma a}. \tag{A.1}$$

We expand this in a Taylor series about $\Omega = 0$,

$$\chi(\Omega) = \sum_{n=0}^{\infty} \frac{\Omega^n \chi^{(n)}(0)}{n!}, \tag{A.2}$$

where

$$\chi^{(n)}(0) \equiv \left.\frac{d^n \chi(\Omega)}{d\Omega^n}\right|_{\Omega=0} \tag{A.3}$$

is the n^{th} order derivative of χ evaluated at $\Omega = 0$. In the high squeezing limit $(1 - \sigma a) \ll 1$ it can be shown that for $n \geq 2$, the n^{th} and $(n-2)^{th}$ derivatives are related by,

$$\frac{\chi^{(n)}(0)}{n!} = -\frac{1}{\epsilon^2}\frac{\chi^{(n-2)}(0)}{(n-2)!}, \tag{A.4}$$

where $\epsilon \equiv 1 - \sigma a$. Using Eq. (A.4) in Eq. (A.2) and after simplifying we find that we can write $\chi(\Omega)$ as

$$\chi(\Omega) \;=\; \frac{1}{\epsilon}\left(\frac{1 + i\Omega/\epsilon}{1 + \Omega^2/\epsilon^2}\right). \tag{A.5}$$

The modulus-squared of this is a good approximation to the buildup factor around the peak at $\Omega = 0$. Now we define the integral in Eq. (2.13) as $A\left(\tilde{t}\right)$. It is given by,

$$A\left(\tilde{t}\right) = \exp\left(\frac{-2\ln(2)\tilde{t}^2}{\tilde{\tau}^2}\right)\int_{-\infty}^{\infty} d\Omega\chi(\Omega)\exp\left[-\left(\frac{\Omega\tilde{\tau}}{\sqrt{8\ln 2}} + i\frac{\sqrt{8\ln 2}\,\tilde{t}}{2\tilde{\tau}}\right)^2\right], \tag{A.6}$$

where we have completed the square in the argument of the exponential in Eq. (2.13) to get this form. Using Eq. (A.5) in Eq. (A.6), we obtain

$$A\left(\tilde{t}\right) = \frac{1}{\epsilon}\exp\left(\frac{-2\ln(2)\tilde{t}^2}{\tilde{\tau}^2}\right)\int_{-\infty}^{\infty} d\Omega\frac{1 + i\Omega/\epsilon}{1 + \Omega^2/\epsilon^2}\exp\left[-\left(\frac{\Omega\tilde{\tau}}{\sqrt{8\ln 2}} + i\frac{\sqrt{8\ln 2}\,\tilde{t}}{2\tilde{\tau}}\right)^2\right]. \tag{A.7}$$

Now we make the following substitutions in Eq. (A.7): $y = \Omega/\epsilon$, $s = 2\ln(2)/(\epsilon^2\tilde{\tau}^2)$, and $x = -i\tilde{t}4\ln(2)/(\epsilon\tilde{\tau}^2)$. Doing this we obtain,

$$A\left(\tilde{t}\right) = \exp\left(\frac{-2\ln(2)\tilde{t}^2}{\tilde{\tau}^2}\right)\int_{-\infty}^{\infty} dy\left[\frac{\mathrm{e}^{-(x-y)^2/(4s)}}{1 + y^2} + i\frac{y\mathrm{e}^{-(x-y)^2/(4s)}}{1 + y^2}\right]. \tag{A.8}$$

The integral in Eq. (A.8) can be expressed in terms of Voigt functions $U(x, s)$ and $V(x, s)$ [122]:

$$U(x, s) = \frac{1}{\sqrt{4\pi s}} \int_{-\infty}^{\infty} dy \frac{\mathrm{e}^{-(x-y)^2/(4s)}}{1 + y^2}, \tag{A.9}$$

and

$$V(x, s) = \frac{1}{\sqrt{4\pi s}} \int_{-\infty}^{\infty} dy \frac{y\mathrm{e}^{-(x-y)^2/(4s)}}{1 + y^2}. \tag{A.10}$$

It can be shown that

$$U(x, s) + iV(x, s) = \sqrt{\frac{\pi}{4s}} \mathrm{e}^{z^2} \operatorname{erfc} z \tag{A.11}$$

with $z = (1 - ix)/(2\sqrt{s})$. The Eqs. (A.9) - (A.11) allow us to write Eq. (A.8) as,

$$A\left(\tilde{t}\right) = \exp\left(\frac{-2\ln(2)\tilde{t}^2}{\tilde{\tau}^2}\right) \pi \mathrm{e}^{z\left(\tilde{t}\right)^2} \operatorname{erfc} z\left(\tilde{t}\right). \tag{A.12}$$

Transforming back to our original variables $\tilde{\tau}$ and $\tilde{t}$ we obtain $z\left(\tilde{t}\right) = (1-\sigma a)\tilde{\tau}/\sqrt{8\ln(2)} - \sqrt{8\ln(2)}\tilde{t}/(2\tilde{\tau})$. Replacing the integral in Eq. (2.13) with the expression in Eq. (A.12) gives Eq. (2.14) in the text.

A.2 Derivation of τ_g

In this section we derive an approximate expression, Eq. (2.27) for the pulse duration τ_g that gives the peak in the pumping strength (see Fig. 2.3). In order to do this, we first hold τ constant and then find the time t_{peak} when the pump is at its peak value. Then we determine the pulse duration that causes the greatest peak value. We solve the following two equations simultaneously;

$$\left.\frac{\partial g(t,\tau)}{\partial t}\right|_{t=t_{peak}} = 0, \tag{A.13}$$

and,

$$\left.\frac{\partial g(t_{peak},\tau)}{\partial \tau}\right|_{\tau=\tau_g} = 0. \tag{A.14}$$

Re-writing Eq. (2.14) in terms of $z(t)$ alone and ignoring the factors that do not depend on t or τ, we find

$$g(\tilde{t}) \propto \sqrt{\tilde{\tau}} \exp\left(-\frac{\epsilon^2\tilde{\tau}^2}{8\ln 2} + \frac{2\epsilon\tilde{\tau}z(\tilde{t})}{\sqrt{8\ln 2}}\right) \operatorname{erfc} z(\tilde{t}), \tag{A.15}$$

where $\epsilon \equiv 1 - \sigma a$, $\tilde{\tau} = \tau/T_R$, and $\tilde{t} = t/T_R$. Also $T_R\partial/\partial t = \partial/\partial\tilde{t}$ and $\partial/\partial\tilde{t} = -(\sqrt{2\ln 2}/\tilde{\tau})\partial/\partial z$. Using Eq. (A.15) in Eq. (A.13) and switching the derivatives to z, we obtain the following implicit equation for $z(\tilde{t}_{peak})$;

$$\mathrm{e}^{z_{peak}^2} \operatorname{erfc} z_{peak} = \frac{1}{\sqrt{\pi}}\frac{\sqrt{8\ln 2}}{\epsilon\tilde{\tau}}, \tag{A.16}$$

where $z_{peak} \equiv z(\tilde{t}_{peak})$. Now, using Eq. (A.15) in Eq. (A.14) and noting that $T_R\partial/\partial\tau = \partial/\partial\tilde{\tau}$, we obtain

$$\begin{aligned} 0 &= \frac{1}{2\tilde{\tau}_g} - \frac{\tilde{\tau}_g\epsilon^2}{4\ln 2} + \frac{2\epsilon z_{peak}}{\sqrt{8\ln 2}} + \\ &+ \left(\frac{2\tilde{\tau}_g\epsilon}{\sqrt{8\ln 2}} - \frac{2}{\sqrt{\pi}}\left[\mathrm{e}^{z_{peak}^2}\operatorname{erfc} z_{peak}\right]^{-1}\right)\left.\frac{\partial z_{peak}}{\partial\tilde{\tau}}\right|_{\tilde{\tau}_g}, \\ 0 &= \frac{1}{2\tilde{\tau}_g} - \frac{\tilde{\tau}_g\epsilon^2}{4\ln 2} + \frac{2\epsilon z_{peak}}{\sqrt{8\ln 2}}, \end{aligned} \tag{A.17}$$

where the second equation is obtained from the first by using Eq. (A.16). Solving Eq. (A.17) for z_{peak} gives,

$$z(\tilde{t}_{peak}) = \frac{\epsilon\tilde{\tau}_g}{\sqrt{8\ln 2}} - \frac{\sqrt{8\ln 2}}{4\epsilon\tilde{\tau}_g}. \tag{A.18}$$

Transforming Eq. (A.18) back to time t and using Eq. (2.15) we find that

$$\tilde{t}_{peak}(\tilde{\tau}_g) = \frac{1}{2(1-\sigma a)} \tag{A.19}$$

is the time when $g(\tau_g)$ is at its peak value. The time $\tilde{t}_{peak}$ is the inverse of the decay rate $1/\tilde{\Gamma}$ in the low-loss limit $(1-\sigma a) \ll 1$. We can determine $\tilde{\tau}_g$ by using Eq. (A.18) in Eq. (A.16). Doing this gives the following transcendental equation:

$$\exp\left(x - \frac{1}{4x}\right)^2 \operatorname{erfc}\left(x - \frac{1}{4x}\right) = \frac{1}{\sqrt{\pi}x}, \tag{A.20}$$

where $x \equiv \epsilon\tilde{\tau}_g/(8\ln 2)^{1/2}$. We have numerically determined that the solution of Eq. (A.20) is $x \approx 0.34189$. Thus, $\tilde{\tau}_g$ is approximately given by

$$\tilde{\tau}_g \approx 0.342\frac{\sqrt{8\ln 2}}{1-\sigma a}, \tag{A.21}$$

which is the expression given in Eq. (2.27).

Appendix B

Supplemental material for Chapter 3

B.1 Deriving the coupled equations for 2 orthogonal modes

In this section we simplify the RHS of Eq. (3.18) in order to find a condition for when the equality is true. We define the first two terms on the RHS of (3.18) to be

$$T1 = \frac{d\hat{\rho}_{th}^{-1/2}}{dt}\hat{S}^{\dagger}\hat{\rho}\hat{S}\hat{\rho}_{th}^{-1/2} + \hat{\rho}_{th}^{-1/2}\hat{S}^{\dagger}\hat{\rho}\hat{S}\frac{d\hat{\rho}_{th}^{-1/2}}{dt}, \tag{B.1}$$

and then using Eq. (3.16) to simplify, we obtain

$$\begin{aligned} T1 &= 2\frac{d\hat{\rho}_{th}^{-1/2}}{dt}\hat{\rho}_{th}^{1/2} \\ &= \sum_{j=1}^{2}\left(-\hat{n}_j\frac{\dot{x}_j}{x_j} + \frac{\dot{x}_j}{1-x_j}\right). \end{aligned} \tag{B.2}$$

We used the two-mode thermal state in Eq. (3.4) to get the last line.

We define the middle two terms on the RHS of (3.18) to be

$$T2 = \hat{\rho}_{th}^{-1/2}\frac{d\hat{S}^{\dagger}}{dt}\hat{\rho}\hat{S}\hat{\rho}_{th}^{-1/2} + \hat{\rho}_{th}^{-1/2}\hat{S}^{\dagger}\hat{\rho}\frac{d\hat{S}}{dt}\hat{\rho}_{th}^{-1/2}, \tag{B.3}$$

and then using Eq. (3.16) to simplify, we obtain

$$T2 = \hat{\rho}_{th}^{-1/2}\frac{d\hat{S}^{\dagger}}{dt}\hat{S}\hat{\rho}_{th}^{1/2} - \hat{\rho}_{th}^{1/2}\frac{d\hat{S}^{\dagger}}{dt}\hat{S}\hat{\rho}_{th}^{-1/2}. \tag{B.4}$$

To simplify this expression we will need to take the time derivative of the two-mode squeezing operator in Eq. (3.2), which is not straightforward, and thus requires us to be careful. We let $\hat{S} = \exp(\sigma)$, where $\sigma = \xi^{*}(t)\hat{b}_1\hat{b}_2 - h.c.$ and $\hat{S}^{\dagger} = \exp(-\sigma)$, then

$$\begin{aligned}\frac{d\hat{S}^{\dagger}}{dt} &= \frac{d}{dt}\left(1 - \sigma + \frac{\sigma^2}{2!} - \frac{\sigma^3}{3!} + ...\right)\\ &= \sum_{n=0}^{\infty}\sum_{k=0}^{\infty}(-1)^{n+k+1}\frac{\sigma^n\dot{\sigma}\sigma^k}{(n+k+1)!}\\ &= -\int_0^1 d\lambda\,\exp(-\lambda\sigma)\dot{\sigma}\exp(\lambda\sigma)\exp(-\sigma),\end{aligned} \tag{B.5}$$

where the integral in the last line can be shown to be equivalent to the sum on the previous line by expanding the exponential operators in a power series in σ and doing the integration over λ from 0 to 1. Multiplying Eq. (B.5) by $\hat{S}$ from the right, we obtain

$$\frac{d\hat{S}^{\dagger}}{dt}\hat{S} = -\int_0^1 d\lambda\,\exp(-\lambda\sigma)\dot{\sigma}\exp(\lambda\sigma). \tag{B.6}$$

Using the well-known Baker-Campbell-Hausdorff formulae on the integrand of Eq. (B.6), and then integrating over λ in each term in the series, we obtain

$$\begin{aligned}\frac{d\hat{S}^{\dagger}}{dt}\hat{S} &= -\dot{\sigma} + \frac{1}{2!}[\sigma,\dot{\sigma}] - \frac{1}{3!}[\sigma,[\sigma,\dot{\sigma}]] + ...\\ &= \sum_{n=1}^{\infty}(-1)^n\frac{L^{(n)}}{n!},\end{aligned} \tag{B.7}$$

where the first three terms in $L^{(n)}$ are defined as $L^{(1)} \equiv \dot{\sigma}$, $L^{(2)} \equiv [\sigma,\dot{\sigma}]$, and $L^{(3)} \equiv$

$[\sigma, [\sigma, \dot{\sigma}]]$. In general, we can write $L^{(n)} = [\sigma, L^{(n-1)}]$ for $n \geq 2$. It is straightforward to show that,

$$L^{(1)} = \dot{u}\left(\mathrm{e}^{-i\phi}\hat{b}_1\hat{b}_2 - \mathrm{e}^{i\phi}\hat{b}_1^\dagger\hat{b}_2^\dagger\right) - iu\dot{\phi}\left(\mathrm{e}^{-i\phi}\hat{b}_1\hat{b}_2 + \mathrm{e}^{i\phi}\hat{b}_1^\dagger\hat{b}_2^\dagger\right) \tag{B.8}$$

$$L^{(n)} = -\frac{i\dot{\phi}}{2}\left(\hat{n}_1 + \hat{n}_2 + 1\right)(2u)^n, \text{ even } n \geq 2 \tag{B.9}$$

$$L^{(n)} = -\frac{i\dot{\phi}}{2}\left(\mathrm{e}^{-i\phi}\hat{b}_1\hat{b}_2 + \mathrm{e}^{i\phi}\hat{b}_1^\dagger\hat{b}_2^\dagger\right)(2u)^n, \text{ odd } n \geq 3. \tag{B.10}$$

We then use Eqs. (B.8) to (B.10) in Eq. (B.7) to simplify the derivative. The sum over even n converges to $\cosh(2u) - 1$ and the sum over odd n converges to $\sinh(2u) - 2u$. Using these results, we put this simplified form of Eq. (B.7) into Eq. (B.4), along with the two-mode thermal state, to obtain

$$T2 = \frac{1 - x_1x_2}{\sqrt{x_1x_2}}\left(\dot{u}\hat{U} + \frac{1}{2}\sinh(2u)\dot{\phi}\hat{V}\right), \tag{B.11}$$

where $\hat{U} = \hat{b}_1\hat{b}_2\exp(-i\phi) + h.c.$ and $\hat{V} = -i\hat{b}_1\hat{b}_2\exp(-i\phi) + h.c.$. We define the last term of Eq. (3.18) to be

$$T3 = \hat{\rho}_{th}^{-1/2}\hat{S}^\dagger\frac{d\hat{\rho}}{dt}\hat{S}\hat{\rho}_{th}^{-1/2}. \tag{B.12}$$

Using Eq. (3.3) in Eq. (B.12) and simplifying by using Eq. (3.16) gives

$$\begin{aligned} T3 = &-\frac{i}{\hbar}\left(\hat{\rho}_{th}^{-1/2}\hat{S}^\dagger\hat{H}\hat{S}\hat{\rho}_{th}^{1/2} - \hat{\rho}_{th}^{1/2}\hat{S}^\dagger\hat{H}\hat{S}\hat{\rho}_{th}^{-1/2}\right) \\ &+ \sum_{j=1}^{2}\Gamma_j\hat{\rho}_{th}^{-1/2}\hat{S}^\dagger\hat{b}_j\hat{S}\hat{\rho}_{th}^{1/2}\hat{\rho}_{th}^{1/2}\hat{S}^\dagger\hat{b}_j^\dagger\hat{S}\hat{\rho}_{th}^{-1/2} \\ &- \frac{1}{2}\sum_{j=1}^{2}\Gamma_j\left(\hat{\rho}_{th}^{-1/2}\hat{S}^\dagger\hat{n}_j\hat{S}\hat{\rho}_{th}^{1/2} + \hat{\rho}_{th}^{1/2}\hat{S}^\dagger\hat{n}_j\hat{S}\hat{\rho}_{th}^{-1/2}\right) \end{aligned} \tag{B.13}$$

which can be simplified using the well-known Baker-Campbell-Hausdorff formulae to obtain

$$
\begin{aligned}
T3 = {} & \frac{1-x_1x_2}{\sqrt{x_1x_2}}\left[\frac{\omega_1+\omega_2}{2}\sinh(2u)\hat{V} + \left(\frac{i}{\hbar}\left(\mathcal{E}_P\gamma \mathrm{e}^{-i\phi}\cosh^2 u \mathcal{E}_P^*\gamma^*\mathrm{e}^{i\phi}\sinh^2 u\right)\frac{\hat{U}+i\hat{V}}{2} + h.c.\right)\right] + \\
& + \left[\left(\frac{1+x_1x_2}{2\sqrt{x_1x_2}} - \sqrt{\frac{x_1}{x_2}}\right)\Gamma_1 + \left(\frac{1+x_1x_2}{2\sqrt{x_1x_2}} - \sqrt{\frac{x_2}{x_1}}\right)\Gamma_2\right]\frac{1}{2}\sinh(2u)\hat{U} \\
& + \left[\Gamma_1(x_1-1)\cosh^2 u + \left(x_1^{-1}-1\right)\Gamma_2\sinh^2 u\right]\hat{n}_1 \\
& + \left[\Gamma_2(x_2-1)\cosh^2 u + \left(x_2^{-1}-1\right)\Gamma_1\sinh^2 u\right]\hat{n}_2 + \\
& + \left[\Gamma_1\left(x_1\cosh^2 u - \sinh^2 u\right) + \Gamma_2\left(x_2\cosh^2 u - \sinh^2 u\right)\right]. \qquad \text{(B.14)}
\end{aligned}
$$

Using expressions for $T1$, $T2$, and $T3$ (see Eqs. (B.2), (B.11), and (B.14)) in Eq. (3.18), formally we can write

$$0 = T1 + T2 + T3. \qquad \text{(B.15)}$$

In order for the equality in Eq. (B.15) to be true for all times we must have that the coefficients in front of the operators, 1, $\hat{n}_1$, $\hat{n}_2$, $\hat{U}$, and $\hat{V}$ are equal to zero for all times. Setting these equal to zero and solving, we obtain the coupled differential equations Eqs. (3.19) to (3.22).

Appendix C

Supplemental material for Chapter 4

C.1 Connection between SVD and the Takagi factorization

As mentioned in the text, the Takagi factorization is a special case of the symmetric SVD, where the diagonal matrix from the Takagi factorization is just a scaled version of the singular values from the SVD. In this section we derive the Takagi factorization from the SVD, and show how the diagonal values are related to the singular values.

The SVD of the nonlinear parameter G is

$$\boldsymbol{G} = \boldsymbol{U}\boldsymbol{\Sigma}\boldsymbol{W}^\dagger, \tag{C.1}$$

where $\boldsymbol{\Sigma}$ is a diagonal matrix of real and positive singular values, and $\boldsymbol{U}^\dagger\boldsymbol{U} = \mathbf{1}$ and $\boldsymbol{W}^\dagger\boldsymbol{W} = \mathbf{1}$. To obtain the Takagi factorization we define the diagonal complex matrix

$$\boldsymbol{\Lambda} = \boldsymbol{\Sigma}\boldsymbol{W}^\dagger\boldsymbol{U}^*, \tag{C.2}$$

where $\boldsymbol{U}^*$ denotes the complex conjugate of $\boldsymbol{U}$. Therefore the Takagi factorization is

$$\boldsymbol{G} = \boldsymbol{U}\boldsymbol{\Lambda}\boldsymbol{U}^{\mathrm{T}}, \tag{C.3}$$

where the SVD can be recovered by putting Eq. (C.2) into Eq. (C.3), since $\boldsymbol{U}^*\boldsymbol{U}^{\mathrm{T}} = \boldsymbol{1}$. Therefore, to obtain the Takagi factorization of $\boldsymbol{G}$, one can perform the SVD to get the matrix $\boldsymbol{U}$, and multiply the singular value matrix $\boldsymbol{\Sigma}$ by the diagonal matrix $\boldsymbol{W}^\dagger\boldsymbol{U}^*$.

Now we prove that $\boldsymbol{W}^\dagger\boldsymbol{U}^*$ in Eq. (C.2) is diagonal. If it is diagonal, then it must be equal to its transpose, such that $\boldsymbol{W}^\dagger\boldsymbol{U}^* = \boldsymbol{U}^\dagger\boldsymbol{W}^*$. Taking the Hermitian conjugate of both sides, we obtain

$$\boldsymbol{W}^{\mathrm{T}}\boldsymbol{U} = \boldsymbol{U}^{\mathrm{T}}\boldsymbol{W}. \tag{C.4}$$

Moreover, since $\boldsymbol{G}$ is a symmetric matrix we have $\boldsymbol{G}^{\mathrm{T}} = \boldsymbol{G}$. Taking the transpose of Eq. (C.1) we obtain

$$\begin{aligned} \boldsymbol{W}^*\boldsymbol{\Sigma}\boldsymbol{U}^{\mathrm{T}} &= \boldsymbol{U}\boldsymbol{\Sigma}\boldsymbol{W}^\dagger, \\ \boldsymbol{\Sigma}\boldsymbol{U}^{\mathrm{T}}\boldsymbol{W} &= \boldsymbol{W}^{\mathrm{T}}\boldsymbol{U}\boldsymbol{\Sigma}, \\ \boldsymbol{\Sigma}\boldsymbol{U}^{\mathrm{T}}\boldsymbol{W}\boldsymbol{\Sigma}^{-1} &= \boldsymbol{U}^{\mathrm{T}}\boldsymbol{W}, \end{aligned} \tag{C.5}$$

where to go from the second line to the third line we used Eq. (C.4). Eq. (C.5) implies that if the singular values $\boldsymbol{\Sigma}$ are distinct and nonzero, then $\boldsymbol{U}^{\mathrm{T}}\boldsymbol{W}$ is a diagonal matrix. Therefore, its Hermitian conjugate $\boldsymbol{W}^\dagger\boldsymbol{U}^*$ is also diagonal, and we have proved that $\boldsymbol{\Lambda}$ is diagonal.

C.2 Deriving the coupled equations for M orthogonal modes

In this section we provide the details on the derivation of the coupled differential equations Eqs. (4.69) -(4.71).

C.2.1 Equations for $\dot{r}_\mu$ and $\dot{\phi}_\mu$

To start, we add Eqs. (4.67) and (4.68), to obtain

$$D_{ml} = -E_{ml}. \tag{C.6}$$

Putting the expression for D_{ml} in Eq. (4.56) into Eq. (C.6), we obtain

$$\frac{x_m x_l - 1}{2\sqrt{x_m x_l}} \sum_\mu U_{m\mu} U_{l\mu} \left(\dot{r}_\mu + \frac{i\dot{\phi}_\mu}{2} \sinh(2r_\mu) \right) \mathrm{e}^{i\phi_\mu} = -E_{ml}. \tag{C.7}$$

Multiplying both sides by $\sum_{m,l} U^*_{\mu m} U^*_{\mu l}$ and using the orthogonality relation $\sum_m U^*_{\nu m} U_{m\mu} = \delta_{\nu\mu}$, we obtain

$$\dot{r}_\mu + \frac{i\dot{\phi}_\mu}{2} \sinh(2r_\mu) = \sum_{m,l} \frac{2\sqrt{x_m x_l} E_{ml} U^*_{\mu m} U^*_{\mu l} \mathrm{e}^{-i\phi_\mu}}{1 - x_m x_l}. \tag{C.8}$$

Equating the real and imaginary parts of both sides of Eq. (C.8) gives the following equations for $\dot{r}_\mu$ and $\dot{\phi}_\mu$

$$\dot{r}_\mu = \sum_{m,l} \frac{\sqrt{x_m x_l} \left(E_{ml} U^*_{\mu m} U^*_{\mu l} \mathrm{e}^{-i\phi_\mu} + E^*_{ml} U_{m\mu} U_{l\mu} \mathrm{e}^{i\phi_\mu} \right)}{1 - x_m x_l}, \tag{C.9}$$

$$\dot{\phi}_\mu = \sum_{m,l} \frac{2\sqrt{x_m x_l} \left(E_{ml} U^*_{\mu m} U^*_{\mu l} \mathrm{e}^{-i\phi_\mu} - E^*_{ml} U_{m\mu} U_{l\mu} \mathrm{e}^{i\phi_\mu} \right)}{i(1 - x_m x_l) \sinh(2r_\mu)}. \tag{C.10}$$

Now, to simplify Eq. (C.9) and Eq. (C.10), we focus on the first term of the sum. Using the expression for E_{ml} in Eq. (4.63), we obtain

$$\begin{aligned}
\sum_{m,l}\frac{\sqrt{x_m x_l}E_{ml}U^*_{\mu m}U^*_{\mu l}\mathrm{e}^{-i\phi_\mu}}{1-x_m x_l} &= \sum_{\sigma,\nu}\sum_{m,l}U_{m\sigma}U_{l\nu}U^*_{\mu m}U^*_{\mu l}\mathrm{e}^{i(\phi_\nu-\phi_\mu)}\cosh(r_\sigma)\sinh(r_\nu)\\
&\times\left(i\Omega_{\sigma\nu}+\frac{1}{2}\Gamma_{\sigma\nu}\frac{1+x_m x_l-2x_m}{1-x_m x_l}\right)\\
&-\frac{i}{\hbar}\sum_{\nu}\sum_{m,l}U_{m\nu}U_{l\nu}U^*_{\mu m}U^*_{\mu l}\mathrm{e}^{i(\phi_\nu-\phi_\mu)}\\
&\times\left(\alpha^2\lambda_\nu\mathrm{e}^{-i\phi_\nu}\cosh^2(r_\nu)+\alpha^{*2}\lambda^*_\nu\mathrm{e}^{i\phi_\nu}\sinh^2(r_\nu)\right)\\
&= i\Omega_{\mu\mu}\cosh(r_\mu)\sinh(r_\mu)\\
&-\frac{i}{\hbar}\left(\alpha^2\lambda_\mu\mathrm{e}^{-i\phi_\mu}\cosh^2(r_\mu)+\alpha^{*2}\lambda^*_\mu\mathrm{e}^{i\phi_\mu}\sinh^2(r_\mu)\right)\\
&+\frac{1}{2}\sum_{\sigma,\nu}\mathrm{e}^{i(\phi_\nu-\phi_\mu)}\Gamma_{\sigma\nu}\cosh(r_\sigma)\sinh(r_\nu)\\
&\times\sum_{m,l}U_{m\sigma}U_{l\nu}U^*_{\mu m}U^*_{\mu l}\frac{1+x_m x_l-2x_m}{1-x_m x_l}. \qquad \text{(C.11)}
\end{aligned}$$

Using Eq. (4.54) we can write Eq. (C.11) in terms of the thermal photon numbers as

$$\begin{aligned}
\sum_{m,l}\frac{\sqrt{x_m x_l}E_{ml}U^*_{\mu m}U^*_{\mu l}\mathrm{e}^{-i\phi_\mu}}{1-x_m x_l} &= i\Omega_{\mu\mu}\cosh(r_\mu)\sinh(r_\mu)\\
&-\frac{i}{\hbar}\left(\alpha^2\lambda_\mu\mathrm{e}^{-i\phi_\mu}\cosh^2(r_\mu)+\alpha^{*2}\lambda^*_\mu\mathrm{e}^{i\phi_\mu}\sinh^2(r_\mu)\right)\\
&-\frac{1}{2}\sum_{\sigma,\nu}\mathrm{e}^{i(\phi_\nu-\phi_\mu)}\Gamma_{\sigma\nu}\cosh(r_\sigma)\sinh(r_\nu)\\
&\times\sum_{m,l}U_{m\sigma}U_{l\nu}U^*_{\mu m}U^*_{\mu l}\frac{-n_m+n_l+1}{n_m+n_l+1}. \qquad \text{(C.12)}
\end{aligned}$$

The complex conjugate of Eq. (C.12) is

$$\begin{aligned}\sum_{m,l}\frac{\sqrt{x_m x_l}E^*_{ml}U_{\mu m}U_{\mu l}\mathrm{e}^{i\phi_\mu}}{1-x_m x_l} &= -i\Omega_{\mu\mu}\cosh(r_\mu)\sinh(r_\mu)\\ &+\frac{i}{\hbar}\left(\alpha^2\lambda_\mu\mathrm{e}^{-i\phi_\mu}\sinh^2(r_\mu)+\alpha^{*2}\lambda^*_\mu\mathrm{e}^{i\phi_\mu}\cosh^2(r_\mu)\right)\\ &-\frac{1}{2}\sum_{\sigma,\nu}\mathrm{e}^{-i(\phi_\nu-\phi_\mu)}\Gamma^*_{\sigma\nu}\cosh(r_\sigma)\sinh(r_\nu)\\ &\times\sum_{m,l}U^*_{m\sigma}U^*_{l\nu}U_{\mu m}U_{\mu l}\frac{-n_m+n_l+1}{n_m+n_l+1},\end{aligned}\tag{C.13}$$

where we have used the fact that $\Omega^*_{\mu\mu}=\Omega_{\mu\mu}$. Adding Eq. (C.12) and Eq. (C.13) together gives the equation for $\dot{r}_\mu$ in Eq. (4.69) in the main text. Subtracting Eq. (C.13) from Eq. (C.12) and dividing by $\frac{i}{2}\sinh(2r_\mu)$ (see Eq. (C.10)) gives the equation for $\dot{\phi}_\mu$ in Eq. (4.70) in the main text.

C.2.2 Equation for $\dot{n}_m$

As mentioned in Sec. 4.4.3 we obtain an equation for $\dot{n}_m$ by writing the operators $\widehat{b}^\dagger_m\widehat{b}_m$ and $\widehat{b}^\dagger_m\widehat{b}_l$ found in the expressions $T1$, $T2$, and $T3$ in terms of the Schmidt operator $\widehat{B}^\dagger_\mu\widehat{B}_\nu$, and then force the sum of the coefficients in front of $\widehat{B}^\dagger_\mu\widehat{B}_\nu$ equal to zero. The appropriate term in $T3$ (*i.e.* Eq. (4.52)) becomes

$$-\sum_m\widehat{b}^\dagger_m\widehat{b}_m\frac{\dot{x}_m}{x_m}=-\sum_{\mu,\nu}\sum_m U^*_{m\mu}U_{m\nu}\frac{\dot{x}_m}{x_m}\widehat{B}^\dagger_\mu\widehat{B}_\nu,\tag{C.14}$$

where we have used Eq. (4.34). The appropriate terms in $T1$ and $T2$ (*i.e.* Eq. (4.60) and Eq. (4.61)) become

$$\sum_{m,l} F_{ml}\widehat{b}_m^\dagger \widehat{b}_l = \sum_{\mu,\nu}\sum_{m,l} F_{ml}U^*_{m\mu}U_{l\nu}\widehat{B}^\dagger_\mu \widehat{B}_\nu, \tag{C.15}$$

and

$$\sum_{m,l} K_{ml}\widehat{b}_m^\dagger \widehat{b}_l = \sum_{\mu,\nu}\sum_{m,l} K_{ml}U^*_{m\mu}U_{l\nu}\widehat{B}^\dagger_\mu \widehat{B}_\nu. \tag{C.16}$$

Since we require that $0 = T1 + T2 + T3$ (see Eq. (4.49)), the sum of the coefficients multiplying $\widehat{B}^\dagger_\mu \widehat{B}_\nu$ in Eqs. (C.14) - (C.16) must be equal to zero

$$\sum_{m,l} U^*_{m\mu}U_{l\nu}\left(F_{ml} + K_{ml} - \frac{\dot{x}_m}{x_m}\right) = 0. \tag{C.17}$$

Multiplying Eq. (C.17) by $\sum_{\mu,\nu} U^*_{m\nu}U_{m\mu}$ and using the orthogonality relation $\sum_\mu U^*_{m\mu}U_{l\mu} = \delta_{ml}$, we obtain

$$F_{mm} + K_{mm} - \frac{\dot{x}_m}{x_m} = 0, \tag{C.18}$$

but from Eq. (4.57) we have that $F_{mm} = 0$. Therefore

$$\frac{\dot{x}_m}{x_m} = K_{mm}. \tag{C.19}$$

Using Eq. (4.64) in Eq. (C.19), we obtain

$$\frac{\dot{x}_m}{1-x_m} = \sum_{\mu,\nu} U_{m\mu}U^*_{m\nu}\Big(- x_m \Gamma_{\mu\nu}\cosh(r_\mu)\cosh(r_\nu) + \Gamma^*_{\mu\nu}\mathrm{e}^{i(\phi_\mu-\phi_\nu)}\sinh(r_\mu)\sinh(r_\nu)\Big). \tag{C.20}$$

Expressing Eq. (C.20) in terms of n_m gives

$$\frac{\dot{n}_m}{1+n_m} = \sum_{\mu,\nu} U_{m\mu}U^*_{m\nu}\Big(- \frac{n_m}{1+n_m}\Gamma_{\mu\nu}\cosh(r_\mu)\cosh(r_\nu) + \Gamma^*_{\mu\nu}\mathrm{e}^{i(\phi_\mu-\phi_\nu)}\sinh(r_\mu)\sinh(r_\nu)\Big), \tag{C.21}$$

which is Eq. (4.71) in the text.

C.3 Solving the coupled equations from an initial vacuum state

In this section we discuss how to solve Eqs. (4.69) - (4.71) for a system that initially starts in the *vacuum state*. At time $t = 0$ the vacuum state is defined by

$$r_\mu(0) = 0, \tag{C.22}$$

$$n_m(0) = 0, \tag{C.23}$$

for all μ and m. Putting these initial conditions into Eq. (4.69) we obtain

$$\dot{r}_\mu(0) = \frac{2\,|\alpha(0)|^2\,|\lambda_\mu|}{\hbar}\sin\left(-\phi_\mu(0)+\theta_\mu\right), \tag{C.24}$$

where we define

$$\alpha(t)^2 = |\alpha(t)|^2 \exp(-2i\omega_P t), \tag{C.25}$$

and

$$\lambda_\mu = |\lambda_\mu| \exp(i\theta_\mu), \tag{C.26}$$

where θ_μ is a real number. We choose the initial squeezing phase, $\phi_\mu(0)$, to be

$$\phi_\mu(0) = \theta_\mu - \frac{\pi}{2}, \tag{C.27}$$

such that is maximizes the squeezing amplitude at the next time-step, $r_\mu(\Delta t)$:

$$r_\mu(\Delta t) = \frac{2\,|\alpha(0)|^2\,|\lambda_\mu|}{\hbar}\Delta t + O\left((\Delta t)^2\right). \tag{C.28}$$

Now, let us move on to the equation for the squeezing phase, Eq. (4.70). It is easily shown that using Eqs. (C.22), (C.23), and (C.27) will result in the second and third terms in Eq. (4.70) being indeterminate (0/0). Thus, at $t = 0$, we write this equation as

$$\dot{\phi}_\mu(0) = -2\Omega_{\mu\mu} - \zeta_\mu, \tag{C.29}$$

where we let ζ_μ be the indeterminate form. We are unable to solve these equations unless we define ζ_μ. We define ζ_μ by requiring that the derivatives of the squeezing phase at $t = \Delta t$ and $t = 0$ are the same,

$$\dot{\phi}_\mu(\Delta t) = \dot{\phi}_\mu(0), \tag{C.30}$$

such that initially the squeezing phase is a linear function of time. Putting Eqs. (C.22), (C.23), (C.27), and (C.28) into Eq. (4.70) and using the fact that $n_m(\Delta t) = 0$ (which can be proven by writing Eq. (4.71) as a difference equation and using the initial conditions) it can be shown that

$$\dot{\phi}_\mu(\Delta t) = -2\omega_P + \zeta_\mu. \tag{C.31}$$

Using Eq. (C.31) in Eq. (C.30), the indeterminate form ζ_μ is defined as

$$\zeta_\mu = -\Omega_{\mu\mu} + \omega_P. \tag{C.32}$$

To solve Eqs. (4.69) - (4.71) we use MATLAB's ode45 function, that is based on a Runge-Kutta method. The initial conditions that we use for the squeezing amplitudes, thermal photon numbers, and squeezing phases are in Eqs. (C.22), (C.23), and (C.27). We have to write an additional condition in the code that imposes the condition that at $t = 0$ the derivatives of the squeezing phases are equal to $\dot{\phi}_\mu(0) = -\Omega_{\mu\mu} - \omega_P$, otherwise the program will return a division-by-zero error (as discussed above). The solution is sensitive to the initial squeezing phases $\phi_\mu(0)$. It is crucial that they are set to precisely the values given in Eq. (C.27) in order to obtain the results we present in Sec. 4.7. We find, however, that the initial value of the derivative of the phase $\dot{\phi}_\mu(0)$ has little impact on the final solution, since it quickly settles to the correct value, given by $-\Omega_{\mu\mu} - \omega_P$.

Appendix D

Supplemental material for Chapter 5

D.1 Nonorthogonal quasimodes

In this section, we define the lossy nonorthogonal quasimodes of a resonant structure and their spatial overlap. We also derive an expression for the upper bound on the overlap.

We consider an open dielectric system with out-going boundary conditions. The positive frequency part of the electric field in a lossy quasimode m takes the form [9]

$$\boldsymbol{E}^{(+)}(\boldsymbol{r},t) = \boldsymbol{N}_m(\boldsymbol{r})\mathrm{e}^{-i\widetilde{\omega}_m t}, \tag{D.1}$$

where $\boldsymbol{N}_m(\boldsymbol{r})$ is the spatial profile of the quasimode, and its complex frequency is $\widetilde{\omega}_m \equiv \omega_m - i\gamma_m$. Each quasimode is a solution to the Helmholtz equation:

$$\nabla \times \nabla \times \boldsymbol{N}_m(\boldsymbol{r}) - \frac{\widetilde{\omega}_m^2}{c^2}\epsilon(\boldsymbol{r})\boldsymbol{N}_m(\boldsymbol{r}) = 0, \tag{D.2}$$

where $\epsilon(\boldsymbol{r})$ is the real, relative dielectric function for the structure. We define the inner product between two quasimodes of different frequency $\widetilde{\omega}_m$ and $\widetilde{\omega}_l$ as

$$\langle \boldsymbol{N}_m | \boldsymbol{N}_l \rangle \equiv \int d^3\boldsymbol{r}\epsilon(\boldsymbol{r})\boldsymbol{N}_m^*(\boldsymbol{r}) \cdot \boldsymbol{N}_l(\boldsymbol{r}). \tag{D.3}$$

The quasimodes are calculated within a computational volume that is bounded by perfectly-matched layers (PMLs) in order to simulate open boundary conditions. The integral in Eq. (D.3) is done over the computational volume only, that excludes the PMLs. Throughout this work, the fields in the PMLs are excluded from all integrals.

The normalized quasimode overlap is

$$O_{ml} \equiv \frac{\langle \boldsymbol{N}_m | \boldsymbol{N}_l \rangle}{\sqrt{\langle \boldsymbol{N}_m | \boldsymbol{N}_m \rangle \langle \boldsymbol{N}_l | \boldsymbol{N}_l \rangle}}. \tag{D.4}$$

Note that $\boldsymbol{O}$ is a Hermitian matrix. For a general system of coupled-cavities, the off-diagonal elements of the overlap are non-zero. Therefore, the quasimodes form a nonorthogonal basis.

As we shall show below, the upper bound on the overlap in Eq. (D.4) is derived by requiring that the quasimodes satisfy outgoing-wave boundary conditions at edge of the computational volume. We will show it is given by

$$|O_{ml}|^2 \leq \frac{4\gamma_m\gamma_l}{(\omega_m - \omega_l)^2 + (\gamma_m + \gamma_l)^2}. \tag{D.5}$$

Using this result one can get some idea if the overlap between two quasimodes is negligible or not. For example, if the difference between the real parts of the frequencies is much larger than the sum of the imaginary parts (*i.e.* $|\omega_m - \omega_l| \gg \gamma_m + \gamma_l$), then the overlap is approximately given by $|O_{ml}|^2 \approx 4\gamma_m\gamma_l/(\omega_m - \omega_l)^2$, and this will approach zero the larger the frequency difference is. Therefore, quasimodes that are separated in frequency by much more than their line-widths will have a negligible overlap and will be approximately orthogonal. Alternatively, if two quasimodes are close in frequency (*i.e.* $\omega_m \approx \omega_l$), then the overlap is approximately given by $|O_{ml}|^2 \approx 4\gamma_m\gamma_l/(\gamma_m+\gamma_l)^2$, which will be close to one. Therefore, quasimodes that are close in frequency can generally have a large overlap, unless some symmetry forbids it. We find that this overlap can be very large in systems of coupled-cavities in a photonic crystal slab, such as the two-defect structure discussed in the paper.

Now we derive Eq. (D.5). First, we combine Eqs. (D.2) and (D.3) to obtain

$$\frac{1}{c^2}\left(\widetilde{\omega}_m^{*2} - \widetilde{\omega}_l^2\right)\langle \boldsymbol{N}_m|\boldsymbol{N}_l\rangle = \mathcal{A}_{ml} - \mathcal{A}_{lm}^*, \tag{D.6}$$

where

$$\mathcal{A}_{ml} \equiv \int d^3\boldsymbol{r}\,[\nabla\times\nabla\times\boldsymbol{N}_m^*(\boldsymbol{r})]\cdot\boldsymbol{N}_l(\boldsymbol{r}). \tag{D.7}$$

Immediately, we see that if $\mathcal{A}$ is a Hermitian matrix, then O_{ml} must be zero and the quasimodes are orthogonal. However, we show that $\mathcal{A}$ is not Hermitian due to the lossy nature of the quasimodes. Using the vector calculus identity $\nabla\cdot(\boldsymbol{P}\times\boldsymbol{Q}) = (\nabla\times\boldsymbol{P})\cdot\boldsymbol{Q} - (\nabla\times\boldsymbol{Q})\cdot\boldsymbol{P}$, with $\boldsymbol{P}\equiv\nabla\times\boldsymbol{N}_m^*$ and $\boldsymbol{Q}\equiv\boldsymbol{N}_l$, Eq. (D.7) can be written as

$$\mathcal{A}_{ml} = \int d^3\boldsymbol{r}\,[\nabla\times\boldsymbol{N}_l(\boldsymbol{r})]\cdot[\nabla\times\boldsymbol{N}_m^*(\boldsymbol{r})] + \int_{\partial V}[(\nabla\times\boldsymbol{N}_m^*(\boldsymbol{r}))\times\boldsymbol{N}_l(\boldsymbol{r})]\cdot d\boldsymbol{A}, \tag{D.8}$$

where we have used the divergence theorem to obtain the last term in Eq. (D.8), with ∂V defined as the surface boundary of the computational volume V and $d\boldsymbol{A}$ is an infinitesimal area element on and normal to the surface boundary. The first term in Eq. (D.8) is clearly Hermitian, however the surface integral in the second term is not. It is this integral of the quasimodes on the surface boundary that causes the problem to be non Hermitian and the quasimodes to be nonorthogonal. Using Eq. (D.8), the right-hand side of Eq. (D.6) can be written as

$$\mathcal{A}_{ml} - \mathcal{A}_{lm}^* = \int_{\partial V} \Big[(\nabla \times \boldsymbol{N}_m^*(\boldsymbol{r})) \times \boldsymbol{N}_l(\boldsymbol{r}) - (\nabla \times \boldsymbol{N}_l(\boldsymbol{r})) \times \boldsymbol{N}_m^*(\boldsymbol{r}) \Big] \cdot d\boldsymbol{A}. \tag{D.9}$$

The surface boundary is taken to be the edge of the computational volume (but excluding the PMLs), and it must be far from any sources, such that the modes are given by out-going waves. In the standard treatment of electric and magnetic field normal modes, the surface integrals in Eq. (D.9) are zero because the normal modes decay to zero at infinity. This is the origin of the orthogonality of the normal modes. However, due to the lossy nature of the quasimodes, mathematically they do not decay to zero at the surface boundary. This is because at the surface the quasimodes are out-going waves, with a complex wavevector that causes them to diverge. Therefore, the surface integral in Eq. (D.6) quantifies the nonorthogonality of the quasimodes.

To evaluate Eq. (D.9) we take the surface boundary to be a sphere of radius r, and we let $r \to \infty$. We assume that at infinity there is a homogeneous background dielectric material of a constant index of refraction. We let the quasimodes be given by spherical outgoing waves as $r \to \infty$, that are polarized tangentially to the surface of the sphere. They have the form

$$\boldsymbol{N}_m(r,\theta,\phi) = [h_{m\theta}(\theta,\phi)\hat{\epsilon}_\theta + h_{m\phi}(\theta,\phi)\hat{\epsilon}_\phi]\,\frac{\mathrm{e}^{i\tilde{k}_m r}}{r}, \tag{D.10}$$

where $\widetilde{k}_m = (\omega_m - i\gamma_m)n/c$ is the complex wavevector, where n is the index of refraction of the homogeneous background dielectric. The components of the quasimodes in the $\hat{\epsilon}_\theta$ and $\hat{\epsilon}_\phi$ directions are $h_{m\theta}(\theta,\phi)$ and $h_{m\phi}(\theta,\phi)$, respectively, and they do not depend on r. There is no component of the quasimodes in the $\hat{\epsilon}_r$ direction. Note that the combination of $i\widetilde{k}_m$ in Eq. (D.10) causes the quasimodes to exponentially increase as $r \to \infty$. This is because the exponential increases faster than $1/r$ decreases. Putting Eq. (D.10) into Eq. (D.9), defining $d\boldsymbol{A} \equiv r^2 \sin(\theta) d\theta d\phi \hat{\epsilon}_r$, and doing the cross-products in spherical coordinates, we obtain

$$\mathcal{A}_{ml} - \mathcal{A}^*_{lm} = \frac{i}{n^2} \langle \boldsymbol{h}_m | \boldsymbol{h}_l \rangle \left(\widetilde{k}^*_m + \widetilde{k}_l \right) \mathrm{e}^{-i(\widetilde{k}^*_m - \widetilde{k}_l)r}, \tag{D.11}$$

where $\langle \boldsymbol{h}_m | \boldsymbol{h}_l \rangle$ is the inner product on the surface boundary, defined by

$$\langle \boldsymbol{h}_m | \boldsymbol{h}_l \rangle \equiv n^2 \iint \boldsymbol{h}^*_m(\theta,\phi) \cdot \boldsymbol{h}_l(\theta,\phi) \sin(\theta) d\theta d\phi. \tag{D.12}$$

Putting Eq. (D.11) into Eq. (D.6), the quasimode inner product can be written as

$$\langle \boldsymbol{N}_m | \boldsymbol{N}_l \rangle = i \langle \boldsymbol{h}_m | \boldsymbol{h}_l \rangle \frac{\mathrm{e}^{-i(\widetilde{k}^*_m - \widetilde{k}_l)r}}{\widetilde{k}^*_m - \widetilde{k}_l}, \tag{D.13}$$

where we used the fact that $\widetilde{\omega}^{*2}_m - \widetilde{\omega}^2_l = (c/n)^2(\widetilde{k}^*_m + \widetilde{k}_l)(\widetilde{k}^*_m - \widetilde{k}_l)$. Therefore if the inner product on the boundary is zero, $\langle \boldsymbol{h}_m | \boldsymbol{h}_l \rangle = 0$, then the quasimodes are orthogonal. Putting Eq. (D.13) into Eq. (D.4), it can be shown that the absolute square of the overlap is given by

$$|O_{ml}|^2 = \frac{|\langle \boldsymbol{h}_m | \boldsymbol{h}_l \rangle|^2}{\langle \boldsymbol{h}_m | \boldsymbol{h}_m \rangle \langle \boldsymbol{h}_l | \boldsymbol{h}_l \rangle} \frac{4\gamma_m \gamma_l}{(\omega_m - \omega_l)^2 + (\gamma_m + \gamma_l)^2}. \tag{D.14}$$

Now using the Cauchy-Schwarz inequality, $|\langle \boldsymbol{h}_m|\boldsymbol{h}_l\rangle|^2 \leq \langle \boldsymbol{h}_m|\boldsymbol{h}_m\rangle \langle \boldsymbol{h}_l|\boldsymbol{h}_l\rangle$, the upper bound of the overlap in Eq. (D.14) is

$$|O_{ml}|^2 = \frac{4\gamma_m\gamma_l}{(\omega_m - \omega_l)^2 + (\gamma_m + \gamma_l)^2}. \tag{D.15}$$

Therefore, $|O_{ml}|^2$ is always less than this upper bound, and we obtain the inequality in Eq. (D.5).

D.2 The Lindblad master equation

In this section, we present the Lindblad master equation, that was derived using the quasimode projection technique [9], written in terms of the quasimode operators. We show that we obtain the exact same form for the Lindblad master equation that was derived using a different quantization approach using quasi-normal modes [111].

The system Hamiltonian can be written as

$$\widehat{H} = \widehat{H}_{\mathrm{L}} + \widehat{H}_{\mathrm{NL}}. \tag{D.16}$$

In the basis of the discrete quasimodes, it can be shown that the linear part is given by [9]

$$\widehat{H}_{\mathrm{L}} = \hbar \sum_{m,l} \widetilde{\omega}_l O_{ml} \widehat{c}_m^\dagger \widehat{c}_l, \tag{D.17}$$

where $\widehat{c}_m^\dagger$ and $\widehat{c}_m$ are the creation and annihilation operators for photons in the mth quasimode. They satisfy the commutation relation

$$\left[\widehat{c}_m, \widehat{c}_l^\dagger\right] = O_{ml}^{-1}, \tag{D.18}$$

where $\boldsymbol{O}^{-1}$ is the inverse of the overlap matrix of Eq. (D.4), satisfying

$$\mathbf{1} = \boldsymbol{O}^{-1}\boldsymbol{O}. \tag{D.19}$$

We let the nonlinear Hamiltonian account for the SFWM interaction that generates the squeezed light. We take the pump to be a classical field in a single quasimode, P. Using the undepleted pump approximation, the nonlinear Hamiltonian is given by

$$\widehat{H}_{\mathrm{NL}} = \hbar\alpha^2(t)\sum_{m,l} G_{ml}\widehat{c}_m^\dagger\widehat{c}_l^\dagger + \mathrm{H.c.}, \tag{D.20}$$

where $\alpha(t) = |\alpha_P|\mathrm{e}^{-i\omega_P t}$ is the pump amplitude with frequency ω_P, and G_{ml} is the nonlinear parameter for SFWM given by

$$G_{ml} \equiv \frac{9\hbar\omega_P}{16\epsilon_0}\sum_{i,j,k,h}\sqrt{\widetilde{\omega}_m^*\widetilde{\omega}_l^*}\int d^3\boldsymbol{r}\chi_{ijkh}^{(3)}(\boldsymbol{r})N_{mi}^*(\boldsymbol{r})N_{lj}^*(\boldsymbol{r})N_{Pk}(\boldsymbol{r})N_{Ph}(\boldsymbol{r}), \tag{D.21}$$

where i, j, k, and h are the Cartesian components of the spatially-dependent third-order nonlinear susceptibility tensor $\chi_{ijkh}^{(3)}(\boldsymbol{r})$.

The Lindblad master equation for the density operator $\widehat{\rho}(t)$ was derived in previous work, using the quasimode projection approach, for nonorthogonal quasimodes. It is given by [97]

$$\frac{d\widehat{\rho}}{dt} = \frac{-i}{\hbar}\left[\widehat{H}_{\mathrm{L}}^{(+)} + \widehat{H}_{\mathrm{NL}}, \widehat{\rho}\right] + \frac{i}{2}\sum_{m,l}\left(\widetilde{\omega}_l - \widetilde{\omega}_m^*\right) O_{ml}\left(2\widehat{c}_l\widehat{\rho}\widehat{c}_m^\dagger - \widehat{\rho}\widehat{c}_m^\dagger\widehat{c}_l - \widehat{c}_m^\dagger\widehat{c}_l\widehat{\rho}\right), \quad \text{(D.22)}$$

where $\widehat{H}_L^{(+)}$ is the Hermitian part of the linear Hamiltonian and is defined as

$$\widehat{H}_L^{(+)} \equiv \frac{\hbar}{2}\sum_{m,l}\left(\widetilde{\omega}_l + \widetilde{\omega}_m^*\right) O_{ml}\widehat{c}_m^\dagger\widehat{c}_l. \quad \text{(D.23)}$$

The expressions for the quantized Hamiltonian and the Lindblad master equation are written in terms of the quasimode annihilation and creation operators, which do not obey the standard commutation relation for bosons. This is a result of the quantization approach used. In a different quantization approach that uses quasinormal modes [111], the Hamiltonian and Lindblad master equation are written in terms of photon operators that do obey the standard commutator. Now we show that we can connect the two approaches by doing a symmetrization transformation of the quasimode operators (similar to Ref. [111])

$$\widehat{a}_m \equiv \sum_l O_{ml}^{1/2}\widehat{c}_l, \quad \text{(D.24)}$$

such that these operators have the standard commutation relation

$$[\widehat{a}_m, \widehat{a}_l^\dagger] = \delta_{ml}, \quad \text{(D.25)}$$

which can be derived using Eqs. (D.18) and (D.19). Writing $\widehat{H}_L^{(+)}$ in Eq. (D.23) in terms of these operators, we obtain

$$\widehat{H}_L^{(+)} = \hbar \sum_{m,l} \chi_{ml}^{(+)} \widehat{a}_m^\dagger \widehat{a}_l, \tag{D.26}$$

and for the Lindblad master equation in Eq. (D.22), we obtain

$$\frac{d\widehat{\rho}}{dt} = \frac{-i}{\hbar}\left[\widehat{H}_{\mathrm{L}}^{(+)} + \widehat{H}_{\mathrm{NL}}, \widehat{\rho}\right] + \sum_{m,l} \chi_{ml}^{(-)} \left(2\widehat{a}_l \widehat{\rho} \widehat{a}_m^\dagger - \widehat{\rho}\widehat{a}_m^\dagger \widehat{a}_l - \widehat{a}_m^\dagger \widehat{a}_l \widehat{\rho}\right). \tag{D.27}$$

Here $\boldsymbol{\chi}^{(-)}$ and $\boldsymbol{\chi}^{(+)}$ are Hermitian matrices defined as

$$\boldsymbol{\chi}^{(-)} \equiv \frac{i}{2}\left(\boldsymbol{\chi} - \boldsymbol{\chi}^\dagger\right), \tag{D.28}$$

$$\boldsymbol{\chi}^{(+)} \equiv \frac{1}{2}\left(\boldsymbol{\chi} + \boldsymbol{\chi}^\dagger\right), \tag{D.29}$$

where,

$$\boldsymbol{\chi} \equiv \boldsymbol{O}^{1/2} \widetilde{\boldsymbol{\omega}} \boldsymbol{O}^{-1/2}, \tag{D.30}$$

where $\widetilde{\boldsymbol{\omega}} \equiv \mathrm{diag}(\widetilde{\omega}_1, \ldots)$. The matrices $\chi_{ml}^{(+)}$ and $\chi_{ml}^{(-)}$ give the coupling between different quasimodes in the Hamiltonian and Lindblad dissipator. The coupling will be strong for quasimodes that have a large overlap. Note that if the quasimodes are orthogonal to each other, with $\boldsymbol{O} = \mathbf{1}$, then $\boldsymbol{\chi}^{(-)} = \mathrm{diag}(\gamma_1, \ldots)$ and $\boldsymbol{\chi}^{(+)} = \mathrm{diag}(\omega_1, \ldots)$ are just proportional to the imaginary and real parts of the complex frequency $\widetilde{\omega}_m$. This will give the usual form of the Hamiltonian and Lindblad dissipator for orthogonal modes.

The nonlinear Hamiltonian in Eq. (D.20) can be written using $\widehat{a}_m$ and $\widehat{a}_m^\dagger$ as

$$\widehat{H}_{\rm NL} = \hbar\alpha^2(t)\sum_{m,l} S_{ml}\widehat{a}_m^\dagger\widehat{a}_l^\dagger + {\rm H.c.}, \tag{D.31}$$

where $\boldsymbol{S}$ is the nonlinear parameter defined by

$$\boldsymbol{S} \equiv \boldsymbol{O}^{-1/2}\boldsymbol{G}\left[\boldsymbol{O}^{-1/2}\right]^{\rm T}. \tag{D.32}$$

Note that $\boldsymbol{S}$ is also a complex symmetric matrix, with $\boldsymbol{S}^{\rm T} = \boldsymbol{S}$.

Equations (D.26) and (D.27), that were derived using the quasimode projection approach, have the exact same form as those that were derived using a different quantization approach using the quasi-normal mode formalism (see Eqs. (28a) and (30) in Ref. [112]). Therefore, the form of the density operator solution to the Lindblad master equation does not depend on the quasimode quantization approach used, and so our analytic solution is applicable to both approaches, provided that the dielectric function for the material is real.

D.2.1 The diagonalized form of the Lindblad master equation

In this subsection we write the Lindblad master equation in Eq. (D.27) in its diagonal form. It is important to do this, because it will help us derive the analytic solution to the Lindblad master equation in the next section. The diagonalization can be achieved by decomposing the quasimode coupling matrix $\boldsymbol{\chi}^{(-)}$ with the singular value decomposition

$$\boldsymbol{\chi}^{(-)} = \boldsymbol{M}^{(-)}\boldsymbol{\gamma}^{\rm s}\boldsymbol{M}^{(-)\dagger}, \tag{D.33}$$

where $\boldsymbol{M}^{(-)}\boldsymbol{M}^{(-)\dagger}=1$ and $\boldsymbol{\gamma}^{\mathrm{s}}\equiv\mathrm{diag}(\gamma^{\mathrm{s}}_1,\ldots)$ is a diagonal matrix of the singular values. Putting Eq. (D.33) into Eq. (D.27), we obtain

$$\frac{d\widehat{\rho}}{dt}=\frac{-i}{\hbar}\left[\widehat{H}^{(+)}_{\mathrm{L}}+\widehat{H}_{\mathrm{NL}},\widehat{\rho}\right]+\sum_{\sigma}\gamma^{\mathrm{s}}_{\sigma}\left(2\widehat{A}_{\sigma}\widehat{\rho}\widehat{A}^{\dagger}_{\sigma}-\widehat{\rho}\widehat{A}^{\dagger}_{\sigma}\widehat{A}_{\sigma}-\widehat{A}^{\dagger}_{\sigma}\widehat{A}_{\sigma}\widehat{\rho}\right), \tag{D.34}$$

which is the diagonal form of the Lindblad master equation. We define the creation operator

$$\widehat{A}^{\dagger}_{\sigma}\equiv\sum_{m}M^{(-)}_{m\sigma}\widehat{a}^{\dagger}_{m}, \tag{D.35}$$

that statisfies the commutator $[\widehat{A}_{\sigma},\widehat{A}^{\dagger}_{\sigma'}]=\delta_{\sigma\sigma'}$.

D.3 Deriving the coupled equations for M nonorthogonal modes

In this section, we show that the analytic solution to the Lindblad master equation for SFWM is the density operator, $\widehat{\rho}(t)$, for an MSTS, given by

$$\widehat{\rho}(t)=\widehat{S}(t)\widehat{\rho}_{\mathrm{th}}(t)\widehat{S}^{\dagger}(t), \tag{D.36}$$

where $\widehat{S}(t)$ is given in Eq. (5.7) and $\widehat{\rho}_{\mathrm{th}}(t)$ is given in Eq. (5.8). To prove that this is the solution, we require that $\widehat{\rho}(t)$ to be a solution of

$$1=\widehat{\rho}_{\mathrm{th}}^{-1/2}(t)\widehat{S}^{\dagger}(t)\widehat{\rho}(t)\widehat{S}(t)\widehat{\rho}_{\mathrm{th}}^{-1/2}(t), \tag{D.37}$$

where we used the fact that $\widehat{S}^\dagger(t)\widehat{S}(t) = 1$. Since Eq. (D.37) is true for all times, if we take the time derivative of both sides, we obtain

$$\begin{aligned} 0 = {} & \widehat{\rho}_{\text{th}}^{1/2}\widehat{S}^\dagger\frac{d\widehat{S}}{dt}\widehat{\rho}_{\text{th}}^{-1/2} - \widehat{\rho}_{\text{th}}^{-1/2}\widehat{S}^\dagger\frac{d\widehat{S}}{dt}\widehat{\rho}_{\text{th}}^{1/2} \\ & + 2\frac{d\widehat{\rho}_{\text{th}}^{-1/2}}{dt}\widehat{\rho}_{\text{th}}^{1/2} + \widehat{\rho}_{\text{th}}^{-1/2}\widehat{S}^\dagger\frac{d\widehat{\rho}}{dt}\widehat{S}\widehat{\rho}_{\text{th}}^{-1/2}, \end{aligned} \tag{D.38}$$

where we dropped the time-dependence of the operators for convenience. We obtain the coupled-equations Eqs. (5.9) - (5.11) by simplifying the four terms on the right-hand side of Eq. (D.38). Our strategy is to put the expressions for $\widehat{S}(t)$, $\widehat{\rho}_{\text{th}}(t)$, and $d\widehat{\rho}(t)/dt$ into Eq. (D.38). As we will show, the right-hand side can be written in terms of three Schrödinger operators: $\widehat{A}_\sigma^\dagger\widehat{A}_\nu$, $\widehat{\mathcal{Q}}_{\sigma\nu}$ (Eq. (D.48)), and $\widehat{\mathcal{P}}_{\sigma\nu}$ (Eq. (D.49)), that are common to each term, and are multiplied by time-dependent coefficients that depend on $r_\mu(t)$, $\phi_\mu(t)$, and $n_\mu(t)$ and their first time-derivatives. To satisfy Eq. (D.38), and obtain the coupled-equations, we let the coefficients in front of the three operators equal zero.

We define the following terms that help in the derivation:

$$T_1 \equiv 2\frac{d\widehat{\rho}_{\text{th}}^{-1/2}}{dt}\widehat{\rho}_{\text{th}}^{1/2}, \tag{D.39}$$

$$T_2 \equiv \widehat{\rho}_{\text{th}}^{1/2}\widehat{S}^\dagger\frac{d\widehat{S}}{dt}\widehat{\rho}_{\text{th}}^{-1/2} - \widehat{\rho}_{\text{th}}^{-1/2}\widehat{S}^\dagger\frac{d\widehat{S}}{dt}\widehat{\rho}_{\text{th}}^{1/2}, \tag{D.40}$$

$$T_3 \equiv \widehat{\rho}_{\text{th}}^{-1/2}\widehat{S}^\dagger\frac{d\widehat{\rho}}{dt}\widehat{S}\widehat{\rho}_{\text{th}}^{-1/2}. \tag{D.41}$$

Using the definition of $\widehat{\rho}_{\text{th}}(t)$ in Eq. (5.8), it can be shown that T_1 simplifies to

$$\begin{aligned} T_1 = &-\sum_{\kappa} \frac{1}{n_\kappa(1+n_\kappa)} \frac{dn_\kappa}{dt} \sum_{\sigma,\nu} W^*_{\kappa\sigma} W_{\kappa\nu} \widehat{A}^\dagger_\sigma \widehat{A}_\nu \\ &+ \sum_\kappa \frac{1}{1+n_\kappa} \frac{dn_\kappa}{dt}. \end{aligned} \tag{D.42}$$

Moving on to T_2, we first simplify the time-derivative of the squeezing operator. It can be shown that [82]

$$\begin{aligned} \widehat{S}^\dagger \frac{d\widehat{S}}{dt} = \sum_\mu \Bigg(&\frac{i}{2} \sinh^2(r_\mu) \frac{d\phi_\mu}{dt} \left(2\widehat{B}^\dagger_\mu \widehat{B}_\mu + 1\right) \\ &+ \left(\frac{1}{2}\frac{dr_\mu}{dt} + \frac{i}{4}\sinh(2r_\mu)\frac{d\phi_\mu}{dt}\right) \mathrm{e}^{i\phi_\mu} \widehat{B}^{\dagger 2}_\mu \\ &- \left(\frac{1}{2}\frac{dr_\mu}{dt} - \frac{i}{4}\sinh(2r_\mu)\frac{d\phi_\mu}{dt}\right) \mathrm{e}^{-i\phi_\mu} \widehat{B}^{2}_\mu \Bigg). \end{aligned} \tag{D.43}$$

Now to simplify T_2 we need to perform the thermal transformations on Eq. (D.43). These can be done with

$$\widehat{\rho}_{\text{th}}^{\pm 1/2} \widehat{B}_\mu \widehat{\rho}_{\text{th}}^{\mp 1/2} = \sum_{\kappa,\sigma} Y^*_{\kappa\mu} x_\kappa^{\mp 1/2} W_{\kappa\sigma} \widehat{A}_\sigma, \tag{D.44}$$

$$\widehat{\rho}_{\text{th}}^{\pm 1/2} \widehat{B}^\dagger_\mu \widehat{\rho}_{\text{th}}^{\mp 1/2} = \sum_{\kappa,\sigma} Y_{\kappa\mu} x_\kappa^{\pm 1/2} W^*_{\kappa\sigma} \widehat{A}^\dagger_\sigma, \tag{D.45}$$

where $\boldsymbol{W} \equiv \boldsymbol{Y}\boldsymbol{V}^\dagger$ and we define

$$x_\mu \equiv \frac{n_\mu}{1+n_\mu}. \tag{D.46}$$

Using Eqs. (D.44) and (D.43), it can be shown that T_2 simplifies to

$$T_2 = \sum_{\sigma,\nu} \left(F_{\sigma\nu} \widehat{A}_\sigma^\dagger \widehat{A}_\nu + \mathrm{Re}[D_{\sigma\nu}] \widehat{\mathcal{Q}}_{\sigma\nu} + \mathrm{Im}[D_{\sigma\nu}] \widehat{\mathcal{P}}_{\sigma\nu} \right), \tag{D.47}$$

where we define two Schrödinger operators

$$\widehat{\mathcal{Q}}_{\sigma\nu} \equiv \widehat{A}_\sigma \widehat{A}_\nu + \widehat{A}_\sigma^\dagger \widehat{A}_\nu^\dagger, \tag{D.48}$$

$$\widehat{\mathcal{P}}_{\sigma\nu} \equiv -i\widehat{A}_\sigma \widehat{A}_\nu + i\widehat{A}_\sigma^\dagger \widehat{A}_\nu^\dagger, \tag{D.49}$$

and the time-dependent coefficients

$$F_{\sigma\nu} \equiv \sum_{\mu,\kappa,\kappa'} i \sinh^2(r_\mu) \frac{d\phi_\mu}{dt} Y_{\kappa\mu} Y_{\kappa'\mu}^* W_{\kappa\sigma} W_{\kappa'\nu}^* \left[x_\kappa^{1/2} x_{\kappa'}^{-1/2} - x_\kappa^{-1/2} x_{\kappa'}^{1/2} \right], \tag{D.50}$$

$$D_{\sigma\nu} \equiv \sum_{\mu,\kappa,\kappa'} \left(\frac{1}{2}\frac{dr_\mu}{dt} + \frac{i}{4}\sinh(2r_\mu)\frac{d\phi_\mu}{dt} \right) \mathrm{e}^{i\phi_\mu} Y_{\kappa\mu} Y_{\kappa'\mu} W_{\kappa\sigma}^* W_{\kappa'\nu}^* \left[x_\kappa^{1/2} x_{\kappa'}^{1/2} - x_\kappa^{-1/2} x_{\kappa'}^{-1/2} \right], \tag{D.51}$$

where $\mathrm{Re}[D_{\sigma\nu}]$ and $\mathrm{Im}[D_{\sigma\nu}]$ are the real and imaginary parts of $D_{\sigma\nu}$.

Moving on to T_3, the squeezing transformation of the Lindblad master equation in Eq. (D.34) can be done using

$$\widehat{S}^\dagger \widehat{A}_\sigma \widehat{S} = \sum_\mu V_{\sigma\mu} \widehat{S}^\dagger \widehat{B}_\mu \widehat{S}, \tag{D.52}$$

$$\widehat{S}^\dagger \widehat{C}_\kappa \widehat{S} = \sum_\mu Y_{\kappa\mu} \widehat{S}^\dagger \widehat{B}_\mu \widehat{S}, \tag{D.53}$$

where the squeezing transformation of the $\widehat{B}_\mu$ operators is

$$\widehat{S}^\dagger \widehat{B}_\mu \widehat{S} = \cosh(r_\mu)\widehat{B}_\mu + \mathrm{e}^{i\phi_\mu}\sinh(r_\mu)\widehat{B}_\mu^\dagger. \tag{D.54}$$

After performing the squeezing transformation in T_3, the remaining thermal transformation can be done using Eq. (D.44). Doing this we obtain

$$\begin{aligned} T_3 = &\sum_{\sigma,\nu}\Big(K_{\sigma\nu}\widehat{A}_\sigma^\dagger \widehat{A}_\nu + \mathrm{Re}[E_{\sigma\nu}]\widehat{\mathcal{Q}}_{\sigma\nu} + \mathrm{Im}[E_{\sigma\nu}]\widehat{\mathcal{P}}_{\sigma\nu}\Big) + 2\sum_{\nu,\sigma,\nu'}\Gamma_{\sigma\nu}\cosh(r_\sigma)\cosh(r_\nu)Y^*_{\sigma\nu'}Y_{\nu\nu'}x_{\nu'} \\ &- 2\sum_{\nu}\Gamma_{\nu\nu}\sinh^2(r_\nu), \end{aligned} \tag{D.55}$$

where

$$
\begin{aligned}
E_{\sigma\nu} = {} & \sum_{\mu,\mu',\kappa',\kappa} \mathrm{e}^{i\phi_{\mu'}} \cosh(r_\mu)\sinh(r_{\mu'}) Y_{\kappa'\mu} Y_{\kappa\mu'} W^*_{\kappa'\sigma} W^*_{\kappa\nu} \\
& \times \left(i\Omega_{\mu\mu'} \left[x_{\kappa'}^{1/2} x_\kappa^{1/2} - x_{\kappa'}^{-1/2} x_\kappa^{-1/2} \right] - \Gamma_{\mu'\mu} \left[x_{\kappa'}^{1/2} x_\kappa^{1/2} + x_{\kappa'}^{-1/2} x_\kappa^{-1/2} - 2 x_\kappa^{-1/2} x_{\kappa'}^{1/2} \right] \right) \\
& + i \sum_{\mu,\kappa',\kappa} \left(\alpha^2(t)\lambda_\mu \cosh^2(r_\mu) + \alpha^{*2}(t)\lambda^*_\mu \sinh^2(r_\mu) \mathrm{e}^{2i\phi_\mu} \right) \\
& \times Y_{\kappa'\mu} Y_{\kappa\mu} W^*_{\kappa'\sigma} W^*_{\kappa\nu} \left[x_{\kappa'}^{1/2} x_\kappa^{1/2} - x_{\kappa'}^{-1/2} x_\kappa^{-1/2} \right]
\end{aligned}
\tag{D.56}
$$

$$
K_{\sigma\nu} = \sum_{\mu,\mu',\kappa',\kappa} Y_{\kappa'\mu} Y^*_{\kappa\mu'} W^*_{\kappa'\sigma} W_{\kappa\nu} \cosh(r_{\mu'}) \cosh(r_\mu) \tag{D.57}
$$

$$
\begin{aligned}
& \times \left(i\Omega_{\mu\mu'} \left[x_{\kappa'}^{1/2} x_\kappa^{-1/2} - x_{\kappa'}^{-1/2} x_\kappa^{1/2} \right] - \Gamma_{\mu'\mu} \left[x_{\kappa'}^{1/2} x_\kappa^{-1/2} + x_{\kappa'}^{-1/2} x_\kappa^{1/2} - 2 x_{\kappa'}^{1/2} x_\kappa^{1/2} \right] \right) \\
& + \sum_{\mu,\mu',\kappa',\kappa} Y_{\kappa'\mu} Y^*_{\kappa\mu'} W^*_{\kappa'\sigma} W_{\kappa\nu} \sinh(r_{\mu'}) \sinh(r_\mu) \mathrm{e}^{i(\phi_\mu - \phi_{\mu'})} \\
& \times \left(i\Omega_{\mu'\mu} \left[x_{\kappa'}^{1/2} x_\kappa^{-1/2} - x_{\kappa'}^{-1/2} x_\kappa^{1/2} \right] - \Gamma_{\mu\mu'} \left[x_{\kappa'}^{1/2} x_\kappa^{-1/2} + x_{\kappa'}^{-1/2} x_\kappa^{1/2} - 2 x_{\kappa'}^{-1/2} x_\kappa^{-1/2} \right] \right) \\
& - 2i \sum_{\mu,\kappa',\kappa} \cosh(r_\mu)\sinh(r_\mu) \left(\alpha^2(t)\lambda_\mu \mathrm{e}^{i\phi_\mu} + \alpha^{*2}(t)\lambda^*_\mu \mathrm{e}^{-i\phi_\mu} \right) \\
& \times Y_{\kappa'\mu} Y^*_{\kappa\mu} W^*_{\kappa'\sigma} W_{\kappa\nu} \left[x_{\kappa'}^{-1/2} x_\kappa^{1/2} - x_{\kappa'}^{1/2} x_\kappa^{-1/2} \right]
\end{aligned}
\tag{D.58}
$$

Now in order for Eq. (D.38) to be satisfied, the three terms must add to zero, $T_1 + T_2 + T_3 = 0$. We achieve this by making the time-dependent coefficients in front of each operator $\widehat{A}^\dagger_\sigma \widehat{A}_\nu$, $\widehat{Q}_{\sigma_\nu}$, and $\widehat{P}_{\sigma_\nu}$ equal zero. First, we let the sum of the coefficients in front of $\widehat{Q}_{\sigma\nu}$ and $\widehat{P}_{\sigma\nu}$ in T_2 and T_3 equal zero

$$0 = \mathrm{Re}[D_{\sigma\nu}] + \mathrm{Re}[E_{\sigma\nu}], \tag{D.59}$$

$$0 = \mathrm{Im}[D_{\sigma\nu}] + \mathrm{Im}[E_{\sigma\nu}]. \tag{D.60}$$

These are satisfied if we let

$$D_{\sigma\nu} = -E_{\sigma\nu}. \tag{D.61}$$

As we shall see, solving Eq. (D.61) gives the differential equations for dr_μ/dt and $d\phi_\mu/dt$. To start, we multiply both sides of Eq. (D.61) by $\sum_{\sigma,\nu} W_{\kappa\sigma}W_{\kappa'\nu}$ and use Eq.(D.51) to obtain

$$\left[x_\kappa^{1/2}x_{\kappa'}^{1/2} - x_\kappa^{-1/2}x_{\kappa'}^{-1/2}\right]\sum_\mu\left(\frac{1}{2}\frac{dr_\mu}{dt} + \frac{i}{4}\sinh(2r_\mu)\frac{d\phi_\mu}{dt}\right)\mathrm{e}^{i\phi_\mu}Y_{\kappa\mu}Y_{\kappa'\mu} = -\sum_{\sigma,\nu}W_{\kappa\sigma}W_{\kappa'\nu}E_{\sigma\nu}, \tag{D.62}$$

where we used the fact that $\boldsymbol{W}^\dagger\boldsymbol{W} = 1$. Multiplying Eq. (D.62) by $\sum_{\kappa,\kappa'} Y^*_{\kappa\mu'}Y^*_{\kappa'\mu'}$ and using the orthogonality relation $\boldsymbol{Y}^\dagger\boldsymbol{Y} = 1$, we obtain

$$\frac{1}{2}\frac{dr_\mu}{dt} + \frac{i}{4}\sinh(2r_\mu)\frac{d\phi_\mu}{dt} = -\mathrm{e}^{-i\phi_\mu}\sum_{\kappa,\kappa'}\frac{Y^*_{\kappa\mu}Y^*_{\kappa'\mu}}{x_\kappa^{1/2}x_{\kappa'}^{1/2} - x_\kappa^{-1/2}x_{\kappa'}^{-1/2}}\sum_{\sigma,\nu}W_{\kappa\sigma}W_{\kappa'\nu}E_{\sigma\nu}. \tag{D.63}$$

Equating the real and imaginary parts of both sides of Eq. (D.63) gives the following equations for dr_μ/dt and $d\phi_\mu/dt$:

$$\frac{dr_\mu}{dt} = -\sum_{\kappa,\kappa',\sigma,\nu}\frac{\mathrm{e}^{-i\phi_\mu}Y^*_{\kappa\mu}Y^*_{\kappa'\mu}W_{\kappa\sigma}W_{\kappa'\nu}E_{\sigma\nu} + \mathrm{e}^{i\phi_\mu}Y_{\kappa\mu}Y_{\kappa'\mu}W^*_{\kappa\sigma}W^*_{\kappa'\nu}E^*_{\sigma\nu}}{x_\kappa^{1/2}x_{\kappa'}^{1/2} - x_\kappa^{-1/2}x_{\kappa'}^{-1/2}}, \tag{D.64}$$

$$\frac{d\phi_\mu}{dt} = \frac{2i}{\sinh(2r_\mu)}\sum_{\kappa,\kappa',\sigma,\nu}\frac{\mathrm{e}^{-i\phi_\mu}Y^*_{\kappa\mu}Y^*_{\kappa'\mu}W_{\kappa\sigma}W_{\kappa'\nu}E_{\sigma\nu} - \mathrm{e}^{i\phi_\mu}Y_{\kappa\mu}Y_{\kappa'\mu}W^*_{\kappa\sigma}W^*_{\kappa'\nu}E^*_{\sigma\nu}}{x_\kappa^{1/2}x_{\kappa'}^{1/2} - x_\kappa^{-1/2}x_{\kappa'}^{-1/2}}. \tag{D.65}$$

Now to simplify Eqs. (D.64) and (D.65) we focus on the first term in the sum. Using the expression for $E_{\sigma\nu}$ in Eq. (D.56), we obtain

$$\begin{aligned}
&\sum_{\kappa,\kappa',\sigma,\nu} \frac{\mathrm{e}^{-i\phi_\mu} Y^*_{\kappa\mu} Y^*_{\kappa'\mu} W_{\kappa\sigma} W_{\kappa'\nu} E_{\sigma\nu}}{x_\kappa^{1/2} x_{\kappa'}^{1/2} - x_\kappa^{-1/2} x_{\kappa'}^{-1/2}} = \\
&= \sum_{\kappa,\kappa',\mu',\sigma'} \mathrm{e}^{i(\phi_{\sigma'}-\phi_\mu)} \cosh(r_{\mu'}) \sinh(r_{\sigma'}) Y_{\kappa\sigma'} Y_{\kappa'\mu'} Y^*_{\kappa\mu} Y^*_{\kappa'\mu} \\
&\times \left(i\Omega_{\mu'\sigma'} - \Gamma_{\sigma'\mu'} \frac{x_{\kappa'}^{-1/2} x_\kappa^{-1/2} + x_{\kappa'}^{1/2} x_\kappa^{1/2} - 2x_\kappa^{-1/2} x_{\kappa'}^{1/2}}{x_\kappa^{1/2} x_{\kappa'}^{1/2} - x_\kappa^{-1/2} x_{\kappa'}^{-1/2}} \right) \\
&+ i\mathrm{e}^{-i\phi_\mu} \sum_{\kappa,\kappa',\mu'} \left(\alpha^2(t) \lambda_{\mu'} \cosh^2(r_{\mu'}) + \alpha^{*2}(t) \lambda^*_{\mu'} \sinh^2(r_{\mu'}) \mathrm{e}^{2i\phi_{\mu'}} \right) Y_{\kappa\mu'} Y_{\kappa'\mu'} Y^*_{\kappa\mu} Y^*_{\kappa'\mu} \\
&= i \left(\alpha^2(t) \lambda_\mu \cosh^2(r_\mu) \mathrm{e}^{-i\phi_\mu} + \alpha^{*2}(t) \lambda^*_\mu \sinh^2(r_\mu) \mathrm{e}^{i\phi_\mu} \right) + i\Omega_{\mu\mu} \cosh(r_\mu) \sinh(r_\mu) \\
&- \sum_{\kappa,\kappa',\mu',\sigma'} \mathrm{e}^{i(\phi_{\sigma'}-\phi_\mu)} \cosh(r_{\mu'}) \sinh(r_{\sigma'}) Y_{\kappa\sigma'} Y_{\kappa'\mu'} Y^*_{\kappa\mu} Y^*_{\kappa'\mu} \Gamma_{\sigma'\mu'} \\
&\times \frac{x_{\kappa'}^{-1/2} x_\kappa^{-1/2} + x_{\kappa'}^{1/2} x_\kappa^{1/2} - 2x_\kappa^{-1/2} x_{\kappa'}^{1/2}}{x_\kappa^{1/2} x_{\kappa'}^{1/2} - x_\kappa^{-1/2} x_{\kappa'}^{-1/2}}. \qquad \text{(D.66)}
\end{aligned}$$

Using Eq. (D.46) we can write Eq. (D.66) in terms of the thermal photon numbers as

$$\begin{aligned}
&\sum_{\kappa,\kappa',\sigma,\nu} \frac{\mathrm{e}^{-i\phi_\mu} Y^*_{\kappa\mu} Y^*_{\kappa'\mu} W^*_{\sigma\kappa} W^*_{\nu\kappa'} E_{\sigma\nu}}{x_\kappa^{1/2} x_{\kappa'}^{1/2} - x_\kappa^{-1/2} x_{\kappa'}^{-1/2}} = \\
&= i \left(\alpha^2(t) \lambda_\mu \cosh^2(r_\mu) \mathrm{e}^{-i\phi_\mu} + \alpha^{*2}(t) \lambda^*_\mu \sinh^2(r_\mu) \mathrm{e}^{i\phi_\mu} \right) + i\Omega_{\mu\mu} \cosh(r_\mu) \sinh(r_\mu) \\
&+ \sum_{\kappa,\kappa',\mu',\sigma'} \mathrm{e}^{i(\phi_{\sigma'}-\phi_\mu)} \cosh(r_{\mu'}) \sinh(r_{\sigma'}) Y_{\kappa\sigma'} Y_{\kappa'\mu'} Y^*_{\kappa\mu} Y^*_{\kappa'\mu} \Gamma_{\sigma'\mu'} \frac{n_\kappa - n_{\kappa'} + 1}{n_{\kappa'} + n_\kappa + 1} \qquad \text{(D.67)}
\end{aligned}$$

The complex conjugate of Eq. (D.67) is

$$\sum_{\kappa,\kappa',\sigma,\nu} \frac{\mathrm{e}^{i\phi_\mu} Y_{\kappa\mu} Y_{\kappa'\mu} W_{\sigma\kappa} W_{\nu\kappa'} E^*_{\sigma\nu}}{x_\kappa^{1/2} x_{\kappa'}^{1/2} - x_\kappa^{-1/2} x_{\kappa'}^{-1/2}} =$$

$$= -i\left(\alpha^2(t)\lambda_\mu \sinh^2(r_\mu)\mathrm{e}^{-i\phi_\mu} + \alpha^{*2}(t)\lambda_\mu^* \cosh^2(r_\mu)\mathrm{e}^{i\phi_\mu}\right) - i\Omega_{\mu\mu}\cosh(r_\mu)\sinh(r_\mu)$$
$$+ \sum_{\kappa,\kappa',\mu',\sigma'} \mathrm{e}^{-i(\phi_{\sigma'}-\phi_\mu)} \cosh(r_{\mu'})\sinh(r_{\sigma'}) Y^*_{\kappa\sigma'} Y^*_{\kappa'\mu'} Y_{\kappa\mu} Y_{\kappa'\mu} \Gamma_{\sigma'\mu'} \frac{n_\kappa - n_{\kappa'} + 1}{n_{\kappa'} + n_\kappa + 1}, \qquad \text{(D.68)}$$

where we used the fact that $\Omega^*_{\mu\mu} = \Omega_{\mu\mu}$. Putting Eqs. (D.67) and (D.68) into Eqs. (D.64) and (D.65) give the equations for dr_μ/dt and $d\phi_\mu/dt$ in the text, Eqs. (5.9) and Eq. (5.10).

Now we derive the equation for dn_μ/dt. To do this, we let the sum of the coefficients in front of the operators $\widehat{A}^\dagger_\sigma \widehat{A}_\nu$ in T_1, T_2, and T_3 be zero. Doing this, we obtain the equation

$$0 = -\sum_\kappa \frac{1}{n_\kappa(1+n_\kappa)} \frac{dn_\kappa}{dt} W^*_{\kappa\sigma} W_{\kappa\nu} + F_{\sigma\nu} + K_{\sigma\nu}. \qquad \text{(D.69)}$$

Multiplying Eq. (D.69) by $\sum_{\sigma\nu} W_{\kappa'\sigma} W^*_{\kappa'\nu}$ and using $\boldsymbol{W}^\dagger \boldsymbol{W} = 1$, we obtain

$$\frac{1}{n_\kappa(1+n_\kappa)} \frac{dn_\kappa}{dt} = \sum_{\sigma\nu} W_{\kappa\sigma} W^*_{\kappa\nu} F_{\sigma\nu} + \sum_{\sigma\nu} W_{\kappa\sigma} W^*_{\kappa\nu} K_{\sigma\nu}. \qquad \text{(D.70)}$$

The first term on the right-hand side of Eq. (D.70) is zero, which can be proved by using Eq. (D.50) and $\boldsymbol{W}^\dagger \boldsymbol{W} = 1$. For the second term, it can be shown that by putting Eq. (D.57) into Eq. (D.70) we obtain

$$\frac{1}{1+n_\kappa}\frac{dn_\kappa}{dt} = -\frac{2n_\kappa}{1+n_\kappa}\sum_{\nu,\sigma} Y_{\kappa\nu}Y^*_{\kappa\sigma}\Gamma_{\sigma\nu}\cosh(r_\nu)\cosh(r_\sigma) + 2\sum_{\nu,\sigma} Y_{\kappa\nu}Y^*_{\kappa\sigma}\Gamma_{\nu\sigma}\sinh(r_\nu)\sinh(r_\sigma)\mathrm{e}^{i(\phi_\nu-\phi_\sigma)}, \tag{D.71}$$

which is Eq. (5.11) in the main text.

Finally we have to show that the sum of the coefficients in front of the identity operator in T_1 and T_3 is zero. Collecting the appropriate coefficients from T_1 and T_3, we obtain

$$0 = \sum_\kappa \frac{1}{1+n_\kappa}\frac{dn_\kappa}{dt} + 2\sum_{\nu,\sigma,\kappa}\Gamma_{\sigma\nu}\cosh(r_\sigma)\cosh(r_\nu)Y^*_{\kappa\sigma}Y_{\kappa\nu}\frac{n_\kappa}{1+n_\kappa} - 2\sum_\nu \Gamma_{\nu\nu}\sinh^2(r_\nu). \tag{D.72}$$

Putting Eq. (D.71) into Eq. (D.72) and using the fact that $\boldsymbol{Y}^\dagger\boldsymbol{Y} = 1$, it can be shown that Eq. (D.72) is satisfied.

Therefore we have proven that the MSTS is the solution to the Lindblad master equation, and we derived three coupled-equations for the squeezing amplitude, squeezing phase, and thermal photon numbers.

D.4 Solving the coupled equations from an initial vacuum state

In this section, we discuss how to solve the coupled-equations (see Eqs. (5.9) - (5.11) in the main text) for a system that initially starts in the *vacuum state*. At time $t = 0$ the vacuum state is defined by

$$r_\mu(0) = 0, \tag{D.73}$$

$$n_\kappa(0) = 0, \tag{D.74}$$

for all μ and κ. Putting these initial conditions into Eq. (5.9), we obtain

$$\dot{r}_\mu(0) = \frac{2\left|\alpha(0)\right|^2 \left|\lambda_\mu\right|}{\hbar} \sin\left(-\phi_\mu(0) + \theta_\mu\right), \tag{D.75}$$

where we define

$$\alpha(t) = \alpha_P(t) \exp(-i\omega_P t), \tag{D.76}$$

and

$$\lambda_\mu = \left|\lambda_\mu\right| \exp(i\theta_\mu), \tag{D.77}$$

where θ_μ is a real number. We choose the initial squeezing phase, $\phi_\mu(0)$, to be

$$\phi_\mu(0) = \theta_\mu - \frac{\pi}{2}, \tag{D.78}$$

such that is maximizes the squeezing amplitude at the next time-step, $r_\mu(\Delta t)$:

$$r_\mu(\Delta t) = \frac{2\left|\alpha(0)\right|^2 \left|\lambda_\mu\right|}{\hbar} \Delta t + O\left((\Delta t)^2\right). \tag{D.79}$$

Now, let us move on to the equation for the squeezing phase, Eq. (5.10). It is easily shown that using Eqs. (D.73), (D.74), and (D.78) will result in the second and third terms in Eq. (10) being indeterminate (0/0). Thus, at $t = 0$, we write this equation as

$$\dot{\phi}_\mu(0) = -2\Omega_{\mu\mu} - \zeta_\mu, \tag{D.80}$$

where we let ζ_μ be the indeterminate form. We are unable to solve these equations unless we define ζ_μ. We define ζ_μ by requiring that the derivatives of the squeezing phase at $t = \Delta t$ and $t = 0$ are the same,

$$\dot{\phi}_\mu(\Delta t) = \dot{\phi}_\mu(0), \tag{D.81}$$

such that initially the squeezing phase is a linear function of time. Putting Eqs. (D.73), (D.74), (D.78), and (D.79) into Eq. (5.10) and using the fact that $n_\kappa(\Delta t) = 0$ (which can be proven by writing Eq. (5.11) as a difference equation and using the initial conditions) it can be shown that

$$\dot{\phi}_\mu(\Delta t) = -2\omega_P + \zeta_\mu. \tag{D.82}$$

Using Eq. (D.82) in Eq. (D.81), the indeterminate form ζ_μ is defined as

$$\zeta_\mu = -\Omega_{\mu\mu} + \omega_P. \tag{D.83}$$

To solve the coupled-equations Eqs. (5.9) - (5.11) we use Matlab's ode45 function, that is based on a Runge-Kutta method. The initial conditions that we use for the squeezing amplitudes, thermal photon numbers, and squeezing phases are in Eqs. (D.73), (D.74), and (D.78). We have to write an additional condition in the code that imposes the condition that at $t = 0$ the derivatives of the squeezing phases are equal to $\dot{\phi}_\mu(0) = -\Omega_{\mu\mu} - \omega_P$, otherwise the program will return a division-by-zero error (as discussed above). The solution is sensitive to the initial squeezing phases $\phi_\mu(0)$. It is crucial that they are set to precisely the values given in Eq. (D.78). However, we find that the initial value of the derivative of the phase $\dot{\phi}_\mu(0)$ has little impact on the final solution, since it quickly settles to the correct value, given by $-\Omega_{\mu\mu} - \omega_P$.

D.5 Details for the two-cavity system results

In this section, we give the details on how we obtain our results for the two-cavity system in the paper. Specifically, we give the physical dimensions of the photonic crystal slab and its material properties, and we derive the nonlinear parameter for SFWM using a Gaussian pump.

We start by giving the details of the structure in Fig. 5.2(a). The structure is placed in a computational volume of $13d \times 14d \times 3d$, where $d = 480$nm is the lattice period. The dielectric slab is parallel to the xy plane and centered at $z = 0$. It is made from silicon with an index of $n = 3.4$ and has a thickness of $0.6d$. The photonic crystal is created by periodically drilling airholes (shown as white circles) of radius $0.35d$ into the silicon slab. The photonic crystal is finite in the x-y plane, with 10 periods in the x direction and 9 periods in the y direction. The individual cavities are formed by removing an airhole.

We apply perfectly-matched layers (PMLs) to the boundary of the computational volume to simulate the transmission of energy into a continuum of modes. For the top (T) and bottom (B) individual cavity modes, we obtain the frequencies $\widetilde{\Omega}_T d/(2\pi c) = 0.3027 - i5.62 \times 10^{-5}\,(Q_T = 2691)$ and $\widetilde{\Omega}_B d/(2\pi c) = 0.3028 - i9.54 \times 10^{-4}\,(Q_B = 159)$. Note that Q_B is less than Q_T, since the bottom cavity mode leaks into the dielectric slab more. The quasimode frequencies that are obtained from tight-binding [9], where the individual cavity modes form the basis, are $\tilde{\omega}_1 d/(2\pi c) = 0.3026 - i3.12 \times 10^{-4}\,(Q_1 = 485)$ and $\tilde{\omega}_2 d/(2\pi c) = 0.3029 - i6.93 \times 10^{-4}\,(Q_2 = 218)$.

Following the presentation of H. Seifoory *et. al.* in Ref. [89] we now give the details on the Gaussian pump that is used to generate the squeezed light in the quasimodes. As shown in Fig. 5.2(a), the two cavities are pumped from above with a Gaussian beam polarized in the y direction. The beam is focused between the two cavities at $z = 0$ and has a Gaussian transverse profile given by

$$f(x,y) \equiv \frac{1}{\sqrt{\pi} W_0} \exp\left[-\frac{2\pi^2}{W_0^2}\left((x-x_0)^2 + y^2\right)\right], \tag{D.84}$$

where W_0 is the spot size at $z = 0$ and x_0 is the position on the x axis where the pulse is at its maximum. The full width at half maximum (FWHM) is related to the spot size with FWHM $= \sqrt{\ln(2)} W_0/\pi$.

Next we derive the nonlinear parameter for SFWM for the Gaussian beam. We assume the slab thickness is much smaller than the curvature of the optical wavefront, such that it does not have a significant effect on the pump. We can thus take the pump modes to be plane waves in free space, polarized in the y direction

$$N_{\boldsymbol{q}y}(\boldsymbol{r}) = \mathrm{e}^{i\boldsymbol{q}\cdot\boldsymbol{r}}, \tag{D.85}$$

where $\boldsymbol{q}$ is a continuous index that labels the different modes in three dimensions. We make the undepleted pump approximation, and let the pump quasimode annihilation operators, $\widehat{c}_{\boldsymbol{q}}$, be replaced by their expectation value using the coherent state amplitude for the Gaussian beam

$$\langle\alpha(t)|\,\widehat{c}_{\boldsymbol{q}}\,|\alpha(t)\rangle \equiv |\alpha_P|\alpha(q_x,q_y)\beta(q_z)\exp\left(-i\omega_{|\boldsymbol{q}|}t\right), \tag{D.86}$$

where the frequency $\omega_{|\boldsymbol{q}|}$ is real since the pump is in free-space modes and $|\boldsymbol{q}|^2 \equiv q_x^2+q_y^2+q_z^2$. The function

$$\alpha(q_x,q_y) = \iint dxdyf(x,y)\mathrm{e}^{-i(q_xx+q_yy)}, \tag{D.87}$$

is the Fourier transform of the transverse profile $f(x,y)$, given in Eq. (D.84). It is normalized according to $\iint dq_xdq_y|\alpha(q_x,q_y)|^2 = 1$. The function $\beta(q_z)$ is sharply peaked at the value q_P

$$\beta(q_z) \equiv \sqrt{\frac{L}{\sqrt{\pi}}}\exp\left(-\frac{L^2}{2}(q_z-q_P)^2\right), \tag{D.88}$$

where $L \equiv 3d$ is the height of the computational volume. It is chosen, such that

$$\int dq_z|\beta(q_z)|^2 = 1. \tag{D.89}$$

The average photon number for the pump is

$$N_P \equiv \int d^3\boldsymbol{q}\, \langle \alpha(t)|\, \widehat{c}^{\dagger}_{\boldsymbol{q}} \widehat{c}_{\boldsymbol{q}}\, |\alpha(t)\rangle \tag{D.90}$$

$$= |\alpha_P|^2, \tag{D.91}$$

which follows from the normalization of $\alpha(q_x, q_y)$ and $\beta(q_z)$.

In order to write $\widehat{H}_{\mathrm{NL}}$ in the form in Eq. (D.20) where the nonlinear parameter, G_{ml} is independent of time, we assume that near the surface of the slab the pump is propagating dominantly in the z direction, by letting $|\boldsymbol{q}| \simeq q_z$. Thus we replace the frequency $\omega_{|\boldsymbol{q}|}$ in Eq. (D.86) with ω_{q_z}. Then $\widehat{H}_{\mathrm{NL}}$ (Eq. (D.20)) can be written

$$\widehat{H}_{\mathrm{NL}} = \hbar|\alpha_P|^2 \sum_{m,l} \widehat{c}^{\dagger}_m \widehat{c}^{\dagger}_l \iint d^3\boldsymbol{q} d^3\boldsymbol{q}' G_{ml\boldsymbol{q}\boldsymbol{q}'} \alpha(q_x, q_y)\beta(q_z)\alpha(q'_x, q'_y)\beta(q'_z) \exp\bigl(-i[\omega_{q_z} + \omega_{q'_z}]t\bigr) + \mathrm{H.c.}, \tag{D.92}$$

where

$$G_{ml\boldsymbol{q}\boldsymbol{q}'} = \frac{9\hbar}{16\epsilon_0} \sum_{i,j} \sqrt{\widetilde{\omega}^*_m \widetilde{\omega}^*_l \omega_{q_z} \omega_{q'_z}} \int d^3\boldsymbol{r} \chi^{(3)}_{ijyy}(\boldsymbol{r}) N^*_{mi}(\boldsymbol{r}) N^*_{lj}(\boldsymbol{r}) \mathrm{e}^{i(\boldsymbol{q}+\boldsymbol{q}')\cdot\boldsymbol{r}}. \tag{D.93}$$

We assume that the interaction is strongest within the slab, and the interaction strength does not vary significantly within the slab, such that we can set $z = 0$ in Eq. (D.93), to obtain $\exp(iq_z z) = 1$.

The integral in Eq. (D.92) can be factored into an integral over q_z only and a separate integral over q_x and q_y only. Doing the integral over q_z we obtain an overall function of time, $\alpha(t)$, for the coherent state, defined as

$$\alpha(t) \equiv |\alpha_P| \sqrt{\frac{L}{2\sqrt{\pi}\omega_P}} \int dq_z \sqrt{\omega_{q_z}} \beta(q_z) \exp\left(-i\omega_{q_z} t\right), \tag{D.94}$$

where $\omega_P \equiv \omega_{q_P}$. Since $\beta(q_z)$ is sharply peaked at q_P, the integral in Eq. (D.94) is dominated by a narrow band of q_z centered on q_P. Thus we can pull out from the integral the fast oscillating exponential term, $\exp(-i\omega_P t)$, and what is left is a slowly-varying function of time. Taking the limit as the height of the computational volume goes to infinity, $L \to \infty$, the function $\alpha(t)$ approaches a continuous-wave, with $\alpha(t) \simeq |\alpha_P| \exp(-i\omega_P t)$. Doing the integrals over q_x and q_y in Eq. (D.92), we obtain the approximate expression

$$G_{ml} \simeq \frac{9\hbar\omega_P}{16\epsilon_0 V_{\text{eff}}} \sqrt{\widetilde{\omega}_m^* \widetilde{\omega}_l^*} \int d^3\boldsymbol{r}\, \chi^{(3)}_{yyyy}(\boldsymbol{r}) N^*_{my}(\boldsymbol{r}) N^*_{ly}(\boldsymbol{r}) \left[f(x,y)\right]^2, \tag{D.95}$$

where we define the effective volume $V_{\text{eff}} \equiv \pi W_0^2 L/(2\sqrt{\pi}(2\pi)^4)$. To obtain this result we assume that only the diagonal components, $\chi^{(3)}_{yyyy}(\boldsymbol{r})$, of the third-order nonlinear tensor for silicon are non-zero [123]. The quasimode profiles $N_{my}(\boldsymbol{r})$ and $N_{ly}(\boldsymbol{r})$ are obtained from the tight-binding model used in Ref. [9]. Therefore, considering Eqs. (D.94) and (D.93), we have shown that Eq. (D.92) is equivalent to Eq. (D.20), as we require.

To obtain our results, we let

$$\frac{9\hbar\omega_P \chi^{(3)}_{yyyy}}{16\epsilon_0 V_{\text{eff}}} |\alpha_P|^2 = 1, \tag{D.96}$$

where $\chi^{(3)}_{yyyy} = 2.45 \times 10^{-19}\text{m}^2\text{V}^{-2}$ is the third-order nonlinear susceptibility for silicon

[123]. Eq. (D.96) is satisfied for a spot size of $W_0 = 20d$, and an average number of photons in the pump of $|\alpha_P|^2 = 3.87 \times 10^7$. We choose this combination of parameters because it produces significant squeezing of the vacuum noise without generating too many photons. Using the nonlinear parameter in Eq. (D.95), we can construct the $\boldsymbol{S}$ matrix in Eq. (D.32), and then perform the Takagi factorization on it to get the matrix $\boldsymbol{U}$ and the singular values $\boldsymbol{\lambda}$.